SYNTHESES AND CHARACTERIZATION OF XeO_4 AND OXIDE FLUORIDES OF XENON(VIII), OSMIUM(VIII), IODINE(VII), AND XENON(II)

By

MICHAEL GERKEN

A Thesis

Submitted to the School of Graduate Studies

in Partial Fulfilment of the Requirements

for the Degree

Doctor of Philosophy

McMaster University

SYNTHESES AND CHARACTERIZATION OF XeO_4 AND OXIDE FLUORIDES OF XENON(VIII), OSMIUM(VIII), IODINE(VII), AND XENON(II)

In memoriam

Jens Gerken

DOCTOR OF PHILOSOPHY (2000) McMaster University

(Chemistry) Hamilton, Ontario

TITLE: Syntheses and Characterization of XeO_4 and Oxide Fluorides of Xenon(VIII), Osmium(VIII), Iodine(VII), and Xenon(II)

AUTHOR: Michael Gerken, Dipl.-Chem. (Gerhard-Mercator Universität Duisburg)

SUPERVISOR: Professor G.J. Schrobilgen

NUMBER OF PAGES: xxix, 354

ABSTRACT

Xenon tetroxide was stabilized in SO_2ClF, BrF_5, and HF solvents rendering its ^{129}Xe and ^{17}O NMR spectroscopic characterization possible. The high symmetry about xenon in XeO_4 allowed for the observation of the first ^{131}Xe resonance of chemically bonded xenon. Spin-lattice relaxation time measurements for ^{129}Xe and ^{131}Xe showed that the spin-rotation and the quadrupolar relaxation, respectively, are the predominent mechanisms of relaxation in XeO_4. The investigation of the ^{129}Xe NMR spectrum of $[Na]_4[XeO_6]$ in solution and solid state corrected the previously reported, erroneous value. Xenon tetroxide was shown to act as a Lewis acid towards CH_3CN solvent and fluoride ions yielding $XeO_4(CH_3CN)$ and $XeO_4F_2^{2-}$, respectively. The $XeO_4(CH_3CN)$ adduct was characterized by ^{129}Xe NMR and Raman spectroscopy and contains the first example of a Xe(VIII)-N bond. The $XeO_4F_2^{2-}$ anion was shown to exist as a mixture of its *cis*- and *trans*-isomers based on Raman spectroscopy. For the first time, XeO_3F_2 was prepared in SO_2ClF, BrF_5, and HF solvents and characterized by ^{19}F and ^{129}Xe NMR spectroscopy. The novel $XeO_3F_3^-$ anion was prepared in low concentrations in SO_2ClF and BrF_5 solvents and was identified by ^{19}F and ^{129}Xe NMR spectroscopy and shown to have a facial trioxo configuration.

In the present work, the OsO_4F^- anion was prepared and characterized by X-ray crystallography and vibrational spectroscopy as its $N(CH_3)_4^+$ salt. The $OsO_4F_2^{2-}$ anion had

been prepared in admixture with the OsO_4F^- anion and was characterized by vibrational spectroscopy showing its *cis*-difluoro arrangement. The OsO_4F^- anion was shown to be identical to the anion that had been previously reported and charactized by vibrational and EXAFS spectroscopy and erroneously assigned as the *cis*-$OsO_4F_2^{2-}$ anion. The Lewis acid-base reaction between OsO_3F_2 and fluoride ions and CH_3CN yielded the $OsO_3F_3^-$ anion and the $OsO_3F_2(CH_3CN)$ adduct, respectively. The unambiguous identification of the $OsO_3F_3^-$ anion as the exclusive, facial trioxo isomer was accomplished by determining the crystal structure of $[N(CH_3)_4][OsO_3F_3]$ and by vibrational spectroscopic characterization of the $N(CH_3)_4^+$ and NO^+ salts. The $OsO_3F_2(CH_3CN)$ adduct, however, exists as a mixture of its *fac*- and *mer*-isomers in solution and in the solid state based on ^{19}F and ^{15}N NMR and Raman spectroscopy.

The Os(VIII) oxide fluoride, OsO_3F_2, acts as a Lewis base towards strong acids like AsF_5 and SbF_5 in HF solvent yielding $[OsO_3F][AsF_6]$, $[OsO_3F][HF]_2[AsF_6]$, $[Os_2O_6F_3][AsF_6]$, $[OsO_3F][HF][SbF_6]$, and $[OsO_3F][HF]_2[SbF_6]$, which were characterized by Raman spectroscopy. The crystal structures of $[OsO_3F][AsF_6]$, $[OsO_3F][HF]_2[AsF_6]$, and $[OsO_3F][HF][SbF_6]$ showed that the strongly electrophilic OsO_3F^+ cation expands its coordination sphere by forming contacts with the PnF_6^- anions (Pn = As, Sb) and by coordination of HF solvent molecules. The closest approximation to a naked OsO_3F^+ cation was found in $[OsO_3F][Sb_3F_{16}]$ which was prepared from pure SbF_5 and was characterized by Raman and ^{19}F NMR spectroscopy and by X-ray crystallography.

Osmium(VIII) in *cis*-OsO_2F_4 was found to expand its coordination number to seven upon reaction with fluoride ions and CH_3CN yielding the $OsO_2F_5^-$ anion and $OsO_2F_4(CH_3CN)$. Raman and ^{19}F NMR spectroscopy showed that the $OsO_2F_5^-$ anion has a structure based on a monocapped trigonal prism with a *cis*-dioxo arrangement and a unique fluorine capping a square face formed by four fluorines. NMR spectroscopic data are consistent with a structure for $OsO_2F_4(CH_3CN)$ that is derived from the $OsO_2F_5^-$ anion by formal replacement of a fluorine of the square face by CH_3CN.

The $IO_2F_5^{2-}$ anion was formed upon reaction of *trans*-$IO_2F_4^-$ and $[N(CH_3)_4][F]$ and was shown to have a pentagonal bipyramidal *trans*-dioxo structure based on Raman spectroscopy. The $[N(CH_3)_4]_2[IO_2F_5]$ salt was prepared in admixture with $[N(CH_3)_4]$[*cis*-IO_2F_4], since the latter salt did not react with fluoride ions. Crystals of $[N(CH_3)_4]_2[IO_2F_2][HF_2]$ were obtained as a reduction product of the $[N(CH_3)_4]_2[IO_2F_5]$/ $[N(CH_3)_4]$[*cis*-IO_2F_4] mixture in CH_3CN solvent and provide a rare example of coordination of a bridging HF_2^- ligand.

The controlled hydrolysis reaction of $[XeF][AsF_6]$ gave rise to the novel H_2OXeF^+ and $Xe_3OF_3^+$ cations, which were characterized by Raman spectroscopy and X-ray crystallography. The $Xe_3OF_3^+$ and H_2OXeF^+ cations provide the first examples of Xe(II) oxide fluorides. The crystal structure of the trigonal modification of $[Xe_2F_3][AsF_6]$ documents the dimorphism of the $[Xe_2F_3][AsF_6]$ salt that has been known for many years exclusively in its monoclinic modification.

ACKNOWLEDGEMENTS

I wish to thank Prof. Gary J. Schrobilgen for giving me such an interesting and exciting research project and, overall, for his guidance, enthusiasm, his vast experience, his support and his confidence in me. I appreciate to have shared his excitement for basic chemistry research.

I would like to thank the other members of my supervisory committee, Prof. Ronald J. Gillespie and Prof. Richard F.W. Bader for their help and their interest in my research.

I thank Helénè P. A. Mercier for her help with many problems, especially concerning X-ray crystallography, and for her unforgetable French cuisine.

I want to thank Ayaaz M. Pirani for his initiation in air and moisture sensitive work and NMR spectroscopy.

I want to thank Nic LeBlond and Janette Campbell for their friendship over the years and their support in my scientific and personal life during my time in Hamilton.

I would like to thank the old and present members of the lab group for their company: Michael Becher, Barbara Fir, Karsten Koppe, John F. Lehmann, Bernie E. Pointner, Neil Vasdev, and Andreas Wegner.

I am grateful to Brian Sayer, Dr. Don Hughes, Dr. Jim Britten, George Timmins, and Michael Palme for their assistance.

I want to thank Janice L. Hellman from Bruker Canada for her help with recording several FT Raman spectra and Valerie Robinson at the University of Guelph for her help with the solid state NMR sample.

I would like to acknowledge the Ontario Ministry of Education and the Department of Chemistry at McMaster University for their financial support.

Finally, I would like to thank my parents for the emotional and financial support during all these years.

KLEINE ASTER

Ein ersoffener Bierfahrer wurde auf den Tisch gestemmt
Irgendeiner hatte ihm eine dunkelhellila Aster
zwischen die Zähne geklemmt.
Als ich von der Brust aus
unter der Haut
mit einem langem Messer
Zunge und Gaumen herausschnitt
muß ich sie angestoßen haben, denn sie glitt
in das nebenliegende Gehirn.
Ich packte sie ihm in die Bauchhöhle
zwischen die Holzwolle,
als man zunähte.
Trinke dich satt in deiner Vase!
Ruhe sanft,
kleine Aster!

(1912, Gottfried Benn)

A drowned truck-driver was propped on the slab.
Someone had stuck a lavender aster
between his teeth.
As I cut out the tongue and the palate,
through the chest
under the skin,
with a long knife,
I must have touched the flower, for it slid
into the brain lying next.
I packed it into the cavity of the chest
among the excelsior
as it was sewn up.
Drink yourself full in your vase!
Rest softly,
little aster!

translated by Babette Deutsch

LIST OF ABBREVIATIONS AND SYMBOLS

General

AWG	American wire gauge
ax	axial
BDH	British drug house
bupy	4-*tert*-butylpyridine
CCD	charge coupled device
DFT	density functional theory
dmpe	$(CH_3)_2PCH_2CH_2P(CH_3)_2$
eq	equatorial
EXAFS	extended X-ray absorption fine structure spectroscopy
FEP	perfluoroethylene/perfluoropropylenecopolymer
HOMO	highest occupied molecular orbital
HPLC	high performance liquid chromatography
i.d.	inner diameter
IR	infrared spectroscopy
Kel-F	chlorotrifluoroethylene polymer
LDFT	local density functional theory
MO	molecular orbital

MP-2	Møller Plessert, second order
MW	microwave spectroscopy
NLDFT	non-local density functional theory
NMR	nuclear magnetic resonance
o.d.	outer diameter
PE	photoelectron spectroscopy
Ph	phenyl
PTFE	tetrafluoroethylene polymer
RHF	restricted Hartree Fock
SAE	Society of Automotive Engineers
SCF	self consistent field
UV	ultraviolet spectroscopy
VSEPR	valence shell electron pair repulsion

Nuclear Magnetic Resonance

δ	chemical shift
I	nuclear spin quantum number
J	scalar coupling constant in Hertz
FID	free induction decay
SF	spectral frequency
SW	sweep width
TD	time domain

PW	pulse width
NS	number of scans
ppm	parts per million
TMS	tetramethylsilane
T_1	spin-lattice relaxation time
T_1^{DD}	dipole-dipole spin-lattice relaxation time
T_1^{CSA}	chemical shift anisotropy spin-lattice relaxation time
T_1^{Q}	quadrupolar spin-lattice relaxation time
T_1^{SC}	scalar coupling spin-lattice relaxation time
T_1^{SR}	spin rotation spin-lattice relaxation time
T_1^{E}	paramagnetic spin-lattice relaxation time
P_u, D_u	imbalance of the valence electrons in the p and d orbitals
$\Delta\nu_{1/2}$	line width at half height
τ_c	rotational correlation time
τ_{SR}	angular momentum correlation time
WF	width factor
Q	quadrupolar moment
q	electric field gradient
η	asymmetry parameter of the electric field gradient
η	solvent viscosity
I_m	moment of inertia

CSA	chemical shift anisotropy

X-ray Crystallography

a, b, c, α, β, γ	cell parameters
V	cell volume
λ	wavelength
Z	molecules per unit cell
mol.wt.	molecular weight
μ	absorption coefficient
$\Delta\delta_{max}$, $\Delta\delta_{min}$	maximum and minimum residual electron density
R	conventional agreement index
R_w	weighted agreement index
w	overall weight parameter
GOOF	goodness of fit

TABLE OF CONTENTS

Page

LIST OF TABLES

LIST OF FIGURES

CHAPTER 1

INTRODUCTION

1.1. Oxidation State +8

The +8 oxidation state is the highest attained oxidation state in the periodic table of the elements and is very rare; only three elements form compounds having the +8 oxidation state, namely, osmium, ruthenium, and xenon.[1] The stabilization of this high oxidation state can only be achieved using highly electronegative elements like F, O, and N. The chemistry of Os(VIII) is the most developed among the three elements because of the high thermodynamic stability of the tetroxide, OsO_4 (ΔH_f° = -390.8 ± 5.9 kJ mol^{-1}),[2] which forms a number of derivatives. While OsO_4 reacts in aqueous alkali solution according to eq. (1.1) yielding red solutions of perosmates $OsO_4(OH)_2^{2-}$, the less stable RuO_4 is readily reduced to $Ru(VII)O_4^-$ under the same conditions (eq. (1.2)).[1,3]

$$OsO_4 + 2OH^- \xrightarrow{NaOH} OsO_4(OH)_2^{2-} \tag{1.1}$$

$$2RuO_4 + 2OH^- \xrightarrow{NaOH} 2RuO_4^- + {}^1/_2O_2 + H_2O \tag{1.2}$$

Other than the stable perxenate anion, XeO_6^{4-}, all the other Xe(VIII) compounds reported in the literature are extremely unstable.[4] Pure XeO_4 is explosive even at -40 °C which renders synthetic chemistry using the tetroxide extremely difficult.[5]

The replacement of oxygen ligands with fluorine ligands generally leads to the destabilization of the +8 oxidation state. While Ru(VIII) oxide fluorides are unkown, *cis*-OsO_2F_4[6,7] and OsO_3F_2[7] are stable compounds and XeO_3F_2[8,9] and XeO_2F_4[9,10] have been prepared in small quantities. In contrast, the highest oxidation state that can be attained in the binary fluorides of these elements is +6 or +7, *i.e.*, XeF_6,[11] RuF_6,[12] and OsF_7,[13] and previous reports of XeF_8[14] and OsF_8[15] have been shown to be erroneous.[16,17]

1.2. Xenon(VIII) Chemistry

Although several chemists suggested the existence[18] of xenon compounds and attempted their syntheses,[19] the reactivity of noble gases was only independently discovered in 1962 by Neil Bartlett (Canada)[20] and Rudolf Hoppe (Germany).[21] Prior to this, the noble gases were generally considered inert and incapable of forming chemical compounds. While the chemistry of krypton is limited to the +2 oxidation state, xenon has been found in the +½, +2, +4, +6, and, +8 oxidation states.[4]

Xenon is the only main-group element occurring in the oxidation state +8 and the first Xe(VIII) compound, $[Na]_4[XeO_6]$, was reported as early as 1963,[22] shortly after the synthesis of the first xenon compounds. Perxenate salts exhibit surprisingly high stabilities and are kinetically and thermodynamically stable at ambient temperatures and pressures. The perxenate anion has been well characterized in the solid state by Raman,[23,24] infrared,[24-26] PE,[27] Auger,[27] and Mössbauer spectroscopy,[28] X-ray crystallography in the $[Na]_4[XeO_6]\cdot 8H_2O$,[22,29] $[Na]_4[XeO_6]\cdot 6H_2O$,[30,31] and, $[K]_4[XeO_6]\cdot 9H_2O$ salts,[32] and X-ray powder diffraction of $[Na]_4[XeO_6]$[33] and in solution by Raman,[23,34] infrared,[23] ^{129}Xe NMR[35] and UV spectroscopy.[36,37] Sodium perxenate can be prepared by hydrolysis of XeF_6 and disportionation of Xe(VI) in alkaline solution according to eqs. (1.3) and (1.4)).[22] A more

$$XeF_{6(s)} + 4OH^-_{(aq)} \xrightarrow{NaOH_{(aq)}} HXeO_{4(aq)}^- + 3HF_{2\,(aq)}^- \quad (1.3)$$

$$2[Na][H][XeO_4]_{(aq)} + 2NaOH_{(aq)} \xrightarrow{NaOH_{(aq)}} [Na]_4[XeO_6]_{(s)} + Xe_{(g)} + O_{2(g)} + 2H_2O_{(l)} \quad (1.4)$$

economic way involves the hydrolysis of XeF_6 in H_2O followed by basification with $NaOH_{(aq)}$ and simultaneous ozonization of the solution (eqs. (1.5) and (1.6)).[38,39] The

$$XeF_6 + 3H_2O \xrightarrow{H_2O} XeO_{3(aq)} + 6HF \quad (1.5)$$

$$XeO_{3(aq)} + O_{3(g)} + 4NaOH_{(aq)} \xrightarrow{NaOH} [Na]_4[XeO_6]_{(s)} + 2H_2O_{(l)} + O_{2(g)} \quad (1.6)$$

potassium salt of perxenate has the propensity to crystallize with XeO_3 in its crystal lattice rendering it explosive in the solid state.[36,40] Foropoulos and Desmarteau[41] generated pure XeO_3 upon reaction of XeF_6 with excess HPO_2F_2 followed by removal of the volatiles at 0 °C. Careful addition of aqueous NaOH to XeO_3 gave an 64% yield of $[Na]_4[XeO_6]$ after two weeks. Other perxenate salts have been prepared by cation exchange in aqueous solution starting from $[Na]_4[XeO_6]$.[23-27,34,40,42,43]

In the late 1960's and early 1970's, the chemistry of Xe(VIII) was extended mainly by John Huston at Argonne National Laboratory who prepared and partially characterized the three other known Xe(VIII) species, XeO_4, XeO_3F_2 and XeO_2F_4. Xenon tetroxide was prepared from perxenate and concentrated H_2SO_4 (eq. (1.7))[44] and is

$$[Na]_4[XeO_6] + 2H_2SO_4 \xrightarrow{H_2SO_{4(conc)}} XeO_4 + 2[Na]_2[SO_4] + 2H_2O \qquad (1.7)$$

reported to be a slightly yellow, extremely unstable, explosive compound having a melting point of -35.9 ± 0.2 °C[9] and a vapour pressure of 25 Torr at 0 °C.[45] The enthalpy of formation for XeO_4 has been determined to be $\Delta H_f° = 642.2$ kJ mol^{-1}.[46] Xenon tetroxide has been structurally characterized in the gas-phase by electron diffraction[47] and infrared spectroscopy,[45] and in the solid state by Raman spectroscopy.[48] The oxide fluoride, XeO_3F_2, has been prepared by the reaction of XeO_4 or $[Na]_4[XeO_6]$ with XeF_6 according to the eqs. (1.8) and (1.9) and has been characterized by mass spectrometry[49] and matrix-

$$XeO_4 + XeF_6 \longrightarrow XeO_3F_2 + XeOF_4 \qquad (1.8)$$

$$[Na]_4[XeO_6] + 3XeF_6 \longrightarrow XeO_3F_2 + 3XeOF_4 + 4NaF \qquad (1.9)$$

isolation Raman and infrared spectroscopy.[8] The vibrational spectra have been interpreted in terms of D_{3h} symmetry. Xenon trioxide difluoride is expected to be monomeric since its melting point is very low (-54.1 ± 0.5 °C) and its vapour pressure at -28 °C (24 Torr) is very high,[9] which contrasts with that of its osmium analogue (see 1.3. Osmium(VIII) Chemistry). The oxide fluoride, XeO_2F_4, was only detected in trace amounts by mass spectrometry and was generated by the reaction of XeO_3F_2 with XeF_6 (eq. (1.10)).[10]

$$XeO_3F_2 + XeF_6 \longrightarrow XeO_2F_4 + XeOF_4 \qquad (1.10)$$

1.3. Osmium(VIII) Chemistry

The starting material for all Os(VIII) chemistry is OsO_4, a stable volatile, yellow solid having a melting point of 40.46±0.1 °C[50] and a vapour pressure of 10 Torr at 26 °C.[51] Osmium tetroxide can be prepared by oxidation of aqueous solutions of osmium species in the +2 to +7 oxidation states using strong oxidizers like HNO_3, $KMnO_4$, HIO_4, Ce(IV), or Cl_2.[1] The Lewis acidity of OsO_4 towards N-bases,[52-62] O-bases,[52,61,63-70] and halides[55,63,65,72-74] has been studied and several adducts have been characterized by vibrational spectroscopy[53-56,62,64,65,70-73] and X-ray diffraction (Table 1.1).[55-61,66-71,73] The tetroxide can bind to one or two donor atoms. In 1:1 Lewis acid base adducts, *e.g.*, $OsO_4(OH)^-$,[71] OsO_4Cl^- (Figure 1.1a),[55] and in 2:1 adducts, *e.g.*, $(OsO_4)_2OH^-$,[71] $(OsO_4)_2\cdot$hexamethylenetetramine (Figure 1.1b),[57] osmium exhibits distorted trigonal bipyramidal coordination. In the case of osmium binding to two donor atoms, the osmium complex has a pseudo-octahedral *cis*-configuration with the two donor atoms belonging to two bases, *e.g.*, $OsO_4(OH)_2^{2-}$,[67,67,69] or to one chelating ligand, *e.g.*, $OsO_4\cdot$ (R,R)-*trans*-1,2-bis(*N*-pyrrolidino)cyclohexane (Figure 1.1c).[59]

The reaction of OsO_4 with Lewis bases such as NH_3 in aqueous KOH solution or primary amines in aqueous and organic solvent media have been shown to yield the nitridoosmate anion[75] and organoimidoosmates[75-77] according to eqs. (1.11) and (1.12),

Table 1.1 Reported OsO_4·Lewis Base Adducts, Their Characterization, and Selected Structural Data

Adduct	Characterization[a]	Os-donor atom bond length *donor atom* [pm]	$O_{ax/trans}$-Os-*donor* [a] bond angle [°]
OsO_4OH^-	e.a.,[52,71] IR[71]		
$(OsO_4)_2OH^-$	e.a.,[52,71] IR,[71] X-ray[68,71]	*O* 221(2)/222(2);[71] 216/222[68]	179(1)/177(1)[71]
$OsO_4(OH)_2^{2-}$	e.a.,[52,63,71] IR,[64,65,70,71] Raman,[65] X-ray[66,67,69,70]	*O* 216/216;[66] 210/217[67]	
OsO_4· *N*-methylmorpholine *N*-oxide	e.a.,[61] IR,[61] X-ray[61]	*O* 230.5(4)[61]	175.1(3)[61]
OsO_4Cl^-	e.a.,[55] IR,[55] X-ray[55]	*Cl* 276.0(2)[55]	179.0(2)[55]
$OsO_4N_3^-$	e.a.,[55] IR[55]		
OsO_4F^-	e.a.,[72] IR,[72,c] Raman[72,c]	*F* 207.5(9)[c]	156.9(4)[c]
$OsO_4F_2^{2-}$	e.a.,[63,72,b] IR,[72,73,b,c] Raman,[65,72,b,c] EXAFS[74,b]		
OsO_4· quinuclidine	e.a.,[54] IR,[54] Raman,[54] X-ray[57]	*N* 237[57]	180.0[57]
$(OsO_4)_2$· hexamethylene tetramine	e.a.,[52,54] IR,[54] Raman,[54] X-ray[57]	*N* 242[57]	n.r.
OsO_4· *N*-methylmorpholine	e.a.,[61] IR,[61] X-ray[61]	*N* 244.0(7)[61]	177.7(3)[61]
OsO_4· pyridine	e.a.,[54] IR,[54,62] Raman[54,62]		
OsO_4· pyrazine	e.a.,[54] IR[54]		
OsO_4· triethylenediamine	e.a.,[54] IR,[54] Raman[54]		

Table 1.1 continued...

Adduct	Characterization[a]	Os-donor atom bond length *donor atom* [pm]	$O_{ax/trans}$-Os-donor[a] bond angle [°]
$(OsO_4)_2$· 5-methylpyrimidine	e.a.,[54] IR[54]		
OsO_4· phthalazine	e.a.,[54] IR,[54] Raman[54]		
OsO_4· isoquinoline	e.a.,[54] IR,[54] Raman[54]		
OsO_4· 1,8-naphthyridine	Raman,[56] X-ray[56]	*N* 243.8(6)[56]	178.4(3)[56]
OsO_4· 4-pyrrolidinopyridine	X-ray[60]	*N* 231.8(13)[60]	179.3(8)[60]
OsO_4· 4-phenylpyridine	X-ray[60]	*N* 241.9(15)[60]	178.8(6)[60]
OsO_4· 4-cyanopyridine	X-ray[60]	*N* 245.2(8)[60]	178.6(4)[60]
OsO_4· (dimethylcarbamoyl) didydroquinidine	X-ray[58]	*N* 249[58]	
OsO_4· (R,R)-*trans*-1,2-bis(*N*-pyrrolidino)cyclohexane	X-ray[59]	*N* 232.9(11)/233.4[59]	167.3/165.8[59]

[a] Abbreviations denote: elemental analysis (e.a.), not reported (n.r.). [b] The previous characterizations were actually performed on the OsO_4F^- anion, as shown in the present work (see Chapter 6). [c] Present work.

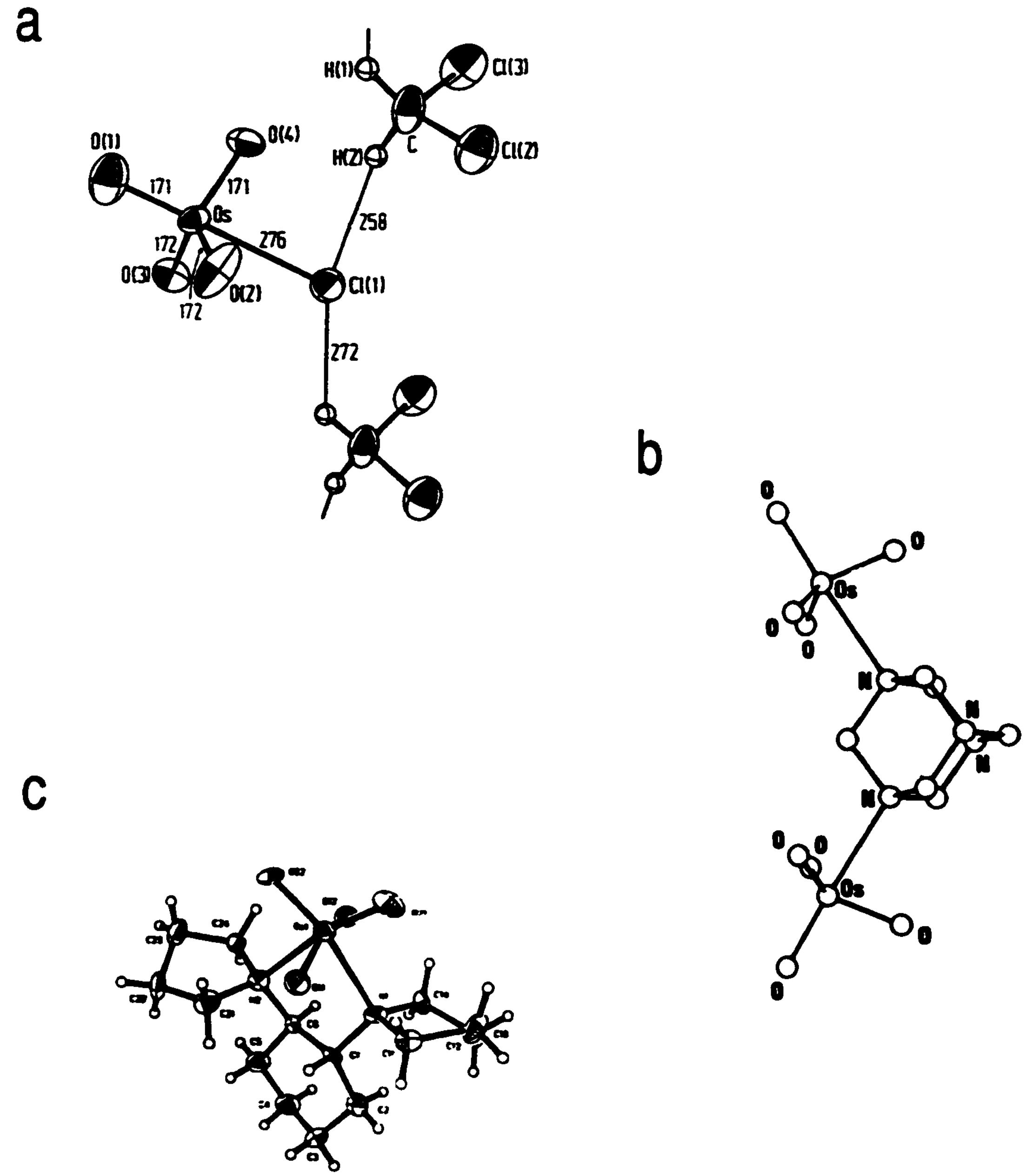

Figure 1.1 Crystal structures of (a) the OsO_4Cl^- anion in $[P(C_6F_5)_4][OsO_4Cl]\cdot CH_2Cl_2$,[55] (b) the 2:1 adduct of OsO_4 and hexamethylenetetramine,[57] and (c) $OsO_4\cdot$ (*R,R*)-*trans*-1,2,-Bis(*N*-pyrrolidino)cyclohexane.[59]

$$OsO_4 + NH_3 + KOH \longrightarrow [K][OsO_3N] + 2H_2O \qquad (1.11)$$

$$OsO_4 + (CH_3)_3CNH_2 \longrightarrow (CH_3)_3NOsO_3 + H_2O \qquad (1.12)$$

respectively. Like OsO_4, imidoosmates can act as Lewis acids towards nitrogen donor molecules, such as 1,4-diazabicyclo[2,2,2]octane (Figure 1.2a),[78] while the OsO_3N^- anion has been utilized as a nitrogen bonded ligand in Rh, Ir, Pt, and Au complexes (Figure 1.2b).[79,80] The preparation of several bis(imido)osmates $O_2Os(NR)_2$,[76,77,81] tris(imido)osmates $OOs(NR)_3$[77,81] and tetrakis(imido)osmates $Os(NR)_4$[82,83] have also been reported.

Six osmium(VIII) oxide fluorides have been prepared prior to this work (Table 1.2) which include only two neutral oxide fluorides of Os(VIII), namely, OsO_3F_2[7] and *cis*-OsO_2F_4.[6,7]

Osmium trioxide difuoride can be prepared by fluorination of OsO_4 with F_2,[84] BrF_3,[85] or ClF_3.[7] The Raman and infrared spectra of matrix-isolated OsO_3F_2 was assigned to monomeric OsO_3F_2 (D_{3h}).[86] However, in contrast to XeO_3F_2, bulk OsO_3F_2 possesses a low vapour pressure indicating an oligomeric or polymeric structure in the solid state. Osmium trioxide difluoride was found to occur in three different modifications, a monoclinic low-temperature (<90 °C) and two orthorhombic high-temperature modifications, which are, according to Raman spectroscopy, composed of fluorine bridged oligomers or polymers.[87] The structure of the monoclinic low-temperature α-modification was determined by single crystal X-ray diffraction and contains a zig-zag chain of fluorine-bridged *fac*-OsO_3F_3 moieties (Figure 1.3a).[7] The fluoride ion adduct of OsO_3F_2,

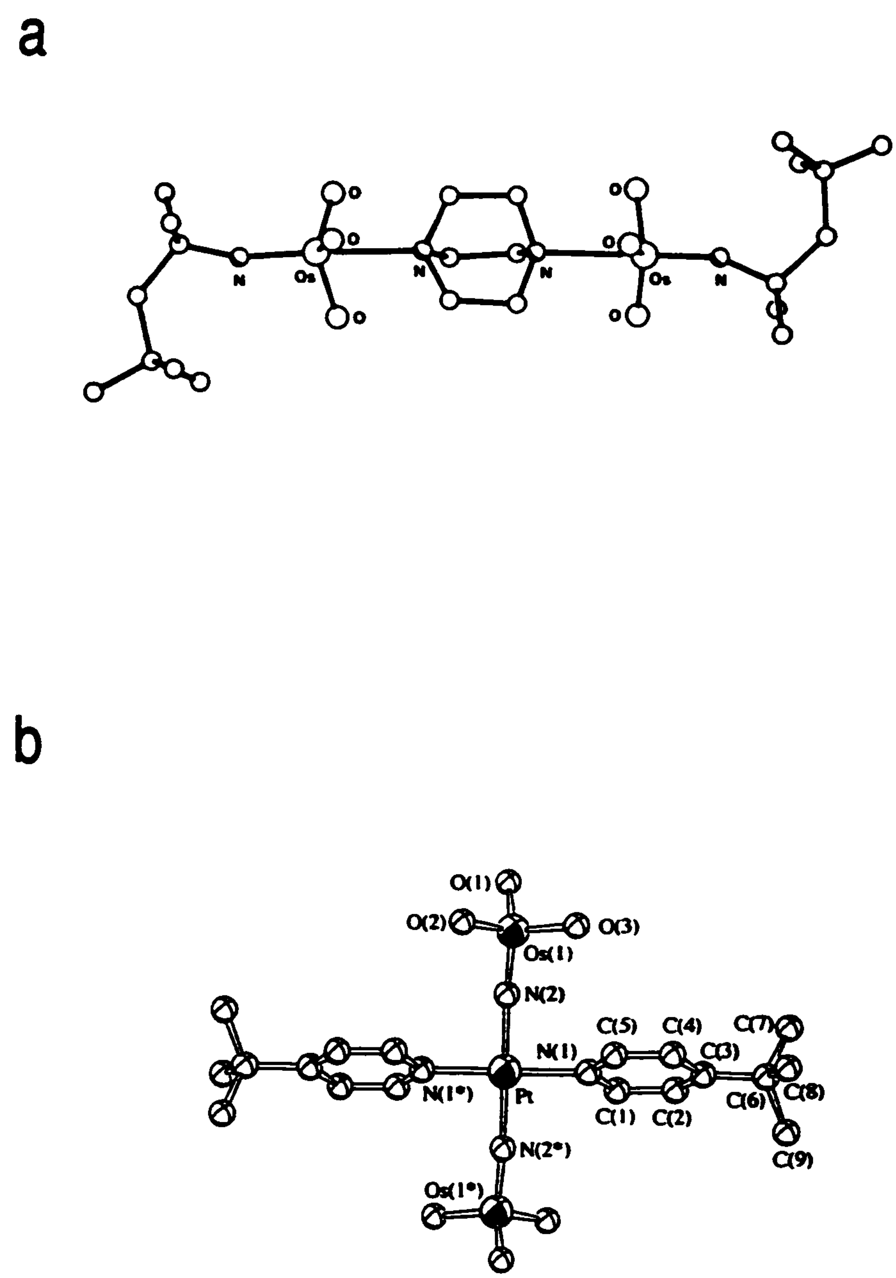

Figure 1.2 Crystal structures of (a) $[OsO_3(NOct^t)]_2 \cdot N_2C_6H_{12}$[77] and (b) *trans*-$[Pt(Bupy)_2(NOsO_3)_2]$.[80]

Table 1.2 Known Neutral and Charged Osmium(VIII) Oxide Fluorides[a]

$$OsO_4 \xrightarrow{+F^-} \mathit{OsO_4F^-} \xrightarrow{+F^-} \mathit{cis\text{-}OsO_4F_2^{2-}}$$

$$\downarrow ClF_3$$

$$\mathit{OsO_3F^+},\ \mathit{\mu\text{-}F(OsO_3F)^+} \xleftarrow{-F^-} OsO_3F_2 \xrightarrow{+F^-} \mathit{fac\text{-}OsO_3F_3^-}$$

$$\downarrow KrF_2$$

$$OsO_2F_3^+,\ \mu\text{-}F(\mathit{cis}\text{-}OsO_2F_3)^+ \xleftarrow{-F^-} \mathit{cis}\text{-}OsO_2F_4 \xrightarrow{+F^-} \mathit{OsO_2F_5^-}$$

[a] Osmium(VIII) oxide fluorides prepared and characterized in the present work are italicized.

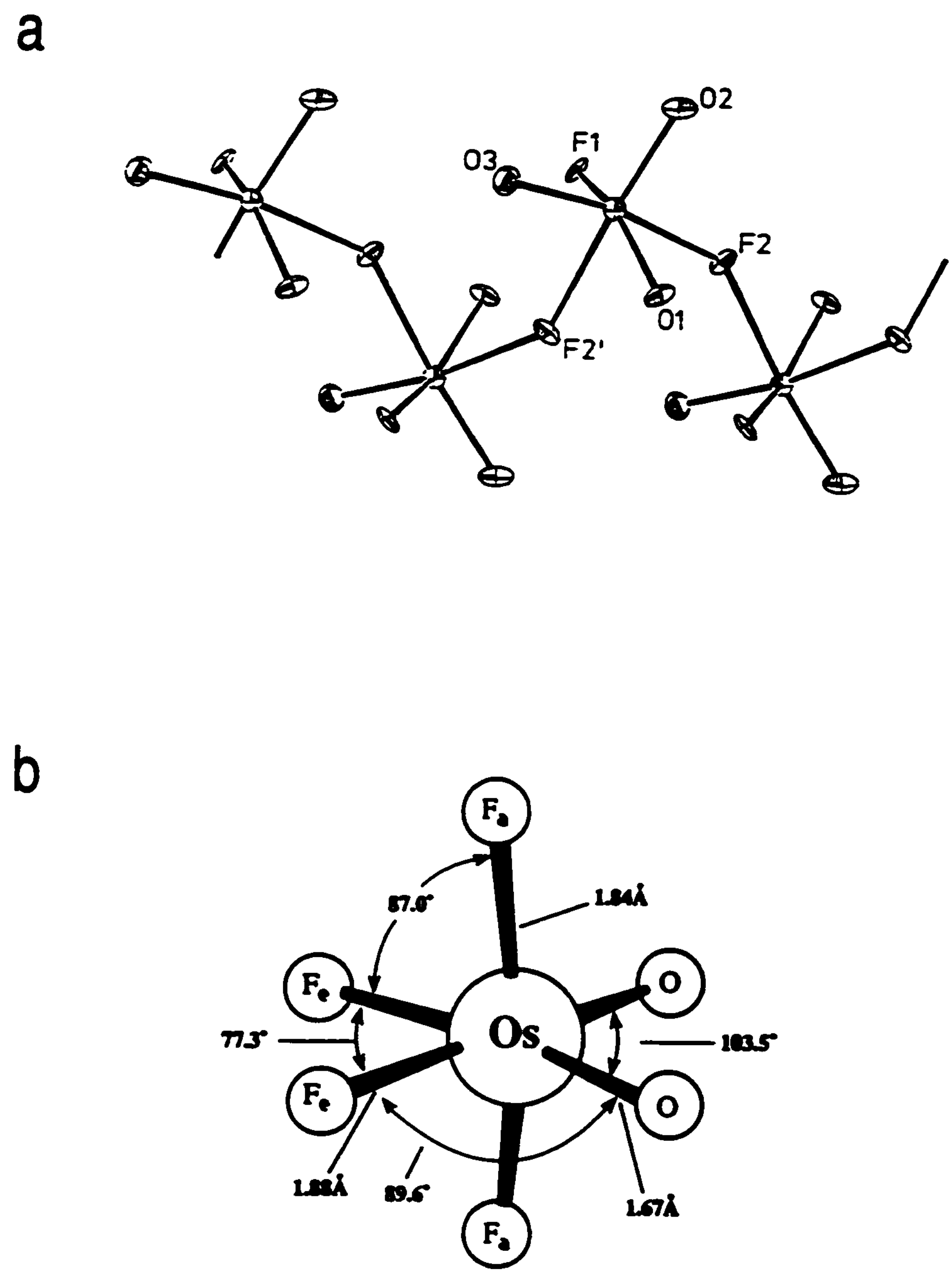

Figure 1.3 Structure of (a) OsO_3F_2 (X-ray diffraction)[7] and (b) *cis*-OsO_2F_4 (gas phase electron diffraction).[6]

$OsO_3F_3^-$, has only been studied by vibrational[7,65,72,88] and EXAFS spectroscopy.[74]

Osmium dioxide tetrafluoride was prepared by fluorination of OsO_4 with KrF_2 according to eq. (1.13)[6,7] and is a magenta coloured solid having a vapour pressure of 1 Torr at room temperature.[6] It was characterized by ^{19}F NMR spectroscopy,[6] electron

$$OsO_4 + 2KrF_2 \xrightarrow{HF} OsO_2F_4 + 2Kr + O_2 \quad (1.13)$$

diffraction,[6] vibrational spectroscopy,[6] but is severely disordered in its crystal structure.[7] The structure of *cis*-OsO_2F_4 is pseudo-octahedral with a *cis*-arrangement of the two oxygen and four fluorine ligands (Figure 1.3b). A report of the preparation of $OsOF_6$[89] was found to be erroneous and the product isolated was subsequently shown to be *cis*-OsO_2F_4.[90]

The only osmium(VIII) oxide fluoride cations synthesized to date have been derived from *cis*-OsO_2F_4 (Table 1.2). They were prepared by reaction of *cis*-OsO_2F_4 with the strong Lewis acids, AsF_5 and SbF_5, in HF solvent or in neat SbF_5 according to eqs. (1.14) to (1.16).[91] The dinuclear cation, μ-F(*cis*-$OsO_2F_3)_2^+$, has been characterized by

$$2cis\text{-}OsO_2F_4 + 2SbF_5 \xrightarrow{HF} [\mu\text{-}F(cis\text{-}OsO_2F_3)_2][Sb_2F_{11}] \quad (1.14)$$

$$2cis\text{-}OsO_2F_4 + 2AsF_5 \xrightarrow{HF} [\mu\text{-}F(cis\text{-}OsO_2F_3)_2][AsF_6] \quad (1.15)$$

$$cis\text{-}OsO_2F_4 + nSbF_5 \xrightarrow{SbF_5} [OsO_2F_3][Sb_nF_{5n+1}] \quad (1.16)$$

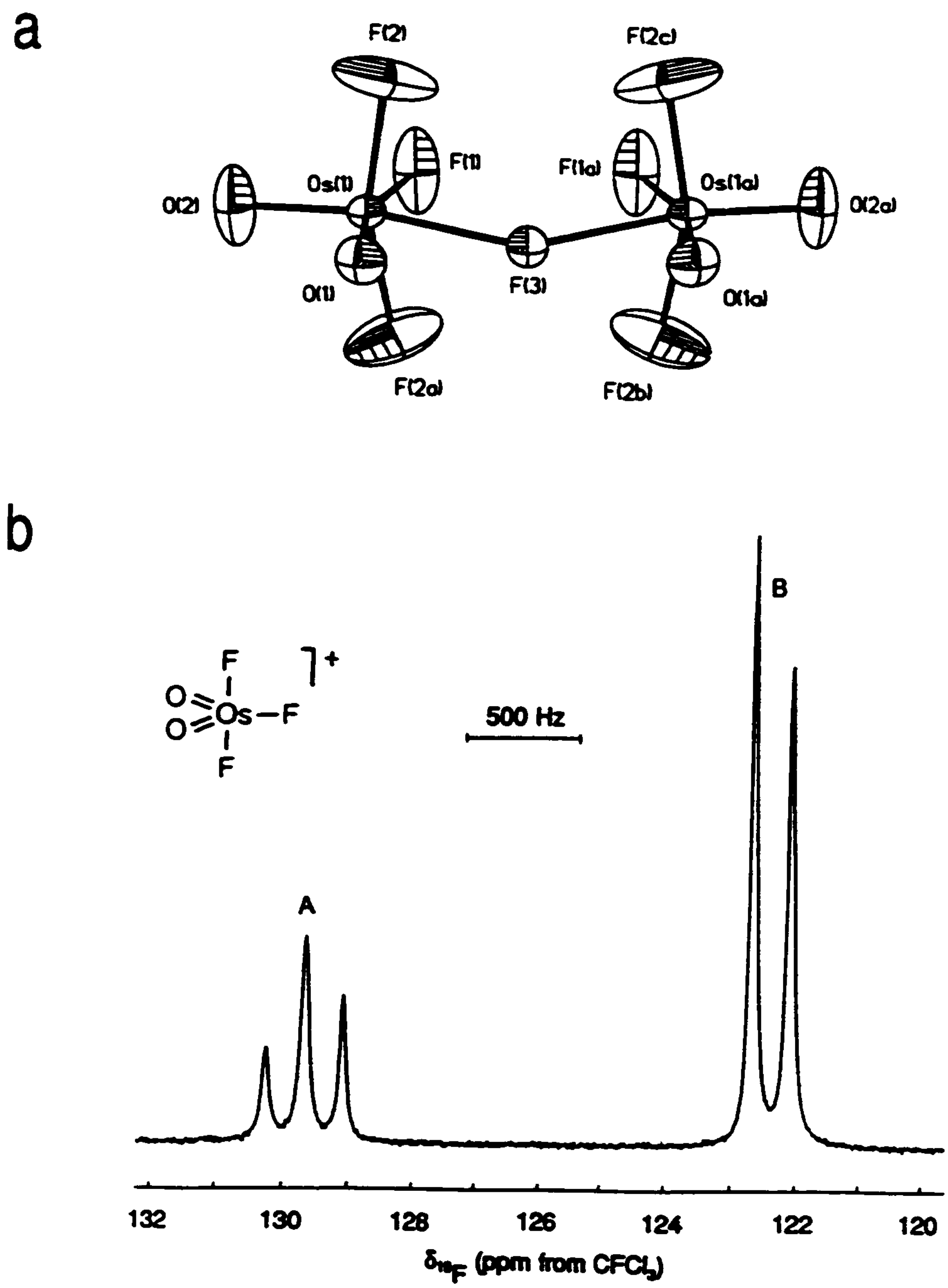

Figure 1.4 (a) Structure of the μ-F(*cis*-$OsO_2F_3)_2^+$ cation in the X-ray structure of [μ-F(*cis*-$OsO_2F_3)_2$][Sb_2F_{11}] and (b) the ^{19}F NMR spectrum of the $OsO_2F_3^+$ cation in SbF_5 solvent at 7 °C containing [XeF][Sb_nF_{5n+1}]: (A) equatorial fluorine, (B) axial fluorine.[91]

Raman spectroscopy and X-ray crystallography (Figure 1.4a), while the mononuclear cation was characterized by Raman and ^{19}F NMR spectroscopy (Figure 1.4b).

Density functional theory (DFT) calculations have been employed to obtained energy minimized geometries and vibrational frequencies for Os(VIII)[6,91] and related transition metal oxide fluoride species, such as Tc(VII)[92,93] and Re(VII) oxide fluorides.[93,94] The agreement between the DFT calculations and the experimental structural parameters and vibrational frequencies was found to be reasonably good and resulted in the complete assignment of vibrational spectra.

1.4. Iodine(VII) Chemistry

Two neutral iodine(VII) oxide fluorides, IO_2F_3[95,96] and IOF_5[97] are known. Reports of periodylfluoride, IO_3F, have not been substantiated,[98] which is in contrast with the stability of ClO_3F[99] and BrO_3F,[100] the only bromine(VII) oxide fluoride reported to date.

The preferred coordination number of iodine(VII) was found to be six which is exemplified by the dimerisation of IO_2F_3 found in the solid state by X-ray crystallography[96] and in solution by ^{19}F NMR spectroscopy.[101] The anion derived from IO_2F_3 also exists as a mixture of the six-coordinate *trans*- and *cis*-$IO_2F_4^-$ isomers,[102,103] unlike the analogous group 7 transition metal oxide fluoride anions, $TcO_2F_4^-$ [92] and $ReO_2F_4^-$,[94] which exclusively occur as *cis*-isomers. The coordination number of iodine(VII) can be extended to seven and eight as in IF_7,[104-107] IOF_6^-,[108-110] and IF_8^{2-}.[108] The IOF_6^- anion was prepared according to eq. (1.17) and was characterized by ^{19}F NMR spectroscopy in

$$IOF_5 + [N(CH_3)_4][F] \xrightarrow{CH_3CN} [N(CH_3)_4][IOF_6] \qquad (1.17)$$

CH_3CN solution and by X-ray crystallography and vibrational spectroscopy in the solid state (Figure 1.5).[110] This anion has a pentagonal bipyramidal structure found for most heptacoordinated main-group fluorides and oxide fluorides, *e.g.*, TeF_7^-,[111,112] $TeOF_6^{2-}$.[113]

The monovalent anions of the iodine(VII) oxides and oxide fluorides are isoelectronic with the analogous neutral xenon(VIII) species (*vide infra*). However, the chemistry and stability of isoelectronic species like IO_4^-/XeO_4 and $IO_2F_4^-$/XeO_2F_4 differ significantly. An extensive and detailed comparison of structural parameters for the two series is very limited because the xenon(VIII) species are thermodynamically and kinetically unstable rendering them difficult to characterize by diffraction and spectroscopic techniques.

1.5. The *Trans*-Influence

The influence of the multiply bonded ligands, oxygen and nitrogen, on the lengths of *trans* metal-ligand single bonds has been extensively discussed in the literature.[114] Besides elongation of the *trans*-bonds, the most dramatic structural effect attributed to the *trans*-influence is the observation that d^0 transition metal dioxo- and trioxo-species exclusively prefer the *cis*- and *fac*-configuration, respectively. The dioxo- and trioxo-species, *cis*-OsO_2F_4,[6] *cis*-$TcO_2F_4^-$,[92] *cis*-$ReO_2F_4^-$,[94] *cis*-$VO_2F_4^{3-}$,[115] *fac*-$ReO_3Cl_3^{2-}$,[116] *fac*-$WO_3F_3^{3-}$,[117] and *fac*-$OsO_3F_3^-$ (see Chapter 7), exemplify this generalization which contrasts

a

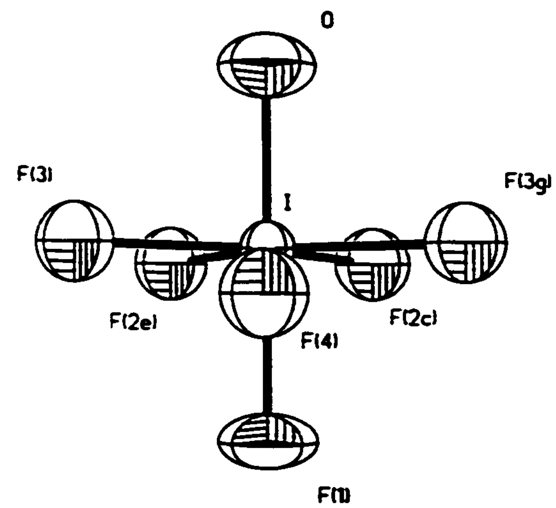

b

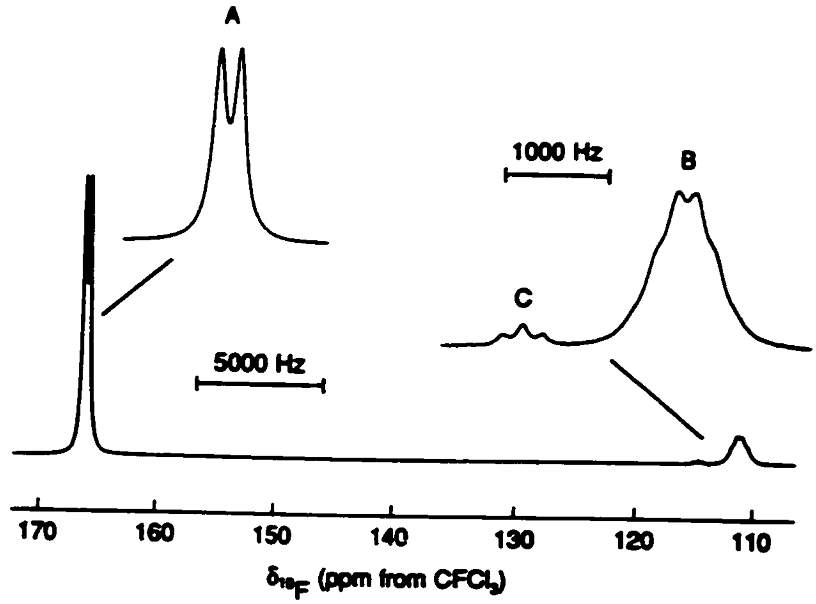

Figure 1.5 (a) Structure of the IOF_6^- anion in $[N(CH_3)_4][IOF_6]$ and (b) the ^{19}F NMR spectrum of a saturated solution of $[N(CH_3)_4][IOF_6]$ in CH_3CN at -40 °C; (A) F_{eq}, (B) F_{ax} of IOF_6^-, (C) *cis*-$IO_2F_4^-$ impurity.[110]

with main-group chemistry, where examples of the *trans*- and *cis*-dioxo isomers are found to coexist as the thermodynamic and kinetic products, respectively, *e.g.*, *trans*- and *cis*-$IO_2F_4^-$,[102,103] *trans*- and *cis*-$Te(OH)_2F_4$.[118]

The *trans*-influence in the dioxo-isomer has been explained in terms of increased d_π-p_π orbital overlap in the *cis*-dioxo configuration when compared with the *trans*-dioxo isomer.[92] The d_{xy}, d_{xz}, and d_{yz} orbitals, the $d_{t_{2g}}$ set of an octahedral complex, are of the correct symmetry to participate in π-bonding to π-donor ligands *cis* to each other (Figure 1.6). In the *trans*-isomer, only two of these three d orbitals have the correct symmetry for π-interaction. In the facial trioxo-isomer, each of the d_{xy}, d_{xz}, and d_{yz} orbitals can interact with two oxygen p_π orbitals, while in the meridional isomer, the p_π orbitals of three oxygens compete for the one d orbital of the octahedral t_{2g} set which is in the plane of the three oxygen ligands.

More recently, Gillespie and Bader[119] have found that an oxygen doubly bonded to a transition metal element results in a charge concentration, in the outer electron core opposite the double bond, that is significantly larger than that produced by a singly bonded ligand such as fluorine. The contour map of the Laplacian of the electron density ($L = -\nabla^2\rho(r)$) for *cis*-$CrO_2F_4^{2-}$, which is isovalent with *cis*-$TcO_2F_4^-$, *cis*-$ReO_2F_4^-$, and *cis*-OsO_2F_4, is shown in Figure (1.7) and clearly shows the local charge concentrations in the outer core of the central chromium atom. Additional doubly bonded oxygens avoid these charge concentrations, disfavouring *trans*-dioxo and *mer*-trioxo arrangements.

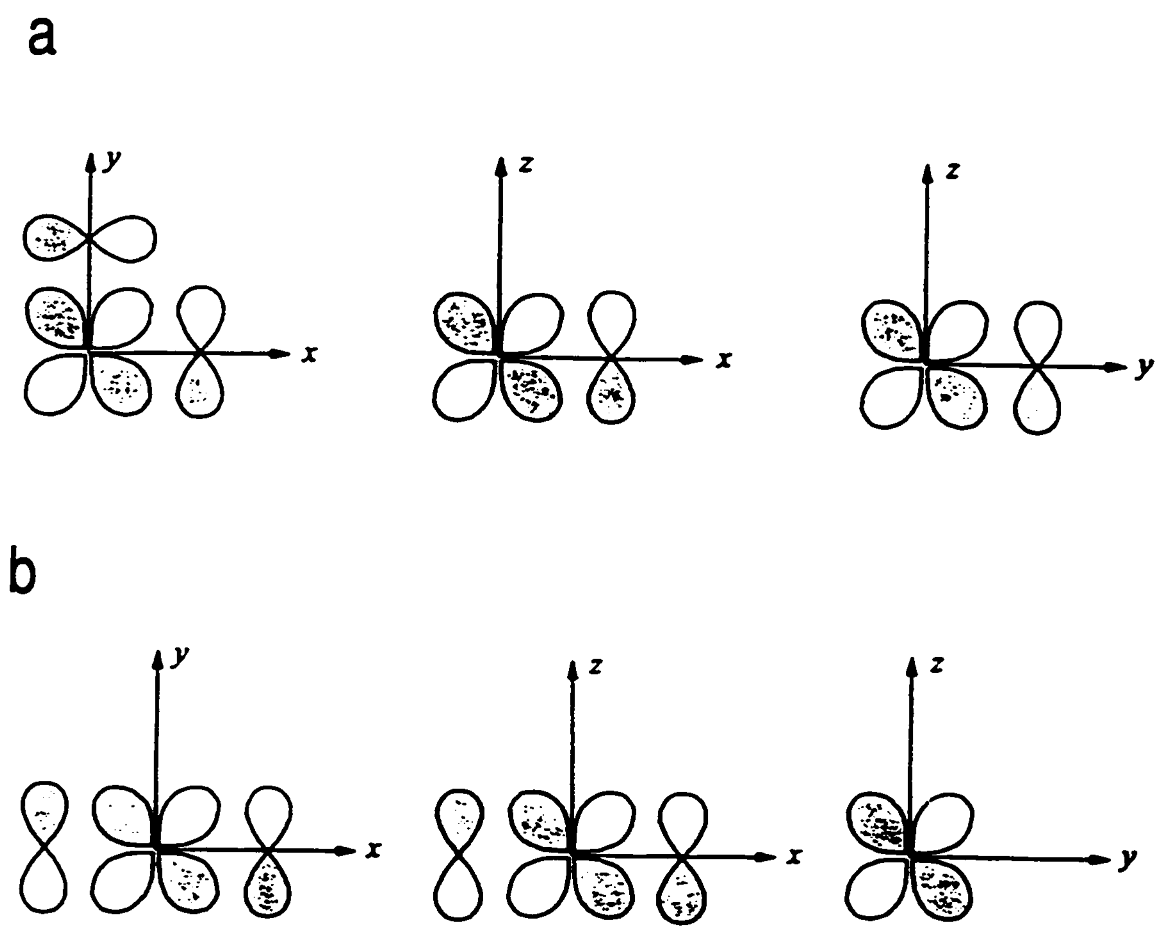

Figure 1.6 Diagram showing the overlap of the filled p orbitals of the oxygen ligands and the empty $d_{t_{2g}}$ orbitals of a transition metal in pseudo-octahedral (a) *cis*-dioxo and (b) *trans*-dioxo complexes.

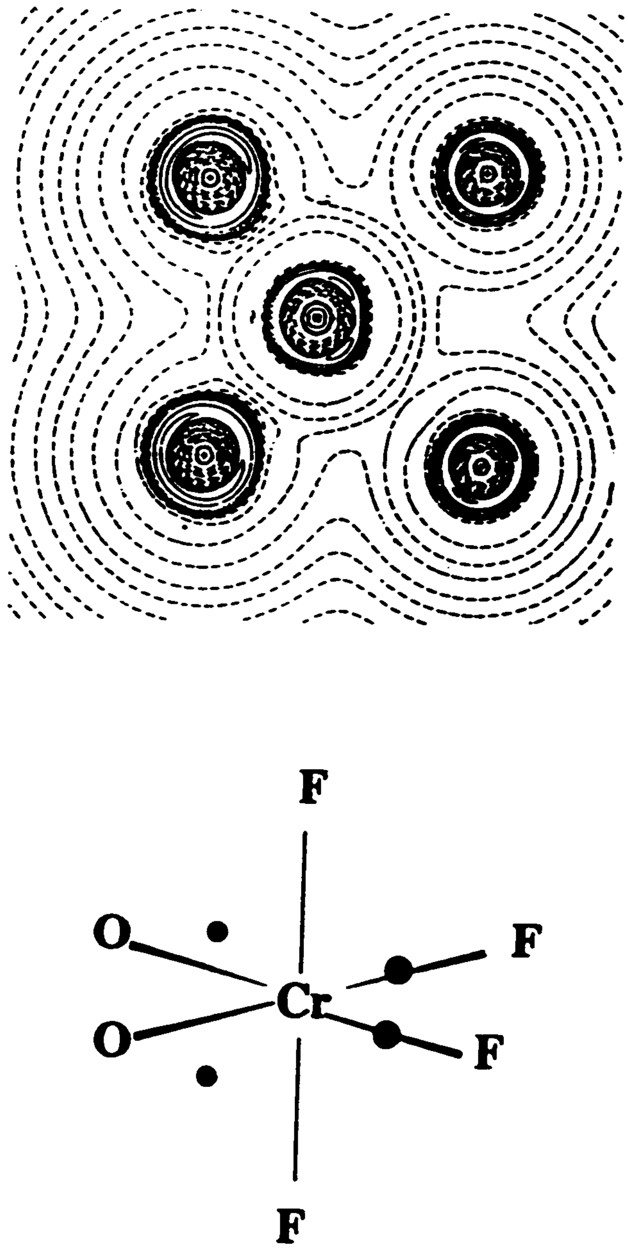

Figure 1.7 Contour maps of the Laplacian, $L = -\nabla^2\rho(r)$, for *cis*-$CrO_2F_4^{2-}$ through the $[O_2CrF_2]$-plane, with a diagram showing the positions and relative sizes of the charge concentrations in the outer shell of the core of Cr.[119]

1.6. Coordination Number Seven

The geometries of seven-coordinate compounds cannot be reliably predicted by the valence shell electron pair repulsion (VSEPR) model.[120] According to the hard-sphere model, where the least distance between points on a sphere is maximized, the monocapped octahedron is the favoured geometry. However, the monocapped trigonal prism and the pentagonal bipyramid are close in energy and are also observed in hepta-coordinate fluorides and oxide fluorides. Heptacoordinate main-group fluorides and oxide fluorides actually seem to favour the pentagonal bipyramidal structure, while some heptacoordinate transition metal species exhibit monocapped octahedral and monocapped trigonal prismatic structures (Table 1.3). A modification of the VSEPR model correlates the minimum energy structure with the exponent n according to the energy law:

$$E = \sum (1/r_{ij}^{n}) \qquad i \neq j \qquad (1.18)$$

where E is the relative energy of seven repelling points on a sphere, r_{ij} is the distance between two of the points, and n is a constant. For $0 < n < 3$ (soft repulsion) the pentagonal bipyramid is the minimum energy structure, while for $3 < n < 6$ (intermediate repulsion) the monocapped trigonal prism and for $n > 6$ (hard repulsion) the monocapped octahedron are the energetically preferred structures (Figure 1.8). The most ionic and softest transition metal AF_7 and AOF_6 species, $TaOF_6^{3-}$,[121] $NbOF_6^{3-}$,[122-125] ZrF_7^{3-},[126] and HfF_7^{3-} [127] have structures based on a pentagonal bipyramid. The disordered structures of the heptafluoride anions, ZrF_7^{3-} and HfF_7^{3-}, which crystallize in a face-centred cubic space

Table 1.3 Geometries of Heptacoordinate Fluorides and Oxide Fluorides[a]

Pentagonal Bipyramid		
AF_7^{n-}	$n = 0$	IF_7,[104-107] ReF_7[134]
	$n = 1$	TeF_7^- [111,112]
	$n = 2$	SbF_7^{2-},[135] BiF_7^{2-} [135]
	$n = 3$	ZrF_7^{3-},[126] HfF_7^{3-} [127]
AOF_6^{n-}	$n = 1$	IOF_6^-,[110] $ReOF_6^-$ [133]
	$n = 2$	$TeOF_6^{2-}$ [113]
	$n = 3$	$NbOF_6^{3-}$,[121-125] $TaOF_6^{3-}$ [121]
$AO_2F_5^{n-}$	$n = 2$	*$IO_2F_5^{2-}$*
	$n = 3$	$UO_2F_5^{3-}$ [136,137]
Monocapped Trigonal Prism		
AF_7^{n-}	$n = 2$	NbF_7^{2-},[129-132] TaF_7^{2-} [131]
AOF_6^{n-}	$n = 3$	$TaOF_6^{3-}$ [138]
$AO_2F_5^{n-}$	$n = 1$	*$OsO_2F_5^-$*
Monocapped Octahedron		
AF_7^{n-}	$n = 1$	MoF_7^-,[133] WF_7^- [133]

[a] Oxide fluorides prepared and characterized in the present work are given in italics. Only fluorides and oxide fluorides with elements in their highest oxidation state are included, however, also heptacoordinate VSEPR geoemetries for lower oxidation states are known: AX_6E (XeF_6[139]), AX_5E_2 (IF_5^{2-},[140] XeF_5^- [141]), and AX_5YE ($XeOF_5^-$ [142,143])

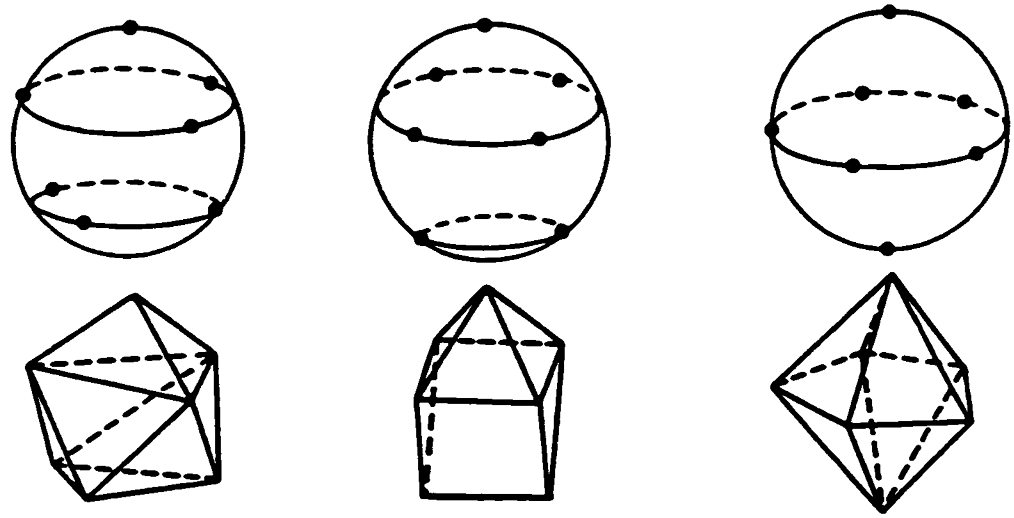

Monocapped Octahedron   Monocapped Trigonal Prism   Pentagonal Bipyramid

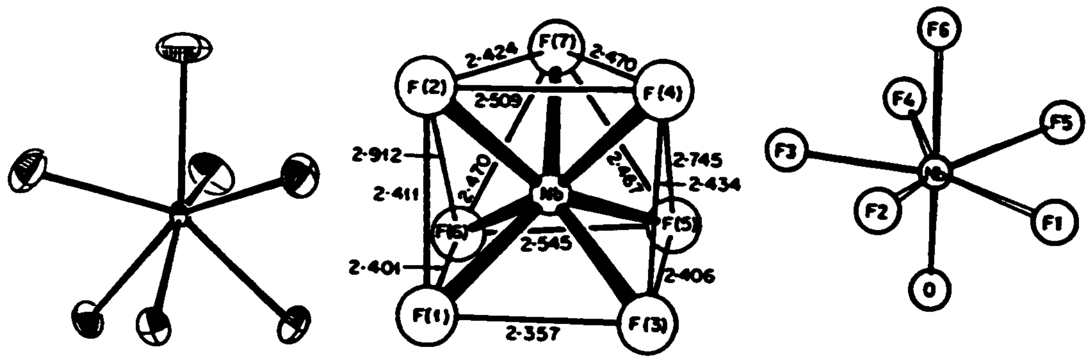

MoF_7^- NbF_7^{2-} $NbOF_6^{3-}$

Figure 1.8 The three main stereochemistries for heptacoordination represented by points-on-a-sphere and polyhedral representations, and the structures of the MoF_7^- anion in [Cs][MoF_7] (X-ray diffraction),[133] the NbF_7^{2-} anion in $[K]_2[NbF_7]$ (neutron diffraction),[130] and the $NbOF_6^{3-}$ anion in α-$[Na]_3[NbOF_6]$ (X-ray diffraction).[122]

group, were initially interpretated in terms of monocapped octahedral anions.[128] Later, this interpretation was rejected in favour of the commonly accepted model for the anions which is based on a pentagonal bipyramid. The intermediate soft anions NbF_7^{2-} [129-132] and TaF_7^{2-} [131] have distorted monocapped trigonal prismatic structures, and the hardest anions, MoF_7^- and WF_7^- [133] possess monocapped octahedral structures. However, the presence of two different ligands (F and O), packing effects in the solid state, and anion-cation contacts can favour one geometry over another.

Potential energy surfaces for AX_7, AX_6Y, and AX_5Y_2 species, where the A-Y bond lengths is defined as 80% of the A-X bond length, have been calculated based on the energy law (1.18) with $n = 6$.[144] For AX_7 species, the monocapped octahedron and the monocapped trigonal prism were found to be the most stable geometries with a very small energy difference. The minima for AX_6Y and AX_5Y_2 on the potential energy surface correspond to pentagonal bipyramidal geometries with the more strongly bonded Y ligands in the axial positions.

Quantitative energy calculations have been performed for the main-group species, TeF_7^-, IF_7, and XeF_7^+ at the MP-2, SCF and NLDFT level[145] and indicate that the pentagonal bipyramidal geometry is favoured over the monocapped trigonal prismatic and monocapped octahedral geometries by 5.4 to 23.4 kJ mol^{-1} and 8.8 to 25.9 kJ mol^{-1}, respectively. The small energy differences are in agreement with the observed fluxionality on the NMR time scale for TeF_7^- and IF_7. Theoretical calculations for MoF_7^-, WF_7^-, IOF_6^-, and $ReOF_6^-$ have been performed at the RHF level of theory.[146] For MoF_7^- and WF_7^-, the monocapped octahedral geometry was found to be more stable than the capped trigonal prismatic (pentagonal bipyramidal) geometry by 1.3 (18.0) and 0.4 (4.2) kJ mol^{-1}, respectively, which is in agreement with the X-ray crystal structures of [Cs][AF_7] (A = Mo, W). The most stable geometries for IOF_6^- and $ReOF_6^-$ were found to be the pentagonal bipyramidal with the monocapped octahedral (monocapped trigonal prismatic) geometries being 117.6 (122.2) and 82.0 (131.8) kJ mol^{-1} higher in energy. The large energy difference parallels the finding that IOF_6^- and $ReOF_6^-$ are non-fluxional on the NMR time scale.[110,133]

The preference of main-group heptafluorides for the pentagonal bipyramidal (D_{5h}) geometry has been rationalized by orbital interaction diagrams (Figure 1.9).[146] In the main-group D_{5h}-AX_7 molecule, three filled molecular orbitals, $2a_1'$ and e_2', are nonbonding. Upon lowering the symmetry to C_{3v} (monocapped octahedron) these three orbitals ($3a_1$ and 2e) can mix with bonding MO's resulting in destabilization of the $3a_1$ and 2e orbitals and the overall structure. A decrease in symmetry in transition metal heptafluorides also allows for mixing between the empty nonbonding d orbitals (e_1'' set in D_{5h} symmetry) with bonding MO's resulting in stabilization of the bonding MO's and the overall structure.

1.7. Xenon Oxide Fluorides

Xenon oxide fluorides have been prepared with xenon in the +4, +6, and +8 oxidation states (Table 1.4).[4] Neutral xenon oxide fluorides with xenon in the oxidation state +4 and +6 can be prepared by controlled hydrolysis of XeF_4 and XeF_6, respectively. Xenon oxide difluoride is unstable with respect to oxygen abstraction (eq. 1.19).[147] While

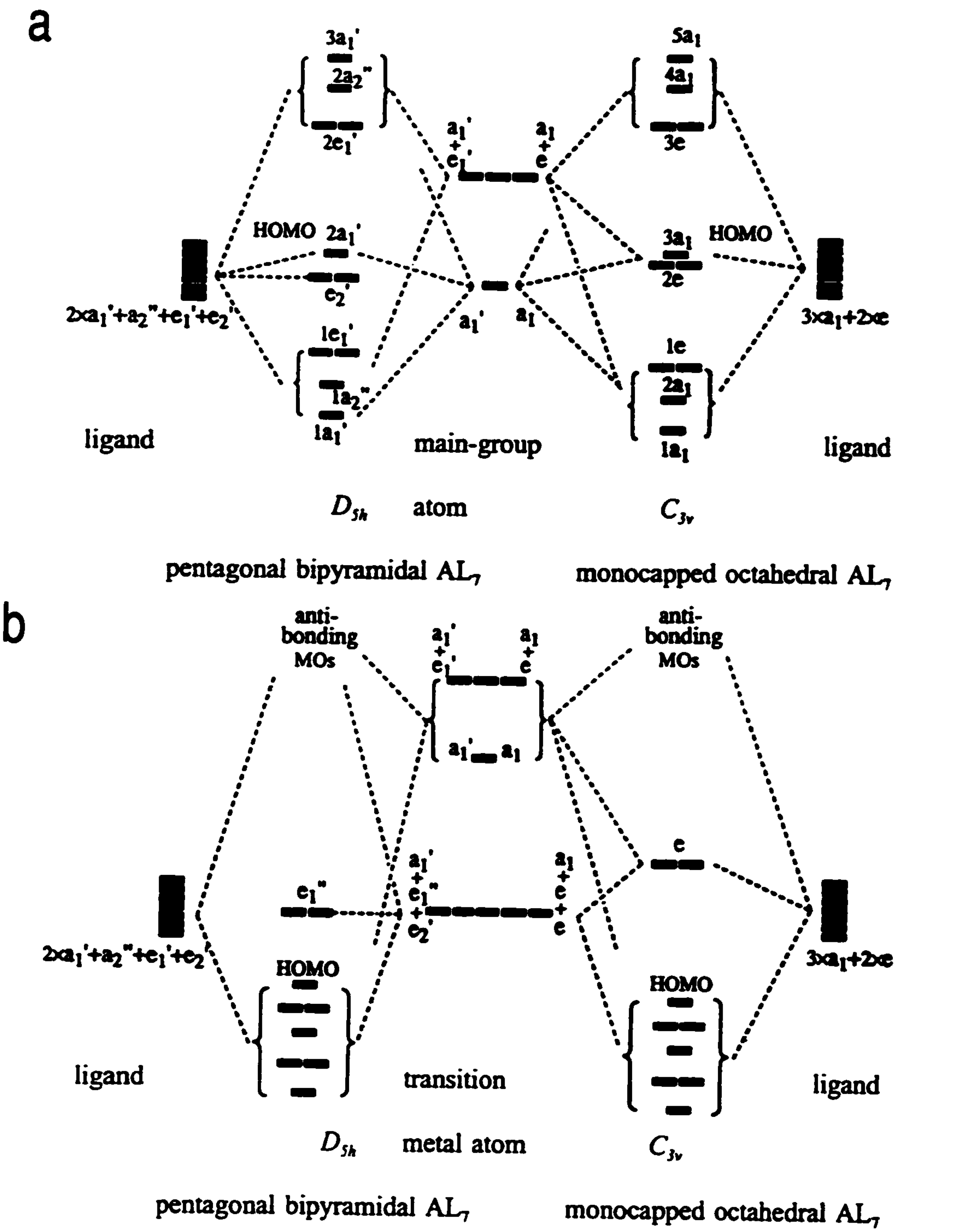

Figure 1.9 Orbital interaction diagrams for (a) a main group and (b) a transition metal AL_7 molecule.[146]

Table 1.4 Known Xenon Oxide Fluorides and Their Methods of Structural Characterization[a]

	Oxide Fluoride	Characterization
Xe(II)	*$Xe_3OF_3^+$*	*X-ray, Raman*
Xe(IV)	$XeOF_2$	$^{17}O/^{19}F/^{129}Xe$ NMR,[148] Raman,[147,149] IR[149,150]
	$XeOF_3^-$	Raman[147]
Xe(VI)	$XeOF_3^+$	X-ray,[151] $^{17}O/^{19}F/^{129}Xe$ NMR,[35,151-153] Raman[152,154,155]
	$XeOF_4$	X-ray,[156] $^{17}O/^{19}F/^{129}Xe$ NMR,[35,157] Raman,[158,159], IR,[159] MW,[160] Mössbauer[28]
	$XeOF_5^-$	$^{17}O/^{19}F/^{129}Xe$ NMR,[143] Raman[142,143]
	$F(XeOF_4)_3^-$	X-ray,[142] Raman[142]
	XeO_2F^+	X-ray,[156] $^{19}F/^{129}Xe$ NMR,[35,152,153] Raman,[152,155,161] Mössbauer[28]
	μ-$F(XeO_2F)_2^+$	X-ray,[156] Raman[161]
	XeO_2F_2	X-ray,[93] neutron,[162] $^{17}O/^{19}F/^{129}Xe$ NMR,[35,148,157] Raman,[163,164] IR[163,164]
	$XeO_2F_3^-$	Raman,[147,164] IR[164]
	XeO_3F^-	X-ray,[165] Raman,[166] IR[166]
Xe(VIII)	XeO_2F_4	mass spec.,[10] no structural information
	XeO_3F_2	*$^{19}F/^{129}Xe$ NMR*, Raman,[8] IR[8]
	fac-$XeO_3F_3^-$	*$^{19}F/^{129}Xe$ NMR*
	cis-$XeO_4F_2^{2-}$	*Raman*
	trans-$XeO_4F_2^{2-}$	*Raman*

[a] Oxide fluorides prepared and characterization in the course of the present work are given in italics.

$$XeOF_2 \longrightarrow Xe_2 + \tfrac{1}{2}O_2 \qquad (1.19)$$

$XeOF_4$ is a thermodynamically stable liquid (estimated ΔH_f° of -25 kJ mol^{-1}),[46] XeO_2F_2 is an endothermic, explosive solid (estimated ΔH_f° of 234 kJ mol^{-1}).[46] Except for $XeOF_3^-$,[147] all anionic and cationic xenon oxide fluorides, that are reported in the literature, are derived from Xe(VI) oxide fluorides. Dinuclear (μ-$F(XeO_2F)_2^+$),[156,161] trinuclear ($F(XeOF_4)_3^-$)[142] and polymeric (XeO_3F^-)[165,166] xenon oxide fluoride species have also been prepared and have fluorine bridged xenon centres.

1.8. Purpose and Scope of the Present Work

The purpose of this research is to extend the very limited chemistry of xenon in its highest oxidation state, +8. This includes the stabilization and NMR spectroscopic characterization of the explosive XeO_4 in solution and fuller characterization of XeO_3F_2 and XeO_2F_4, the only oxide fluorides reported in the literature. The preparation and NMR and Raman spectroscopic characterization of new Xe(VIII) species is another goal of the present work. The geometries of these xenon(VIII) compounds are analysed with respect to VSEPR rules. Xenon(VIII) species are the only main-group examples that can be directly correlated to analogous osmium(VIII) species and, therefore, are essential for the comparison of main-group and transition metal molecular geometries. In this context, the series of well-characterized anionic and cationic osmium (VIII) oxide fluorides derived from the known neutral oxide and oxide fluorides, *i.e.*, OsO_4, OsO_3F_2, and OsO_2F_4, had to be completed.

Another facet of the present research is the preparation and characterization of oxide fluoride species of Xe(VIII), Os(VIII), and I(VII) having coordination numbers exceeding six. Of particular interest are comparisons between geometries found for main-group and transition metal oxide fluorides of the type AO_2F_5, becauce the *trans*-influence of the oxygen ligands on the geometries of transition metal oxide fluorides has not been studied for the coordination number 7.

The striking absence of any reports of xenon(II) oxide fluorides, which contrasts Xe(IV), Xe(VI) and Xe(VIII) chemistry, rendered the investigation of the reaction of $[XeF][AsF_6]$ with water important.

Oxides and oxide fluorides are considered model compounds, since steric effects of the ligands do not dominate the structure. The simplicity of the molecules under investigation renders it possible to verify geometries predicted by models like VSEPR or by theoretical calculations, as performed in the literature by density functional theory calculations.

CHAPTER 2

EXPERIMENTAL SECTION

2.1. Standard Techniques

The compounds used in the course of this work were all moisture-sensitive, consequently, all manipulations were carried out under rigorously anhydrous conditions on glass and metal vacuum line systems, in a dry nitrogen filled glove bag or in the oxygen- and moisture-free (<0.1 ppm) nitrogen atmosphere of a Vacuum Atmospheres Model DLX drybox. Preparative work inside the drybox requiring low temperatures was carried out either in a glass cryowell mounted in the floor of the dry box or in a metal Dewar filled with 4.5 mm copper plated spheres (air rifle BB's) which had been previously cooled in the cryowell by immersion of the cryowell and contents in liquid nitrogen for several hours.

Volatile materials that were noncorrosive towards glass in the absence of water (*e.g.*, SO_2ClF and CH_3CN) were manipulated on a Pyrex glass vacuum line equipped with grease-free 6-mm J. Young glass stopcocks equipped with PTFE barrels (Figure 2.1). Pressures inside the glass manifold were monitored using a mercury manometer.

Volatile materials which attacked glass (*e.g.*, XeF_6 and HF) were handled on a metal vacuum line constructed from nickel and 316 stainless steel, and equipped with 316

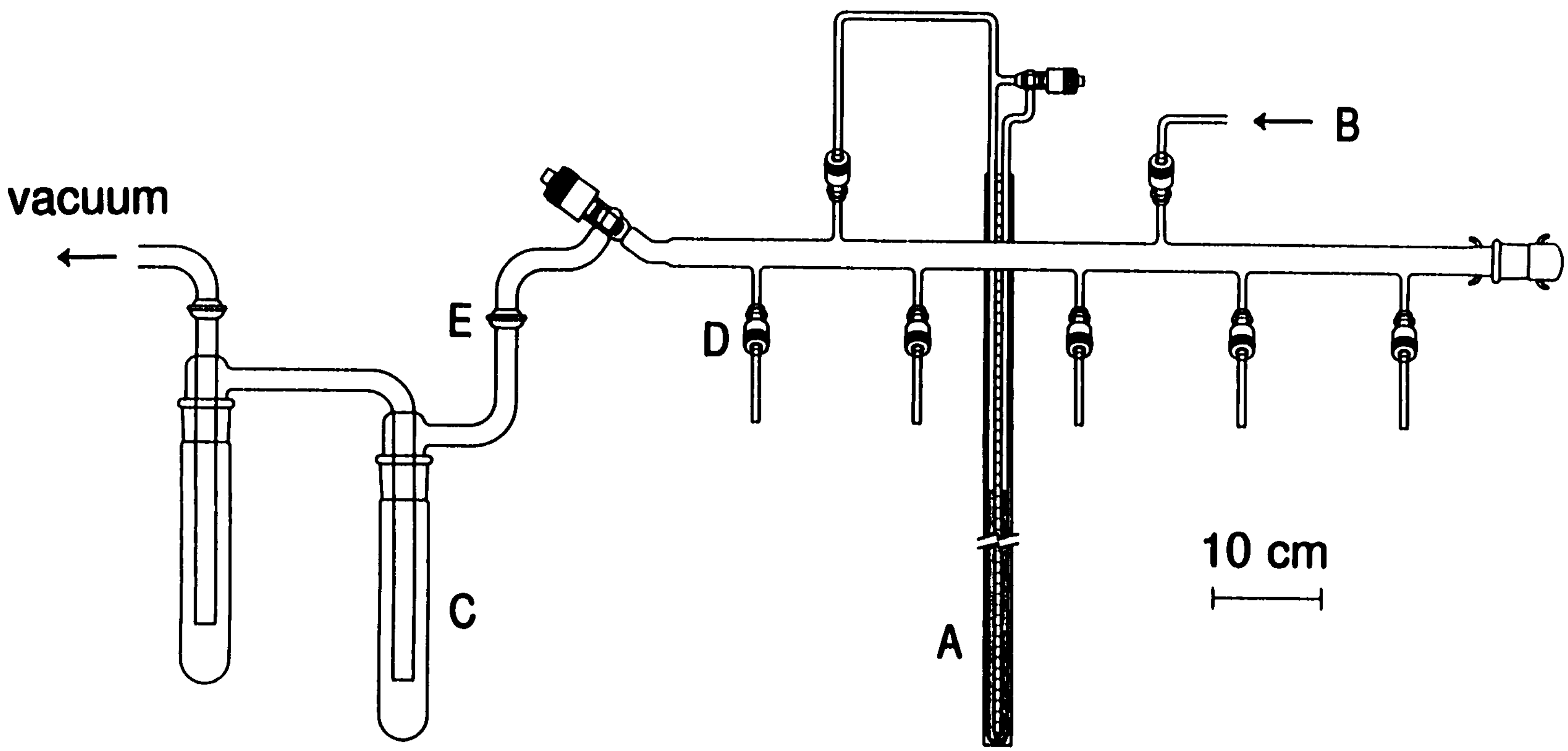

Figure 2.1 Glass vacuum line system; (A) mercury manometer, (B) dry N_2 inlet, (C) liquid nitrogen trap, (D) 6-mm J. Young PTFE/glass valve, (E) ball and socket joint.

stainless steel valves and fittings (Autoclave Engineers, Inc.), PTFE, FEP and Kel-F (Figure 2.2). Pressures were measured at ambient temperature using an MKS Model PDR-5B power supply and digital readout in conjunction with pressure transducers (effective range, 0 - 1000 Torr) having inert wetted surfaces constructed of Inconel. The pressures were accurate to ±0.5% of the scale.

Vacuum on the glass (*ca.* 10^{-5} Torr) and metal lines (*ca.* 10^{-3} to 10^{-4} Torr) was attained by use of Edwards two stage E2M8 direct drive vacuum pumps. Two vacuum pumps were used on the metal vacuum line; one, a roughing pump, was connected to a fluoride/fluorine trap consisting of a stainless tube (*ca.* 75 cm long, 15 cm dia.) packed with soda lime absorbent (Fisher Scientific, 4-8 mesh). Removal and disposal of volatile, reactive fluorinated compounds was accomplished by pumping through, and entrapment on, a bed of soda lime followed by trapping of the volatile reaction products, CO_2 and H_2O in a glass liquid nitrogen trap. The second vacuum pump provided the high vacuum source for the manifold and was cold trapped with a glass liquid nitrogen trap.

All preparative work involving XeF_6, KrF_2, AsF_5, BrF_5 and anhydrous HF was carried out in ¼-in. or 4-mm (AWG #9) o.d. FEP tubes which were heat sealed at one end and connected through 45° flares to Kel-F or stainless steel valves. The FEP sample tubes were dried under dynamic vacuum overnight on a glass vacuum line prior transfer onto a metal vacuum line where they were checked for leaks, passivated with F_2 at 1 atm for 12 h, re-evacuated and then back filled with dry N_2 before transferring to the dry box. Pyrex glass reaction vessels were dried under dynamic vacuum overnight and periodically flamed out by use of a Bunsen flame.

Figure 2.2 Metal vacuum system; (A) outlet to liquid nitrogen and charcoal traps followed by a two-stage direct-drive rotary vacuum pump (Edwards, E2M8) - hard vacuum, (B) outlet to soda lime and liquid nitrogen traps followed by a two-stage direct drive rotary vacuum pump (Edwards, E2M8) - rough vacuum, (C) dry N_2 inlet, (D) F_2 inlet, (E) pressure gauge (0-1500 Torr), (F) MKS Model PDR-5B pressure transducers (0-1000 Torr), (G) MKS Model PDR-5B pressure transducer (0-1 Torr), (H) $^3/_8$-in. stainless steel high pressure valve (Autoclave Engineers, 30BM6071), (I) 316 stainless steel cross, (J) 316 stainless steel L-piece, (K) $^3/_8$-in. o.d., $^1/_8$-in. i.d. nickel connectors, (L) $^1/_4$-in. o.d., $^1/_8$-in. i.d. nickel tube.

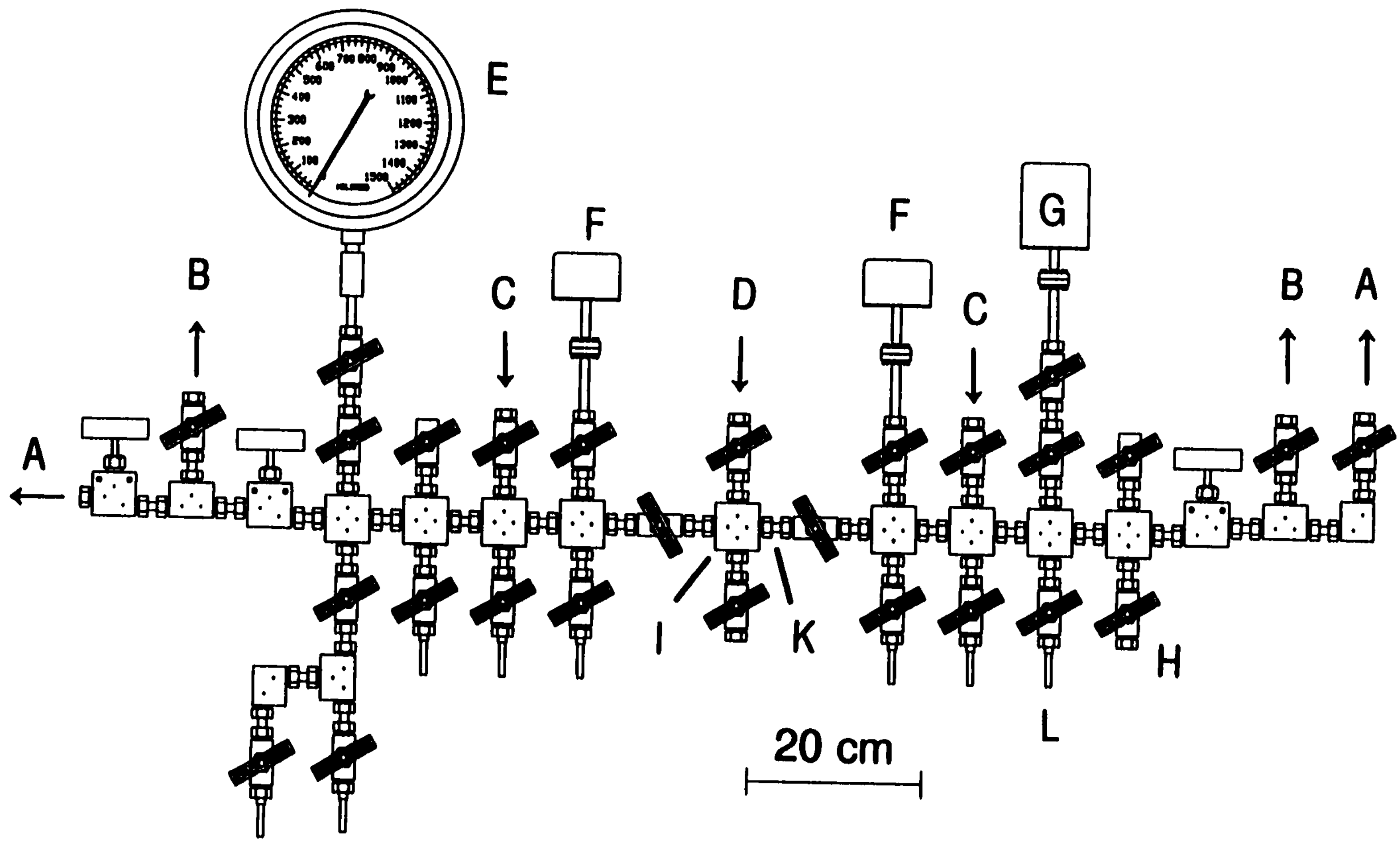

Figure 2.2 Metal vacuum system.

Nuclear magnetic resonance (NMR) spectra were recorded on samples prepared in FEP tubes (9-mm, ¼-in., or 4-mm o.d.). The 9-mm o.d. FEP NMR tubes were constructed from lengths of ³/₈-in. (9.5-mm) o.d. FEP tubing by reducing their diameter to 9 mm o.d. in a heated brass cylindrical form using mechanical pressure. One end of the tube was heat sealed by pushing it into the end of a heated thin-walled 10-mm o.d. glass NMR tube previously heated in a Bunsen flame. The other end was fused to ca. 5 cm of ¼-in. o.d. FEP tubing, which was heat-flared and equipped with a Kel-F valve. The 4-mm o.d. NMR tubing had one end sealed by pushing the tube into the end of a thin-walled 5-mm o.d. NMR tube and the other end was heat-flared for direct attachment to a Kel-F valve. The sample tubes used for recording the NMR spectra were heat sealed under dynamic vacuum at -196 °C with a small diameter nichrome wire resistance furnace. All heat-sealed samples were stored submerged in liquid nitrogen (-196 °C) until they could be spectroscopically characterized. For NMR measurements, the 4-mm, ¼-in., or 9-mm FEP tubes were inserted into standard 5-mm and 10-mm precision Wilmad NMR tubes before insertion into the NMR probe.

Raman spectra of solids that are stable at room temperature and which do not attack glass were recorded on samples in Pyrex glass melting point capillaries. Before use, the melting point capillaries were heated under dynamic vacuum for 24 h at 200 °C and then stored in a drybox in a closed dry N_2-filled glass vessel where they were loaded with the appropriate materials. The ends of the loaded melting point capillaries were filled with dry Kel-F grease before removal from the drybox. The capillaries were then immediately heat-sealed with a miniature oxygen-natural gas torch.

Vessels were attached to vacuum lines through thick-walled FEP tubing and ¼-in. PTFE Swagelok connectors by means of PTFE compression fittings or ¼-in. stainless steel Cajon Ultra-Torr connectors fitted with Viton rubber O-rings.

2.2. Preparation and Purification of Starting Materials

2.2.1. Purification of HF, BrF_5, SO_2ClF, CH_3CN, $(CH_3)_2CHOH$, and CHF_3 Solvents

Anhydrous hydrogen fluoride (Harshaw Chemical Co.) was purified as described previously[167] and stored at room temperature in a Kel-F storage vessel equipped with a Kel-F valve. Hydrogen fluoride was transferred into reaction vessels by vacuum distillation on a metal vauum line through connections constructed of Teflon, Kel-F and FEP as shown in Figure 2.3.

Bromine pentafluoride (Ozark-Mahoning Co.) was purified as described earlier,[168] and stored over dry KF in a ³/₄-in. o.d. FEP storage tube equipped with a Kel-F valve. Bromine pentafluoride solvent was transferred into reaction vessels by vacuum distillation through fluoroplastic connections.

Sulfurylchlorofluoride, SO_2ClF (Research Organic/Inorganic Chemicals Corp.), was purified according to the literature method[35] and stored over KF in a glass vessel equipped with a 6-mm J. Young glass stopcock equipped with a glass barrel. Transfers of SO_2ClF were performed under vacuum using a vacuum line and a Y-shaped side manifold constructed of glass, similar to that shown in Figure 2.4. Fluorine-19 NMR indicated the presence of a trace of SO_2F_2 impurity [$\delta(^{19}F)$ = 32.4 ppm].

Acetonitrile (Caledon HPLC Grade) was purified according to the literature

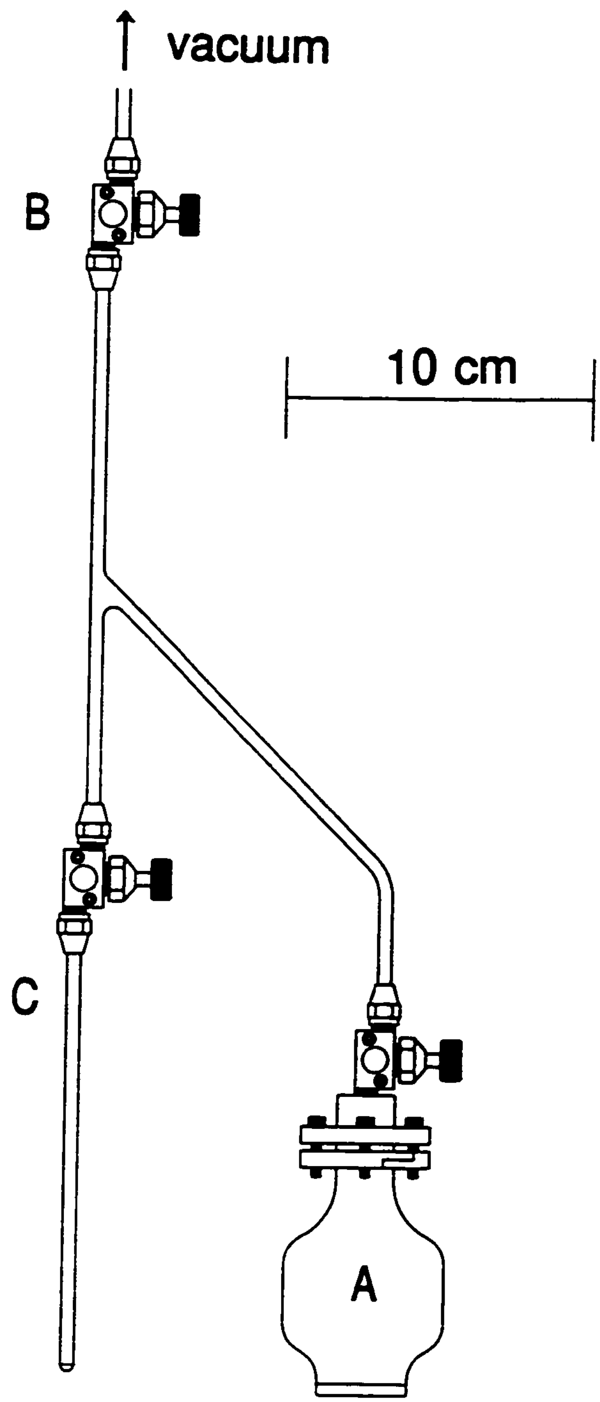

Figure 2.3 Hydrogen fluoride distillation apparatus; (A) Kel-F HF storage vessel, (B) Kel-F valve, (C) FEP reaction vessel.

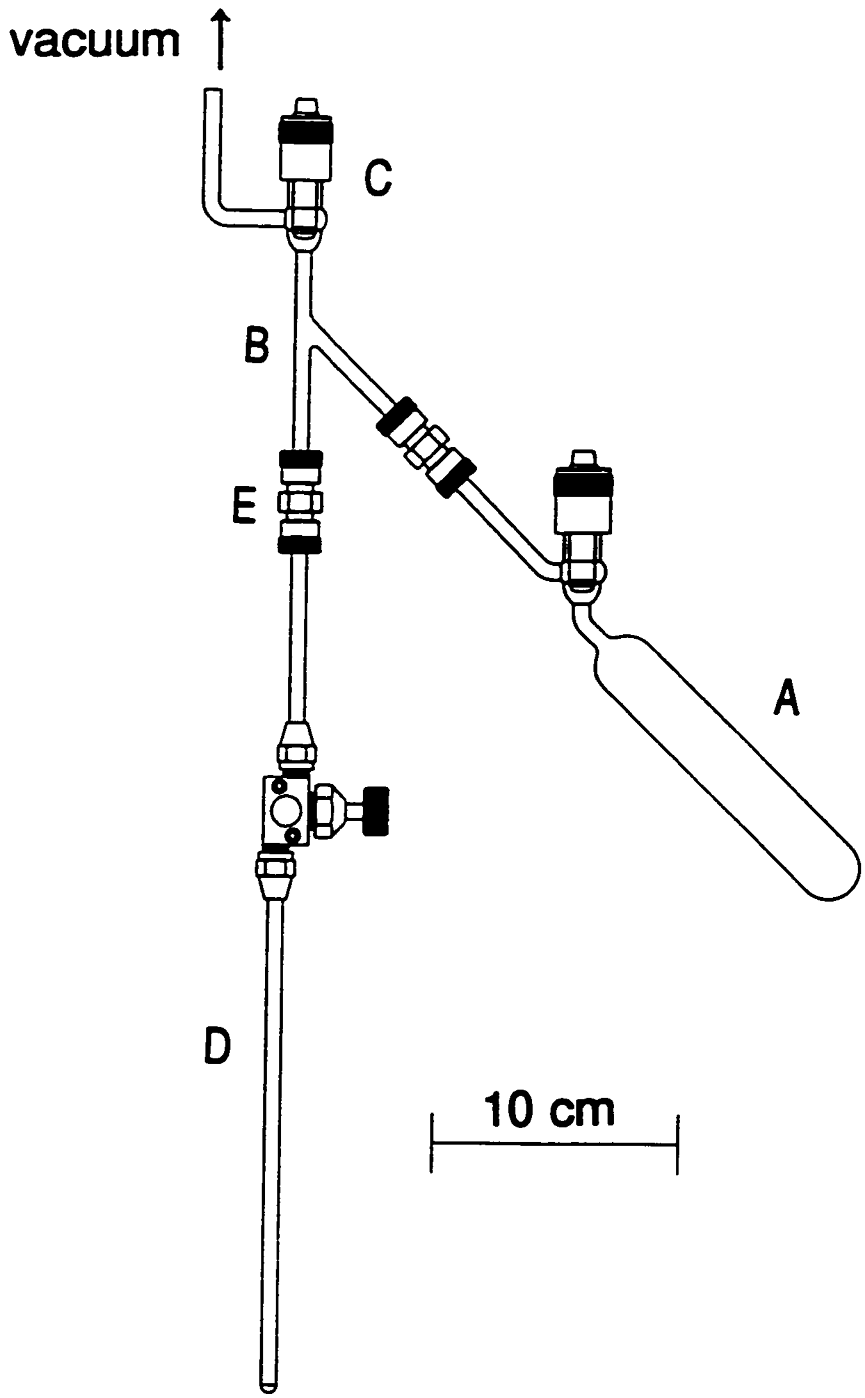

Figure 2.4 Acetonitrile distillation apparatus; (A) Pyrex CH_3CN storage vessel, (B) glass Y-piece, (C) 6-mm J. Young PTFE/glass valve, (D) FEP reaction vessel fitted with a Kel-F valve, (E) stainless steel Cajon connector.

procedure[169] and was transferred under vacuum using a glass vacuum line and a glass Y-piece as shown in Figure 2.4.

Isopropanol (Fluka Chemika, 99.5%) was dried over molecular sieves (Type 4A, Caledon) in a dry glass bulb equipped with a 4-mm J. Young glass stopcock. The molecular sieves were dried under dynamic vacuum for 24 h at 250 °C prior to use as a drying agent.

Fluoroform, CHF_3 (Canadian Liquid Air, 98%) was transferred through the metal line. Before entering the vacuum manifold, CHF_3 gas was passed through a copper coil cooled to -78 °C in solid dry ice.

2.2.2. Purification of SbF_3, SbF_5 and Preparation of AsF_5

Antimony trifluoride, SbF_3 (Aldrich) was sublimed under vacuum and transferred into a drybox prior to use.

Antimony pentafluoride, SbF_5 (Ozark-Mahoning Co.) was purified by vacuum distillation in an all-glass apparatus and stored in a glass vessel inside a desiccator. Subsequent transfers of SbF_5 were performed by use of an all-glass syringe in the inert atmosphere of a glove bag which had been previously purged with dry nitrogen for 12 h.

Arsenic pentafluoride was prepared according to the literature method by the fluorination of AsF_3 in a nickel can.[151] The AsF_5 was distilled into a nickel storage cylinder from which it was used without further purification. The metal vacuum line was passivated using AsF_5 prior to distillation of AsF_5 onto a reaction mixture.

2.2.3. Sources and Purification of N_2, F_2, Xe, Kr, BF_3, NO, NO_2, and O_3

House nitrogen gas was generated from a liquid nitrogen boil off and redried by passing it through a freshly regenerated bed of type 4A molecular sieves. Fluorine gas (Air Products), Xe (Air Products, 99.995%), Kr (Air Products, 99.995%), BF_3 (Matheson, >99.8%) were used without further purification. Nitrogen oxide, NO (Matheson, >99%), was purified by condensation into a 30-mL nickel can at -196 °C followed by warming the can and contents to -110 °C using an ethanol slush, at which temperature, the N_2O_3 contaminant is involatile, and expanding the NO gas into the reaction can. Nitrogen dioxide, NO_2 (Matheson, >99.5%), was dried over P_2O_5 at room temperature in a Pyrex glass vessel equipped with a 9-mm J.Young Teflon/glass stopcock. Ozone, O_3, was generated by a Welsbach T-408 ozonator using high-purity O_2 (Canadian Liquid Air, zero grade).

2.2.4. Preparation of XeF_2, XeF_6, and KrF_2

Xenon difluoride was prepared according to the literature method[151] and was stored inside a drybox.

Xenon hexafluoride was prepared by a method similar to that outlined by Chernick and Malm.[11] Xenon and fluorine gas were transferred into a nickel can with a xenon to fluorine ratio of 1 : 22 and a total autogeneous pressure of 56 atm at room temperature. The mixture was heated to 250 °C for 24 h and slowly cooled to 47 °C over a period of 16 h before turning off the furnace and allowing the mixture to cool to room temperature. The product was vacuum distilled into a ½-in. o.d. FEP storage vessel equipped with a

Whitey ORM2 stainless steel valve. The purity was assessed using Raman spectroscopy and by comparing the sharp, intense XeF_4 bands at 503 and 543 cm^{-1} to the broad XeF_6 bands at 582, 636, and 655 cm^{-1}. Only trace amounts of XeF_4 were detected.

Krypton difluoride was prepared using a method originally described by Bezmel'nitsyn *et al.*[170] which was subsequently modified by Kinhead *et al.*[171] The stainless steel hot wire reactor used in the present work is a modification of the design reported by Kinhead *et al.* (Figure 2.5).[171] The hot-wire reactor was filled with approximately 1000 Torr (0.5 mol) of krypton and subsequently immersed in a 20-L Dewar filled with liquid nitrogen. The reactor was then filled with F_2 to *ca.* 30 Torr and the DC power source (Miller, Thunderbolt AC/DC arc welder) was adjusted to approximately 6 V and 30 A, giving a dull red nickel filament at thermal equilibrium. The F_2 pressure was maintained between 40 and 35 Torr for each 12 h run. At the end of a run, excess fluorine was pumped off through a ½-in. FEP U-trap -196 °C before allowing the reactor to slowly warm to room temperature while unreacted krypton and pink, crude KrF_2 contaminated with CrO_2F_2 and $CrOF_4$ was pumped dynamically into the FEP U-trap at -196 °C. The trap was warmed to -78 °C, while pumping, to remove unreacted krypton. The U-tube containign crude KrF_2 was warmed to room temperature and a portion of crude KrF_2 along with the more volatile chromium oxide fluorides were flash distilled into a 9-mm FEP tube equipped with a Kel-F valve. The remaining KrF_2 was distilled into a 9-mm FEP tube equipped with a Kel-F valve for storage at -78 °C.

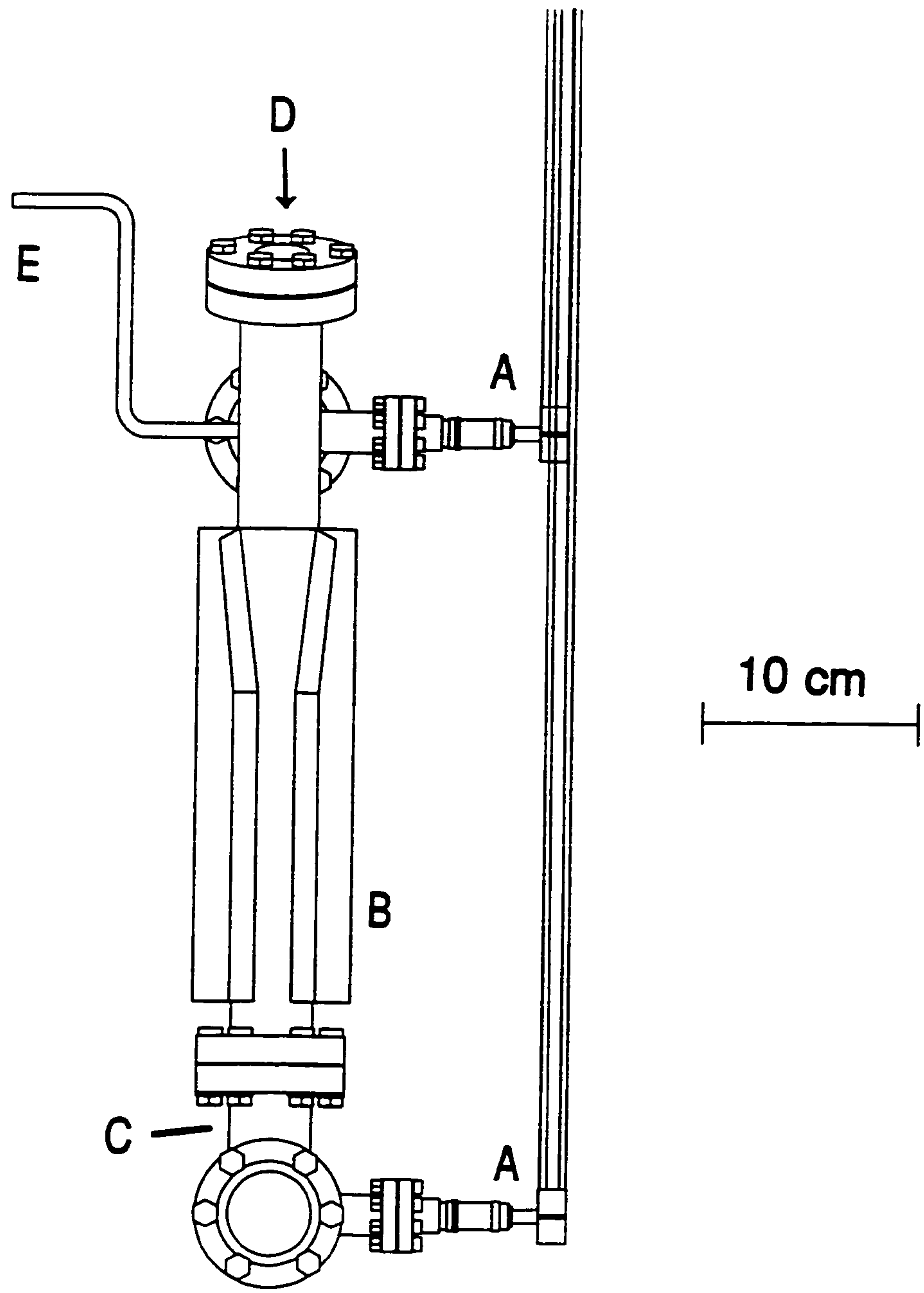

Figure 2.5 Hot-wire reactor used for the preparation of KrF_2 containing a 0.062-in. nickel filament; (A) 1.33-in. medium current solid conductor electrical feedthroughs, (B) copper cooling fins (6 each), (C) #316 S.S. reactor body, (D) viewport, (E) gas inlet.

2.2.5. Drying of CsF, and Preparation of $[N(CH_3)_4][F]$, NOF and NO_2F

The CsF (ICN-KCK Laboratories Inc., 99.9%) was dried by fusion in a platinum crucible, followed by transfer of the red hot clinker to the drybox port where it was immediately evacuated. Upon transferring to the dry nitrogen atmosphere of the glove box, the sample was ground to a fine powder and stored in the drybox until used.

The naked fluoride ion source, $[N(CH_3)_4][F]$, was prepared according to the literature method.[172] In a glove bag previously purged with nitrogen, $[N(CH_3)_4][OH]$ was titrated with 47% aqueous HF (Fisher Chemical) to the exact equivalence point (measured with a pH electrode). The product was transferred into a Pyrex drying tube and H_2O was removed under dynamic vacuum at 150 °C. The crude $[N(CH_3)_4][F]$ was recrystallized from isopropanol. After distillation of sufficient isopropanol onto the product to dissolve all the $[N(CH_3)_4][F]$, the water/isopropanol azeotrope was removed under dynamic vacuum, first at room temperature and later at 150 °C by heating with a furnace. The solid, white residue was finely ground inside the drybox and returned to a glass vacuum line port where it was pumped for 12 h at 150 °C. This procedure was repeated until the infrared absorption bands of $[N(CH_3)_4][F]\cdot H_2O$ at 822 and 895 cm^{-1} showed an intensity comparable to or less than that of the weak $N(CH_3)_4^+$ band at 1203 cm^{-1}. Infrared spectroscopy showed the $[N(CH_3)_4][F]$ product was free of SiF_6^{2-} and showed the presence of a small amount of HF_2^-, *ca.* 3 mol% estimated by ^{19}F NMR spectroscopic characterisation of the $[N(CH_3)_4][F]$ solution in CH_3CN which was maintained below -30 °C to avoid additional HF_2^- formation. The latter forms above -20 °C and is the result of proton abstraction from CH_3CN.[172,173]

Nitrosylfluoride, NOF, was prepared by reaction of NO and F_2 in a 30-mL nickel can. Approximately 0.077 mol (713 Torr) of pure NO was measured using a 2-L nickel measuring can and was condensed into the 30-mL reaction can at -196 °C. After evacuation, the line and 2-L can were filled with F_2, which was condensed into the intermediate 30-mL can at -196 °C. This can was warmed to -183 °C with a liquid oxygen bath and the fluorine, free of non-volatile contaminants (HF), was allowed to expand into the line and the measuring can. A total of *ca.* 0.046 mol (427 Torr) of F_2 was condensed, in two steps, into a 30-mL reaction can and onto the purified NO sample. The reaction can was first warmed to -183 °C for several minutes and was then allowed to warm slowly to room temperature. The excess fluorine was removed under dynamic vacuum at liquid oxygen temperature (-183 °C). This procedure was repeated a second time, resulting in a combined yield of *ca.* 7.71 g (0.157 mol) NOF. The small amounts of NO_2F (0.5%) and NOF_3 (0.4%) present in the sample were estimated by ^{19}F NMR spectroscopy [-85 °C; NOF, singlet at 485.37 ppm; NO_2F, triplet at 393.83 ppm, $^{1}J(^{19}F-^{14}N)$ = 114 Hz; NOF_3, triplet at 365.07 ppm, $^{1}J(^{19}F-^{14}N)$ = 135 Hz]. The metal vacuum line was passivated at least twice with NOF prior to condensing NOF into a reaction vessel.

Nitrylfluoride, NO_2F, was prepared by reaction of NO_2 and F_2 in a 30-mL nickel can and was similar to the procedure used to prepare NOF. Approximately 12 g of dry NO_2 was vacuum distilled into a ½-in. o.d. FEP tube that was fused to *ca.* 5 cm length of ¼-in. o.d. FEP tubing which was flared and fitted to a Kel-F valve. Approximately 3 g of NO_2 was allowed to react with excess F_2 to generate NO_2F that was used for passivation of the nickel can and the metal line. After removal of the crude NO_2F, NO_2 and a small excess of F_2 (purified as described above) were allowed to react in two steps, yielding approximately 13 g of NO_2F. The presence of small amounts of NOF (2.5%) was estimated by ^{19}F NMR spectroscopy. The metal vacuum line was passivated at least twice with NO_2F prior to condensing NO_2F into a reaction vessel.

2.2.6. Preparation of $[XeF][AsF_6]$ and $[H_3O][AsF_6]$ and Purification of $CH_3C^{15}N$

The $[XeF][AsF_6]$[174] and $[H_3O][AsF_6]$,[175] salts have been prepared as described before. Nitrogen-15 enriched $CH_3C^{15}N$ (MSD, 99% enriched) was dried over CaH_2 (BDH Chemicals, 99.5%) and vacuum distilled into another vessel onto fresh CaH_2 prior to use.

2.2.7. Preparation of OsO_3F_2 and *cis*-OsO_2F_4

Osmium trioxide difluoride, OsO_3F_2,[7] and *cis*-OsO_2F_4[6] were prepared as described in the literature from OsO_4 (Aldrich, 99.8%) and ClF_3 (Matheson, C.P. grade), and from OsO_4 (Aldrich, 99.8%) and KrF_2 in HF solvent, respectively. The purities of the compounds were checked by Raman spectroscopy to ensure completeness of the reactions.

2.2.8. Preparation of $[Na]_4[XeO_6]$

Sodium perxenate was prepared according to the method of Jaselskis *et al.*[176] and Appelman *et al.*[39] The apparatus used for the generation of an aqueous XeO_3 solution is depicted in Figure 2.6 and consisted of an ½-in. o.d. FEP U-trap containing XeF_6 that was equipped with two Whitey ORM2 stainless steel valves. One side of the U-trap was

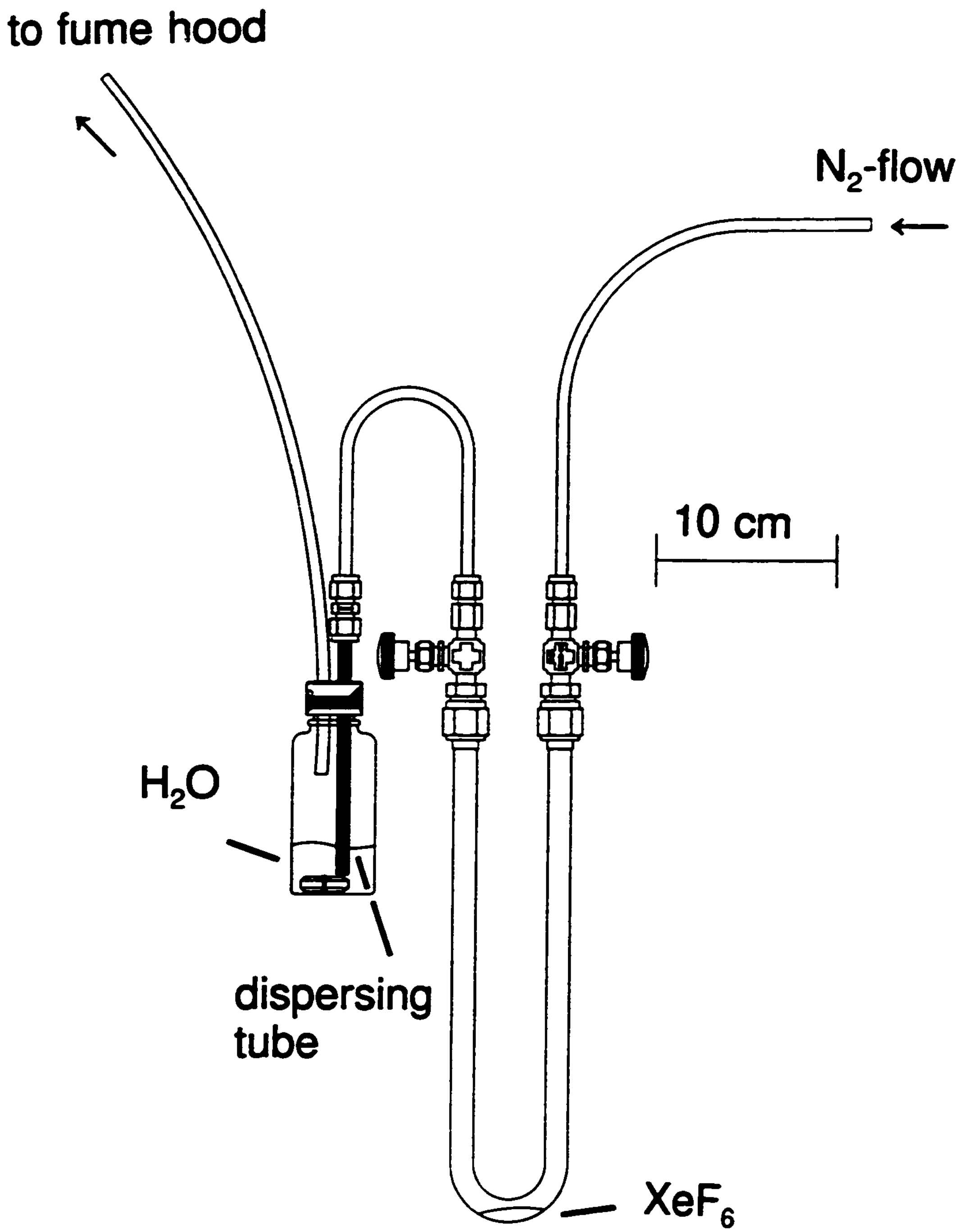

Figure 2.6 Apparatus for the generation of an aqueous XeO_3 solution; (A) ½-in. FEP trap equipped with Whitey ORM2 stainless steel valves, (B) Telfon capped FEP bottle with Teflon coated stirring bar.

connected to a dry N_2 supply while the other end was connected to a dispersing tube comprising 19 Teflon capillary tubes nested together inside a ¼-in. heat shrunk Teflon tube. The dispersing tube was inserted through the Teflon cap of a 130-mL FEP bottle.

In a typical preparation, 50 mL of H_2O (Caledon, HPLC grade) was stirred vigorously inside the FEP bottle with a magnetic stirring bar while a dry nitrogen flow was slowly passed through the FEP U-trap carrying XeF_6 vapour into the water. After *ca.* 4½ h, 5.329 g (0.022 mol) of XeF_6 had been transferred yielding a pale pink 0.43 M XeO_3 solution. Magnesium oxide (BDH) [4.877 g (0.121 mol)] was then added in several steps over a period of 30 min while stirring vigorously. The resulting MgF_2 suspension was centrifuged and the pink solution was decanted off. The remaining solid was washed twice with water and centrifuged. The combined decantates were centrifuged again, yielding a clear, pale pink solution which was stored at 9 °C in a capped FEP bottle until used for the synthesis of $[Na]_4[XeO_6]$.

The XeO_3 solution was converted to $[Na]_4[XeO_6]$ in two batches. Half of the XeO_3 solution was transferred into an FEP bottle and saturated with O_3 for 5 min. After addition of 6 mL of 16 M aqueous NaOH (BDH, >97%), which was freshly prepared to minimize the CO_3^{2-} contamination, a pale yellow solution resulted. Ozone was passed through the solution for *ca.* 2½ h until the yellow colouration disappeared and a white precipitate of $[Na]_4[XeO_6]\cdot nH_2O$ had formed. The $[Na]_4[XeO_6]\cdot nH_2O$ was isolated by vacuum filtration on a coarse porosity glass frit and washed with small amounts of cold (0 °C) water until the filtrate became yellow, *i.e.*, after the fourth wash. The wet $[Na]_4[XeO_6]$ was dried under dynamic vacuum at room temperature, readily loosing H_2O

to give 2.4769 (7.76 mmol) and 2.6359 g (8.26 mmol) of dry $[Na]_4[XeO_6]$ for each of two steps and corresponding to a total yield of 74%.

2.2.9. Preparation of $[N(CH_3)_4][IO_4]$ and $[N(CH_3)_4][IO_2F_4]$

Tetramethylammonium metaperiodate, $[N(CH_3)_4][IO_4]$, was prepared by a metathesis reaction analogous to that used to synthesize $[Cs][IO_4]$.[103] Approximately 30 mL of a 0.76 M aqueous solution of $[N(CH_3)_4][Cl]$ (Fluka Chemika, 98%) (2.500 g, 22.80 mmol) was slowly added, with stirring, to *ca.* 40 mL of aqueous $[Na][IO_4]$ (Matheson Coleman & Bell, 99.8%) (4.871 g, 22.77 mmol). A white precipitate formed almost immediately and the resulting mixture was stirred in an ice water bath for 30 min. The powdery, white precipitate was filtered and washed with ice cold water, and the sample dried for 15 h at 88 °C under dynamic vacuum inside a glass vessel. A yield of 3.2643 g (53.7 %) was obtained for $[N(CH_3)_4][IO_4]$. The purity of the compound was checked by infrared and Raman spectroscopy to ensure no water was present after drying.

Tetramethylammonium tetrafluoroperiodate was prepared according to the method of Christe *et al.*[103] In the drybox, $[N(CH_3)_4][IO_4]$ (0.7937 g, 2.995 mmol) was loaded into a 20 cm long ½-in. o.d. FEP tube heat fused to a 6 cm length of ¼-in. o.d. FEP tubing which was flared and attached to a Kel-F valve. Anhydrous HF solvent (*ca.* 3.4 mL) was distilled onto the $[N(CH_3)_4][IO_4]$. The sample was allowed to warm to room temperature, giving a colourless solution. The tube was then agitated for 3 days on a mechanical shaker. The HF was pumped off at 0 °C on the metal line until solid formed, followed by an additional 2 h at room temperature. The tube was then connected to the glass line and any traces of H_2O and HF remaining in the sample were pumped off for 12 h under dynamic vacuum at 45 °C. Fresh anhydrous HF was once again distilled onto the sample and the tube was agitated for a further 2 days, followed by removal of the solvent under dynamic vacuum to give 0.8959 g (96.8% conversion) of a white, crystalline solid. The purity was verified by recording the low-temperature Raman spectrum, which showed the presence of a mixture of $[N(CH_3)_4][$*cis*-$IO_2F_4]$ and $[N(CH_3)_4][$*trans*-$IO_2F_4]$ (*cis*-$IO_2F_4^-$: 207 (3), 235 (<0.5), 330 (35), 366 sh, lattice modes; 394 (19), $\nu_4(A_1)$; 560 (24), $\nu_3(A_1)$; 610 (74), $\nu_2(A_1)$; 847 (75), $\nu_1(A_1)$; and 870 (13), 880 sh cm^{-1}, $\nu_{12}(B_2)$; *trans*-$IO_2F_4^-$: 251 (5), $\nu_6(B_{2g})$; 380 (41), $\nu_8(E_g)$; 560 (24), $\nu_5(B_{1g})$; 571 (65), $\nu_2(A_{1g})$; and 813 (100) cm^{-1}, $\nu_1(A_{1g})$). Fluorine-19 NMR spectroscopy of $[N(CH_3)_4][IO_2F_4]$ in HF solvent indicated an approximate *cis*- to *trans*-isomer ratio of 70:30.

2.3. Solution Studies of XeO_4

2.3.1. Preparation of XeO_4 in SO_2ClF Solutions

The experimental apparatus for the preparation of an SO_2ClF solution of xenon tetroxide is depicted in Figure 2.7. The apparatus consisted of a glass vessel with a rotatable side arm (A). This vessel was connected to the metal submanifold through a 20-cm length of ¼-in. FEP tubing which provided enough flexability to allow agitation. A ¼-in. FEP U-trap (B), equipped with two Whitey ORF2 stainless steel valves, was attached to the main vacuum manifold. A ¼-in. FEP tube (C) was fused to the bottom of the U-tube. A graduated glass vessel (D) equipped with a 6-mm J. Young glass stopcock was connected to the metal vacuum line through a monel Nupro M-4MG-KZ-VH fine

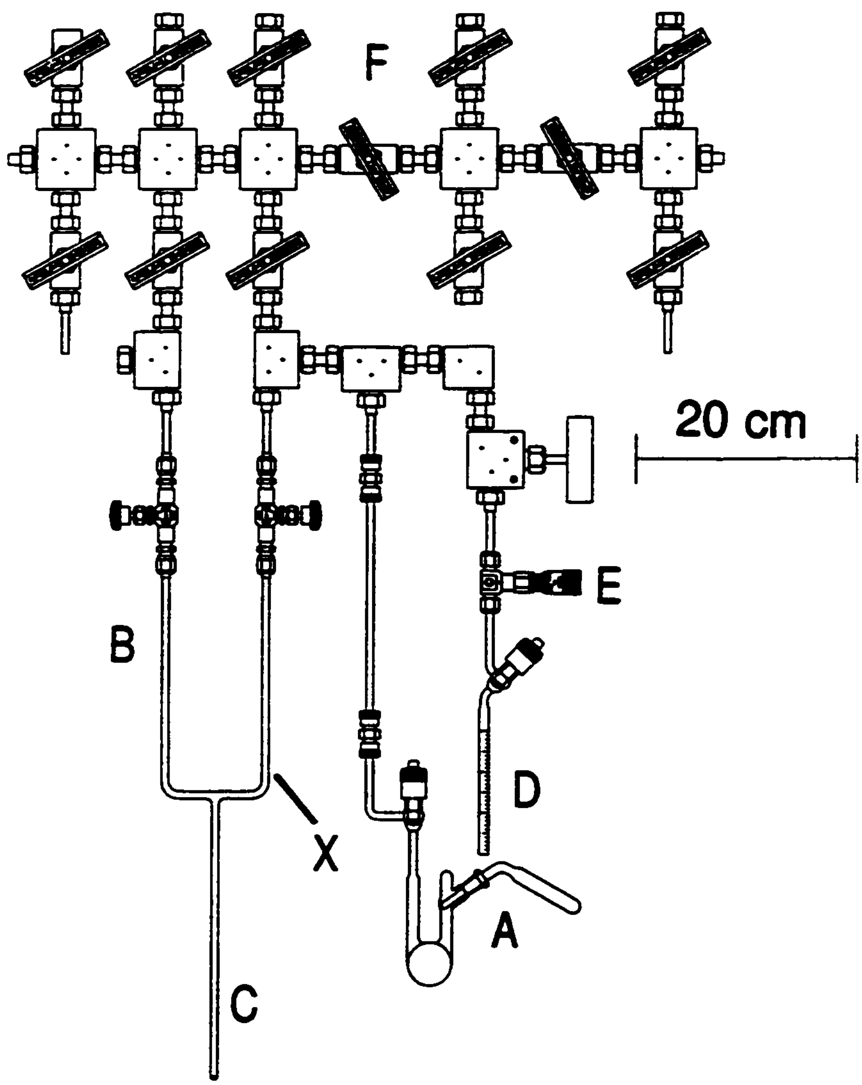

Figure 2.7 Experimental apparatus for the generation of XeO_4 in SO_2ClF solutions; (A) glass vessel with rotable side arm, (B) ¼-in. o.d. FEP U-trap equipped with two Whitey ORF2 stainless steel valves, (C) terminal ¼-in. FEP tube, (D) graduated glass vessel, (E) fine metering monel valve (Nupro M-4MG-KZ-VH) (F) main metal vacuum manifold (see Figure 3.2).

metering valve (E).

Sodium perxenate (0.13 g, 0.41 mmol) was transferred into the glass side arm. The glass bulb contained a mixture of 8 mL of concentrated sulfuric acid (BDH, 95 - 98%) and 7.8 mL of oleum (Baker Analyzed Reagent, 11 - 17% free SO_3). Free SO_3 was removed from the mixture by pumping under dynamic vacuum for at least 1 h on a glass vacuum line prior to use. After cooling the H_2SO_4 vessel and contents in an ice bath, sodium perxenate was slowly added while condensing the generated XeO_4 with liquid nitrogen under dynamic vacuum at point X in the FEP U-tube. This was followed by slowly condensing at -196 °C, under dynamic vacuum, *ca.* 0.5 mL of SO_2ClF from the graduated glass vessel (D) into the FEP trap *ca.* 15 cm above the point where XeO_4 had been condensed. The rate of distillation was regulated by a metering valve. Under static vacuum, the SO_2ClF solvent was allowed to slowly melt down onto the XeO_4, washing the XeO_4 into the ¼-in. FEP tube (C). After warming the mixture to -78 °C, a clear yellow solution was obtained and the FEP tube was heat sealed. **[Caution! Condensing SO_2ClF too rapidly onto XeO_4 resulted in several detonations even at temperatures near -196 °C because of thermal or pressure shock.]**

2.3.2. Preparation of XeO_4 in BrF_5 and HF Solutions

The experimental apparatus is shown in Figure 2.8 and is similar to the apparatus described in Section 2.3.1. Xenon tetroxide was generated from 0.1281 g (0.401 mmol) [84 mg (0.26 mmol)] of $[Na]_4[XeO_6]$ as described in Section 2.3.1 and was condensed at -196 °C under dynamic vacuum at point X in the FEP U-tube. Approximately 0.5 mL of

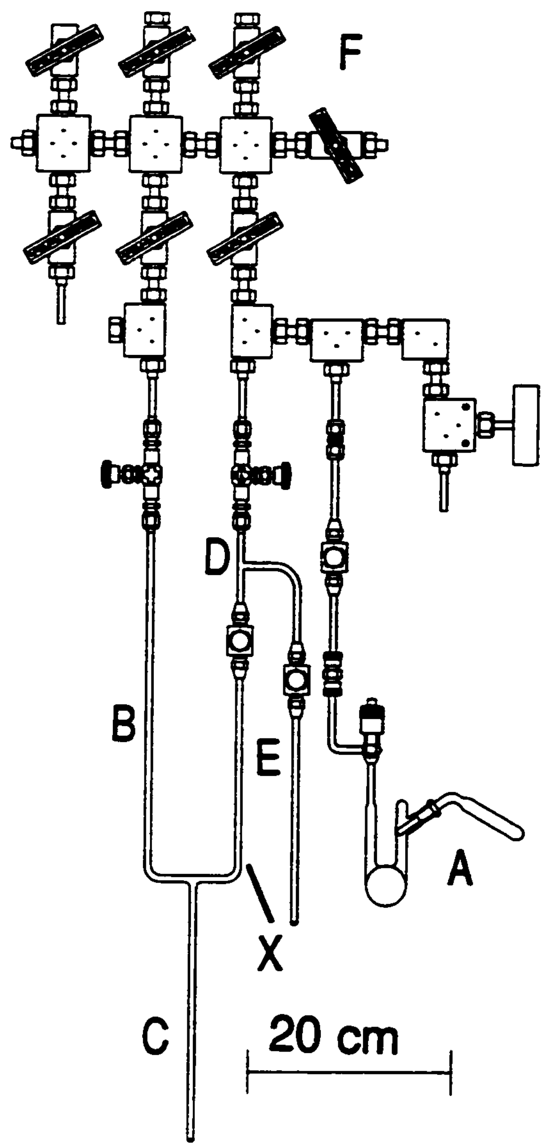

Figure 2.8 Experimental apparatus for the generation of XeO_4 in BrF_5 solvent, (A) glass vessel with turnable side arm, (B) ¼-in. o.d. FEP U-tube equipped with two Whitey ORF2 stainless steel valves, (C) ¼-in. FEP sample tube, (D) FEP T-piece, (E) ¼-in. o.d. FEP tube equipped with a Kel-F valve, (F) metal vacuum line.

BrF_5 [0.4 mL of HF] was slowly condensed under dynamic vacuum from the ¼-in. FEP tube (E) at 0 °C into the U-tube at -196 °C *ca.* 15 cm above the XeO_4. The BrF_5 [HF] solvent was slowly allowed to melt down onto the XeO_4 washing the XeO_4 into the terminal ¼-in. FEP tube under static vacuum. The sample in BrF_5 solvent was allowed to warm to -57 °C, yielding a clear, pale yellow solution before the sample was heat sealed at -196 °C. The sample in HF solvent was not allowed to warm above -196 °C before heat sealing the tube. Melting at -75 °C yielded a clear, pale yellow solution. Samples were stored at -196 °C until it could be characterized by NMR spectroscopy.

The sample in BrF_5 [HF] solvent was warmed to -25 °C for 5 min and to 0 °C for 2 min [-23 °C for 3 min] and monitored by low-temperature ^{129}Xe NMR spectroscopy after each warming cycle.

2.4. Lewis-Acid Properties of XeO_4

2.4.1. Preparation of XeO_4 in CH_3CN Solutions

The experimental setup and the procedure was the same as for the preparation of an XeO_4 solution in BrF_5 (see 2.3.2. Preparation of an XeO_4 Solution in BrF_5 and HF). Sodium perxenate (54 mg, 0.17 mmol) and *ca.* 0.4 mL of CH_3CN were used for this preparation. The tube was heat sealed under dynamic vacuum at -196 °C without melting the acetonitrile. The sample was allowed to melt inside a fume hood at -35 °C yielding a clear, colourless solution. The sample was stored under liquid nitrogen until it could be characterized by NMR and Raman spectroscopy.

2.4.2. Attempted Preparation of $XeO_4(CH_3CN)$ in SO_2ClF Solutions

The experimental setup and the procedure was a combination of those used for the preparation of an XeO_4 solution in SO_2ClF (see 2.3.1. Preparation of a XeO_4 Solution in SO_2ClF) and BrF_5 (see 2.3.2. Preparation of a XeO_4 Solution in BrF_5). Sodium perxenate (107.3 mg, 0.336 mmol) and *ca.* 0.6 mL of SO_2ClF were used. After the preparation of a XeO_4 solution in SO_2ClF solvent, approximately 0.45 mmol of CH_3CN was condensed onto the solution at -196 °C. The tube was heat sealed prior to melting the acetonitrile. The sample was allowed to melt inside a fume hood at -78 °C and the CH_3CN dissolved, yielding a clear, colourless solution. The sample was subsequently characterized by NMR and Raman spectroscopy.

2.4.3. Reaction of XeO_4 with CsF in HF and CH_3CN Solvents

The experimental apparatus is depicted in Figure 2.8 and the procedure is similar to the preparation of XeO_4 in BrF_5 solvent (see 2.3.2. Preparation of a XeO_4 Solution in BrF_5). A ¼-in. FEP sample tube (C) heat fused to a ¼-in. U-trap (B) was fitted with a Whitey ORF2 stainless steel valve and a Kel-F valve as depicted in Figure 2.8 and dried. The entire assembly was brought into the drybox and loaded with 0.0332 g, 0.219 mmol [0.0302 g, 0.199 mmol] CsF for the HF [CH_3CN] sample. The U-tube was reconnected to the metal line as shown in Figure 2.8. For the generation of XeO_4, 0.0705 g, 0.221 mmol [0.0727 g, 0.228 mmol] of $[Na]_4[XeO_6]$ was weighed into the glass side arm A. Initially, a small amount of HF [CH_3CN] was distilled into the FEP U-tube to wash down small amounts of CsF that had adhered to the upper walls in order to avoid direct contact of solid XeO_4 with CsF. After the XeO_4 had condensed, the remaining solvent was distilled into the FEP U-tube. A total of *ca.* 0.4 mL of HF [CH_3CN] was used.

Melting of the HF sample at -78 °C resulted in a clear, colourless solution. In the case of the acetonitrile, melting at -40 °C yielded a cloudy, pale yellow solution with small amounts of fine white solid at the bottom (CsF). After several minutes, a gel-like precipitate formed and slowly settled. The colour of the solution became lighter and finally colourless. Approximately ⅓ of the sample volume was white precipitate.

2.4.4. Reaction of XeO_4 with [$N(CH_3)_4$][F] in CH_3CN Solvents

The experimental apparatus is depicted in Figure 2.8 and the procedure is similar to that for the reaction between XeO_4 and CsF in CH_3CN solvent (see **2.4.3. Reaction of XeO_4 with CsF in HF and CH_3CN Solvents**). Inside the drybox, a ¼-in. FEP sample tube fused to a ¼-in. FEP U-tube, that was fitted with a Whitey ORF2 stainless steel valve and a Kel-F valve, was loaded with 0.0147 g (0.158 mmol) [$N(CH_3)_4$][F]. The U-tube was reconnected to the metal line as shown in Figure 2.8. For the generation of XeO_4, 0.0945 g, 0.296 mmol of $[Na]_4[XeO_6]$ was weighed into the glass side arm A. A small amount of CH_3CN was initially distilled into the FEP U-tube in order to wash down any [$N(CH_3)_4$][F] adhering to the upper walls in order to prevent direct contact of solid XeO_4 with [$N(CH_3)_4$][F]. After condensing XeO_4, the remaining solvent was distilled into the FEP U-tube. A total of *ca.* 0.4 mL CH_3CN was used. After melting the CH_3CN solvent at -40 °C, a yellow solution with a suspension of a fine, white precipitate was obtained and the sample was heat sealed. A second sample was prepared using 0.0153 g

(0.1643 mmol) of [N(CH_3)$_4$][F], 0.0934 g (0.2926 mmol) of [Na]$_4$[XeO_6] and *ca.* 0.4 mL of CH_3CN and yielded a yellow solution containing a fine suspension of a white solid. Most of the CH_3CN solvent was removed under dynamic vacuum at -30 °C yielding a yellow-orange slush. During the heat sealing of both samples, small detonations occurred close to the sealing region that were caused by white particles that remained above the solvent level.

2.5. Synthesis and Characterization of Xenon(VIII) Oxide Fluorides

2.5.1. Reaction of XeO_4 with XeF_6 in SO_2ClF, HF, and BrF_5 Solvents

The experimental apparatus is depicted in Figures 2.7 and 2.8 and the procedures for the preparation of the solutions have been described above. The weighing vessel containing XeF_6 was connected to the FEP T-piece (D) for the reactions in HF and BrF_5, while in the case of SO_2ClF, glass vessel (A) was substituted by the ¼-in. FEP weighing vessel equipped with a Kel-F valve. Prior to distillation, the connections were passivated using fluorine while the XeO_4 solution in SO_2ClF was stored under 1 atm of dry nitrogen at -78 °C. For the reaction in SO_2ClF/HF/BrF_5, 0.1238 g (0.3878 mmol)/0.08205 g (0.257 mmol)/0.1095 g (0.3428 mmol) of Na_4XeO_6 was used for the generation of XeO_4. Approximately 0.6 mL/0.28 mL/0.47 mL of SO_2ClF/HF/BrF_5 solvent followed by 0.0951 g (0.3877mmol)/0.0936 g (0.3816 mmol)/0.1286 g (0.524 mmol) of XeF_6 were condensed onto the XeO_4. The samples were heat sealed and stored at -196 °C until characterized by NMR spectroscopy.

The samples were slowly warmed to -10 °C and monitored by low temperature

NMR spectroscopy between each warming cycle.

2.5.2. Reaction of $[Na]_4[XeO_6]$ with XeF_6 in SO_2ClF, HF, and BrF_5 Solvents

For the reactions in SO_2ClF/HF/BrF_5 solvents, a 4-mm [¼-in. o.d.] FEP tube fitted with a Kel-F valve was loaded with 0.035 g (0.11 mmol) [0.0555 g (0.1738 mmol)]/0.0135 g (0.0433 mmol)/0.0162 g (0.051 mmol) of $[Na]_4[XeO_6]$ inside the drybox followed by condensing 0.26 mL [0.66 mL]/0.53 mL/0.35 mL of SO_2ClF/HF/BrF_5 solvent onto the solid. Xenon hexafluoride from a ¼-in. o.d. FEP weighing vessel 0.0292 g (0.119 mmol) [0.4952 g (2.02 mmol)/0.1498 g (0.611 mmol)/0.0969 g (0.4 mmol)] was distilled into the reaction tube followed by heat-sealing the sample. The samples were gradually allowed to warm up to -10 °C and monitored by low-temperature NMR spectroscopy between each warming cycle.

2.5.3. Reaction of $[Na]_4[XeO_6]$ with HF

In a typical experiment, 0.0256 g (0.0802 mmol) of $[Na]_4[XeO_6]$ was loaded into a 4-mm FEP tube fitted with a Kel-F valve inside the drybox. Approximately 0.3 mL HF was slowly condensed from an ¼-in. o.d. FEP tube at 0 °C equipped with a Kel-F valve into the 4-mm FEP tube above the perxenate at -196 °C. The HF was allowed to melt at -78 °C onto the $[Na]_4[XeO_6]$ which yielded a pale yellow solid and occasionally resulted in small explosions which did not rupture the sample tube. The tube was heat sealed and stored at -196 °C. **[Caution! Rapid distillation of HF at room temperature onto $[Na]_4[XeO_6]$ at -196 °C caused an explosion that ruptured the FEP tube and**

destroyed a glass Dewar.] The sample was characterized by ^{129}Xe NMR and Raman spectroscopy before and after it was allowed to warm to -10 °C.

2.5.4. Reaction of $[Na]_4[XeO_6]$ with AsF_5 in HF Solution

Inside the drybox, 0.0184 g (0.0576 mmol) of $[Na]_4[XeO_6]$ was loaded into a 4-mm FEP tube fitted with a Kel-F valve. Approximately 0.18 mL of HF was slowly condensed, at 0 °C, above the perxenate at -196 °C from a ¼-in. FEP HF storage tube fitted with a Kel-F valve. The HF was allowed to melt onto the solid at -78 °C. The manifold was pressurized with AsF_5 (218 Torr, 0.224 mmol) and the gas was condensed into the reactor by cooling the reaction vessel with liquid nitrogen. The tube was heat sealed and stored at -196 °C until characterized by NMR spectroscopy.

2.5.5. Reaction of $[Na]_4[XeO_6]$ with BrF_5

Inside the drybox, 0.0155 g (0.049 mmol) of $[Na]_4[XeO_6]$ was loaded into a 4-mm FEP tube fitted with a Kel-F valve. Approximately 0.32 mL of BrF_5 was distilled onto the solid at -196 °C and the tube was heat sealed. The sample was warmed to -10 °C and monitored by low-temperature NMR and Raman spectroscopy between before and after warming of the sample.

2.5.6. Reaction of $[Na]_4[XeO_6]$ with BF_3 in BrF_5 Solvent

Inside the drybox 0.01338 g (0.042 mmol) $[Na]_4[XeO_6]$ was loaded into a 4-mm FEP tube fitted with a Kel-F valve. Approximately 0.28 mL of BrF_5 was distilled onto the perxenate sample. The mixture was allowed to warm to 0 °C for 10 min and was frozen again at -196 °C. The manifold was then pressurized with BF_3 (119.5 Torr, 0.1226 mmol) and was condensed into the reactor by cooling with liquid nitrogen. The mixture was allowed to melt at -50 °C, yielding a yellow solution and white precipitate. The sample was heat sealed and stored at -196 °C until characterized by NMR spectroscopy.

2.5.7. Reaction of XeO_4 with KrF_2 in SO_2ClF and HF Solvents

The experimental apparatus is depicted in Figure 2.8. The procedures for the generation of the XeO_4 solutions have been described above. Krypton difluoride was distilled from a ¼-in. o.d. FEP weighing tube into a reaction vessel containing the appropriate XeO_4 solution. In the case of HF solutions, the ¼-in. FEP tube (E) was replaced by the KrF_2 weighing tube and was followed by passivation of the connections using fluorine prior to KrF_2 distillation. During passivation, the XeO_4 solution was kept under 1 atm of nitrogen pressure at -78 °C. Sodium perxenate was used for the generation of XeO_4 solutions in SO_2ClF [HF]; 0.102g, 0.32 mmol [0.07395 g, 0.2316 mmol]. Samples were prepared by distilling 1.04 mL of SO_2ClF [0.21 mL HF] and 0.155 g, 1.27 mmol [0.055 g, 0.4516 mmol] of KrF_2 onto the XeO_4 solution.

The sample in SO_2ClF was gradually allowed to warm to -30 °C whereupon gas evolution commenced. The sample was was cooled to and maintained at -35 °C for several minutes prior to heat-sealing. The sample was stored at -196 °C until it could be characterized by NMR spectroscopy.

The sample in HF was allowed to warm to -30 °C for 2½ min and was then heat sealed. The sample was subsequently warmed up to 0 °C for 12 min while being monitored by ^{129}Xe NMR spectroscopy.

2.5.8. Reaction of $[Na]_4[XeO_6]$ with KrF_2 in HF, BrF_5, and SO_2ClF Solvents

For the reaction of KrF_2 with XeO_6^{4-} in HF/BrF_5/SO_2ClF, 0.013 g (0.041 mmol)/0.0154 g (0.048 mmol)/0.0364 g (0.114 mmol) of $[Na]_4[XeO_6]$ was loaded inside the drybox into a 4-mm FEP tube fitted with a Kel-F valve. Approximately 0.6 mL/0.32 mL/0.25 mL of HF/BrF_5/SO_2ClF solvent was distilled onto the solid followed by condensing 0.0772 g (0.634 mmol)/0.1049 g (0.86 mmol)/0.0135 g (0.111 mmol) of KrF_2 into the reaction tube. The samples in HF and SO_2ClF were heat sealed under dynamic vacuum. The sample in BrF_5 was gradually warmed up to 0 °C at which point slow gas evolution was observed. The sample was then cooled and heat sealed and stored at -196 °C until characterized by NMR spectroscopy.

2.5.9. Reaction of XeO_4 with $[KrF][AsF_6]$ in HF Solvent

The experimental apparatus is depicted in Figure 2.8 and the procedure for the preparation of a solution of XeO_4 in HF is described above. Sodium perxenate (0.08365 g, 0.262 mmol) was used for the generation of XeO_4. After distillation of *ca.* 0.57 mL of HF onto the XeO_4, the solution was melted at -78 °C and the ¼-in. o.d. FEP tube (E) containing HF was replaced by a weighing tube containing KrF_2. During passivation of the connections with F_2, the solution of XeO_4 in HF was maintained under 1 atm of dry nitrogen at -78 °C. Krypton difluoride (0.046 g, 0.378 mmol) was distilled under dynamic vacuum into the FEP trap and was condensed into the terminal FEP tube (C) under static vacuum. The manifold was pressurized with AsF_5 and the gas was condensed in two portions into a ¼-in. FEP tube by cooling it with liquid nitrogen (total; 1500 Torr, 1.54 mmol). The FEP tube was replaced by the weighing vessel and after F_2 passivation of the connections, AsF_5 was condensed under dynamic vacuum into the tube. Addition of AsF_5 to the clear, pale yellow solution of XeO_4 and KrF_2 in HF resulted in cloudiness and some gas evolution. After 3 min, the sample was heat sealed. While recording the NMR spectrum at -78 °C, the sample developed large amounts of white precipitate, which was subsequently characterized by Raman spectroscopy.

2.5.10. Reaction of XeO_3 with $[KrF][AsF_6]$ in HF Solvent

Inside a glove bag, 27 μL (1.5 mmol) of H_2O was syringed into a ¼-in. FEP sample tube equipped with a stainless steel valve. After distillation of approximately 0.6 mL of HF onto the water and thorough mixing, 0.1238 g (0.5047 mmol) of XeF_6 was condensed onto the solution at -196 °C. The mixture was allowed to warm stepwise to -78 °C and to room temperature to ensure complete hydrolysis of XeF_6 to XeO_3. Krypton difluoride (0.1180 g, 0.9688 mmol) followed by *ca.* 1.54 mmol of AsF_5 were condensed onto the frozen mixture. Upon melting the HF at -78 °C, slow gas evolution ensued and the solution became yellow and a white precipitate formed. The reaction tube was heat sealed after the sample had been maintained at -78 °C for *ca.* 20 min. at which time gas evolution still had not ceased.

2.6. Fluoride Ion Acceptor Properties of OsO_4

2.6.1. Synthesis of $[N(CH_3)_4][OsO_4F]$

Anhydrous CH_3CN (0.95 mL) was condensed into a tube containing 0.2293 g (0.9021 mmol) of OsO_4 at -196 °C. The OsO_4 dissolved upon warming the mixture to room temperature to give a pale yellow solution to which, after transferring to a drybox and cooling to -110 °C, a stoichiometric amount of $[N(CH_3)_4][F]$ (0.0858 g, 0.9212 mmol) was added. Upon thawing and warming to -20 °C outside the drybox, a red-brown precipitate formed at the $[N(CH_3)_4][F]$ - OsO_4/CH_3CN solution interface. Upon mixing at room temperature, the red-brown precipitate merged with the yellow OsO_4/CH_3CN solution to produce a homogeneous orange precipitate. Removal of CH_3CN under dynamic vacuum at room temperature yielded a very finely divided orange powder.

2.6.2. Crystal Growth of $[N(CH_3)_4][OsO_4F]$

Sufficient CH_3CN (0.76 mL) was distilled onto 0.0483 g (0.1768 mmol) of $[N(CH_3)_4][OsO_4F]$ to solubilize the solid at 40 °C. Large orange, plate-shaped crystals were grown by placing the tube inside a closed Dewar of water at 40 °C and allowing it to cool to ambient temperature over a period of five days. The supernatant was carefully pipetted off the sample inside a glovebag previously purged with dry N_2 and residual CH_3CN was removed from the tube containing the crystals by rapid evacuation at room temperature for *ca.* 30 s. The FEP reaction tube containing the crystals was transferred to a drybox equipped with a microscope where the crystals were removed, mounted inside 0.5-mm i.d. Lindemann capillaries, and heat sealed. The crystal used for X-ray data collection had the dimensions, 0.400 x 0.442 x 0.0084 mm^3.

2.6.3. Synthesis of $[N(CH_3)_4]_2[OsO_4F_2]$

Approximately 0.4 mL of anhydrous CH_3CN was condensed onto 0.1642 g (0.6460 mmol) of OsO_4 at -196 °C and warmed to room temperature to effect dissolution. Approximately two equivalents of $[N(CH_3)_4][F]$ (0.1219 g (1.3087 mmol)) were added to the frozen OsO_4/CH_3CN mixture at -110 °C as described in the preceding section. Upon warming to -25 °C, a red-brown precipitate formed at the $[N(CH_3)_4][F]$ - OsO_4/CH_3CN solution interface, which when agitated, yielded a homogeneous, brown precipitate. The solvent was removed under dynamic vacuum at -20 °C followed by pumping at ambient temperature to give 0.2645 g of a light brown, ochre-colored powder. Raman spectroscopy revealed the presence of a mixture of $[N(CH_3)_4]_2[OsO_4F_2]$, $[N(CH_3)_4][OsO_4F]$, and $[N(CH_3)_4][F]$. The product mixture (0.2289 g) was loaded into arm A of a two-arm (h-shaped) Pyrex glass vessel (Figure 2.9) and approximately 1.2 mL of CH_3CN was condensed onto the mixture at -196 °C. The mixture was washed 12 times at -30 °C by decanting the faint yellow solution together with some suspended material into arm B of the vessel at -30 °C followed by back-distillation of the CH_3CN onto the brown mixture under static vacuum. After removal of CH_3CN, 0.1818 g (80%) of an ochre-colored material was recovered, which, according to its Raman spectrum, still contained significant amounts of $[N(CH_3)_4][OsO_4F]$. Thirteen additional washings were performed on 0.1727 g of material between -25 and -30 °C, yielding 0.1205 g (70%) of ochre $[N(CH_3)_4]_2[OsO_4F_2]$ containing only a minor amounts of $[N(CH_3)_4][OsO_4F]$ impurity. The

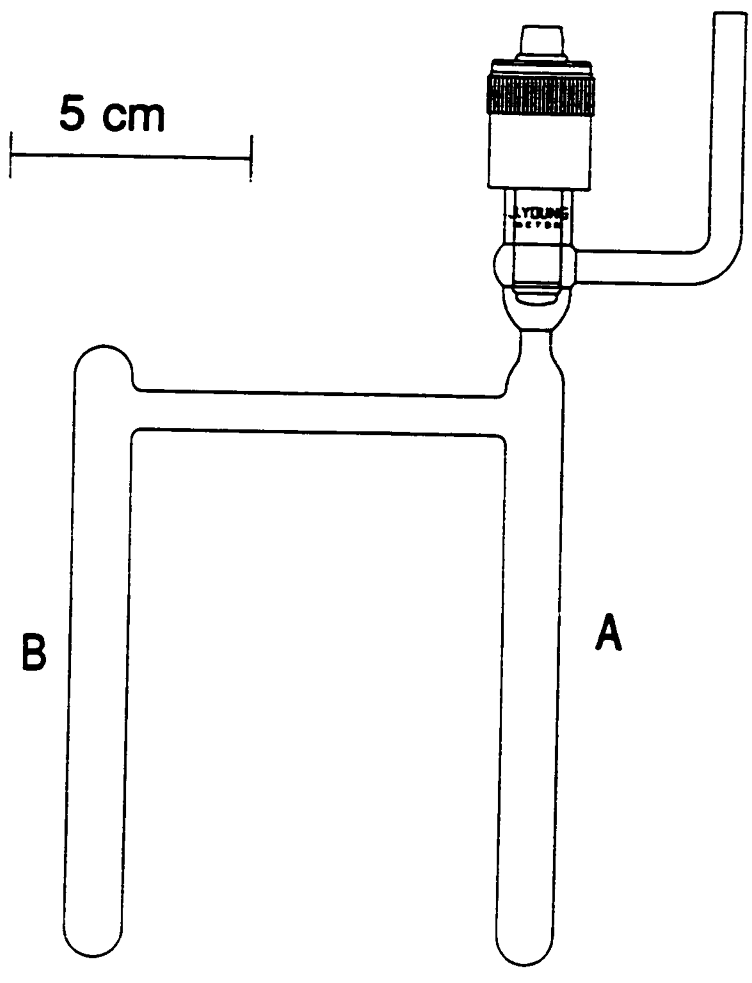

Figure 2.9 Pyrex glass reaction vessel equipped with a 4-mm J.Young Teflon/glass stopcock.

$[N(CH_3)_4]_2[OsO_4F_2]$ salt was found to be a significantly weaker Raman scatterer and more prone to decomposition in the laser beam (1064-nm excitation) than $[N(CH_3)_4][OsO_4F]$.

2.6.4. Synthesis of $[NO]_n[OsO_4F_n]$

Approximately 1.8 mmol NOF was condensed onto 0.0657 g (0.2585 mmol) of OsO_4 inside a 4-mm FEP tube equipped with an Kel-F valve at -196 °C. Upon melting the NOF at -78 °C a yellow-brown solid was initially observed. After agitation, a dark brown suspension formed. Excess NOF was removed under dynamic vacuum at -78 °C, yielding a brown, finely divided solid. The tube was sealed under dynamic vacuum and stored at -196 °C.

2.6.5. Attempted Synthesis of $[NO_2]_n[OsO_4F_n]$

Approximately 0.07 mL NO_2F was condensed onto 0.0156 g (0.061 mmol) of OsO_4 in a 4-mm FEP tube equipped with a Kel-F valve at -196 °C. Maintaining the sample at -78 °C for two days and subsequent removal of the NO_2F at -78 °C did not provide any evidence for reaction when monitored by Raman spectroscopy. Condensation of 0.3 mmol of NO_2F (*ca.* 5.5 atm) onto the OsO_4, followed by warming to 55 °C for 1 h, also did not result in a reaction.

2.7. Lewis-Acid Properties of OsO_3F_2

2.7.1. Synthesis of $[N(CH_3)_4][OsO_3F_3]$

Approximately 0.4 mL of anhydrous HF was condensed onto 0.1005 g (0.364

mmol) of OsO_3F_2 in a ¼-in. FEP tube at -196 °C. Upon warming to room temperature, OsO_3F_2 was found to be insoluble in HF. Addition of $[N(CH_3)_4][F]$ (0.0342 g, 0.367 mmol) to the frozen OsO_3F_2/HF mixture at -110 °C followed by warming to room temperature and mixing, resulted in a clear orange solution. Removal of HF solvent under dynamic vacuum at -78 °C yielded 0.1299 g (0.3517 mmol; 97% yield) of an orange powder. Samples for NMR spectroscopy were prepared using 0.0487 g (0.1319 mmol) [0.0191 g (0.0517 mmol)] and 0.2 [0.2] mL of CH_3CN [HF] solvent in 4-mm FEP tubes and resulted in a yellow-orange supernatant and an orange precipitate in CH_3CN and a clear, yellow solution in HF.

2.7.2. Crystal Growth of $[N(CH_3)_4][OsO_3F_3]$

Approximately 0.57 mL of CH_3CN was condensed onto 0.0034 g (0.0123 mmol) $[N(CH_3)_4][OsO_3F_3]$ at -196 °C which yielded a clear orange solution upon warming to 0 °C. Removal of CH_3CN solvent at 0 °C over a period of *ca.* 1 h yielded thin orange plates as a coating on the walls of the FEP tube. Crystals were selected and mounted at -120 °C as described in Section 2.12.1. The crystal used in this study had the dimensions, 0.30 × 0.15 × 0.01 mm^3.

2.7.3. Synthesis of $[N(CH_3)_4]_2[OsO_3F_4]$

Inside a drybox, 0.0471 g (0.1717 mmol) of OsO_3F_2 and 0.03205 g (0.34409 mmol) $[N(CH_3)_4][F]$ were loaded into a ¼-in. FEP reactor at -150 °C. After condensing approximately 0.55 mL of CH_3CN onto the mixture, the CH_3CN solvent was allowed to melt at -40 °C resulting in a dark brown suspension upon agitation. After 1h of reaction time, the CH_3CN was removed under dynamic vacuum at -38 to -32 °C yielding a grey, finely divided solid.

2.7.4. Synthesis of [NO][OsO_3F_3]

Approximately 0.04 mL of NOF was condensed into a 4-mm FEP reaction tube containing 0.0500 g (0.181 mmol) of OsO_3F_2 at -196 °C, warmed to -78 °C and agitated for ca. 90 min. Removal of excess NOF at -78 °C yielded a light orange, ochre-colored solid, which was found to decompose upon warming to room temperature.

2.7.5. Synthesis of $OsO_3F_2(CH_3CN)$

Approximately 0.1 mL of CH_3CN was condensed onto 0.0545 g (0.1973 mmol) of OsO_3F_2 in a ¼-in. FEP tube at -196 °C. Upon warming to -40 °C and agitation, a red-brown precipitate formed under an orange solution. Excess CH_3CN was removed under dynamic vacuum at -40 °C initially yielding a dark red-brown solid. Further pumping gave an orange-ochre solid. An NMR sample was prepared from 0.0305 g (0.1104 mmol) of OsO_3F_2 and approximately 0.3 mL of CH_3CN in a 4-mm FEP tube. NMR samples of $OsO_3F_2(CH_3CN)$ [$OsO_3F_2(CH_3C^{15}N)$] in SO_2ClF solvent were prepared by condensing 0.02 mL CH_3CN [0.0065 g (0.1546 mmol) $CH_3C^{15}N$] onto 0.0335 g (0.129 mmol) [0.02081 g (0.0753 mmol)] of OsO_3F_2 in a 4-mm FEP tube at -196 °C. After melting the CH_3CN at -40 °C and initial mixing, *ca.* 0.3 mL [0.2 mL] of SO_2ClF was condensed onto the mixture at -196 °C.

2.8. Fluoride Ion Donor Properties of OsO_3F_2

2.8.1. Synthesis of $[OsO_3F][HF]_2[AsF_6]$, $[Os_2O_6F_3][AsF_6]$, and $[OsO_3F][AsF_6]$ and Crystal Growth of $[OsO_3F][AsF_6]$

Inside a drybox, 0.09203 g (0.333 mmol) OsO_3F_2 was loaded into a ¼-in. o.d. FEP reaction tube equipped with a Kel-F valve. Approximately 0.5 mL of HF was condensed into the tube at -196 °C and followed by *ca.* 0.7 mmol of AsF_5. Osmium trioxide difluoride dissolved upon warming to ambient temperature yielding a clear yellow-orange solution. Removal of most of the HF solvent and excess AsF_5 at -78 °C for *ca.* 3 h resulted in the formation of an orange crystalline precipitate under *ca.* 0.1 mL of HF, which was identified by Raman spectroscopy as $[OsO_3F][HF]_2[AsF_6]$. Addition of *ca.* 0.5 mmol of AsF_5 and 0.57 mL of HF followed by complete removal of the HF solvent at -78 °C over a period of *ca.* 5 h yielded straw-yellow $[OsO_3F][AsF_6]$. Distillation of *ca.* 0.3 mL of HF onto the solid resulted in a yellow solution above a heterogenous mixture of yellow ($[OsO_3F][AsF_6]$) and orange ($[Os_2O_6F_3][AsF_6]$) solids at -78 °C as identified by Raman spectroscopy. Thorough agitation at -78 °C resulted in an orange precipitate comprised exclusively of $[Os_2O_6F_3][AsF_6]$. Condensation of an additional 0.4 mmol of AsF_6 onto the mixture resulted in complete dissolution of the solid close to room temperature and did not yield a precipitate at -78 °C. Approximately 0.05 mL HF was removed at -78 °C resulting in yellow precipitate, which was identified by Raman spectroscopy as $[OsO_3F][AsF_6]$. After redissolving the precipitate, yellow crystals were grown at -78 °C over a period of 12 h. The solvent was removed under dynamic vacuum at -78 °C and yellow crystals were selected and mounted at -110 °C as described in

Section 2.12.1. The crystal used in this study had the dimensions, 0.12 × 0.10 × 0.10 mm^3.

An NMR sample in a 4-mm. o.d. FEP tube was prepared using 0.0303 g (0.1097 mmol) of OsO_3F_2, 0.2 mL of HF, and 1.5 mmol of AsF_5 (*ca.* 13.5-fold molar excess).

2.8.2. Crystal Growth of $[OsO_3F][HF]_2[AsF_6]$

Crystals of $[OsO_3F][HF]_2[AsF_6]$ were obtained from a sample composed of 0.1032 g (0.374 mmol) of OsO_3F_2 and *ca.* 0.9 mmol of AsF_5 in 0.85 mL of HF. Orange crystals of $[OsO_3F][HF]_2[AsF_6]$ grew during slow removal of the HF solvent and excess AsF_5 under vacuum at -78 °C. After almost complete removal of the HF solvent, a portion of the crystalline sample turned yellow ($[OsO_3F][AsF_6]$). The pumping was discontinued and the FEP tube was immediately back-filled with dry nitrogen while maintaining the sample at -78 °C. Orange crystals were selected and mounted at -117 °C as described in Section 2.12.1. The crystal used in this study had the dimensions, 0.25 × 0.20 × 0.05 mm^3.

2.8.3. Synthesis $[OsO_3F][HF][SbF_6]$ and $[OsO_3F][HF]_2[SbF_6]$ and Crystal Growth of $[OsO_3F][HF][SbF_6]$

Inside the drybox, 0.03962 g (0.2217 mmol) of SbF_3 was transferred into the vertical arm of a ¼-in. o.d. FEP T-shaped reactor equipped with a Kel-F valve. After condensation of approximately 0.6 mL of HF onto the SbF_3, the mixture was allowed to react with F_2 at room temperature until white solid SbF_3 had dissappeared, *i.e.*, completely reacted to form SbF_5. Inside the drybox, 0.06342 g (0.2296 mmol) of OsO_3F_2 was added to the frozen solution. Warming to room temperature yielded a clear yellow-orange solution. Upon cooling to -78 °C, clusters of orange needles grew and were identified as $[OsO_3F][HF]_2[SbF_6]$ by Raman spectroscopy. Removal of the HF solvent at -78 °C and briefly at room temperature under dynamic vacuum yielded solid straw-yellow $[OsO_3F][HF][SbF_6]$. After redissolving the yellow solid in approximately 0.6 mL of HF at room temperature, orange clusters of cyrstals and yellow plates grew upon cooling to -78 °C over a period of *ca.* 12 h. The HF solvent was decanted into the side arm of the T-reactor, which was subsequently heat sealed under dynamic vacuum while the crystals were maintained at -75 °C. Yellow crystals were selected and mounted at -100 °C as described in Section 2.12.1. The crystal used in this study had the dimensions, 0.08 × 0.04 × 0.03 mm^3.

In a separate experiment using 0.538 g (0.3001 mmol) of SbF_3, 0.0695 g (0.2516 mmol) OsO_3F_2 and *ca.* 0.6 mL of HF, small amounts of $[OsO_3F][SbF_6]$ were observed by Raman spectroscopy upon removal of the HF solvent (pumped on for 3h at -78 °C and 5 min at room temperature). Pumping at room temperature for 5 h did not increase the amount of $[OsO_3F][SbF_6]$ significantly. Pumping on the sample at 45 °C, at which temperature the sample was a liquid, for 2 h using a mercury diffusion pump, resulted in a decrease in the relative Raman intensities of the OsO_2 stretches of $[OsO_3F][SbF_6]$ compared to those of $[OsO_3F][HF][SbF_6]$. Distillation of 0.6 mL of HF onto the solid resulted in dissolution of the solid at room temperature and slow precipitation of yellow $[OsO_3F][HF][SbF_6]$. Reduction of the solution volume to 0.17 mL at -78 °C followed by redisolution of the solid at room temperature resulted in the precipitation of

$[OsO_3F][HF]_2[SbF_6]$ at -78 °C.

2.8.4 Synthesis and Crystal Growth of $[OsO_3F][Sb_3F_{16}]$

Inside a glove bag, 0.9393 g (4.334 mmol) of SbF_5 was syringed into a ¼-in. o.d. FEP reaction tube equipped with a Kel-F valve. Inside a drybox, 0.0847 g (0.3067 mmol) of OsO_3F_2 was added to the frozen solution (*ca.* -140 °C) and the reaction mixture was warmed to 55 °C outside the drybox, yielding a clear straw-yellow solution upon sonication. The solution was placed in a water bath at 55 °C and allowed to cool to 35 °C for 2 h yielding copious amounts of straw-yellow flaky crystals. Excess SbF_5 was removed under dynamic vacuum at ambient temperature over a period of 5½ h yielding 0.2906 g of straw-yellow plates of $[OsO_3F][Sb_3F_{16}]$ (theor. 0.2841 g for a 1:3 stoichiometry of OsO_3F_2:SbF_5). Straw-yellow crystals were selected and mounted at -120 °C as described in Section 2.12.1. The crystal used in this study had the dimensions, 0.14 × 0.10 × 0.005 mm^3.

An NMR sample of OsO_3F_2 in neat SbF_5 was prepared in a ¼-in. o.d. FEP tube using 0.0538 g (0.1948 mmol) of OsO_3F_2 and 2.41 g of SbF_5. Samples for NMR spectroscopy were prepared in 4-mm o.d. FEP tubes equipped with Kel-F valves by dissolving 0.0274 g (0.0296 mmol) [0.0302 g (0.0326 mmol)] of $[OsO_3F][Sb_3F_{16}]$ in *ca.* 0.35 mL of SO_2ClF [0.18 mL of HF], yielding a clear yellow solution upon warming to -78 °C [clear yellow solution upon warming to room temperature].

2.9. Lewis-Acid Properties of OsO_2F_4

2.9.1. Preparation of [Cs][OsO_2F_5]

Inside the drybox, 0.071 g (0.238 mmol) of OsO_2F_4 and 0.0325 g (0.214 mmol) of CsF (10% excess of OsO_2F_4) were loaded into a 4-mm FEP tube fitted with a Kel-F valve. The mixture was heated to 90 °C several times for periods of one minute followed by Raman characterization of the dark coloured solid. The mixture was then heated to 150 °C until the Raman spectrum of the now red solid showed only small amounts of unreacted OsO_2F_4. The reactor was connected to the glass vacuum line through a ¼-in. FEP trap and the excess OsO_2F_4 was pumped off under dynamic vacuum at room temperature for *ca.* 1 min until no further OsO_2F_4 condensed into the trap at -196 °C; 0.0961 g of a light brown solid was recovered. Decomposition occurred during the transfer into a dry glass NMR tube.

2.9.2. Synthesis of [NO][OsO_2F_5] in NOF Solutions

Inside the drybox, 0.0586 g (0.1965 mmol) of OsO_2F_4 was transferred into a 4-mm FEP tube. Approximately 0.18 mL of NOF was condensed onto the solid yielding a red-brown solution above undissolved OsO_2F_4.

2.9.3. Synthesis of [$N(CH_3)_4$][OsO_2F_5]

Inside the drybox, 0.0408 g (0.1368 mmol) of OsO_2F_4 and 0.0157 g (0.1685 mmol) of [$N(CH_3)_4$][F] were loaded into a 4-mm FEP tube at low temperature (ca. -150 °C). Upon condensation of approximately 0.04 mL of NOF onto the solid and melting the NOF at -78 °C, a vigorous reaction (boiling of the NOF solvent) ensued during which the purple/white heterogeneous mixture progressively changed in colour from green-brown to ochre and finally to orange. The NOF solvent was removed under dynamic vacuum at -78 °C. An NMR sample in 0.2 mL NOF was prepared using 0.0634 g (0.2126 mmol) of OsO_2F_4 and 0.0207 g (0.2222 mmol) of $[N(CH_3)_4][F]$.

Samples for NMR spectroscopy in CH_3CN [HF] solvents were prepared from 0.0373 g (0.1268 mmol) [0.02758 g (0.0925 mmol) of OsO_2F_4, 0.0127 g (0.1363 mmol) [0.00873 g (0.0937 mmol)] of $[N(CH_3)_4][F]$ and excess NOF solvent. After removal of the NOF, approximately 0.3 [0.3] mL of CH_3CN [HF] solvent was condensed onto the solid.

2.9.4. Attempted Preparation of $[N(CH_3)_4][OsO_2F_5]$ from CHF_3 Solvent

Inside the drybox, 0.0549 g (0.184 mmol) of OsO_2F_4 and 0.0176 g (0.189 mmol) of $[N(CH_3)_4][F]$ were transferred into a 4-mm FEP tube at low temperature (*ca.* -140 °C). After condensation of approximately 0.18 mL CHF_3 onto the mixture, melting the CHF_3 solvent at -105 °C resulted in dissolution of $[N(CH_3)_4][F]$ and a pale orange colouration of the solution. Raman and ^{19}F NMR spectroscopy only showed OsO_2F_4 as the solid and CHF_3, $[N(CH_3)_4][F]$ and an HF_2^- impurity in the solution.

2.9.5. Attempted Preparation of $[NO_2][OsO_2F_5]$

Approximately 1 mmol of NO_2F was condensed onto 0.0493 g (0.165 mmol) of OsO_2F_4 in a 4-mm FEP sample tube and was maintained at -78 °C for 12 h with no apparent reaction between the colourless, clear NO_2F and OsO_2F_4. After removal of the

NO_2F under dynamic vacuum at -78 °C, only OsO_2F_4 was detected by Raman spectroscopy. Approximately 0.35 mmol of NO_2F was condensed onto OsO_2F_4 and the reactor was warmed to 55 °C for approximately 1h (*ca.* 6 atm NO_2F). After removal of the NO_2F at -78 °C, no evidence for the formation of $[NO_2][OsO_2F_5]$ was found by Raman spectroscopy.

2.9.6. Synthesis of $OsO_2F_4(CH_3CN)$ in CH_3CN and SO_2ClF Solvents

Approximately 0.25 [0.2] mL of CH_3CN [SO_2ClF] was condensed onto 0.0353 g (0.118 mmol) [0.0026 g (0.0087 mmol)] of OsO_2F_4 in a 4-mm FEP tube, resulting in a deep red-brown solution at -40 °C [clear, colourless solution on top of a purple solid at -78 °C]. Subsequent distillation of excess CH_3CN (*ca.* 0.014 mL) onto the sample in SO_2ClF and mixing at -78 °C yielded a pale red solution on top of small amounts of orange precipitate.

2.10. Fluoride Ion Acceptor Properties of $IO_2F_4^-$

2.10.1. Preparation of $[N(CH_3)_4]_2[IO_2F_5]$/$[N(CH_3)_4][$*cis*$\text{-}IO_2F_4]$ in CH_3CN Solvent

Inside the drybox, $[N(CH_3)_4][IO_2F_4]$ (0.5726 g, 1.853 mmol) was added to side B of the previously vacuum dried glass reaction vessel depicted in Figure 2.10. A stoichiometric amount of $[N(CH_3)_4][F]$ (0.1753 g, 1.882 mmol) was added to side A of the reaction vessel. Anhydrous CH_3CN was condensed into side B of the reaction vessel, and then into side A at -196 °C on a glass vacuum line. The $[N(CH_3)_4][F]/CH_3CN$ mixture was transferred to side B of the reaction vessel containing $[N(CH_3)_4][IO_2F_4]$ in CH_3CN

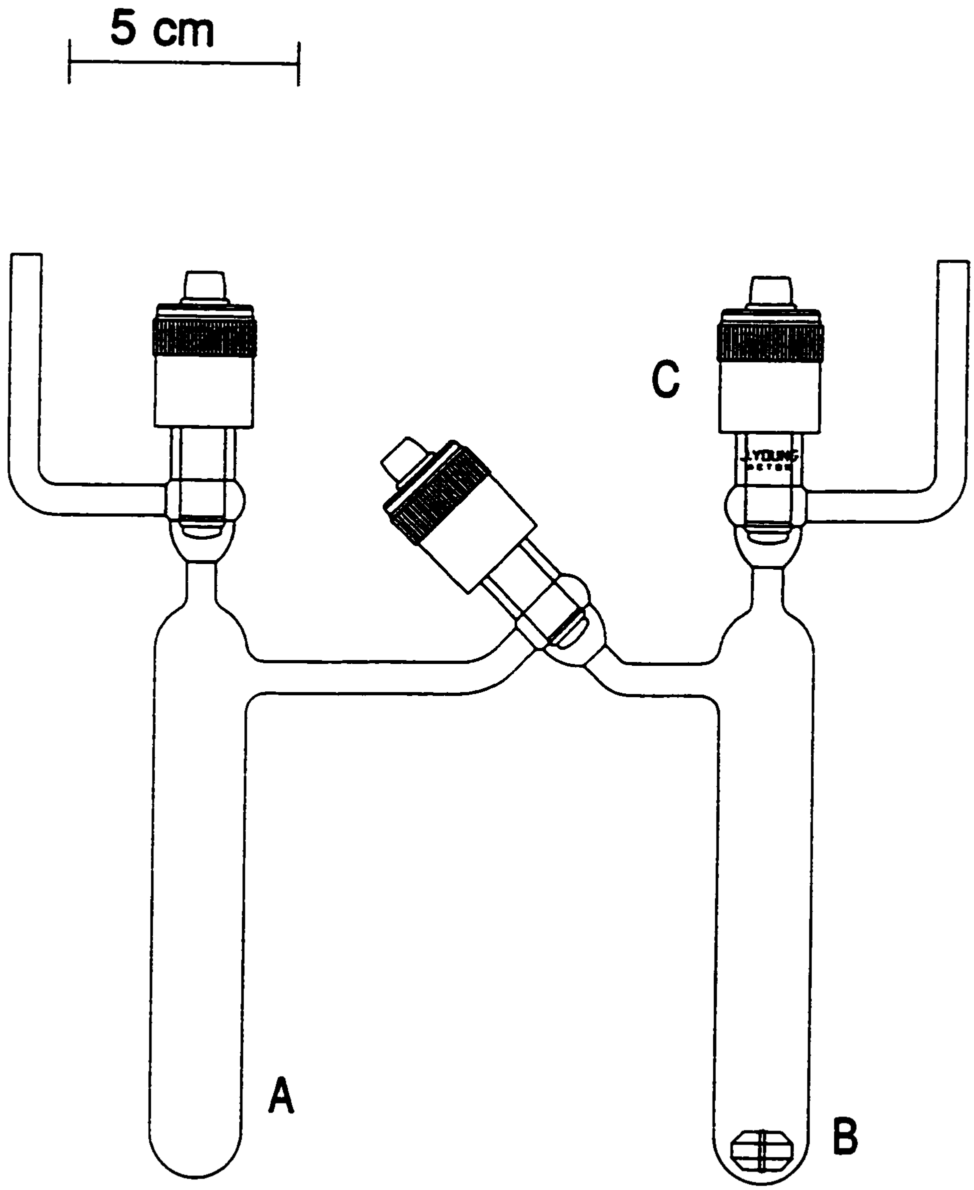

Figure 2.10 Glass reaction vessel used to prepare $[N(CH_3)_4]_2[IO_2F_5]$; (A) Pyrex glass reaction vessel (side A), (B) Pyrex glass reaction vessel (Side B) containing a Telfon coated magnetic stir bar, (C) 4-mm J. Young Telfon/glass stopcock.

while both arms were immersed in an acetone bath adjusted to -30 °C with dry ice. The reactants were stirred for 2 h at -30 °C using a magnetic stir bar. Anhydrous CH_3CN was removed under dynamic vacuum over a period of 16 h while slowly warming from -20 to 0 °C, yielding 0.7970 g of a fine, white powder.

Inside the drybox, the $[N(CH_3)_4]_2[IO_2F_5]$/$[N(CH_3)_4]$[*cis*-IO_2F_4] mixture (0.3433 g) was loaded into side A of the glass reaction vessel depicted in Figure 2.9. Anhydrous CH_3CN was distilled onto the mixture under static vacuum at -196 °C. The mixture was allowed to warm to -20 °C, was agitated, and then allowed to settle. After 2 h, the CH_3CN solvent was decanted to side B of the reaction vessel, and then distilled back to side A at -196 °C. Washing of the $[N(CH_3)_4]$[*cis*-IO_2F_4] salt was carried out two more times at 4 h intervals before the CH_3CN solvent was pumped off on the glass vacuum line for 12 h while warming from -30 to 25 °C. Distillation of CH_3CN onto the mixture was repeated, followed by eight more washings of $[N(CH_3)_4]$[*cis*-IO_2F_4] and the removal of CH_3CN under dynamic vacuum, to yield 0.1382 g (0.3436 mmol) of a fine, white powder.

2.10.2. Preparation of $[N(CH_3)_4]_2[IO_2F_5]$/$[N(CH_3)_4]$[*cis*-IO_2F_4] in CHF_3 Solvent

Inside the drybox, $[N(CH_3)_4][IO_2F_4]$ (0.0771 g, 0.2495 mmol) was loaded into side B of the thick wall glass reaction vessel depicted in Figure 2.11. A stoichiometric amount of $[N(CH_3)_4][F]$ (0.0258 g, 0.2770 mmol) was then loaded into side A of the reaction vessel. The reaction vessel was attached to the metal line and anhydrous CHF_3 was condensed into the vessel by passing the CHF_3 through a previously vacuum dried helix made of ¼-in. copper tubing and packed in solid dry ice. Once the reaction vessel was

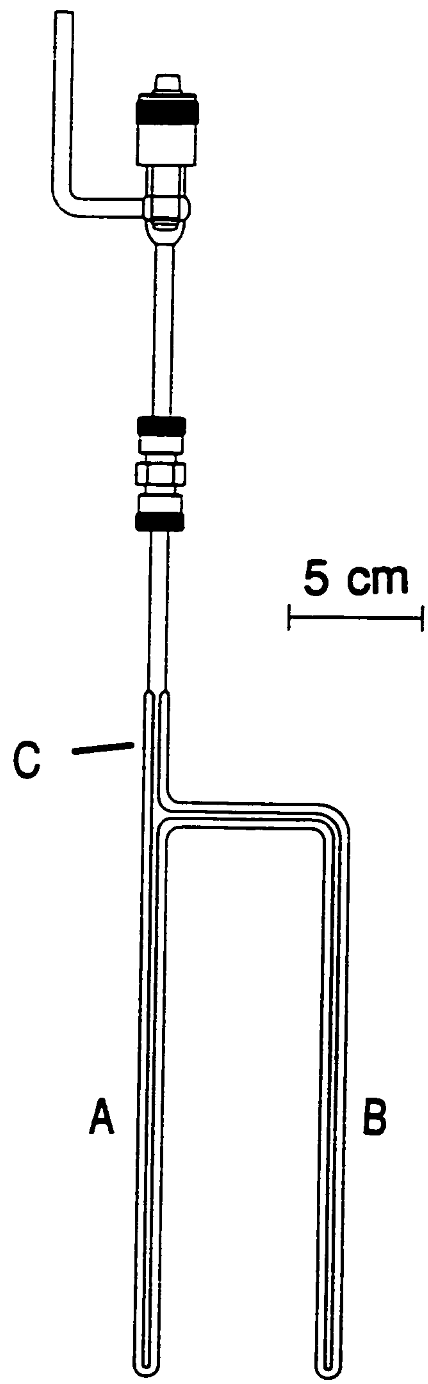

Figure 2.11 Thick wall glass reaction vessel (9 mm o.d., 2.5 mm i.d.) used for reactions in CHF_3.

flame sealed below the ¼-in. Teflon Swagelok union (point C), the vessel was placed in a Dewar containing a 95% ethanol/liquid nitrogen slush at -107 °C, the $[N(CH_3)_4][F]/CHF_3$ mixture was combined with $[N(CH_3)_4][IO_2F_4]$ inside tube B of the reaction vessel and was shaken for 30 min at 0 °C. After the mixture was allowed to stand at 0 °C for 12 h, CHF_3 was distilled back to side A of the reaction vessel at -196 °C and side B of the reaction vessel was flame sealed off. A white crystalline powder was obtained. A Raman spectrum of the sample was recorded directly on the sealed off portion of the thick wall glass reaction vessel containing the solid sample.

2.10.3. Crystal Growth of $[N(CH_3)_4]_2[IO_2F_2][HF_2]$

The white solid obtained from the extraction of a $[N(CH_3)_4]_2[IO_2F_5]/[N(CH_3)_4][cis\text{-}IO_2F_4]$ mixture using acetonitrile (see 2.10.1. Preparation of $[N(CH_3)_4]_2[IO_2F_5]/[N(CH_3)_4][cis\text{-}IO_2F_4]$ in CH_3CN) was used for crystal growth. Approximately 6 mL of CH_3CN was distilled onto the solid in arm B of the apparatus (Figure 2.9) followed by dissolution of the solid at 50 °C. Side arm B was placed inside a glass Dewar containing water at 50 °C, covered with a styroform lid, and was allowed to cool to room temperature over a period of 4 days. Some solvent condensed into side arm A and several needle shaped crystals were observed above the solvent level in arm B. Side arm A was placed inside a ice water bath for three days reducing the volume of solvent in arm B at which point, in addition to the long needle-like crystals, cubic crystals were also observed. The acetonitrile from arm A was pipetted out inside a glove bag before pumping off the residual CH_3CN inside arm B on a glass vacuum line for 1 min. The reactor was pressurized with one atmosphere of dry nitrogen and transferred to the drybox. As noted earlier, two different crystal morphologies were obtained and both were mounted inside the drybox and heat sealed inside 0.1 mm glass Lindemann capillaries. The needle-like crystal used for X-ray data collection had the dimensions: 0.8 × 0.02 × 0.08 mm^3.

2.11. Preparation of Xenon(II) Oxide Fluorides

2.11.1. Reaction of [XeF][AsF_6] and H_2O in HF Solvent

In a typical experiment, 8.0 μL of H_2O (0.44 mmol) was syringed into a ¼-in. o.d. FEP reaction tube equipped with a Kel-F valve inside a well-purged dry nitrogen-filled glove bag. Approximately 0.4 mL of HF was condensed into the tube at -196 °C and the water was mixed with the HF at room temperature. After transferring the FEP tube into a drybox at room temperature, 0.1549 g (0.4566 mmol) of [XeF][AsF_6] was added to the frozen H_2O/HF mixture followed by warming to -78 °C outside the drybox. The sample was maintained at -78 °C.

An NMR sample was prepared by loading, inside the drybox, 0.20849 g (0.6146 mmol) [XeF][AsF_6] into a 10-mm o.d. FEP tube fused to a piece of ¼-in. o.d. FEP tubing connected to a Kel-F valve. Approximately 2.35 mL of HF was condensed onto the [XeF][AsF_6] at -196 °C. The [XeF][AsF_6] dissolved upon warming the mixture to room temperature. Inside the drybox, 11.5 μL (0.60 mmol) of enriched H_2O (21.9% ^{17}O and 42.7% ^{18}O) was syringed on top of the frozen [XeF][AsF_6]/HF mixture and the vessel and reactants were transferred cold (<-100 °C) to the outside the drybox where the sample was heat sealed and stored at -196 °C until it could be studied by NMR spectroscopy.

2.11.2. Reaction of XeF_2 and $[H_3O][AsF_6]$ in BrF_5 Solvent

Inside the drybox, 0.0419 g (0.2015 mmol) $[H_3O][AsF_6]$ and 0.0372 g (0.2197 mmol) XeF_2 were loaded at low temperature (*ca.* -150 °C) into a 4-mm o.d. FEP tube connected to a Kel-F valve. Approximately 0.25 mL of BrF_5 was condensed into the tube at -196 °C and the FEP tube was heat sealed.

2.11.3. Crystal Growth of $[H_2OXeF]_2[F][AsF_6]$

Inside a glove bag well purged with dry N_2, 8.0 μL (0.44 mmol) of H_2O was syringed into a ¼-in. o.d. FEP tube with a ¼-in. o.d. FEP side arm fused to it and equipped with a Kel-F valve. Approximately 0.38 mL of HF was condensed into the tube at -196 °C and the water was mixed well with the HF at room temperature. After transferring the reaction tube into the drybox at room temperature, 0.14871 g (0.4384 mmol) of $[XeF][AsF_6]$ was added to the frozen H_2O/HF mixture followed by warming to -78 °C outside the drybox. After approximately 12 h at 78 °C, an orange solid was present. The supernatant was decanted into the cooled side arm, which was subsequently sealed off, followed by removal of the residual HF solvent in the main FEP tube at -78 °C under dynamic vacuum. Crystals were selected and mounted at -110 °C as described in Section 2.12.1. The crystal used for the X-ray structure determination had the dimensions, 0.2 × 0.18 × 0.08 mm^3.

2.11.4. Crystal Growth of Trigonal $[Xe_2F_3][AsF_6]$

Inside a well-purged glove bag, 8.0 μL (0.44 mmol) of H_2O was syringed into the vertical arm of an FEP T-shaped reactor (*vide supra*). Approximately 0.5 mL of HF was condensed onto the water at -196 °C which dissolved at room temperature. After transferring the reaction tube into a drybox at room temperature, 0.4446 g (1.311 mmol) of $[XeF][AsF_6]$ was added to the frozen H_2O/HF mixture followed by warming to -78 °C outside the drybox. After maintaining the sample for 7½ months at -78 °C, the Raman spectrum of the solid under HF solvent showed only the presence of $[Xe_2F_3][AsF_6]$ and $[XeF][AsF_6]$. The solid was dissolved at approximately -20 °C, where gas evolution was observed, and immediately cooled to -30 °C where gas evolution almost ceased and a white solid started to precipitate. Cooling the sample to -40 °C for *ca.* 1 h resulted in the growth of colorless crystals of $[Xe_2F_3][AsF_6]$. The temperature was gradually lowered to -75 °C with no significant further crystallization. The supernatant was decanted into the side arm at -78 °C, which was subsequently sealed off, followed by removal of residual HF solvent at -75 °C under dynamic vacuum. Crystals were selected and mounted at -94 °C as described in Section 2.12.1. The crystal used for the X-ray data acquisition had the dimensions 0.1 × 0.08 × 0.05 mm^3.

2.11.5. Crystal Growth of $[Xe_3OF_3][AsF_6]$

Inside a well-purged glove bag, 11.0 µL (0.61 mmol) of H_2O was syringed into a ¼-in. o.d. FEP tube with a ¼-in. o.d. FEP side arm fused to it and equipped with a Kel-F valve. Approximately 0.5 mL of HF was condensed into the tube at -196 °C and the water was mixed well with the HF at room temperature. After transferring the reaction tube into the drybox at room temperature, 0.2082 g (0.6138 mmol) of $[XeF][AsF_6]$ was added to the frozen H_2O/HF mixture followed by warming to -78 °C outside the drybox. After maintaining the sample at -78 °C for *ca.* three weeks, red dendrimeric clusters of crystals appeared above orange-brown precipitate. The red crystals were isolated after approximately 4½ months by decanting the supernatant into the cooled side arm, which was subsequently sealed, followed by removal of the residual HF solvent from the crystals under dynamic vacuum at -78 °C. Crystals were selected and mounted at -90 °C as described in Section 2.12.1. The crystal used in the X-ray data collection had the dimensions, 0.14 × 0.12 × 0.10 mm^3.

2.12. X-ray Crystallography

2.12.1. Low-Temperature Crystal Mounting

A low-temperature crystal mounting technique was utilized for thermally unstable and/or moisture sensitive crystals. Each FEP reactor containing crystals was cut open below the Kel-F valve under a flow of dry nitrogen while maintaining the crystals at -78 °C. The crystals were then quickly dumped from the chilled tube onto an aluminum trough cooled by passing a flow of dry nitrogen through a 5-L Dewar of liquid nitrogen (Figure 2.12). The temperature of the trough had been previously adjusted between -100 and -120 °C and had been measured with a copper-constantan thermocouple inserted midway into the stream *ca.* 2-mm above the trough. Each crystal was selected under a stereo-zoom microscope and mounted on a glass fibre using an inert perfluorinated polyether, Fomblin Z-15, Z-25, and Z-60 (Ausimont Inc.). The glass fibre had previously been attached using epoxy to a metallic pin that was, in turn, magnetically mounted on

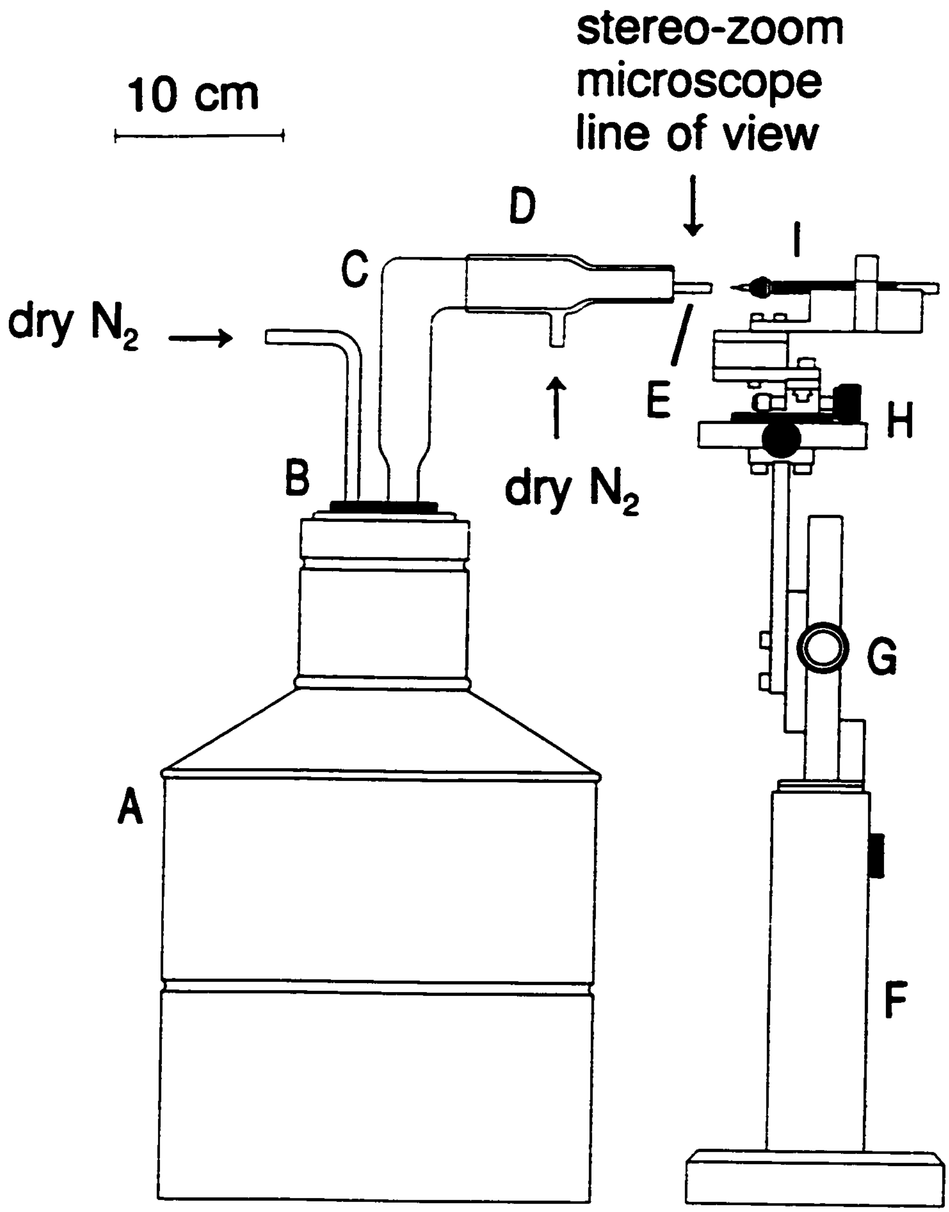

Figure 2.12 Low-temperature crystal mounting apparatus, (A) 5-L silvered glass Dewar containing liquid N_2 enclosed in a metal container, (B) two-hole rubber stopper, (C) silvered glass Dewar, (D) glass jacket, (E) aluminum trough chilled by cold N_2 flow, (F) metal stand, (G) z-adjustable dial, (H) xy-adjustable dial, (I) glas fibre attached to metallic pinon a wand.

a wand. The polyethers selected for crystal mounting were sufficiently viscous to adhere to the crystal, engulf it, and freeze quickly thereafter. The attached crystal was quickly (< 30 s) transferred to the goniometer head of the X-ray instrument using cryotongs, which had been chilled by liquid nitrogen for *ca.* 5 min prior to use, and attached by means of a magnetic interface.

2.12.2. Data Collections

The parameters used for the collection of diffraction data are summarized in Table 2.1. The diffraction data for $[N(CH_3)_4][OsO_4F]$ were collected on a Syntex $P2_1$ diffractometer with graphite-monochromatized Ag-K_α radiation (λ = 56.086 pm). Accurate cell dimensions were determined at T = -50 °C from a least-squares refinement of the setting angles (χ, ϕ, and 2θ) obtained from 29 accurately centered reflections (with 15.32° ≤ 2θ ≤ 32.25°) chosen from a variety of points in reciprocal space. Integrated diffraction intensities were collected using a θ - 2θ scan technique with scan rates varying from 1.5 to 14.65°/min. (in 2θ) and a scan range of ± 0.50° so that the weaker reflections were examined most slowly to minimize counting errors. During data collection, the intensities of three standard reflections were monitored every 97 reflections to check for crystal stability and alignment. Over the course of data collection, no decay was observed. Corrections were made for Lorentz and polarization effects. Empirical absorption corrections were applied using the Ψ-scan method ($\Delta\phi$ = 10°, 0 0 1).

The data sets for $[N(CH_3)_4][OsO_3F_3]$, $[OsO_3F][AsF_6]$, $[OsO_3F][HF]_2[AsF_6]$, $[OsO_3F][HF][SbF_6]$, $[OsO_3F][Sb_3F_{16}]$, $[N(CH_3)_4]_2[HF_2][IO_2F_2]$, $[H_2OXeF]_2[F][AsF_6]$,

Table 2.1 Summary of X-Ray Data Collection Parameters.

	$[N(CH_3)_4][OsO_4F]$	$[N(CH_3)_4][OsO_3F_3]$	$[OsO_3F][AsF_6]$	$[OsO_3F][HF]_2[AsF_6]$
diffractometer	Syntex $P2_1$	Siemens P4 with CCD	Siemens P4 with CCD	Siemens P4 with CCD
crystal-to-detector distance [cm]		3.9910	4.9870	5.0000
λ [pm]	56.086	71.073	71.073	71.073
T [K]	223	156	147	156
abs. corrections	psi scan	SADABS	SADABS	SADABS
h	-11 to 11	-20 to 19	-9 to 9	-4 to 6
k	-18 to 18	-16 to 16	-14 to 14	-6 to 10
l	-14 to 18	-14 to 14	-11 to 11	-25 to 25
θ [deg.]	2.82 to 27.58	2.30 to 26.45	2.95 to 27.58	2.08 to 27.88
no. measured refl.	3996	6005	6546	5212
no. indep. refl.	1214 (R_{int} = 0.0636)	1739 (R_{int} = 0.0958)	1535 (R_{int} = 0.0703)	1887 (R_{int} = 0.0417)

Table 2.1 continued...

	$[OsO_3F][HF][SbF_6]$	$[OsO_3F][Sb_3F_{16}]$	$[H_2OXeF]_2[F][AsF_6]$	$[Xe_2F_3][AsF_6]$
diffractometer	Siemens P4 with CCD	Siemens P4 with CCD	Siemens P4 with CCD	Siemens P4 with CCD
crystal-to-detector distance [cm]	4.9870	5.0140	5.0140	4.9870
λ [pm]	71.073	71.073	71.073	71.073
T [K]	140	160	147	157
abs. corrections	-	SADABS	SADABS	SADABS
h	-6 to 6	-11 to 11	-10 to 10	-11 to 11
k	-12 to 12	-11 to 11	-10 to 10	-11 to 11
l	-18 to 19	-8 to 8	-16 to 16	-13 to 13
θ [deg.]	2.11 to 27.51	2.69 to 23.60	3.12 to 27.50	2.73 to 24.92
no. measured refl.	7515	4041	4546	5348
no. indep. refl.	3278 (R_{int} = 0.0678)	620 (R_{int} = 0.2172)	327 (R_{int} = 0.0346)	802 (R_{int} = 0.0573)

Table 2.1 continued...

	$[Xe_3OF_3][AsF_6]$	$[N(CH_3)_4]_2[HF_2][IO_2F_2]$
diffractometer	Siemens P4 with CCD	Siemens P4 with CCD
crystal-to-detector distance [cm]	4.9840	3.9910
λ [pm]	71.073	71.073
T [K]	156	210
abs. corrections	SADABS	SADABS
h	-9 to 8	-18 to 18
k	-12 to 12	-10 to 6
l	-10 to 11	-17 to 17
θ [deg.]	3.06 to 28.67	1.69 to 26.32
no. measured refl.	3798	6405
no. indep. refl.	1215 (R_{int} = 0.0371)	1584 (R_{int} = 0.0249)

$[Xe_2F_3][AsF_6]$, and $[Xe_3OF_3][AsF_6]$ were collected with the program SMART[177] on a P4 Siemens diffractometer equipped with a Siemens SMART 1K CCD detector and a rotating anode with graphite-monochromated Mo K_α radiation (λ = 71.073 pm). The diffraction data collection consisted of a full ψ rotation at $\chi = 0°$ using (1200 + 50) 0.3° frames, followed by a series of short (100 frames) ω scans at various χ and ψ settings to fill the gaps. The data collection was carried out in a 512 × 512 pixel mode using 2 × 2 pixel binning. A complete sphere of data was collected, to better than 0.8 Å resolution. The data was reduced with the program SAINT,[177] which applied Lorentz and polarization corrections to three-dimensionally integrated diffraction spots. The program SADABS[178] was used for the scaling of diffraction data, the application of a decay correction, and an empirical absorption correction based on redundant reflections.

2.12.3. Solution and Refinement of the Structures

The final refinement results for each compound are listed in the crystal data and refinement result Tables, which can be found in subsequent Chapters. The final atomic coordinates and equivalent isotropic displacement coefficients for each structure are listed in Appendix I.

The XPREP program[179] was used to confirm the unit cells and the crystal lattices. Direct methods were used to solve the structures in the appropriate space groups which generally located the positions of the heavy atoms. Full-matrix least-squares refinements of the positions and isotropic thermal parameters of the assigned atoms and successive difference Fourier syntheses revealed the positions of the remaining atoms. The final structure solutions usually involved the refinement of anisotropic thermal parameters and the setting of the weight factor to the values recommended by the program.

The crystal of $[OsO_3F][HF][SbF_6]$ was a merohedral twin (*ca.* 40:60). Therefore, a proper absorption correction could not be performed and the fluorine and oxygen atoms were only refined isotropically. In the structure of $[OsO_3F][Sb_3F_{16}]$, the Os atom was found on a special position ($\bar{4}$ . .) resulting in a disorder between the three O and the F atoms in the cation. In addition, the fluorine atoms in the $Sb_3F_{16}^-$ anion were disordered between two orientations. As a consequence, the oxygen and fluorine atoms of the anion and cation could only be refined isotropically.

In the structure of $[H_2OXeF]_2[F][AsF_6]$, the atom at the special position (*m.mm*) was defined as a fluoride ion. On the basis of the Raman spectra, the two crystallographically related ligands around xenon were defined as a positionally disordered oxygen and a fluorine. In the trigonal $[Xe_2F_3][AsF_6]$ structure, the $Xe_2F_3^+$ cations suffer from an orientational disorder around the two Xe atoms. While it was not possible to define the two positions for the terminal fluorine atoms, it was possible to split the positions of the F_b atoms. The AsF_6^- anion exhibits a 70:30 orientational disorder and the fluorine atoms of the AsF_6^- anion were refined isotropically. In the structure of $[Xe_3OF_3][AsF_6]$, Xe(1) was located at a general position which results in a positional disorder. The electroneutrality required the presence of an oxygen bridge in the $Xe_3OF_3^+$ cation which, in conjunction with the split Xe(1) position, results in two possible disorder models (see 11.2.3.2. X-Ray Crystal Structures; $[Xe_3OF_3][AsF_6]$). The AsF_6^- anion in this structure is disordered between two orientations.

2.13. Nuclear Magnetic Resonance Spectroscopy

2.13.1. Routine Measurements

NMR spectra were recorded unlocked (field drift < 0.1 Hz h^{-1}) on a Bruker AC-300 spectrometer (7.0463 T) equipped with an Aspect 3000 computer and a Bruker DRX-500 spectrometer (11.7440 T) connected to a Silicon Graphics Indy workstation. Typical acquisition parameters are given in Table 2.2. For low-temperature work, the NMR probe was cooled using a nitrogen flow and variable temperature controller (BV-T 2000). Bruker 5-mm $^{1}H/^{13}C/^{19}F/^{31}P$ QNP and 10-mm broad band probes were used with the AC-300 console. The DRX-500 spectrometer was equipped with a Bruker 5-mm broad band inverse probe tunable from 23 to 202 MHz and a Bruker 10-mm broad band probe. The ^{1}H, ^{13}C, ^{15}N, ^{17}O, ^{19}F, and ^{129}Xe NMR spectra were referenced at room temperature to external samples of neat TMS, TMS, CH_3NO_2, H_2O, $CFCl_3$, and $XeOF_4$, respectively. The ^{131}Xe NMR spectra were referenced to xenon gas dissoved in Freon-114 (-5262 ppm) and the absolute frequency was determined (see Chapter 3). The chemical shift convention used is that a positive (negative) sign indicates a chemical shift to high (low) frequency of the reference compound.

2.13.2. Static Solid State NMR Spectroscopic Characterization of $[Na]_4[XeO_6]$

A static ^{129}Xe NMR spectrum of solid $[Na]_4[XeO_6]$ was recorded on a Bruker ASX-200 spectrometer using a solenoid probe. The ^{129}Xe NMR spectrum was referenced using xenon dissolved in Freon-114 in a glass capsule at room temperature as the secondary standard, which has previously been referenced to the primary standard, $XeOF_4$,

Table 2.2 Typical NMR Spectroscopic Acquisition Parameters for ^{1}H, ^{13}C, ^{15}N, ^{17}O, ^{19}F, ^{129}Xe, and ^{131}Xe NMR Spectroscopy

Acquisiton Parameter[a]	^{1}H	^{13}C	^{15}N	^{17}O	^{19}F	^{129}Xe	^{131}Xe
SF [MHz]	300.135	75.469		40.688	282.231	82.981	24.598
TD	16 K [16 K]	[16 K]		16 K	[64 K]	32 K	32 K
SW [kHz]	7 [3.6-10]	[18]		50	[50-100]	100	20
Hz/Pt	0.860 [0.439-1.221]	[2.180]		6.104	[1.526-3.052]	6.104	2.441
PW [μs]	2 [2]	[2]		20	[3]	14	30
NS	500 [100-750]	[3700]		400	[1000-10000]	1000-40000	2000
SF	500.133	125.761	50.687	67.784	470.385	138.302	40.998
TD	[32 K]	[16 K]	[16 K]	8 K	64 K [64 K]	32 K	32 K
SW [kHz]	[10]	[29]	[50]	30	100 [100]	100	100
Hz/Pt	[0.305]	[1.769]	[3.052]	3.67	1.526 [1.526]	3.05	3.07
PW [μs]	[2.5]	[5]	[12]	15.7	2.5 [2.5]	10	43.5
NS	[100]	[9000]	[150000]	48600	500 [350-2000]	1000 to 21000	1000

a Values are for a 10-mm [5-mm] probe.

on an Bruker AC-300 spectrometer (*vide supra*): -5263 ppm. The sample was placed inside the magnet for *ca.* 15 hours prior to acquisition and several spectra using one pulse were acquired in order to identify foldings. The spectra were acquired in a 64 K memory with a spectral setting of 125 kHz, yielding an acquisition time of 0.262 s and data point resolution of 1.907 Hz/data point. The FID was processed with a line broadening of 50 Hz.

2.13.3. T_1-Measurements

Measurements of the spin-lattice relaxation times, $T_1(^{129}Xe)$ and $T_1(^{131}Xe)$ of XeO_4 in SO_2ClF at variable temperatures were performed on the Bruker AC-300 [DRX-500] spectrometer using a 10-mm BB probe and a regular inversion-recovery experiment (pulse sequence: π-τ-$\pi/2$-acquisition). A total of 50 [15/30] and 200 [50] scans were accumulated for each ^{129}Xe and ^{131}Xe NMR spectrum, respectively, which were acquired using sweep widths of 20 kHz [^{129}Xe: 10 kHz; ^{131}Xe: 20 kHz] and TD = 16 [16] K. The FIDs were processed using a line broadening of 20 [2] Hz. A total of 10 to 14 [16] τ values were used including τ_∞ = 5 [8 and 5] s and 300 [300] ms for ^{129}Xe and ^{131}Xe, respectively. The T_1 values were obtained by iterative exponential fitting of the intensity values *versus* τ using standard Bruker software.

2.13.4. 2D-COSY

The 2-dimensional ^{19}F COSY-45 NMR spectra were recorded on a Bruker DRX-500 spectrometer using sweep widths of 60 to 80 kHz and 32 to 64 scans. The number of data points in the F1 [F2] dimension was 2 [8] K resulting in a data point resolution of 8.5636 and 9.766 Hz/data point in the F2 dimension.

2.14. Raman Spectroscopy

Raman spectra were recorded on a Jobin-Yvon Mole S-3000 spectrograph system equipped with a 0.32 m prefilter, adjustable 25 mm entrance slit, and a 1.00 m triple monochromator. Holographic gratings were used for the prefilter (600 groves mm^{-1}, blazed at 500 nm) and double monochromator (1800 groves mm^{-1}, blazed at 550 nm) stages. The 514.5 nm line of an Ar^+ ion laser and the 647.1 nm line of a Kr^+ ion laser were used for excitation of the samples. The spectra were recorded by signal averaging using a Spectraview-2D CCD detector equipped with a 25 mm chip (1152 × 298 pixels) and at a laser powers of 300 mW for Ar^+ and 100 mW for Kr^+ at the sample and slit settings corresponding to a resolution of 1 cm^{-1}. In the case of micro samples prepared in melting point capillaries, an Olympus metallurgical microscope (Model BHSM-L-2) was used to focus the excitation laser to a 1 μm spot on the sample. Low-temperature spectra of samples in sealed Pyrex melting point capillaries were recorded in a low-temperature microchamber mounted on the microscope stage. Low-temperatures were achieved by flowing dry N_2 gas, chilled by passing through a 50 L tank of liquid nitrogen, along the external walls of the sample tube or capillary. The temperature was measured using a copper-constantan thermocouple (error ± 0.8 °C). Low temperature spectra of flame sealed 5 mm o.d. thin wall Pyrex glass NMR tubes, 4-mm FEP tubes, and ¼-in. FEP tubes were recorded using the macro chamber (Figure 2.13). The Raman spectrometer

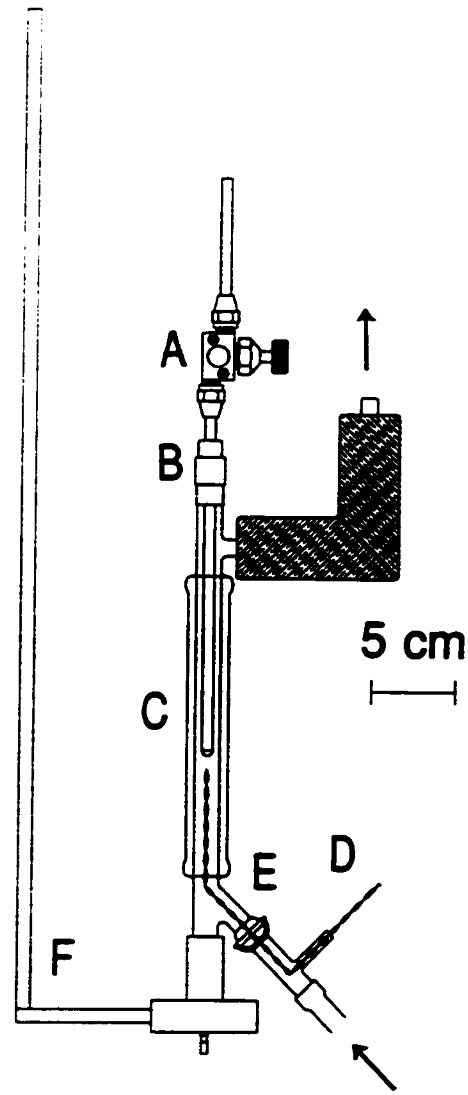

Figure 2.13 Apparatus for low temperature Raman spectroscopy using the macro chamber of the Jobin-Yvon Mole 3000 instrument; (A) Kel-F valve flare-sealed (45° SAE) onto the FEP sample tube, (B) rubber septum, (C) unsilvered glass Dewar, (D) copper-constantan thermocouple, (E) glass ball and socket joint, (F) steel mount for adjustment of the sample tube in the laser beam.

was frequency calibrated using the 730.4 cm^{-1} line of neat indene prior to running samples. Typically, 10 reads having 30 s integration times were summed for the Raman spectra.

Raman spectra were also recorded on a Bruker RFS 100 FT Raman spectrometer equipped with a quartz beam splitter, a liquid nitrogen cooled Ge diode detector and an R495 low-temperature accessory. The backscattered (180°) radiation was sampled. The scanner velocity was 5 kHz and the wavelength range for acquisition was 5894 to 10394 cm^{-1} when shifted relative to the laser line at 9394 cm^{-1}, giving a spectral range of 3501 to -999 cm^{-1}. The actual usable Stokes range was 50-3500 cm^{-1} with a spectral resolution of 1 cm^{-1}. The Fourier transformations were carried out by using a Blackman Harris 4-term apodization and a zero-filling factor of 2. The 1064-nm line of a Nd YAG laser (400 mW maximum output) was used for excitation of the sample with a laser spot of < 0.1 mm at the sample. Typically, 500 scans or 1000 scans for weak scatterers were acquired using laser powers of 200 mW.

2.14. Infrared Spectroscopy

FT-infrared spectra were recorded on a Bio-Rad FTS-40 spectrometer at ambient temperatures on AgCl discs or on powders in sealed polyethylene bags for regular and far infrared acquisition, respectively. The polyethylene bags were filled with a sample and temporarily sealed with Kel-F grease inside the drybox before they were heat sealed outside the drybox. Silver chloride (Alfa, Premion, 99.999%) pellets were made in three layers from vacuum dried AgCl using a Wilks minipress inside the drybox. The middle layer of a AgCl sample mixture was hermetically sealed by the two outer AgCl layers. The spectra consisted of 64 scans acquired with a resolution of ±2 cm^{-1} and a 5 kHz scan speed and the background which was recorded prior to spectral acquisition was subsequently substracted from the spectrum. An 6 micron mylar beam splitter was used for the far infrared spectrum.

CHAPTER 3

SOLUTION STUDY OF XeO_4 AND NMR SPECTROSCOPIC CHARACTERIZATION OF $[Na]_4[XeO_6]$

3.1. Introduction

Xenon forms two binary oxides, namely solid XeO_3 and gaseous XeO_4, which are both endothermic compounds decomposing explosively into their elements releasing 402[180] and 642 kJ mol^{-1},[46] respectively. Despite their hazardous natures, structural data have been obtained by an X-ray diffraction study of $XeO_{3(s)}$[181] and an electron diffraction study of $XeO_{4(g)}$.[47] Two xenon oxide anions, the $HXeO_4^-$ and XeO_6^{4-} anions, have been isolated as the Na^+,[23,182] K^+,[182] Cs^+,[182,183] and Rb^+ [182] salts and as the Li^+,[40] Na^+,[22,23,26,29,30,31,33,36,39,41] K^+,[32,36,40] Cs^+,[23,34,40] Rb^+,[40] Ba^{2+},[24,36] La^{3+},[24,40] Am^{3+},[25] Cu^{2+},[40] Ag^{2+},[40] Zn^{2+},[40] Pb^{4+},[40] Th^{4+},[40] and UO_2^{2+} [40] salts, respectively. While salts of the XeO_6^{4-} anion were found to be remarkably stable, $[Na][HXeO_4]$ is less stable than $[Na]_4[XeO_6]$, but more stable than XeO_3.[182] Unlike its frequent use for the structural characterization of xenon fluoride and oxide fluoride species,[148] NMR spectroscopy had not played an important role in the characterization of the $HXeO_4^-$ and XeO_6^{4-} anions, because of the absence of spin-spin coupling information in natural abundance samples and their instability in aqueous media.

Xenon possesses two spin-active isotopes, ^{129}Xe ($I = {}^1/_2$, 26.4 % natural abandance) and ^{131}Xe ($I = {}^{3}/_{2}$, 21.1 % natural abandance). Xenon-129 is widely used for the characterization of xenon compounds and porous materials such as zeolites loaded with xenon gas.[184,185] Far less work has been done on ^{131}Xe NMR spectroscopy. Although the natural abundance of ^{131}Xe is similar to that of ^{129}Xe, the quadrupolar nature of ^{131}Xe causes fast spin-lattice relaxation in asymmetric environments resulting in no reported ^{131}Xe chemical shift of chemically bonded xenon. Prior to this study, only ^{131}Xe NMR spectra of elemental xenon have been reported in the literature.[184,186] Xenon-131 chemical shifts and spin-lattice relaxation times have been determined for liquid and solid xenon and the solvent dependence of ^{131}Xe chemical shift and T_1-values have been investigated for xenon in various solvents.

3.2. Results and Discussion

3.2.1. Characterization of XeO_4 in SO_2ClF, BrF_5, and HF Solvent by ^{129}Xe NMR Spectroscopy

Solutions of XeO_4, which is highly explosive in the solid and gaseous states, have been prepared for the first time making non-hazardous handling of XeO_4 possible at low temperatures. The preparation of SO_2ClF, BrF_5, and HF solutions of XeO_4 have provided the solution NMR spectroscopic characterization of XeO_4 for the first time. The ^{129}Xe chemical shifts of XeO_4 in SO_2ClF (-80 °C), BrF_5 (-50 °C), and HF (-75 °C) solutions are -92.9, -94.7 and -85.5 ppm, respectively (Figure 3.1 and Table 3.1).

Compared to other xenon species, *e.g.*, XeF_2 ($\delta(^{129}Xe)$ = -1905 ppm in SO_2ClF, 25 °C; -1592 ppm in HF, 25 °C), these changes in chemical shift are very small, indicating

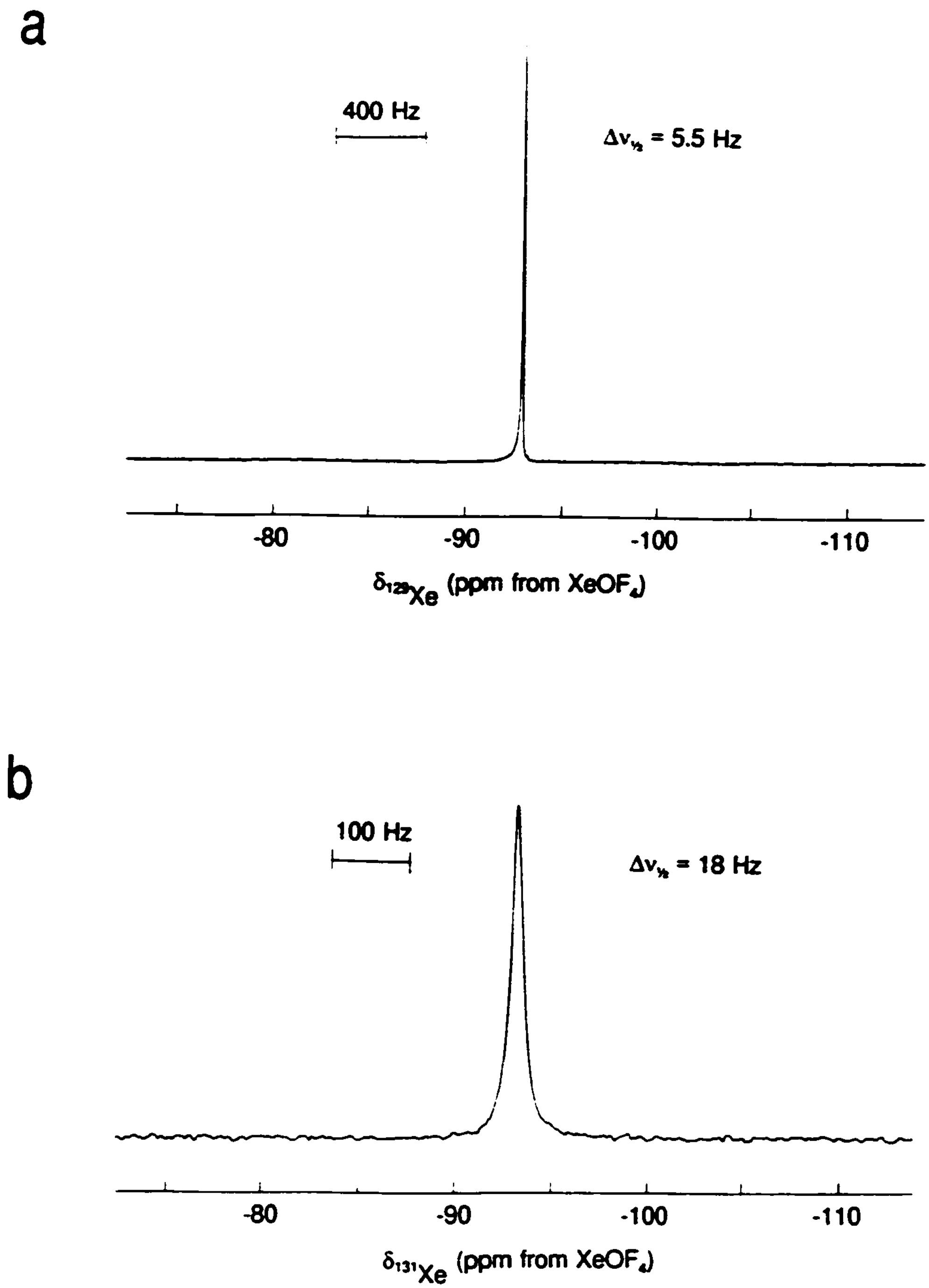

Figure 3.1 (a) ^{129}Xe NMR spectrum (82.981 MHz) at -78.5 °C and (b) ^{131}Xe NMR spectrum (24.598 MHz) of XeO_4 in SO_2ClF at -76 °C.

Table 3.1 ^{129}Xe and ^{131}Xe NMR Parameters of XeO_4

$\delta(^{129}Xe)$ [ppm]	$\Xi(^{131}Xe)$ [Hz]	$\delta(^{131}Xe)$ [ppm][a]	Solvent	T [°C]
-92.9	8 243 147	-93.2	SO_2ClF	-78.5
-85.8	8 243 133	-86.2	HF	-75
-94.7	8 243 205	-94.9	BrF_5	-50

[a] Calculated using eqs. (3.6) and (3.7), with respect to the hypothetical ^{131}Xe signal of $XeOF_4$ (see text for details).

Table 3.2 Temperature Dependence of the ^{129}Xe Chemical Shift and ^{131}Xe Absolute Frequency of XeO_4 in SO_2ClF

T, °C	$\delta(^{129}Xe)$ [ppm]	$\Xi(^{131}Xe)$ [Hz]
-42	-90.0	8 243 172
-50	-90.8	8 243 163
-60	-91.6	8 243 158
-70	-92.5	8 243 150
-78.5	-92.9	8 243 148

that the tetrahedral molecule interacts only weakly with its solvent environment (see 3.2.3. Characterization of XeO_4 in SO_2ClF, BrF_5, and HF Solvent by ^{131}Xe NMR Spectroscopy). The small differences are likely attributable to differences in the bulk susceptibility of the solvents which can also vary with temperature. The temperature dependence of the ^{129}Xe chemical shift of XeO_4 was studied in SO_2ClF solvent up to 0 °C where decomposition becomes rapid. The chemical shifts and the corresponding temperatures are listed in Table 3.2 and are found to increase slightly with increasing temperature.

Only XeO_4 was observed by ^{129}Xe NMR spectroscopy in HF and BrF_5 solutions, indicating that no fluorination or fluorine-oxygen exchange between XeO_4 and HF and BrF_5 had occurred, and is in agreement with the Raman spectroscopic characterization of XeO_4 in HF solvent (see 3.2.5. Raman Spectroscopic Characterization of XeO_4 in HF Solution), but contrasts with the solvolytic behaviour of the isoelectronic IO_4^- anion (eqs. (3.1) and (3.2)).

$$IO_4^- + 4\ HF \longrightarrow IO_2F_4^- + 2\ H_3O^+ + 2\ HF_2^- \qquad (3.1)$$

$$IO_4^- + 2\ BrF_5 \longrightarrow IO_2F_4^- + 2\ BrOF_3 \qquad (3.2)$$

The dynamic chemical shift ranges reported for ^{129}Xe in different oxidation states are very large:[148]

$\delta(^{129}Xe(0))$ = -5460 to -5331 ppm

$\delta(^{129}Xe(II))$ = -3967.5 to -574 ppm

$\delta(^{129}Xe(IV))$ = -662.8 to 595 ppm

$\delta(^{129}Xe(VI))$ = -357.9 to 704.3 ppm

The ^{129}Xe environments of Xe(VIII) compounds are expected to be less shielding than those of Xe(VI) compounds. It is therefore suprising that ^{129}Xe in XeO_4 is significantly more shielded (-92.9 ppm for XeO_4 in SO_2ClF at -80 °C) than in XeO_3 (217 ppm for XeO_3 in H_2O at room temperature).[148,187] The low-frequency chemical shift of XeO_4 can be explained with Jameson and Gutowsky's formulation for the paramagnetic shielding term (eq. (3.3)),[188] which normally dominates the chemical shifts of heavy nuclei,

$$\sigma^{p} = -\left(\frac{2e^{2}\hbar^{2}}{3\Delta m^{2}c^{2}}\right)\left(\left\langle\frac{1}{r^{3}}\right\rangle_{p} P_{u} + \left\langle\frac{1}{r^{3}}\right\rangle_{d} D_{u}\right) \tag{3.3}$$

where Δ is the average excitation energy, $\langle 1/r^3\rangle_p$ and $\langle 1/r^3\rangle_d$ are the expectation values for $1/r^3$ with r as the radius of the valence p and d orbitals, P_u and D_u represent the "imbalance" of the valence electrons in the p and d orbitals centred on the atom in question. Calculations on a small number of xenon species have shown that a localized description of the bonding employing d hybridization provides a more satisfactory description than a delocalized description without d hybridization. Moreover, the approach showed that ΔE, $\langle r^{-3}\rangle_{5p}$ and $\langle r^{-3}\rangle_{5d}$ can be regarded as essentially constant over the entire range of $\delta(^{129}Xe)$ so that P_u and D_u determine variations in $\delta(^{129}Xe)$. For spherically symmetric closed shell atoms, P_u and D_u have their minimum value of zero. In the tetrahedral XeO_4 molecule P_u and D_u are close to zero, resulting in a small paramagnetic contribution to the chemical shift, *i.e.*, higher shielding of the xenon nucleus.

3.2.2. Characterization of XeO_4 in SO_2ClF Solvent by ^{17}O NMR Spectroscopy

The ^{17}O NMR spectrum of natural abundance XeO_4 in SO_2ClF was recorded at -78 °C. Besides the solvent signal at δ = 226 ppm ($\Delta\nu_{½}$ = 80 Hz), a weak signal at 509 ppm ($\Delta\nu_{½}$ = 46 Hz) was observed. The ^{17}O chemical shift of XeO_4 follows the previously noted trend for tetrahedral MO_4^{n-} molecules in which ^{17}O becomes more deshielded as the atomic number of M increases within a period. The $^{1}J(^{129}Xe-^{17}O)$ coupling was not observed because of the low intensity and broadness of the signal. The broadness of the ^{17}O resonance is partially a consequence of the quadrupolar nature of the ^{17}O nucleus (I = $^5/_2$, natural abundance = 0.037%). The low temperature and the relatively high viscosity of SO_2ClF at that temperature decrease the rotational correlation time, τ_c, and therefore, the quadrupolar relaxation rate and the line width (see eqs. (3.9), (3.10) and 3.2.4. T_1 Relaxation of the ^{129}Xe and ^{131}Xe Nuclei in XeO_4).

The ^{17}O chemical shift for XeO_4 complements the table of chemical shift values for the known tetrahedral MO_4^{n-} species with M in the highest possible oxidation state (Table 3.3).[189] With an ^{17}O chemical shift of 509 ppm, the oxygens in XeO_4 are far more deshielded than in IO_4^- (243 ppm). Since the hypothetical anions SbO_4^{3-} and TeO_4^{2-} have not been prepared yet, the comparison cannot be extended to the next nearest neighbours in the periodic table. Compared to the ^{17}O chemical shift of XeO_3 in H_2O (278 ppm),[190] the XeO_4 resonance is, as expected, far more deshielded. Similar pronounced differences among the ^{17}O chemical shifts of the MO_4^{n-} species could not be found among the MO_3^{n-} series and the ^{17}O resonances of ClO_3^-, BrO_3^- and XeO_3 lie close together (287, 297, 278 ppm).[190,191] The high-frequency ^{17}O chemical shift is evidence for the extremely high

Table 3.3 ^{17}O Chemical Shifts [ppm] of Main Group and Transition Metal Element Tetraoxo Species[189]

Group							
5	6	7	8	15	16	17	18
				PO_4^{3-}	SO_4^{2-}	ClO_4^-	
				99	167	292	
VO_4^{3-}	CrO_4^{2-}	MnO_4^-	-	AsO_4^{3-}	SeO_4^{2-}	BrO_4^-	
568	835	1230		108	204	360	
-	MoO_4^{2-}	TcO_4^-	RuO_4	-	-	IO_4^-	XeO_4[a]
	831	748	1106			243	509
-	WO_4^{2-}	ReO_4^-	OsO_4				
	420	569	796				

[a] Present work.

electron withdrawing power of Xe(VIII).

3.2.3. Characterization of XeO_4 in SO_2ClF, BrF_5, and HF Solvent by ^{131}Xe NMR Spectroscopy

Besides the ^{129}Xe nucleus (I = ½), which is frequently used in NMR spectroscopic characterization of xenon containing compounds, ^{131}Xe is the only other naturally occurring xenon isotope (21.4% natural abundance) which is NMR active. It is, however, quadrupolar with I = $^3/_2$, providing the very efficient quadrupolar relaxation pathway (see 3.2.4. T_1 Relaxation of the ^{129}Xe and ^{131}Xe Nuclei in XeO_4). Interaction of the quadrupole moment with an electric field gradient (efg) often broadens the NMR resonances to the extent that they are indistinguishable from the spectral baseline. The line width factor, WF (eq. (3.4)) which is characteristic for a specific quadrupolar nucleus, gives an indication

$$WF = Q^2 \left[\frac{2I + 3}{I^2\,(2I - 1)}\right] \qquad (3.4)$$

of the size of the interaction between the nuclear quadupole moment and the efg. Until recently, WF of ^{131}Xe (19 x 10^{-59} m^4)[192] only permitted the observation of ^{131}Xe NMR signals from monoatomic xenon gas.[184,186] The high symmetry of XeO_4 (T_d symmetry) has made possible the observation of the first ^{131}Xe NMR chemical shift of chemically bound xenon (Figure 3.1). Since the standard for ^{129}Xe NMR spectroscopy, neat $XeOF_4$, does not give rise to an observable ^{131}Xe NMR signal, the ^{131}Xe NMR signal of XeO_4 was referenced to the ^1H NMR signal of TMS at exactly 100 MHz by determination of its absolute frequency Ξ (eq. (3.5)). For practical use, ^{131}Xe chemical shift with respect to

$$\Xi(^{131}Xe) = \frac{\nu(^{131}Xe,\ XeO_4)}{\nu(^{1}H,\ TMS)} \cdot 100\ MHz \qquad (3.5)$$

xenon gas dissolved in Freon 114, δ', can be calculated according to eq. (3.6). The absolute frequency for xenon gas dissolved in Freon 114 at 30 °C was determined to be

$$\delta' = \frac{[\Xi(^{131}Xe,\ XeO_4) - \Xi(^{131}Xe,\ Xe\ gas,\ solvent\ Freon\ 114)]}{\Xi(^{131}Xe,\ XeO_4)} \times 10^6 \qquad (3.6)$$

8 200 540 Hz. Since the value for the ^{131}Xe frequency of $XeOF_4$ is not available, the frequency of the ^{131}Xe resonance of XeO_4 is used in the denominator of eq. (3.6), instead. This introduces a small systematic error with the $\delta(^{131}Xe)$ values being too low by approximately 0.5 ppm. Ignoring any significant primary isotope effects the chemical shift with respect to the hypothetical ^{131}Xe NMR signal for $XeOF_4$ can be calculated using eq. (3.7). The absolute frequencies and calculated chemical shift $\delta(^{131}Xe)$ of XeO_4 in SO_2ClF,

$$\delta(^{131}Xe) = \delta'(^{131}Xe) - 5262\ ppm \qquad (3.7)$$

HF, and BrF_5 solvent are listed in Table 3.1. The observation of a ^{131}Xe NMR signal in SO_2ClF, BrF_5 and HF solvents unambiguously proves the assignment of the ^{129}Xe chemical shift to tetrahedral XeO_4. It also shows that no static or dynamic interaction between the solvent molecules and XeO_4 occurs since any distortion of XeO_4 from its ideal T_d symmetry would cause the ^{131}Xe nucleus to relax by means of quadrupolar relaxation and broaden the signal significantly and also serves to support the inertness of XeO_4 towards HF and BrF_5 established by ^{129}Xe NMR spectroscopy. The calculated ^{131}Xe chemical shifts are in excellent agreement with the $\delta(^{129}Xe)$ values.

The linewidth of the ^{131}Xe resonance with $\Delta\nu_{½}$ = 18 Hz (SO_2ClF solvent at -79 °C) is surprisingly narrow. Nuclei with comparable width factors like ^{71}Ga and ^{209}Bi with WF = 16 x 10^{-59} m^4 and 10 x 10^{-59} m^4,[192] respectively, exhibit larger line widths in highly symmetric environments at room temperature. For GaX_4^-, X = Cl, Br, I, line widths of 100 Hz have been observed[193] and the line width of the ^{209}Bi signal of BiF_6^- at room temperature was found to be 44 Hz.[194] Unlike XeO_4, the anionic nature of these tetrahedral and octahedral species result in ion pairing in solution possibly causing distortion of the symmetry and an increase in the effective volume (see eq. 3.10 in 3.2.4. T_1 Relaxation of the ^{129}Xe and ^{131}Xe Nuclei in XeO_4) and, as a consequence, in broader NMR signals. The line width of 18 Hz for XeO_4 indicates the absence of any significant distortion from T_d symmetry as a consequence of the pronounced rigidity of the tetrahedral molecule with four large Xe=O double bond domains.

3.2.4. T_1 Relaxation of the ^{129}Xe and ^{131}Xe Nuclei in XeO_4

Spin-lattice relaxation rates for the ^{129}Xe and ^{131}Xe nuclei in XeO_4 dissolved in SO_2ClF were studied at variable temperatures and two different magnetic field strengths using a standard inversion recovery experiment. The T_1-values and their corresponding temperatures are given in Table 3.4. The spin-lattice relaxation times of ^{129}Xe and ^{131}Xe

Table 3.4 T_1-Values for XeO_4 in SO_2ClF Solution at Different Temperatures at 7.0463 (11.744) T

T [°C]	T_1(^{129}Xe) [ms]	T_1(^{131}Xe) [ms]
-42	423	46.1
-50	444	40.3
-61	554	36.2
-70	701 (743)	29.6 (29.4)
-76	801	26.7
-79	(834)	(24.9)

range from 423 to 834 ms and from 24.9 to 46.1 ms, respectively.

Several relaxation mechanisms can contribute to the observed total spin-lattice relaxation time T_1, the nuclear dipole-dipole interaction (T_1^{DD}), the chemical shift anisotropy mechanism (T_1^{CSA}), the nuclear quadrupole interaction (T_1^{Q}), scalar coupling (T_1^{SC}), spin rotation mechanism (T_1^{SR}) and the interaction with paramagnetic species, *i.e.*, unpaired electrons (T_1^{E}). The overall relaxation time is given by eq. (3.8). For quadrupolar

$$\frac{1}{T_1^{TOT}} = \frac{1}{T_1^{DD}} + \frac{1}{T_1^{CSA}} + \frac{1}{T_1^{Q}} + \frac{1}{T_1^{SC}} + \frac{1}{T_1^{SR}} + \frac{1}{T_1^{E}} \tag{3.8}$$

nuclei the very strong quadrupolar interaction normally dominates the spin lattice relaxation time. The rate of quadrupolar relaxation is given by eq. (3.9) where I is the

$$\frac{1}{T_1^{Q}} = \frac{3}{40}\left[\frac{(2I+3)}{I^2(2I-1)}\right]\left[1+\frac{\eta^2}{3}\right]\left[\frac{e^2Qq}{\hbar}\right]^2 \tau_c \tag{3.9}$$

nuclear spin quantum number, η the asymmetry parameter, Q the quadrupole moment, q the electric field gradient, e the electronic charge, and τ_c the rotational correlation time. The rotational correlation time is the average time for a molecule to rotate by one radian and is a function of temperature T, effective volume of the molecule V and the viscosity of the solvent η as described by the Stokes-Einstein equation (3.10). In the extreme

$$\tau_c = \frac{V \eta}{k T} \tag{3.10}$$

narrowing condition the tumbling of the molecule increases with increasing temperature and less effectively induces relaxation. Therefore, T_1^Q increases with increasing temperature as can be seen from equations (3.9) and (3.10) and was found for ^{131}Xe in XeO_4. For some low Q nuclei, like ^9Be (I = 3/2, Q = 52.88(38) x 10^{-31} m^2)[195] in $Be(H_2O)_4^{2+}$, it was found that the spin rotation mechanism becomes the important relaxation pathway at higher temperatures, *i.e.*, > 50 °C.[196] This results in a maximum in a plot of T_1 *vs.* T since T_1^{SR} follows an inverse T dependence (*vide infra*). This could not be observed for ^{131}Xe in XeO_4 because the magnitude of its quadrupole moment (Q = -120(12) x 10^{-31} m^2)[195] is much larger than that of ^9Be and it is not possible to increase the temperature sufficiently because of the kinetic and thermodynamic instability of XeO_4.

The inverse temperature dependence of $T_1(^{129}Xe)$ in XeO_4 indicates that the spin rotation relaxation is the dominant relaxation pathway. The spin-rotation mechanism is the only spin-lattice relaxation mechanism which exhibits a decrease in T_1 with increasing temperature. Spin-rotation relaxation is induced by the interaction of the nuclear spin with the fluctuating local magnetic field generated by the angular change of rotation of the molecules and its bonding electrons and is given by eq. (3.11) where C is the spin

$$\frac{1}{T_1^{SR}} = \frac{2kT}{3\hbar^2} I_m C^2 \tau_{SR} \tag{3.11}$$

rotation coupling constant, I_m is the moment of inertia, and τ_{SR} is the angular momentum correlation time. The average time a molecule spends in any given angular momentum state τ_{SR} is given by eq. (3.12) As expected for the highly symmetric XeO_4 molecule, the

$$\tau_{SR} \cdot \tau_C = \frac{I_m}{6kT}, \quad for\ \tau_{SR} < \tau_C \tag{3.12}$$

CSA relaxation mechanism was not found to play a role in the total spin lattice relaxation time, since no significant differences in T_1 values were found for ^{129}Xe- and ^{131}Xe-T_1 measured at two different field strengths (T = 7.0464 T and 11.744 T) (Table 3.4). Seppelt *et al.*[187,197] reported ^{129}Xe T_1 values for several xenon compounds assuming a dominant dipole-dipole mechanism. A thorough study of spin-lattice relaxation rates of ^{129}Xe in XeF_2 was performed by Jokisaari *et al.*[198] They estimated the dipole-dipole mechanism to be negligible. The T_1 *vs.* temperature plot showed a maximum indicating that the CSA mechanism was dominant at low temperatures and that the spin-rotation mechanism was dominant at high temperatures. No maximum in the T_1 *vs.* temperature plot could be found for ^{129}Xe in XeO_4. The nuclear dipole-dipole relaxation mechanism is not expected to make a significant contribution to T_1^{TOT} because only spin-dilute nuclei are present in XeO_4.

3.2.5. Raman Spectroscopic Characterization of XeO_4 in HF Solution

The Raman spectrum of XeO_4 in HF solvent was recorded at -74 °C (Figure 3.2) and the observed frequencies are listed in Table 3.5 and are compared with those of gaseous[45,48] and solid XeO_4.[48] The solution spectrum resembles that of XeO_4 in the gas

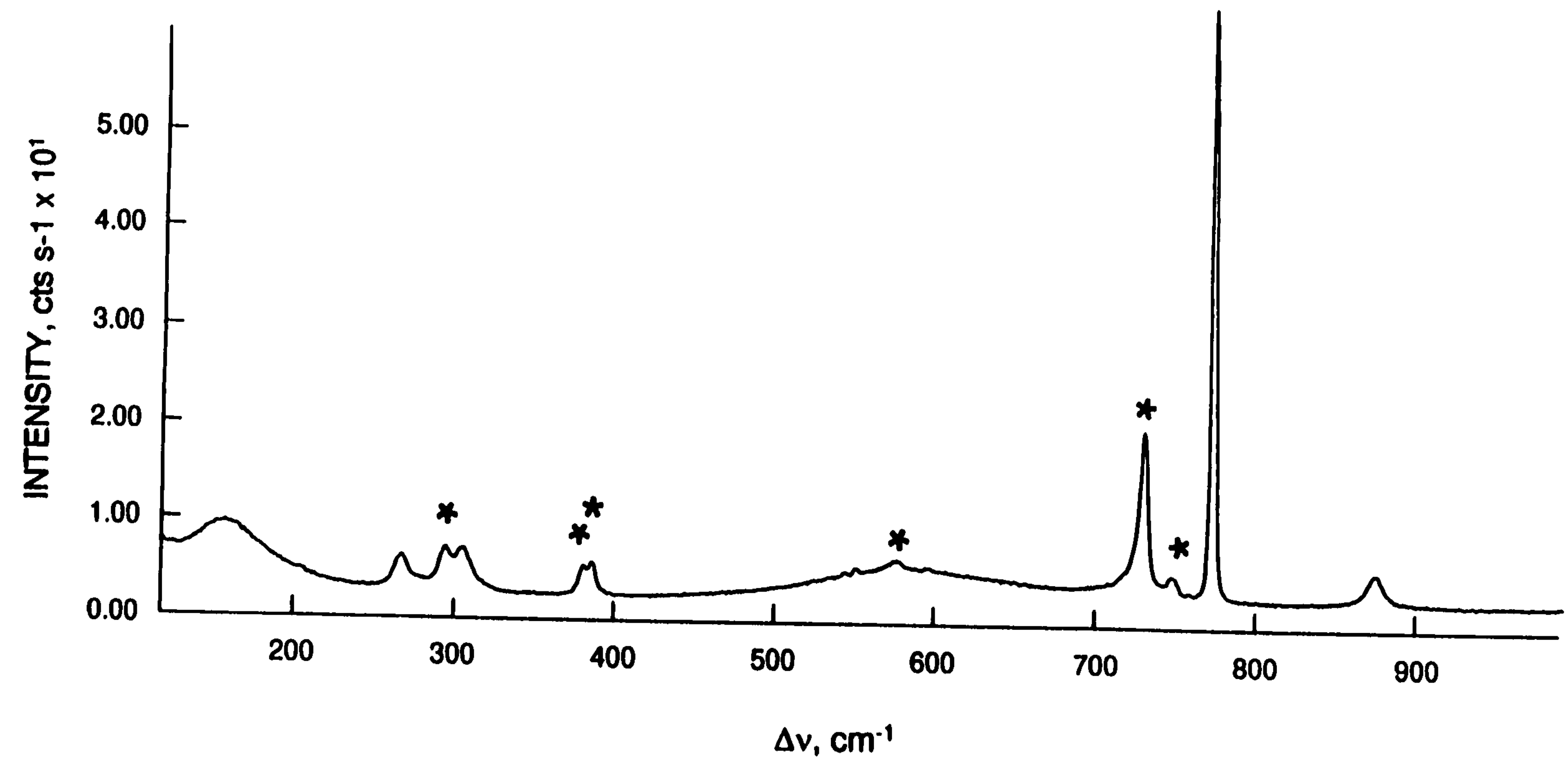

Figure 3.2 Raman spectrum of an HF solution of XeO_4 recorded in FEP at -74 °C using 514.5-nm excitation. Asterisks (*) denote FEP sample tube lines.

Table 3.5 Vibrational Frequencies and Their Assignments for Solid and Gaseous XeO_4 and for a Solution of XeO_4 in HF

Frequencies[a] [cm^{-1}]			Assignment
$XeO_{4(s)}$[48]	$XeO_{4(g)}$[45,48]	XeO_4 in HF solvent[b]	XeO_4 (T_d)
-195 °C	r.t.	-74 °C	
875.9 867.0 860.5	877[c]	878 (5.5)	$\nu_3(T_2)$
767.1	773	776 (100)	$\nu_1(A_1)$
		580 v.br.	unassigned
311.5 301.8 295.7	305.7[c]	305 (7.5)	$\nu_4(T_2)$
280.0 273.6	n. obs.	267 (5.5)	$\nu_2(E)$
		156 (7)	unassigned

[a] Values in parentheses denote relative Raman intensities; abbreviations denote: not observed (n.obs.); room temperature (r.t.), very broad (v.br.). Frequencies were obtained by Raman spectroscopy if not indicated otherwise.

[b] Bands arising from the FEP sample tube were observed at 294 (8), 381 (5), 386 (6), 578 (1), 733 (27), and 750 (3).

[c] Bands were observed in the infrared spectrum of XeO_4 vapour.[45]

phase (differences ≤ 3 cm^{-1}), indicating that the structure of XeO_4 in HF solvent is that of the undistorted tetrahedral molecule found in the gas phase and is in accord with the ^{131}Xe NMR spectroscopic findings (see 3.2.3. Characterization of XeO_4 in SO_2ClF, BrF_5, and HF Solvent by ^{131}Xe NMR Spectroscopy).

3.3.6. Characterization of $[Na]_4[XeO_6]$ by ^{129}Xe NMR Spectroscopy

The previously reported ^{129}Xe chemical shift of XeO_6^{4-} (2077 ppm)[35] has been frequently quoted as the upper limit of the dynamic range of the ^{129}Xe nucleus.[184,199] In light of the high shielding observed for ^{129}Xe in XeO_4, an extreme high-frequency shift of the XeO_6^{4-} anion seemed unlikely. Therefore, $[Na]_4[XeO_6]$ was reinvestigated by ^{129}Xe NMR spectroscopy.

A sample of solid $[Na]_4[XeO_6]$ placed inside the magnet for less than one hour, did not give rise to any observable ^{129}Xe NMR signal after one scan. However, after allowing the sample to equilibrate inside the magnet for *ca.* 12 h, *i.e.*, after the spins had alligned in the magnetic field, a very broad resonance was observed at *ca.* -720 ppm ($\Delta\nu_{½}$ = 5000 Hz) with one scan (Figure 3.3). The long time required for equilibration (spin allignment) corresponds to a very long spin-lattice (T_1) relaxation time which is consistent with solid $[Na]_4[XeO_6]$ being a spin-dilute system without a facile T_1 relaxation pathway. The ^{129}Xe nucleus in $[Na]_4[XeO_6]$ is far more shielded than in XeO_4, which is consistent with the large negative charge. The chemical shift of -720 ppm falls into the range found for Xe(II) compounds, such as XeF^+ in SbF_5 solvent (25 °C) at -574 ppm,[35] and is lower than any ^{129}Xe chemical shifts reported for Xe(IV) and Xe(VI) species (*vide supra*).[148] The broadness of the NMR line presumably is a consequence of anion distortion from ideal O_h symmetry in the solid state. The assumption of a significant distortion is supported by the failure to observe a ^{131}Xe NMR signal.

A saturated aqueous solution of $[Na]_4[XeO_6]$ (pH ~ 14) gave rise to a broad ^{129}Xe NMR signal at -748 ppm ($\Delta\nu_{1/2}$ = 450 Hz) at 30 °C (Figure 3.3) which is in good agreement with the value obtained from the static solid state spectrum. It has been shown by UV spectrophotometry that $[Na]_4[XeO_6]$ dissolves in water (0.003 M) according to eq. (3.13) with $HXeO_6^{3-}$ as the major xenon species in solution at pH > 12. At pH 6 to 8,

$$[Na]_4[XeO_6] + H_2O \rightleftharpoons 4Na^+ + HXeO_6^{3-} + OH^- \qquad (3.13)$$

$$HXeO_6^{3-} + H_2O \rightleftharpoons H_2XeO_6^{2-} + OH^- \qquad (3.14)$$

$H_2XeO_6^{2-}$ was found to be the predominant species in solution (eq. (3.14)).*36,37* In acidic solutions, $[Na]_4[XeO_6]$ decomposes almost instantaneously upon formation of $H_3XeO_6^-$ (eqs. (3.15) and (3.16)). Even at pH 11.5, an aqueous solution of $[Na]_4[XeO_6]$ (0.003 M)

$$H_2XeO_6^{2-} + H_2O \rightleftharpoons H_3XeO_6^- + OH^- \qquad (3.15)$$

$$H_3XeO_6^- \rightarrow HXeO_4^- + \tfrac{1}{2}O_2 + H_2O \qquad (3.16)$$

was found to decompose at a rate of about 1% per hour. The ^{129}Xe chemical shift of -748 ppm has to be attributed to the $HXeO_6^{3-}$ anion. The broadness of the ^{129}Xe NMR signal

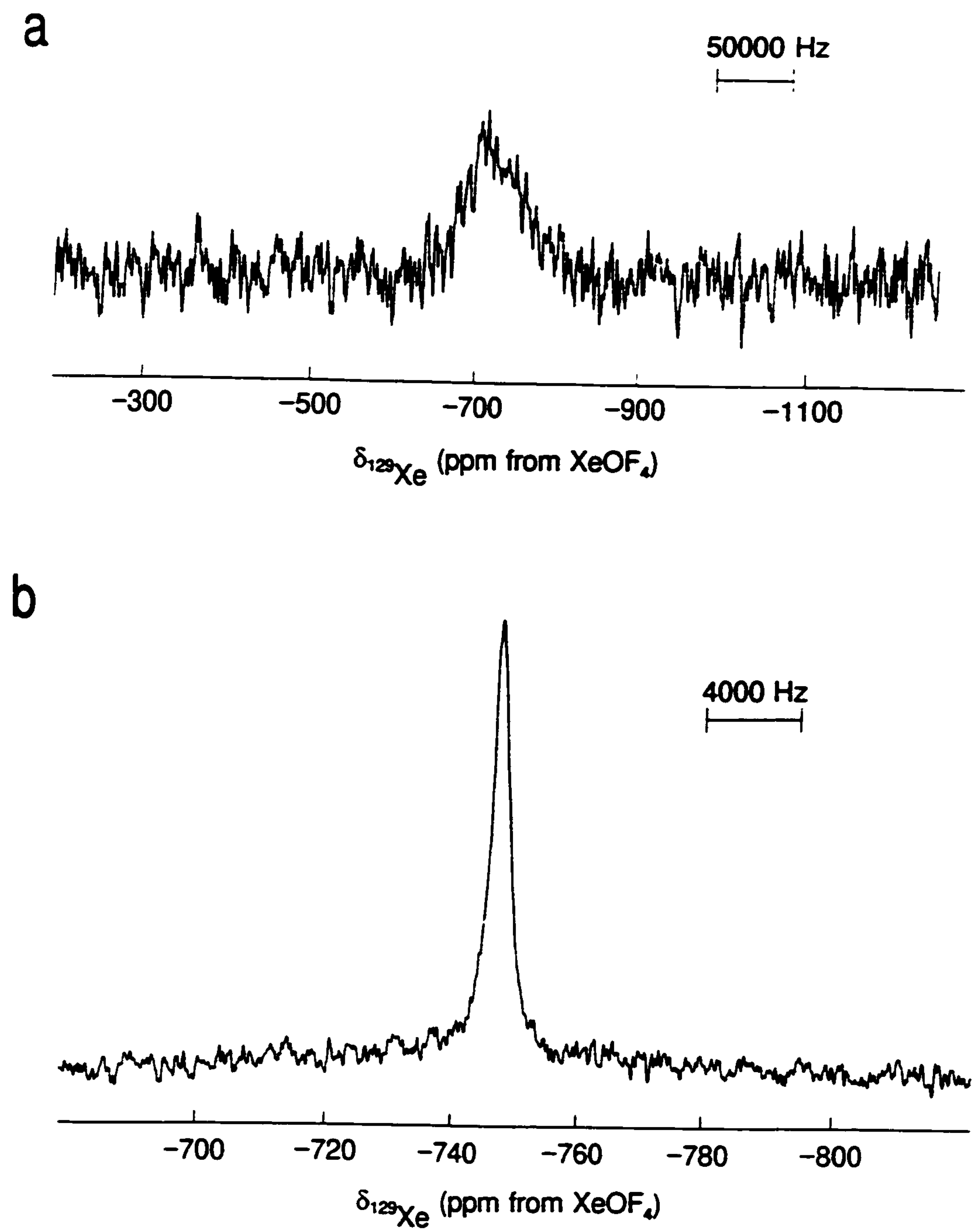

Figure 3.3 (a) Static ^{129}Xe NMR spectrum (55.640 MHz) of solid $[Na]_4[XeO_6]$ at room temperature and (b) ^{129}Xe NMR spectrum (138.983 MHz) of a saturated aqueous solution of $[Na]_4[XeO_6]$ at -30 °C.

is likely a consequence of acid-base equilibria (3.13) to (3.15) and slow decomposition yielding paramagnetic O_2.

3.3. Conclusion

The previously known XeO_4 has been stabilized in solution and characterized by ^{129}Xe, ^{131}Xe, and ^{17}O NMR spectroscopy. The highly symmetric environment around xenon in XeO_4 gave rise to a surprisingly narrow ^{131}Xe NMR signal ($\Delta\nu_{1/2}$ = 18 Hz; SO_2ClF solvent at -79 °C), the first reported ^{131}Xe NMR resonance of chemically bound xenon. The temperature dependance of ^{129}Xe spin-lattice relaxation time established the dominance of the spin-rotation relaxation mechanism. The temperature dependance of ^{131}Xe T_1-values is in agreement with the dominant quadrupolar relaxation. The investigation of solid and aqueous $[Na]_4[XeO_6]$ by ^{129}Xe NMR spectroscopy showed that the previously reported chemical shift[35] was erroneous and the correct value exhibits an extreme low-frequency shift.

CHAPTER 4

LEWIS-ACID PROPERTIES OF XeO_4

4.1. Introduction

Xenon tetroxide is the only neutral main-group tetroxide that has been prepared.[1] Its infamous instability in the solid state has thus far prevented investigations of its Lewis-acid properties. The stability of XeO_4 in solution (see Chapter 3) made it possible to study its solution chemistry. The transition metal analogue, OsO_4, behaves as a Lewis acid towards a variety of nitrogen donor molecules and fluoride ions (see 1.3. Osmium(VIII) Chemistry and Chapter 6). The present Chapter investigates Lewis acid properties of XeO_4. Xenon tetroxide is expected to behave in a similar fashion as OsO_4.

4.2. Results and Discussion

4.2.1. Lewis-Acid Properties of XeO_4 Towards CH_3CN

4.2.1.1 Preparation and NMR Spectroscopic Characterization of $XeO_4(CH_3CN)$. Xenon tetroxide dissolves in CH_3CN solvent yielding a clear, colourless solution (eq. (4.1)) which was characterized by ^{129}Xe NMR spectroscopy at -40 °C. In the ^{129}Xe

$$XeO_4 + CH_3CN \rightleftharpoons XeO_4(CH_3CN) \tag{4.1}$$

NMR spectrum, only a singlet at 224.9 ppm was observed. This extreme high-frequency shift with respect to δ(^{129}Xe) of XeO_4 in SO_2ClF (-92.9 ppm; -80 °C), HF(-85.8 ppm; -75 °C), and BrF_5 (-94.7 ppm; -50 °C) solvents indicates a strong interaction between XeO_4 and the donor solvent acetonitrile resulting in the formation of the $XeO_4(CH_3CN)$ (I)

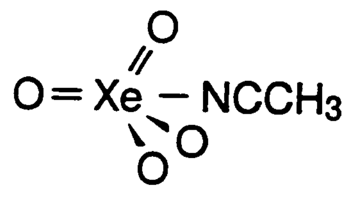

I

adduct with approximate C_{3v} symmetry, analogous to the adduct formation of OsO_4 with various N donor molecules (see 1.3. Osmium(VIII) Chemistry).[53-61] The deshielding of the ^{129}Xe nucleus in $XeO_4(CH_3CN)$ can be explained in terms of Jameson and Gutowsky's formula for the paramagnetic shielding term (eq. (3.3)).[188] For spherically symmetric closed shell cases like $Xe_{(g)}$, the minimum value of zero results and corresponds to the most shielded NMR environment for the nuclide in question. In the tetrahedral molecule, XeO_4, the "imbalance" in the electron population, P_u and D_u, is small. Upon coordination of CH_3CN, the P_u and D_u terms are expected to increase resulting in a paramagnetic shift (shift to higher frequency) of the ^{129}Xe NMR signal.

No signal near the corresponding chemical shift value of $XeO_4(CH_3CN)$ (5487 ppm with respect to Xe gas in Freon 114) was detected in the ^{131}Xe NMR spectrum of XeO_4 in CH_3CN indicating that the tetrahedral symmetry of XeO_4 is significantly lowered in the CH_3CN adduct. No separate ^1H and ^{13}C NMR signal for complexed CH_3CN in the adduct could be detected because of fast exchange on the NMR time scale between complexed CH_3CN and free CH_3CN solvent.

Prior to this work, a significant high-frequency shift has also been found for the ^{129}Xe resonance in xenon(VI) oxide fluorides, $XeOF_4$ and XeO_2F_2, in CH_3CN solvent (Table 4.1).[148] Only a small difference in chemical shift values for XeO_3 dissolved in H_2O and CH_3CN has been found and indicates strong interactions of XeO_3 with both solvents. No ^{129}Xe chemical shift value for XeO_3 in a non-coordinating solvent is available.

The attempted reaction of XeO_4 with an excess (>1.5-fold) CH_3CN in SO_2ClF solvent gave rise to an ^{129}Xe NMR signal at -95.64 ppm (-80 °C) corresponding to XeO_4 dissolved in SO_2ClF. The absence of a ^{129}Xe resonance for $XeO_4(CH_3CN)$ indicates the presence of equilibrium (4.1), where adduct formation is only observed with a large excess of CH_3CN.

4.2.1.2. Raman Spectroscopic Characterization of $XeO_4(CH_3CN)$. A Raman spectrum of the clear solution of XeO_4 in CH_3CN was recorded at -37 °C. A trace of the spectrum is shown in Figure 4.1 and the Raman frequencies with their tentative assignments are listed in Table 4.2.

Eight bands, excluding the internal ligand bands, are expected for XeO_4L (C_{3v}), L = CH_3CN and belong to the irreducible representations $4A_1 + 4E$ with all modes being Raman and infrared active. Three bands were observed in the Xe-O stretching region. The stretching modes at 782 and 902 cm^{-1} are shifted by 6 and 14 cm^{-1}, respectively, to higher frequency compared to those of XeO_4 in HF solvent. However, the weighted average of the stretching frequencies decreases from 853 cm^{-1} for XeO_4 to 841 cm^{-1} for $XeO_4(CH_3CN)$

Table 4.1 ^{129}Xe Chemical Shifts of $XeOF_4$, XeO_2F_2, XeO_3 and XeO_4 in Various Solvents[148]

Species	$\delta(^{129}Xe)$ [ppm]	Solvent	T [°C]
$XeOF_4$	0	neat	25
	23.7	HF	-50
	-29.9	$CFCl_3$	24
	164.7	CH_3CN	-40
XeO_2F_2	171.0	HF	-50
	263.0	CH_3CN	-40
XeO_3	217.0	H_2O	25
	218.1	CH_3CN	-40
XeO_4[a]	-85.8	HF	-75
	224.9	CH_3CN	-40

[a] Present work.

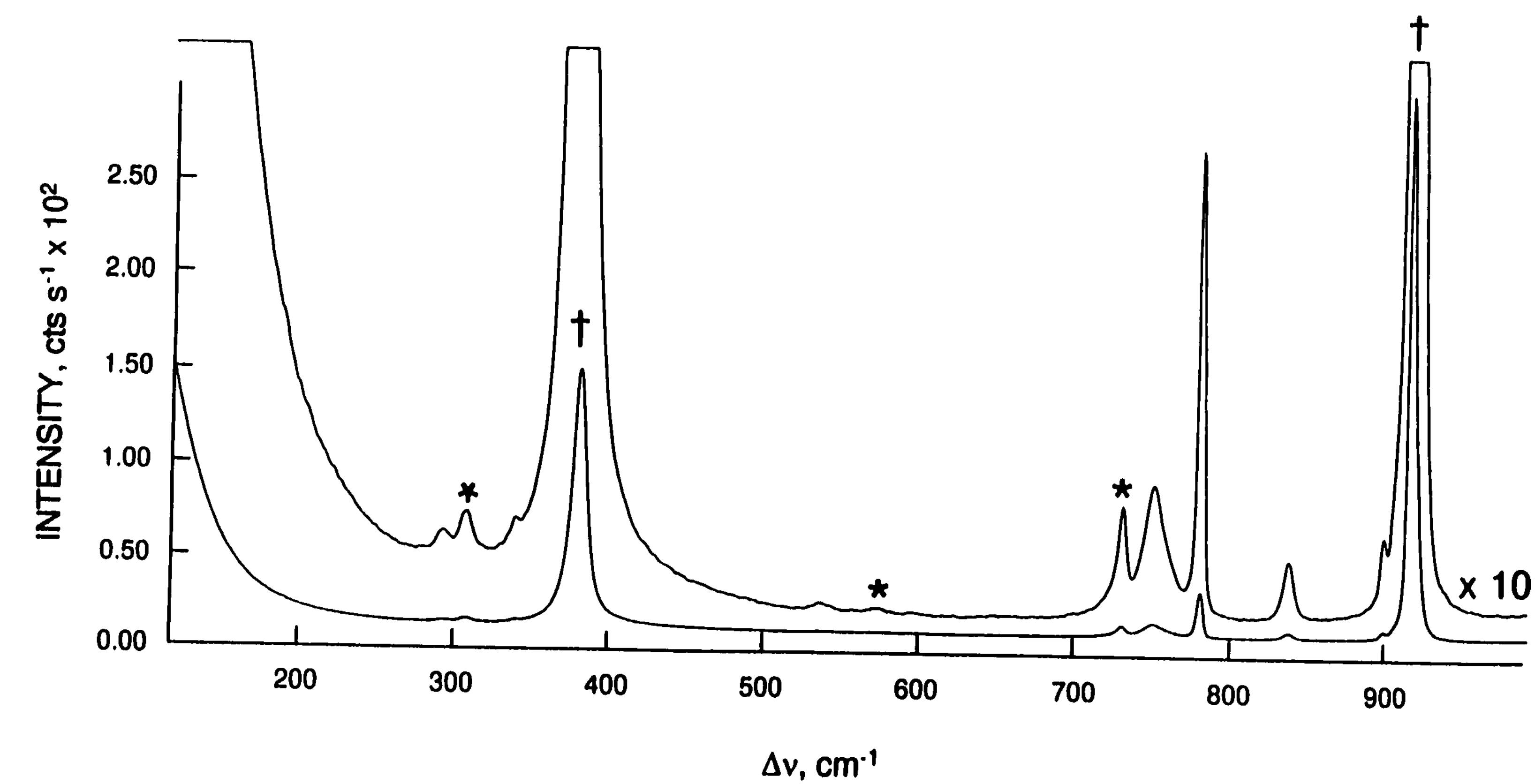

Figure 4.1 Raman spectrum of a solution of XeO_4 in CH_3CN recorded in ¼-in. FEP tube at -38 °C using 514.5-nm excitation. Asterisks (*) denote FEP sample tube lines; daggers (†) denote CH_3CN bands.

Table 4.2 Raman Frequencies and Their Assignments for a Solution of XeO_4 in CH_3CN

Frequencies[a] [cm^{-1}]	Assignment
$XeO_4(CH_3CN)$[b]	XeO_4L (C_{3v}); L = CH_3CN
2272 (67)sh	$\nu(CN)$
942 (8)sh	$\nu(CC)$
902 (19)	$\nu_1(A_1)$, $\nu_{as}(XeO_4)$
840 (13)	$\nu_5(E)$, $\nu_{as}(XeO_4)$
782 (100)	$\nu_2(A_1)$, $\nu_s(XeO_4)$
538 (2)	$\nu_3(A_1)$, $\nu_s(XeN)$
340 (7)	$\delta(XeO_4)$
308 (9)	$\delta(XeO_4)$

[a] Values in parentheses denote relative Raman intensities.

[b] Bands arising from the FEP sample tube were observed at 733 (25), 594 (1), 572 (<0.5), and 292 (4) cm^{-1}; bands arising from CH_3CN solvent were observed at 381 (542), $\nu_8(E)$; 920 (1142), $\nu_4(A_1)$; 1041 (14), $\nu_7(E)$; 1374 (256), $\nu_3(A_1)$; 1414 (78), 1448 (100), $\nu_6(E)$; 1827 (6), 2090 (2), 2204 (96), $2\nu_4+\nu_4$; 2228 (33), 2253 (3311), $\nu_2(A_1)$; and 2293 (222) cm^{-1}, $\nu_3+\nu_4$ (see ref. (200)).

which correspond to an overall weakening of the Xe-O bonds upon adduct formation. The weak, new band at 538 cm^{-1} is tentatively assigned to the Xe-N stretch, since no XeO_4 or CH_3CN bands appear in this region. Only two of the four bending modes were observed. The two unobserved bending modes are likely hidden by the strong CH_3CN solvent band at 381 cm^{-1} or are too weak to be observed. Complexation shifts for some of the CH_3CN bands of $XeO_4(CH_3CN)$ were observed as weak shoulders on the intense, broad CH_3CN solvent bands.

4.2.2. Fluoride Ion Acceptor Properties of XeO_4

4.2.2.1. Preparation of the *cis*- and *trans*-$XeO_4F_2^{2-}$ Anions. The reaction of XeO_4 and CsF in HF solvent did not yield a new Xe(VIII) oxide fluoride anion. The ^{129}Xe and ^{131}Xe NMR and Raman spectra showed only the presence of XeO_4 in solution. Thus, XeO_4 is a weaker Lewis acid than HF (eq. (4.2)). However, when the reaction was carried out in

$$CsF + HF + XeO_4 \xrightarrow{HF} [Cs][HF_2] + XeO_4 \qquad (4.2)$$

$$2CsF + XeO_4 \xrightarrow{CH_3CN} [Cs]_2[XeO_4F_2] \qquad (4.3)$$

CH_3CN solution, a white precipitate formed according to eq. (4.3). While the ^{129}Xe NMR spectrum of the solution showed that small amounts of $XeO_4(CH_3CN)$ (δ = 224.9 ppm) were still present, the Raman spectrum of the white solid established the presence of the new xenon oxide fluoride anions, *trans*-$XeO_4F_2^{2-}$ (II) and *cis*-$XeO_4F_2^{2-}$ (III).

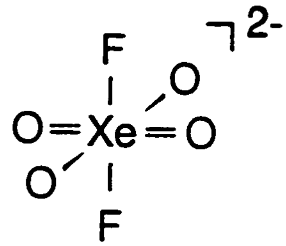

II

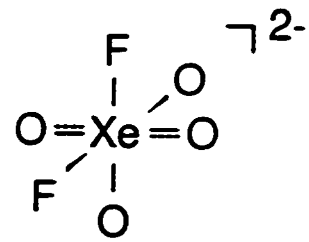

III

The reaction of XeO_4 and $[N(CH_3)_4][F]$ in CH_3CN solvent yielded a white solid according to eq. (4.4) under a yellow solution. The yellow colouration of the solution is

$$2[N(CH_3)_4][F] + XeO_4 \xrightarrow{CH_3CN} [N(CH_3)_4]_2[XeO_4F_2] \quad (4.4)$$

in contrast to the colourless solution of XeO_4 in CH_3CN in the absence of $[N(CH_3)_4][F]$, indicating the presence of a new xenon(VIII) oxide fluoride in solution, presumably $[N(CH_3)_4][XeO_4F]$. However, ^{129}Xe NMR spectrum of the yellow solution did not show a signal. This behaviour resembles that of a solution of $[N(CH_3)_4][OsO_4F]$ in CH_3CN which also did not produce a ^{19}F NMR signal and is a consequence of exchange (see Chapter 6). Other than the colouration, no further evidence for the XeO_4F^- anion was found. The white precipitate was characterized by Raman spectroscopy showing the presence of the *trans*-$XeO_4F_2^{2-}$ (II) and *cis*-$XeO_4F_2^{2-}$ (III) anion bands as well as the $N(CH_3)_4^+$ cation bands.

During the preparation, a small amount of the white solid was left above the solvent level at room temperature for several minutes. It only detonated when the FEP sample tube was heat-sealed near the solid deposit. This indicates that the $[N(CH_3)_4]_2$[*cis*-XeO_4F_2] and $[N(CH_3)_4]_2$[*trans*-XeO_4F_2] salts are remarkably stable and is likely a consequence of pseudo-octahedral xenon environment, as found for the XeO_6^{4-} anion.

4.2.2.2. Raman Spectroscopic Characterization of the *cis*- and *trans*-$XeO_4F_2^{2-}$ Anions. The Raman spectra of $[Cs]_2[XeO_4F_2]$ and $[N(CH_3)_4]_2[XeO_4F_2]$ are shown in Figures 4.2 and 4.3 and the observed frequencies with their tentative assignments are listed in Table 4.3.

A priori, three different anions can possibly be formed, XeO_4F^- (C_{3v}), *trans*-$XeO_4F_2^{2-}$ (D_{4h}), and *cis*-$XeO_4F_2^{2-}$ (C_{2v}). In the case of XeO_4F^-, the normal modes span the reducible representation $\Gamma = 4A' + 4E$ where all modes are Raman and infrared active and three Xe-O stretching bands are expected (2A' + E). A total of 15 bands are expected for *cis*-$XeO_4F_2^{2-}$ ($6A_1 + 2A_2 + 3B_1 + 4B_2$) where all modes are Raman active, while A_1, B_1, and B_2 are infrared active and the four Xe-O stretches should be observed in the Raman spectrum. For *trans*-$XeO_4F_2^{2-}$, 11 bands are expected ($2A_{1g} + 2A_{2u} + B_{1g} + B_{2g} + B_{2u} + E_g + 3E_u$) where only A_{1g}, B_{1g}, B_{2g}, and E_g are Raman active, while the other modes are infrared active and the two Xe-O stretching bands (A_{1g} and B_{1g}) should be observed in the Raman spectrum.

Several Raman spectra of the white precipitate resulting from the reaction between XeO_4 and CsF or $[N(CH_3)_4][F]$ in CH_3CN were recorded at different reaction times in different sample regions which allowed a distinction to be made between two groups of signals in the Xe-O stretching region. For the Cs^+ ($N(CH_3)_4^+$), salts Xe-O stretching bands were observed at 767 and 793 (770 and 800) cm^{-1} for the one compound and at 825, 809, and 757 (828, 785, 760, and 722) cm^{-1} for a second compound. Since the stretching

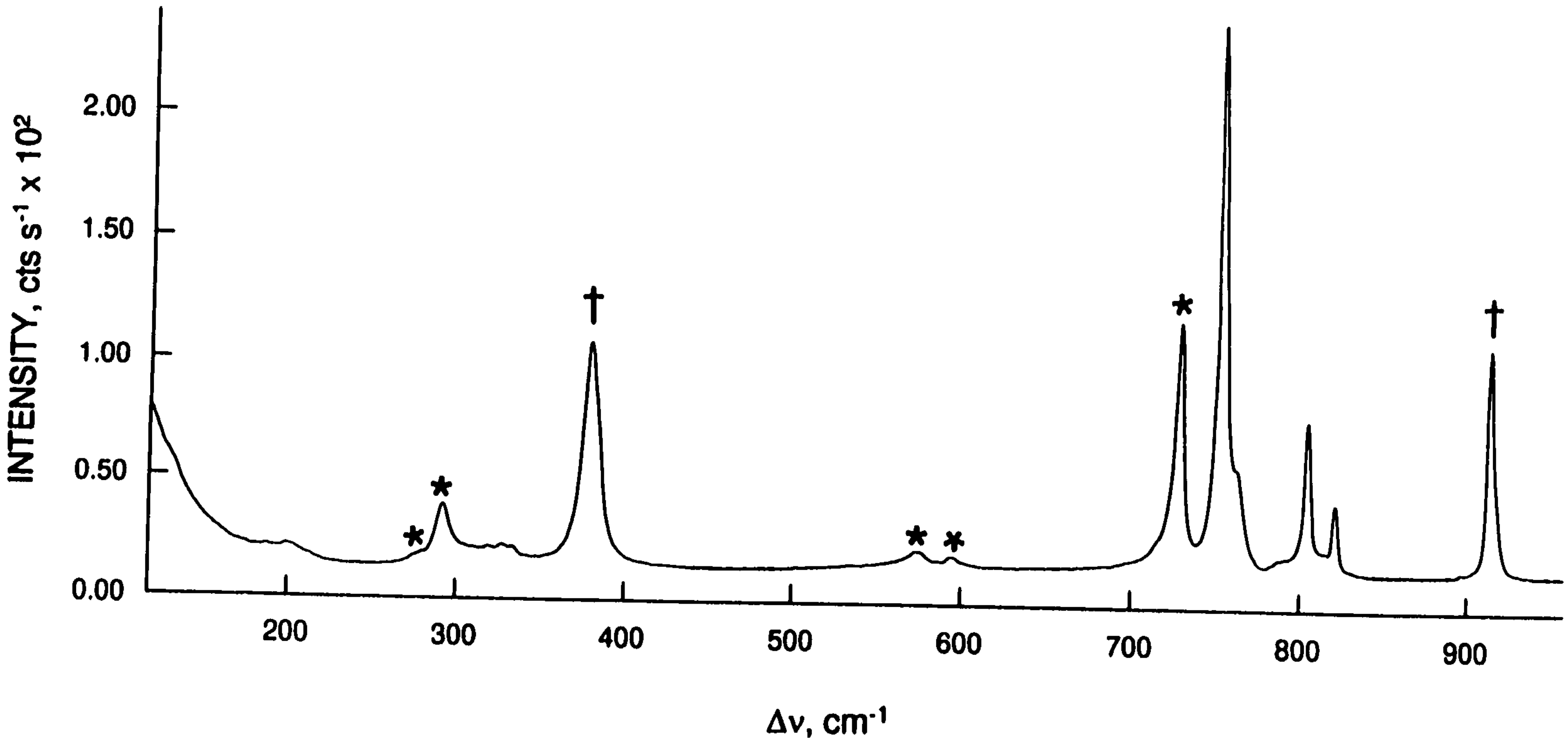

Figure 4.2 Raman spectrum of the white reaction product resulting from the reaction of XeO_4 with CsF recorded in a ¼-in. FEP tube at -39 °C using 514.5-nm excitation. Asterisks (*) denote FEP sample tube lines; daggers (†) denote CH_3CN bands.

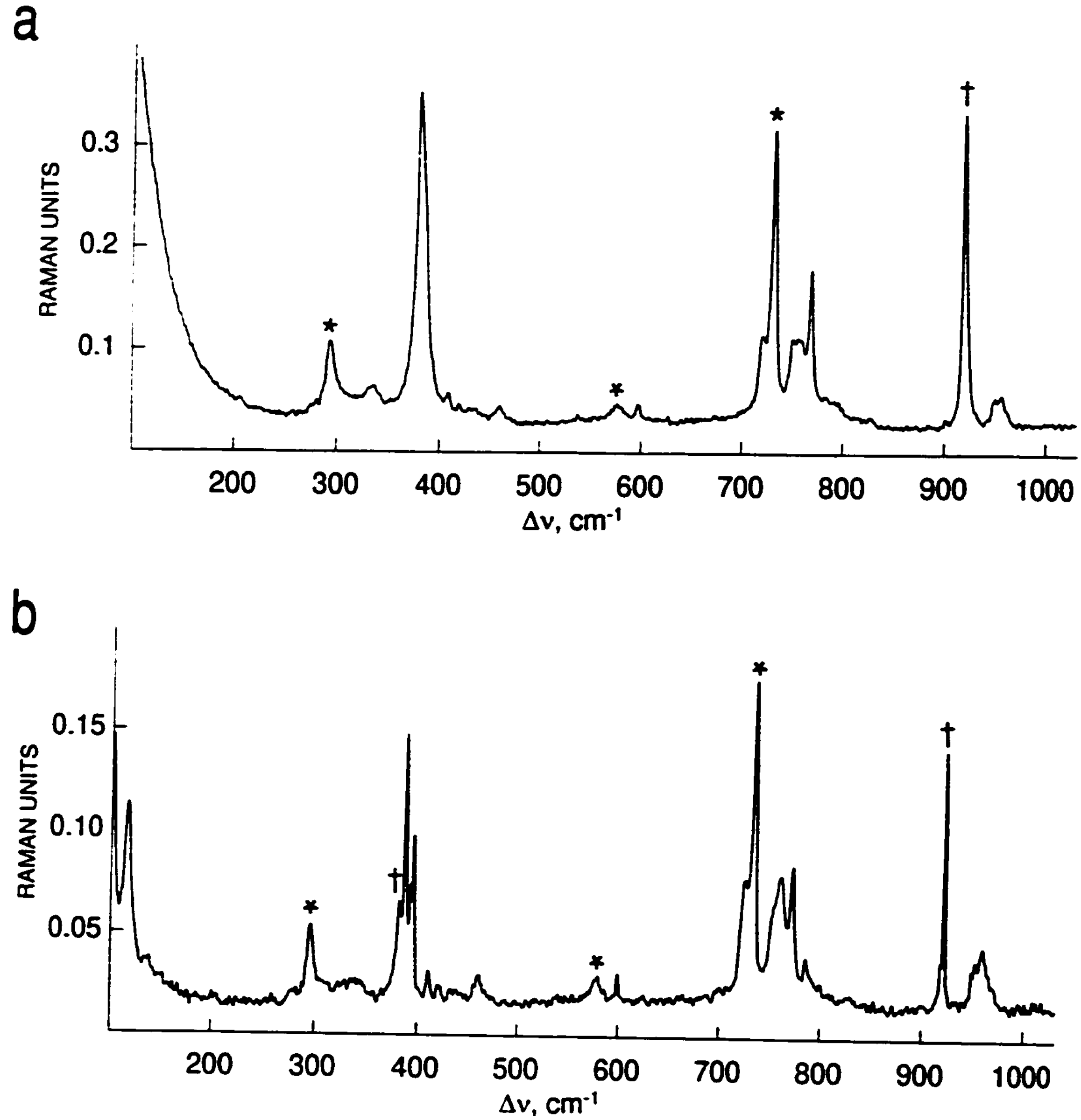

Figure 4.3 Raman spectrum of the white reaction product resulting from the reaction of XeO_4 with $[N(CH_3)_4][F]$ in CH_3CN recorded in a ¼-in. FEP tube at (a) -40 °C and (b) -165 °C on two different samples using 1064-nm excitation. Asterisks (*) denote FEP sample tube lines; daggers (†) denote CH_3CN bands.

Table 4.3 Raman Frequencies and Their Assignments for $[N(CH_3)_4]_2[XeO_4F_2]$ and $[Cs]_2[XeO_4F_2]$

Frequencies[a] [cm^{-1}]		Assignment	
$[N(CH_3)_4]_2[XeO_4F_2]$[b,c]	$[Cs]_2[XeO_4F_2]$[d]	*trans*-$XeO_4F_2^{2-}$	*cis*-$XeO_4F_2^{2-}$
	833 (2)sh		
828 vw	825 (13)		$\nu_{as}(XeO_4)$
	817 (16)sh		
785 w	809 (29)		$\nu_{as}(XeO_4)$
800 w	794 (3)	$\nu_{as}(XeO_4)$	
770 s	765 (19)	$\nu_s(XeO_4)$	
760 m	757 (100)		$\nu_s(XeO_4)$
720 s			$\nu_{as}(XeO_4)$
598 w	597 (3)[e]	ν(Xe-F)	ν(Xe-F)
538 vw	536 (1)	ν(Xe-F)	
420 vw		Xe-O/F bends	
409 w			
394 s			
391 m			
336 w	334 (4)	δ(XeO)	
	327 (4)		
	319 (4)		
	198 (2)		
	186 (1)		
	127 (<0.5)		

[a] Values in parentheses denote relative Raman intensities; abbreviations denote: shoulder (sh), very strong band (vs), strong (s), medium (m), weak (w), very weak (vw).

[b] Because of low signal-to-noise ratio and significant overlap, numerical relative intensities are not listed (see Figure 4.3).

[c] The $N(CH_3)_4^+$ cation modes were observed at 460 vw, $\nu_{19}(T_2)$; and 958 m cm^{-1}, $\nu_{18}(T_2)$ (see ref. (201, 202); bands arising from the FEP sample tube were observed at 293 s, 380 s, 386 vs, 579 w, 734 vs cm^{-1}; bands arising from CH_3CN solvent were observed at 380 s, $\nu_8(E)$; and 921 vs cm^{-1}, $\nu_4(A_1)$ (see ref. (200)).

[d] Bands arising from the FEP sample tube were observed at 732 (47), 597 (3), 576 (4), 386 (29)sh, 381 (42), 292 (12), and 280 (3) cm^{-1}; bands arising from CH_3CN solvent were observed at 381 (42), $\nu_8(E)$; 919 (43) cm^{-1}, $\nu_4(A_1)$ (see ref. (200)).

[e] This band overlaps with a band arising from the FEP sample tube.

frequencies of these two XeO_4/F^- adducts appear in the same frequency range, the formation of the *trans*- and *cis*-$XeO_4F_2^{2-}$ anions was assumed, rather than the XeO_4F^- and $XeO_4F_2^{2-}$ anions. A significant difference in the Xe-O stretching frequencies of the $XeO_4F_2^{2-}$ and the XeO_4F^- anions is expected, by analogy with the OsO_4F^- and $OsO_4F_2^{2-}$ anions (see Chapter 6). The assignment of the *trans*- and *cis*-isomer to the two groups of Xe-O stretching bands is based on the number of observed Raman bands. The bands at 757 (760) and 765 (770) cm^{-1} are assigned to the symmetric Xe-O stretching frequencies of the *cis*- and *trans*-$XeO_4F_2^{2-}$ anions and are shifted to lower frequency with respect to the symmetric stretch of XeO_4 at 776 cm^{-1} (see 3.2.5. Raman Spectroscopic Characterization of XeO_4 in HF Solvent). The asymmetric Xe-O stretching bands of both anions appear at much lower frequencies than that of XeO_4 (878 cm^{-1}) indicating a more polar, weaker Xe-O bonds in the anions. Two weak bands were detected at 536 and 597 cm^{-1} in the Xe-F stretching region providing additional support for two xenon oxide fluoride species.

The salts, $[N(CH_3)_4]_2$[*cis*-XeO_4F_2] and $[N(CH_3)_4]_2$[*trans*-XeO_4F_2], were significantly weaker Raman scatterers than their Cs^+ analogues. The occurance of fluorescence in the case of the $N(CH_3)_4^+$ salts in Raman spectra excited by the Ar^+ (514.5-nm) and Kr^+ (647.1-nm) lasers complicated the characterization.

4.3. Conclusion

It was shown that XeO_4 acts as a Lewis acid towards fluoride as well as nitrogen bases, like its more stable transition metal analogue, OsO_4. In contrast to $OsO_4F_2^{2-}$ (see

Chapter 6), which exists only as the *cis*-isomer, Raman spectroscopic evidence was found for the presence of the *cis*-$XeO_4F_2^{2-}$ and *trans*-$XeO_4F_2^{2-}$ anions. The $XeO_4(CH_3CN)$ adduct provides the first example of a Xe(VIII)-N bond.

CHAPTER 5

PREPARATION AND NMR SPECTROSCOPIC CHARACTERIZATION OF XeO_3F_2 AND THE ATTEMPTED PREPARATION OF NEW XENON(VIII) OXIDE FLUORIDES

5.1. Introduction

Two oxide fluorides of xenon(VIII), XeO_3F_2 and XeO_2F_4, have been reported in the literature. Xenon trioxide difluoride has been prepared by Huston from the reaction of solid XeO_4 or $[Na]_4[XeO_6]$ with XeF_6 by fluorine-oxygen metathesis.[8,9,49] The first evidence for XeO_3F_2 was obtained from mass spectrometry,[49] followed by Raman and infrared spectroscopic characterization of matrix-isolated XeO_3F_2[8] which indicated a monomeric structure with D_{3h} symmetry (structure I). Xenon dioxide tetrafluoride was

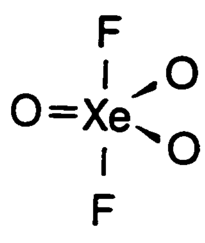

I

only observed in the mass spectrum as the product of the reaction between XeO_3F_2 and XeF_6 in $XeOF_4$ solvent.[10] Rapid decomposition to $XeOF_4$ prevented the structural elucidation of XeO_2F_4. Unlike OsO_2F_4, XeO_2F_4 is expected to exist as its *cis*- (structure

II) and *trans*-isomer (Structure III), since the isoelectronic $IO_2F_4^-$ anion has been found

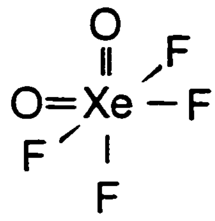

II

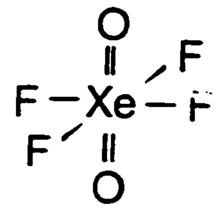

III

as a mixture of *cis*- and *trans*-$IO_2F_4^-$ (see Chapter 10).[102,103]

Attempts to fluorinate XeO_4 to XeO_3F_2 using FSO_3H, F_2, KrF_2, SbF_5, ClF_3, ClF_5, IF_5, and IF_7 have failed.[9,10] Chlorine trifluoride and ClF_5 act as reducing agents towards XeO_3F_2 forming ClO_3F and lower, non-specified xenon compounds.[10] Also, the reaction of XeO_3F_2 with SbF_5 and IF_7 did not yield XeO_2F_4.[9,10] Instead, solid adducts have been reported which were not further investigated.

5.2. Results and Discussion

5.2.1. Preparation and NMR Spectroscopic Characterization of XeO_3F_2

Xenon trioxide difluoride, XeO_3F_2, was prepared by reaction of XeO_4 with XeF_6 in SO_2ClF, HF, and BrF_5 solvents by a fluorine/oxygen metathesis reaction (eq. (5.1)) by

$$XeO_4 + XeF_6 \longrightarrow XeO_3F_2 + XeOF_4 \qquad (5.1)$$

analogy with the synthetic approach of Huston.[9] The reaction of $[Na]_4[XeO_6]$ with XeF_6 in SO_2ClF and BrF_5 yielded XeO_4 and $XeOF_4$ as the initial products according to eq. (5.2)

$$[Na]_4[XeO_6] + 2XeF_6 \longrightarrow XeO_4 + 2XeOF_4 + 4NaF \quad (5.2)$$

based on ^{129}Xe ($[Na]_4[XeO_6]$ + 16.5XeF_6 in SO_2ClF, -78 °C; $XeOF_4$: 13.4 ppm, $^1J(^{129}Xe-^{19}F)$ = 1119 Hz; XeO_4: -93.40 ppm; XeF_6: -41.0 ppm, $\Delta\nu_{1/2}$ = 340 Hz) and ^{19}F ($[Na]_4[XeO_6]$ + XeF_6 in SO_2ClF, -82 °C; $XeOF_4$: 94.89 ppm, $^1J(^{129}Xe-^{19}F)$ = 1114 Hz; XeF_6: 115.92 ppm; $[Na]_4[XeO_6]$ + 8XeF_6 in BrF_5, -55.5 °C; $XeOF_4$: 94.89 ppm, $^1J(^{129}Xe-^{19}F)$ = 1101 Hz; XeF_6: 118.23 ppm) NMR spectroscopy. Reaction (5.2) occurs at temperatures as low as -80 °C in SO_2ClF. Huston reported reaction (5.2), in the absence of a solvent, and characterized the products by mass spectrometry.[49] The vigorous, sometimes explosive interaction of $[Na]_4[XeO_6]$ with HF solvent at -78 °C yields XeO_4 according to eq. (5.3) and two new, insoluble xenon oxide species, whose nature could

$$[Na]_4[XeO_6] + 8HF \longrightarrow XeO_4 + 2H_2O + 4[Na][HF_2] \quad (5.3)$$

not be unambiguously determined (see 5.2.3, Interaction of $[Na]_4[XeO_6]$ with HF). Xenon tetroxide generated by eqs. (5.2) or (5.3) subsequently reacts with XeF_6 according to eq. (5.1) yielding low concentrations of XeO_3F_2.

The rate of reaction (5.1) was very slow at -40 °C. Only a very small amount of XeO_3F_2 was observed in the ^{19}F NMR spectrum after warming a sample of $[Na]_4[XeO_6]$ with an excess of XeF_6 in SO_2ClF to -40 °C for 15 min. Reaction (5.1) was found to be rapid above -20 °C, and after 2 to 3 min at -10 °C, ^{129}Xe and ^{19}F NMR signals arising from XeO_3F_2 could be detected in samples of XeO_4 or $[Na]_4[XeO_6]$ with XeF_6 in BrF_5

solvent. The concentration of XeO_3F_2 increased at -10 or 0 °C, however, the increase in the total amount of $XeOF_4$ indicated that decomposition of XeO_3F_2 to $XeOF_4$ and O_2, likely through XeO_2F_4 as an intermediate (eqs. (5.4) and (5.5)), was also taking place at

$$XeO_3F_2 + XeF_6 \longrightarrow [XeO_2F_4] + XeOF_4 \qquad (5.4)$$

$$[XeO_2F_4] \longrightarrow XeOF_4 + \tfrac{1}{2}O_2 \qquad (5.5)$$

a significant rate. No direct NMR spectroscopic evidence for the intermediate formation of XeO_2F_4 was found at any time during the experiment, presumably because decomposition (5.5) is rapid above -40 °C. The rapid decomposition of XeO_3F_2 in the presence of XeF_6 has also been reported by Huston.[8] However, when a sample of XeO_4 with excess XeF_6 in BrF_5 was allowed to warm between -30 and -25 °C for 3 h and 40 min, the ^{129}Xe NMR spectrum showed that the signal for XeO_4 had disappeared while the signal for XeO_3F_2 was still present, indicating that the decomposition of XeO_3F_2 does not occur at an appreciable rate at -30 °C. Even at 0 °C, the decomposition of XeO_3F_2 was not as rapid as described by Huston.[8] It has not been possible to prepare XeO_3F_2 in the higher concentrations needed for synthetic work because it is difficult to control the rates of XeO_3F_2 formation and the competing decomposition. Huston's preparative approach of reacting neat XeO_4 and XeF_6 will be utilized in the future, followed by the stablization of the generated XeO_3F_2 in SO_2ClF, BrF_5, and HF solvents, and may provide a means to obtain concentrations of XeO_3F_2 sufficient to investigate its Lewis acid and base chemistry.

In samples of $[Na]_4[XeO_6]$ and XeO_4 with XeF_6 in HF solvent, XeO_2F_2 was detected in solution besides $XeOF_4$ (^{19}F; $[Na]_4[XeO_6]$ + $8XeF_6$, -80 °C; $XeOF_4$: 91.00 ppm, $^1J(^{129}Xe-^{19}F)$ = 1146 Hz; XeO_2F_2 88.45 ppm, $^1J(^{129}Xe-^{19}F)$ = 1218 Hz). The formation of XeO_2F_2 can be explained according to reaction (5.6) or by the decomposition of XeO_3F_2 to O_2 and XeO_2F_2 (eq. (5.7)), which was suggested by Huston.[9] In the sample of $[Na]_4[XeO_6]$ with XeF_6 in HF, also hydrolysis reactions (5.8) and (5.9) with water that was generated by eq. (5.3) will increase the concentrations of $XeOF_4$ and XeO_2F_2. Several

$$2XeO_4 + XeF_6 \xrightarrow{HF} 2XeO_3F_2 + XeO_2F_2 \qquad (5.6)$$

$$XeO_3F_2 \longrightarrow XeO_2F_2 + \tfrac{1}{2}O_2 \qquad (5.7)$$

$$XeF_6 + H_2O \longrightarrow XeOF_4 + 2HF \qquad (5.8)$$

$$XeOF_4 + H_2O \longrightarrow XeO_2F_2 + 2HF \qquad (5.9)$$

samples in HF and BrF_5 solvents also generated XeF_2 at temperatures as low as -30 °C (^{129}Xe; XeO_4 + XeF_6 in BrF_5, -50 °C; XeF_2: -1665.8 ppm, $^1J(^{129}Xe-^{19}F)$ = 5623 Hz). The formation of XeF_2 in these reactions is not well understood, but might result from the decomposition of XeO_2F_2 (eq. (5.8)), which is formed by reaction (5.6) or (5.7). Xenon difluoride dioxide is known to be thermodynamically unstable with respect to decomposition to O_2 and XeF_2, however, it was found to be kinetically stable at room temperature for several weeks.[203] The reaction conditions may somehow lower the kinetic barrier to decomposition (5.10).

$$XeO_2F_2 \longrightarrow O_2 + XeF_2 \tag{5.10}$$

In contrast to Huston's preparation, XeO_3F_2 was obtained in SO_2ClF, HF, and BrF_5 solutions making possible the first NMR spectroscopic characterization of XeO_3F_2. The ^{19}F NMR spectrum of XeO_3F_2 obtained from the reactions of $[Na]_4[XeO_6]$ with XeF_6 in SO_2ClF is shown in Figure 5.1, and the ^{129}Xe NMR spectrum of XeO_3F_2 obtained from a sample of XeO_4 and XeF_6 in BrF_5 is shown in Figure 5.2. The NMR spectroscopic data for XeO_3F_2 in SO_2ClF, HF, and BrF_5 at -80, -75, and -50 °C, respectively, are listed in Table 5.1.

The presence of XeO_3F_2 was established based on the multiplicity of the ^{129}Xe NMR signal. The ^{129}Xe NMR spectrum of XeO_3F_2 consists of a triplet at -414.5 ppm with $^{1}J(^{129}Xe-^{19}F)$ = 991 Hz (-80 °C in SO_2ClF) and results from coupling between ^{129}Xe with two equivalent fluorine atoms. The ^{19}F NMR spectrum shows a singlet at 229.5 ppm (-80 °C in SO_2ClF) with a single set of ^{129}Xe satellites and arises from the two equivalent fluorine ligands in XeO_3F_2 spin-spin coupled to the central ^{129}Xe (natural abundance, 26.44%). The ^{129}Xe chemical shift of XeO_3F_2 appears at lower frequency than the resonance of XeO_4 (-92.9 ppm at -79 °C in SO_2ClF; see Chapter 3) and is in accord with the general trend of monotonic deshielding of the central atom with increasing oxygen substitution that is, for instance, found for the series $(XeF_6)_4$ (-35 to -60.8 ppm), $XeOF_4$ (-29.9 to 23.7 ppm), XeO_2F_2 (171.0 to 173.2 ppm), XeO_3 (217.0 ppm).[148] This trend has been attributed to resonance structures $Xe{=}O \leftrightarrow Xe^{+}{-}O^{-}$, which result in increases in the P_u and D_u terms in eq. (3.1) and a decrease in the paramagnetic shielding term.[188]

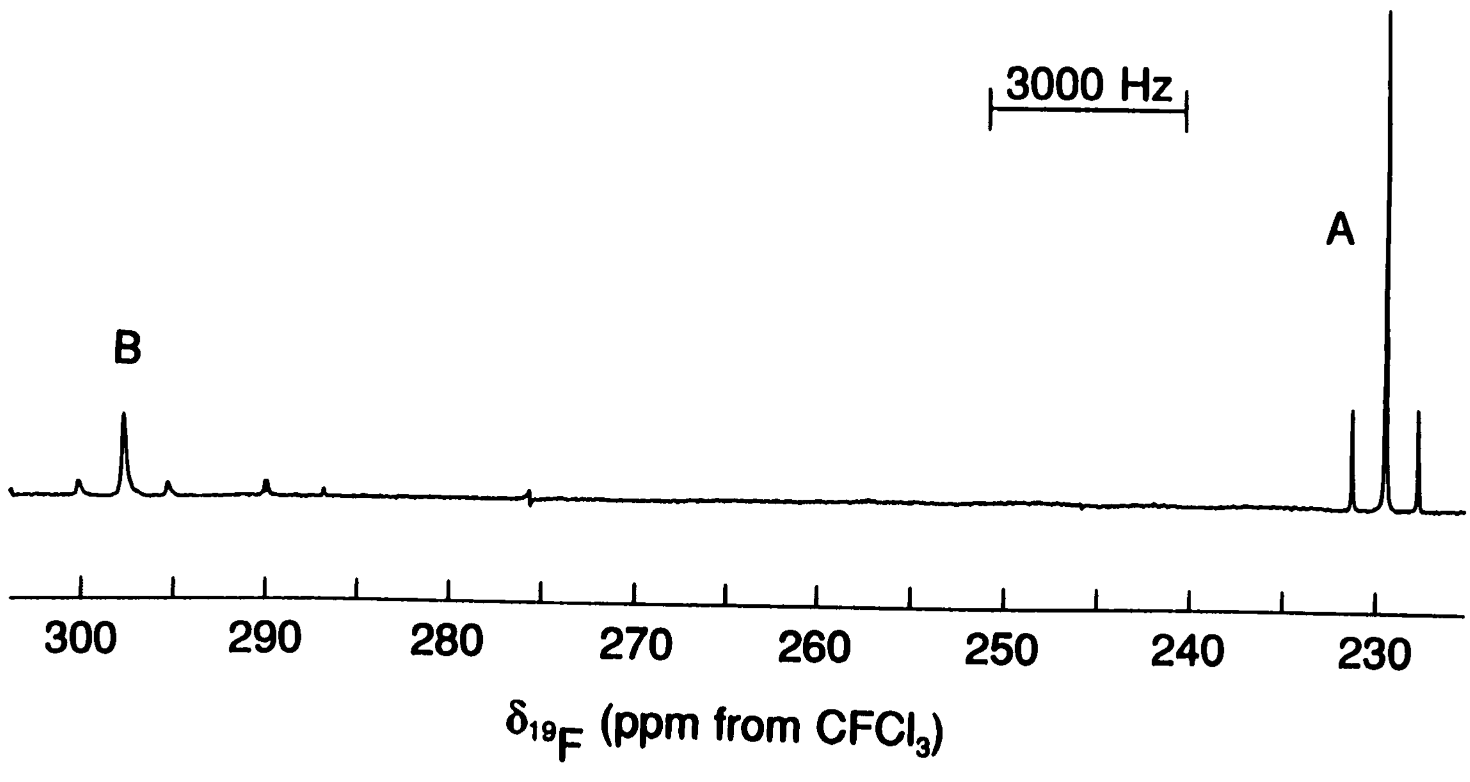

Figure 5.1 ^{19}F NMR spectrum (282.409 MHz) of XeO_3F_2 (A) and $XeO_3F_3^-$ (B) in SO_2ClF at -80 °C.

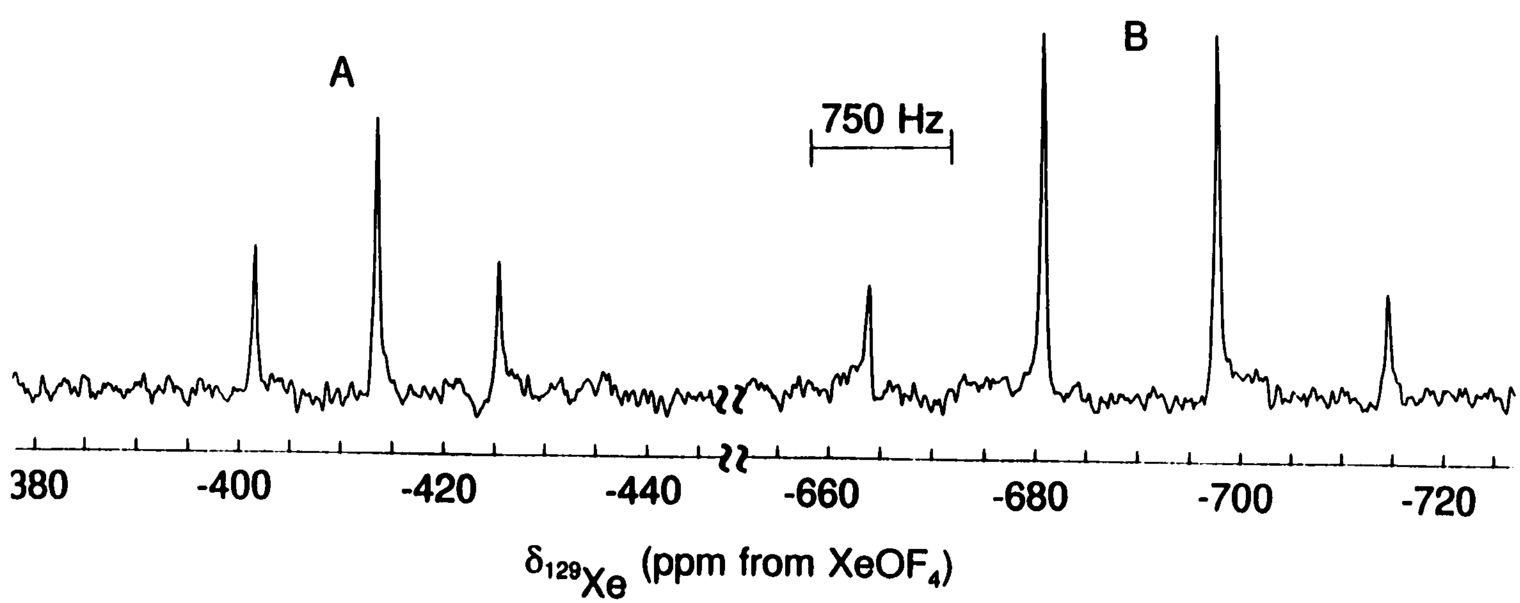

Figure 5.2 ^{129}Xe NMR spectrum (83.47 MHz) of XeO_3F_2 (A) and $XeO_3F_3^-$ (B) in BrF_5 at -50 °C.

Table 5.1 NMR Spectroscopic Data for XeO_3F_2 and $XeO_3F_3^-$

	Chemical Shift [ppm]		$^1J(^{129}Xe-^{19}F)$ [Hz]	Solvent	T [°C]
	^{19}F	^{129}Xe			
XeO_3F_2	229.5	-414.5	991	SO_2ClF	-80
	223.9	-412.9	1015	HF	-75
		-413.5	994	BrF_5	-50
$XeO_3F_3^-$		-689.3	1403	BrF_5	-50
	300.5		1349	BrF_5	-50
	297.7		1373	SO_2ClF	-80

However, the ^{129}Xe chemical shift of -414.5 ppm (-80 °C in SO_2ClF) is lower than the known chemical shift range of Xe(VI) species (-357.9 to 704.3 ppm) and contrasts with the general trend of increasing chemical shift with increasing formal oxidation number found for Xe(0) to Xe(VI) (see Chapter 3) and for the positive oxidation states of other spin-active nuclei.[204] The ^{19}F chemical shift of XeO_3F_2 at 229.5 ppm (-80 °C in SO_2ClF) is significantly more deshielded than ^{19}F resonances in lower oxidation state xenon fluorides and oxide fluorides confirming the presence of a Xe(VIII) species. This high-frequency shift is expected since xenon in its highest oxidation states efficiently removes electron density from the fluorine ligands and deshields the latter. The coupling constant of 991 Hz (-80 °C in SO_2ClF) is consistent with a change in the sign of the coupling constants occurring on going from Xe(VI) to Xe(VIII) as suggested by Gillespie and Schrobilgen.[205] This finding will be discussed in the following section together with the $^1J(^{129}Xe-^{19}F)$ coupling constant of the novel $XeO_3F_3^-$ anion.

5.2.2. Preparation and NMR Spectroscopic Characterization of the $XeO_3F_3^-$ Anion

The $XeO_3F_3^-$ anion was prepared in low concentrations in samples containing XeO_4 and XeF_6 in BrF_5 as well as in samples of $[Na]_4[XeO_6]$ and XeF_6 in BrF_5 and SO_2ClF. The anion was generated, together with XeO_3F_2, after allowing the samples to warm between -15 to -10 °C for several minutes. However, the exact conditions for the formation of $XeO_3F_3^-$ are presently not well understood. Attempts to generate larger amounts of $XeO_3F_3^-$ failed and the reproducibility of its preparation was poor. Reaction temperatures as low as -25 °C do not seem to give rise to detectable amounts of $XeO_3F_3^-$, moreover, $XeO_3F_3^-$ that was previously present disappeared at that temperature. Longer reaction times at -10 °C did not yield higher concentrations of $XeO_3F_3^-$ presumably because of a competing decomposition. The counter cations are thought to be the $XeF_5^+/Xe_2F_{11}^+$ cations in the sample containing XeO_4 and XeF_6 in BrF_5 since XeF_6 is known to be a good fluoride ion donor (eq. (5.11)).[4] Fast exchange of the xenon and

$$n\mathrm{XeF_6} + \mathrm{XeO_3F_2} \xrightarrow{\mathrm{BrF_5}} [\mathrm{Xe}_n\mathrm{F}_{5n+1}][\mathrm{XeO_3F_3}]\ ;\ n = 1,2 \qquad (5.11)$$

fluorine environments of the $XeF_5^+/Xe_2F_{11}^+$ cations with those of XeF_6 prevented the NMR spectroscopic observation of the cations. No fluorine ligand exchange between the $XeF_5^+/Xe_2F_{11}^+$ cations and the BrF_5 solvent occurs, since the ^{19}F resonances of BrF_5 show well resolved ^{19}F-^{19}F couplings (-55 °C; F_{ax}: 274.21 ppm; F_{eq}: 136.21 ppm; $^2J(^{19}F-^{19}F)$ = 75 Hz). The NaF generated in samples containing $[Na]_4[XeO_6]$ and XeF_6 in SO_2ClF and BrF_5 (eq. (5.2)) presumably acts as the fluoride ion source according to eq. (5.12). The

$$\mathrm{NaF} + \mathrm{XeO_3F_2} \xrightarrow{\mathrm{SO_2ClF/BrF_5}} [\mathrm{Na}][\mathrm{XeO_3F_3}] \qquad (5.12)$$

$XeO_3F_3^-$ anion was never observed in HF solvent indicating that HF is a better fluoride ion acceptor than XeO_3F_2.

The ^{129}Xe and ^{19}F NMR spectra of $XeO_3F_3^-$ are shown in Figures 5.1 and 5.2, respectively, and the corresponding NMR data are listed in Table 5.1. The presence of

$XeO_3F_3^-$ was established based on the mulitplicity of the ^{129}Xe NMR signal. The ^{129}Xe NMR spectrum of $XeO_3F_3^-$ shows a quartet at -689.3 ppm with $^1J(^{129}Xe\text{-}^{19}F)$ = 1403 Hz (-50 °C in BrF_5) arising from three equivalent fluorine ligands coupled to the central xenon. The ^{129}Xe chemical shift is more shielded than the neutral parent compound, XeO_3F_2. This is in agreement with the general finding that the central atoms in the anions are more shielded than in their neutral precursors.[204] The binomial quartet multiplicity of the ^{129}Xe NMR signal indicates a *fac*-arrangement of the three fluorine ligands (structure IV) whereas the *mer*-arrangement is expected to give rise to a binomial doublet and

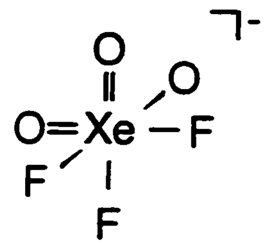

IV

triplet. Although a fast intramolecular exchange in a pseudo-octahedral *mer*-$XeO_3F_3^-$ isomer could account for the observed ^{129}Xe NMR spectrum, it is not very likely at low temperature. The detection of the ^{131}Xe NMR signal or $^{131}Xe\text{-}^{19}F$ coupling in the ^{19}F spectrum would unambiguously confirm the *fac*-geometry, since the electric field gradient at the central nucleus for *fac*-ligand arrangements is zero.[206] Unfortunately, the low intensity of the NMR signals did not permit the observation of a ^{131}Xe NMR signal or ^{131}Xe satellites at -50 and -80 °C in BrF_5 and SO_2ClF solvents, respectively.

The ^{19}F NMR spectrum consists of a singlet at 300.5 ppm (-50 °C in BrF_5) with ^{129}Xe satellites, $^1J(^{129}Xe\text{-}^{19}F)$ = 1349 Hz. Although a dissociative chemical exchange of F^- would give a single ^{19}F resonance, it would also lead to collapse of the $^1J(^{129}Xe\text{-}^{19}F)$

coupling and can be ruled out on the basis of the observation of the 1:3:3:1 quartet in the ^{129}Xe NMR spectrum (*vide supra*). The difference between the coupling constants obtained in the ^{19}F and ^{129}Xe NMR spectra arises from the poor signal to noise ratio in the ^{129}Xe NMR spectrum. The size of this coupling constant confirms the suggested reversal in the sign of the one-bond ^{129}Xe-^{19}F coupling constants on going from Xe(VI) to Xe(VIII) species.[205] It has been noted that the ranges of $^{1}J(^{129}Xe-^{19}F)$ for Xe(II), Xe(IV), and Xe(VI) fluorides and oxide fluorides are nearly non-overlapping:[148]

$$^{1}J(^{129}Xe(II)-^{19}F_{terminal}) = -7594 \text{ to } -5572 \text{ Hz}$$

$$^{1}J(^{129}Xe(II)-^{19}F_{bridge}) = -5117 \text{ to } -4828 \text{ Hz}$$

$$^{1}J(^{129}Xe(IV)-^{19}F) = -3913 \text{ to } -2384 \text{ Hz}$$

$$^{1}J(^{129}Xe(VI)-^{19}F) = -2724 \text{ to } 1512 \text{ Hz}$$

$$^{1}J(^{129}Xe(VIII)-^{19}F) = 991 \text{ and } 1373 \text{ Hz}$$

The $^{1}J(^{129}Xe-^{19}F)$ coupling constants for XeO_3F_2 and $XeO_3F_3^-$ are 991 Hz and 1373 Hz (-80 °C in SO_2ClF), respectively, and are the first reported $^{1}J(^{129}Xe-^{19}F)$ couplings for Xe(VIII) compounds. Originally reported by Frame[207] and significantly extended by Gillespie and Schrobilgen,[205,208] an empirical correlation was found between $^{1}J(^{129}Xe-^{19}F)$ and the ^{19}F chemical shift. This correlation suggests the opposite sign for the coupling constants of $XeOF_3^+$ and XeF_5^+ relative to those of the remaining species (Figure 5.3). The NMR spectroscopic data of XeO_3F_2 and $XeO_3F_3^-$ extend the validity of this empirical correlation to xenon(VIII) species and, since $\delta(^{19}F)$ for XeO_3F_2 and $XeO_3F_3^-$ are at higher frequency, the empirical correlation implies a positive $^{1}J(^{129}Xe-^{19}F)$ coupling constant. However, the range for $^{1}J(^{129}Xe(VIII)-^{19}F)$ overlaps with that of Xe(VI) species.

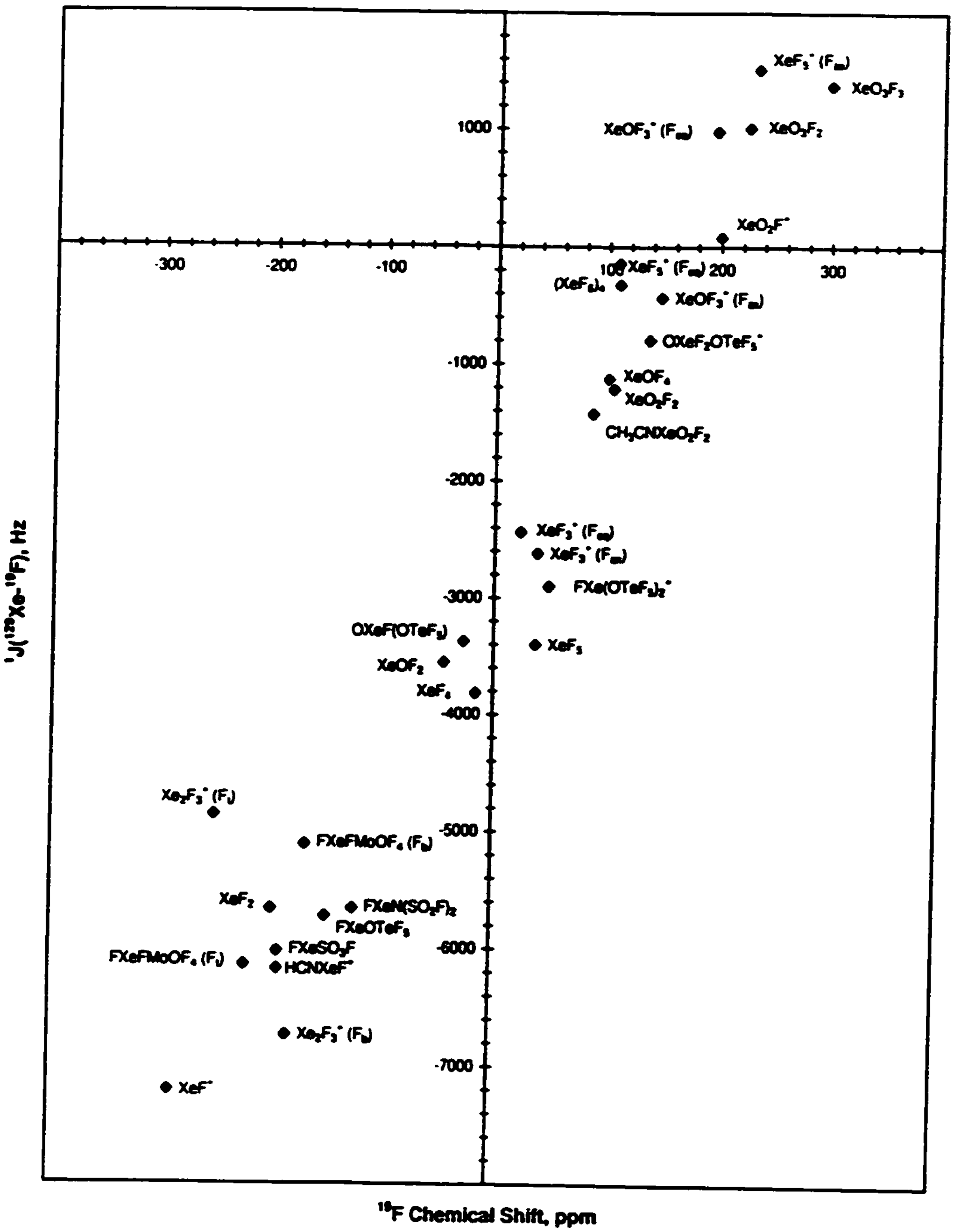

Figure 5.3 Empirical correlation of the ^{19}F chemical shift and $^1J(^{129}Xe-^{19}F)$ coupling constant for selected xenon compounds.

5.2.3. Interaction of $[Na]_4[XeO_6]$ with HF

Condensation of HF onto dry sodium perxenate resulted in a vigorous, sometimes explosive reaction. Rapid distillation of HF solvent led to detonations that ruptured the FEP sample tube. It was therefore important to slowly condense and freeze HF at -196 °C onto the sample tube walls above the $[Na]_4[XeO_6]$ followed by slow melting of the HF at -78 °C. Even during this improved procedure some smaller detonations have occurred which, however, were not intense enough to rupture the FEP sample tubes. The interaction between $[Na]_4[XeO_6]$ and HF at -78 °C yields a pale yellow precipitate under HF solvent. Characterization of the solution by ^{129}Xe NMR spectroscopy before and after warming the sample to -40 °C showed only the presence of XeO_4 which is formed according to eq. (5.3). The pale yellow solid was characterized by Raman spectroscopy at -78 °C under liquid HF. The spectrum is shown in Figure 5.4 and the frequencies are listed in Table 5.2. After allowing the sample to warm to -40 °C, a Raman spectrum of the white solid was recorded (Figure 5.5 and Table 5.2).

The Raman spectrum of the pale yellow solid contained signals attributed to solid XeO_4 exhibiting splitting of the degenerate modes previously reported for the solid state Raman spectrum of XeO_4.[48] In addition, six new Raman bands were observed. The solid did not contain any perxenate after contact with HF, since the intense perxenate band at 679 cm^{-1} was not detected. The pale yellow colour of the solid is most probably caused by XeO_4.

Upon warming to -40 °C, XeO_4 dissolved and its Raman bands disappeared. All bands that were observed in the Raman spectrum of the pale yellow solid, except a weak

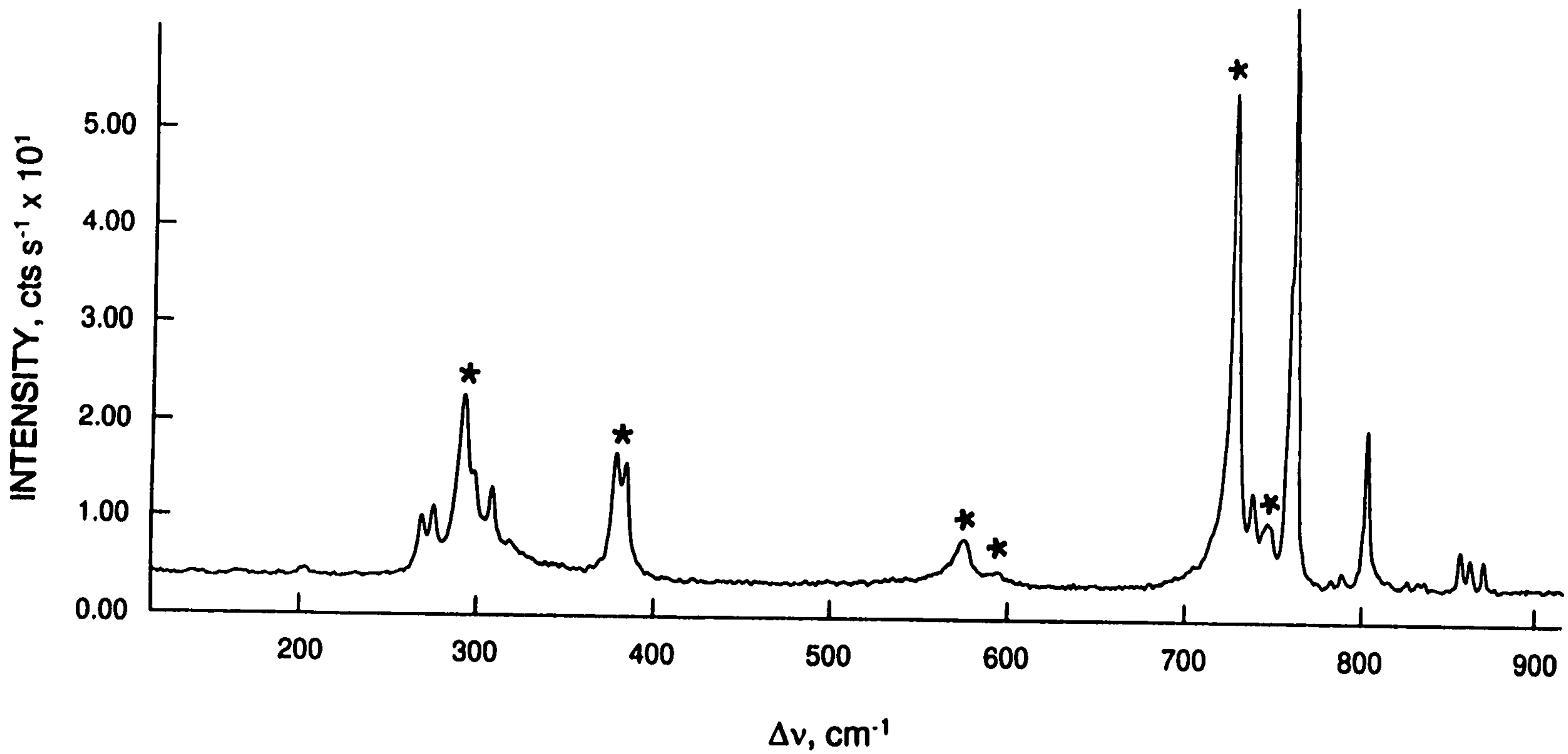

Figure 5.4 Raman spectrum of the pale yellow solid product of the reaction between $[Na]_4[XeO_6]$ and HF solvent without warming above -78 °C, recorded in a 4-mm FEP tube at -78 °C using 514.5-nm excitation. Asterisks (*) denote FEP sample tube lines.

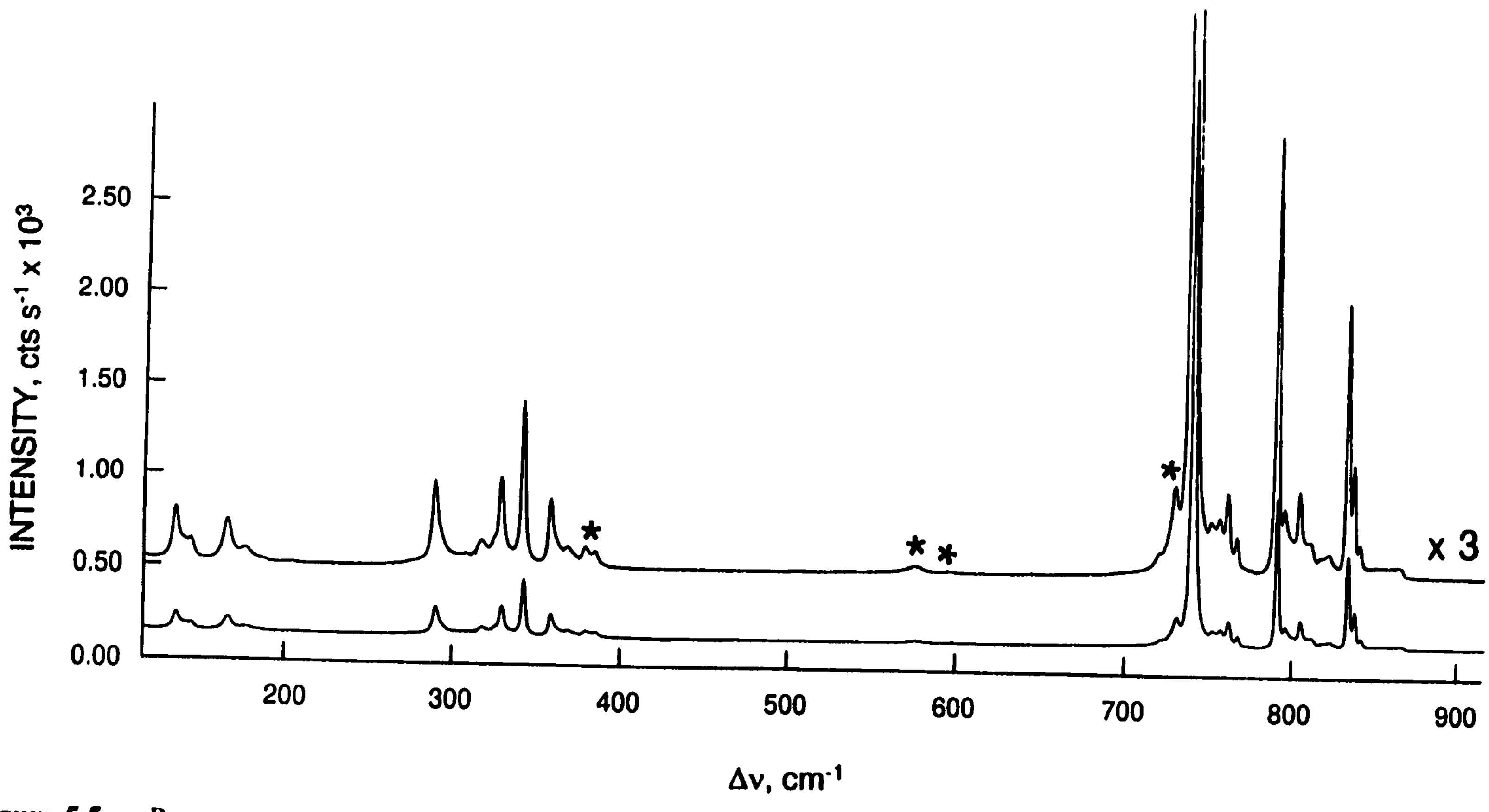

Figure 5.5 Raman spectrum of white solid product of the reaction between $[Na]_4[XeO_6]$ and HF solvent after warming to -40 °C, recorded in a 4-mm FEP tube at -78 °C using 514.5-nm excitation. Asterisks denote (*) FEP sample tube lines.

Table 5.2 Raman Frequencies and Their Assignments of the Solid Products of the Interaction Between $[Na]_4[XeO_6]$ and HF at two Different Stages of the Reaction.

Frequency[a] [cm^{-1}] sample maintained below -78 °C[c]	-40 °C[d]	Assignment[b]
875 (5)		XeO_4, $\nu_3(T_2)$
867 (5)		
861 (6)		
	869 (1)	B, ν(Xe-O)
	844 (2)	
	840 (6)	
	837 (16)	
	826 (1)	
	821 (1)	
	814 (2)	
808 (28)	808 (5)	A, ν(Xe-O)
	799 (4)	B, ν(Xe-O)
793 (3)	794 (26)	B
787 (2)		
	770 (2)	B
767 (100)		XeO_4, $\nu_1(A_1)$
764 (53)sh	765 (5)	A, ν(Xe-O)
	759 (3)	B, ν(Xe-O)
	755 (3)	B
742 (17)	743 (100)	B
	724 (1)	B

Table 5.2 continued...

Frequency[a] [cm^{-1}] sample maintained below -78 °C[c]	-40 °C[d]	Assignment[b]
	370 (1)	B, bending modes
	360 (4)	
	343 (10)	
	330 (5)	
	327 (2)sh	
320 (7)	318 (1)	A
310 (16)		XeO_4, $\nu_4(T_2)$
300 (19)[e]		
	290 (5)	B
277 (13)		XeO_4, $\nu_2(E)$
270 (11)		
	205 (<0.5)	B
	177 (1)	
	166 (3)	
	144 (1)	
	135 (3)	

[a] Spectra recorded on solid under HF solvent in ¼-in. FEP sample tubes at -80 °C using the 514.5-nm excitation. Relative Raman intensities are given in parentheses. [b] The two groups of frequencies that could be distinguished are assigned to the yet unidentified products A and B. [c] Bands arising from the FEP sample tube were observed at 751 (12), 733 (86), 597 (3), 578 (8), 386 (21), 381 (22), and 293 (32) cm^{-1}. [d] Bands arising from the FEP sample tube were observed at 733 (5), 597 (<0.5), 578 (<0.5), 386 (1), 381 (1), and 293 (2)sh cm^{-1}. [e] This band overlaps with a band arising from the FEP sample tube.

band at 787 cm^{-1}, were found in the Raman spectrum of the white solid after warming the sample to -40 °C. Recording Raman spectra at different reaction times allowed the identification of two groups of Raman bands based on their simultaneous increase or decrease in relative intensities. The bands at 808, 764, and 320 cm^{-1} are assigned to product A, which decreased in relative intensity, while bands assigned to product B increased in intensity upon warming the sample to -40 °C for nine hours (Table 5.2).

Because XeO_4 does not interact with fluoride ion in HF solvent and because of the apparent absence of Xe-F stretches in the Raman spectra, products A and B are unlikely to be xenon oxide fluorides. Moreover, water generated by reaction (5.3) would be expected to hydrolyze intermediate oxide fluorides. A sample of $[Na]_4[XeO_6]$ treated with excess AsF_5 in HF that was not allowed to warm above -78 °C only displayed a ^{129}Xe NMR signal for XeO_4, indicating the absence of oxide fluoride anions, which are expected to react with AsF_5 to give neutral or cationic oxide fluorides.

The primary reaction of the XeO_6^{4-} anion with anhydrous HF likely leads to the formation of intermediate perxenic acid, H_4XeO_6, according to eq. (5.13), which rapidly

$$XeO_6^{4-} + 8HF \xrightarrow{HF} [H_4XeO_6] + 4HF_2^- \quad (5.13)$$

$$[H_4XeO_6] \xrightarrow{HF} XeO_4 + 2H_2O \quad (5.14)$$

$$[H_4XeO_6] \xrightarrow{HF} H_2XeO_5 + H_2O \quad (5.15)$$

$$[H_4XeO_6] \xrightarrow{HF} XeO_3 + 2H_2O + ½O_2 \quad (5.16)$$

decomposes upon water abstraction to XeO_4 (eq. (5.14)) or possibly to H_2XeO_5 (eq. (5.15)). Another decomposition pathway is reduction to Xe(VI) and O_2 evolution according to eq. (5.16), which has been documented in aqueous solutions.[36,209] The Raman frequencies of product A resemble those found for $HXeO_4^-$,[23] however, the intensities of the Xe-O stretches are not in agreement. Product A could be an anionic derivative of the presently unknown metaperxenic acid, H_2XeO_5. The existence of monomeric XeO_3F_2 (D_{3h}) with a xenon coordination number five suggests the possible existence of the H_2XeO_5 (= $XeO_3(OH)_2$) molecule, which is the product of formal exchange of the two fluorines in XeO_3F_2 with two hydoxide groups. The larger number of bands for product B compared to A indicates that B has a lower symmetry. A condensation reaction of A could occur at -40 °C yielding a dinuclear Xe(VIII) oxide species corresponding to B, similar to eq. (5.17). The hydrogen metaperxenate anion, $HXeO_5^-$, in equation (5.17) would be the

$$H_2XeO_5 + HXeO_5^- \longrightarrow (HO)O_3XeOXeO_4^- + H_2O \qquad (5.17)$$

Lewis acid-base adduct between XeO_4 and OH^-, whose osmium analogue OsO_4OH^- has been prepared and characterized by infrared spectroscopy.[71]

5.2.4. Interaction of $[Na]_4[XeO_6]$ with BrF_5

Sodium perxenate and BrF_5 did not react at -10 °C, a temperature at which XeO_4 does not decompose at a significant rate. The addition of a Lewis acid (BF_3) also did not result in reaction. The only signals observed in the ^{19}F NMR spectrum of the solution were those of BrF_5 and a minor amount of BrO_2F (209 ppm), which is not believed to be generated by reaction with perxenate, since no evidence for a fluorinated xenon product was found. Hydrolysis (5.18) of BrF_5 with residual H_2O from $[Na]_4[XeO_6]$ is likely the cause for the small amount of BrO_2F.

$$BrF_5 + 2H_2O \longrightarrow BrO_2F + 4HF \qquad (5.18)$$

5.2.5. Interaction of XeO_4 and $[Na]_4[XeO_6]$ with KrF_2 in Various Solvents

The reaction of XeO_4 with KrF_2 in SO_2ClF and HF did not result in any reaction other than the decomposition of KrF_2 close to 0 °C and the fluorination of SO_2ClF to SO_2F_2. The reaction of sodium perxenate with KrF_2 in SO_2ClF only gave rise to the fluorination of the solvent. However, the reactions of $[Na]_4[XeO_6]$ with KrF_2 in HF yielded small amounts of $XeOF_4$ ($\delta(^{19}F)$ = 89 ppm , $^1J(^{129}Xe-^{19}F)$ = 1209 Hz) without warming the sample above -78 °C and no evidence for Xe(VIII) oxide fluoride formation was obtained. The reaction mixture of $[Na]_4[XeO_6]$ and KrF_2 in BrF_5 gave small amounts of BrO_2F ($\delta(^{19}F)$ = 207.9 ppm) and $XeOF_4$ ($\delta(^{19}F)$ = 98.2 ppm; $^1J(^{129}Xe-^{19}F)$ = 1205 Hz) after warming the sample to 0 °C for 1 h and 15 min without any evidence for the formation of a Xe(VIII) oxide fluoride species in the ^{19}F NMR spectrum. Warming the mixture to room temperature for 10 min resulted in an additional weak ^{19}F NMR signal for XeO_2F_2 ($\delta(^{19}F)$ = 96.3 ppm). The intermediate formation of XeO_3F_2 is unlikely, since no evidence for its presence was found in the ^{19}F NMR spectrum. The observation of $XeOF_4$, XeO_2F_2, and BrO_2F is likely the result of hydrolyses (5.6), (5.7), and (5.18) with residual water from the $[Na]_4[XeO_6]$ sample.

5.2.6. Reaction of XeO_4 with $[KrF][AsF_6]$ in HF Solvent

Warming a sample of XeO_4 and $[KrF][AsF_6]$ in HF to -78 °C resulted in gas evolution and the formation of a yellow solution and large amounts of white solid. The ^{129}Xe NMR spectrum of the yellow solution showed a broad resonance at 543.7 ppm, $\Delta\nu_{1/2}$ = 170 Hz and no XeO_4 was detected. The nature of the broad singlet cannot be unambiguously determined and the presence of the Xe(VIII) cation, XeO_3F^+, is possible, since a high-frequency shift with respect to its neutral parent compound, XeO_3F_2 (-414.5 ppm in SO_2ClF, -80 °C) is expected. However, since the XeO_2F^+ cation exhibits a similar high-frequency shift (600 ppm in SbF_5),[35] a reduction from Xe(VIII) to Xe(VI) cannot be excluded. Such a reduction could proceed via an intermediate XeO_3F^+ cation, which decomposes according to eq. (5.19) to XeO_2F^+ and O_2. The $^1J(^{129}Xe-^{19}F)$ coupling constant

$$[XeO_3F][AsF_6] \longrightarrow [XeO_2F][AsF_6] + \tfrac{1}{2}O_2 \qquad (5.19)$$

of XeO_2F^+ (95 Hz)[35] is too small to be observed in the present case. The broadness of the signal likely arises from large amounts of solid present in the NMR sample. The Raman spectrum of the white precipitate showed unreacted starting material, $[KrF][AsF_6]$, and the presence of $[O_2][AsF_6]$ indicating that oxidation of oxygen from XeO_4 to O_2^+ and possibly reduction of Xe(VIII) had occurred. No Xe-O stretching band was observed in the Raman spectrum of the solid indicating that all xenon oxide and oxide fluoride species are dissolved in HF solvent.

5.2.7. Reaction of XeO_3 with $[KrF][AsF_6]$ in HF Solvent

The reaction of XeO_3 with $[KrF][AsF_6]$ in HF to -78 °C resulted in gas evolution and the formation of a yellow solution and large amounts of white precipitate similar to the analogous reaction using XeO_4 (see 5.2.6, Reaction of XeO_4 with $[KrF][AsF_6]$ in HF). After allowing the mixture to react at -78 °C for *ca.* 20 min, two broad singlets were observed at 540 and -450 ppm, while the reaction and the gas evolution continued. Over a period of approximately 30 minutes, the signal at -450 ppm disappeared, while the intensity of the broad singlet at 565 ppm ($\Delta\nu_{½}$ = 500 Hz) increased and another signal appeared at 186 ppm. The ^{129}Xe resonance at 540 ppm has also been observed in the reaction between XeO_4 and $[KrF][AsF_6]$ (see 5.2.6, Reaction of XeO_4 with $[KrF][AsF_6]$ in HF) and possibly corresponds to the XeO_3F^+ cation, as the oxidative fluorination product, or the XeO_2F^+ cation. Since the Raman spectrum of the white precipitate showed the presence of O_2^+ (1859 and 1865 cm^{-1}), indicating the oxidation of oxygen from XeO_4, the presence of the latter xenon cation seems more plausible. No Xe-O stretches were observed in the Raman spectrum of the white precipitate. The ^{129}Xe NMR signal at -450 ppm is attributed to the xenon(VIII) oxide fluoride, XeO_3F_2, which presumably forms according to eq. (5.20) and (5.21) via the XeO_3F^+ cation. However, oxygen from XeO_3F_2

$$XeO_3 + [KrF][AsF_6] \xrightarrow{HF} [XeO_3F][AsF_6] + Kr \qquad (5.20)$$

$$[XeO_3F][AsF_6] + 2HF \xrightarrow{HF} XeO_3F_2 + [H_2F][AsF_6] \qquad (5.21)$$

is presumably oxidized to O_2^+, which has been observed in the white precipitate, yielding XeO_2F^+ and small amounts of $XeOF_3^+$, which was also found in the ^{19}F NMR spectrum (186 ppm) as a product.

5.3. Conclusion

The xenon(VIII) oxide fluoride, XeO_3F_2, has been characterized by ^{129}Xe and ^{19}F NMR spectroscopy for the first time in HF, SO_2ClF, and BrF_5 solvents. The novel $XeO_3F_3^-$ anion has been prepared and characterized by NNR spectroscopy and is shown to have a facial arrangement in solution. The ^{129}Xe-^{19}F spin-spin couplings observed for XeO_3F_2 and the *fac*-$XeO_3F_3^-$ anion provide the first examples of $^1J(^{129}Xe^{VIII}\text{-}^{19}F)$ coupling and extend the previously established empirical correlation between $^1J(^{129}Xe\text{-}^{19}F)$ and $\delta(^{19}F)$. Based on this correlation, values of $^1J(^{129}Xe^{VIII}\text{-}^{19}F)$ have a positive sign, which is opposite to the signs of most $^1J(^{129}Xe\text{-}^{19}F)$ couplings. Attempts to obtain sufficiently high concentrations of XeO_3F_2 for preparative use, were not successful. The reaction between $[Na]_4[XeO_6]$ and HF yields XeO_4 and two new xenon oxide species that could not be unambiguously identified.

CHAPTER 6

FLUORIDE ION ACCEPTOR PROPERITIES OF OsO_4

6.1. Introduction

Osmium tetroxide has been shown to act as a Lewis acid towards a large number of organo-nitrogen bases,[52-61] which have been characterized by vibrational spectroscopy[52-56] and by single crystal X-ray diffraction.[55-61] Lewis acid-base adducts of OsO_4 with oxygen donor molecules have been prepared with the bases, OH^- [52,63-71] and *N*-methylmorpholine *N*-oxide.[61] Halide adducts of osmium tetroxide with fluoride[63,65,72,74] and chloride[55] have been reported. The OsO_4Cl^- and $OsO_4N_3^-$ anions were synthesized in CH_2Cl_2 solvent using the PPh_4^+ cation and characterized by infrared spectroscopy and the OsO_4Cl^- anion has been structurally characterized by X-ray crystallography as the $[PPh_4][OsO_4Cl]$ salt.[55] The *cis*-$OsO_4F_2^{2-}$ anion has reportedly been obtained as its Cs^+ and Rb^+ salts from aqueous solutions,[63,65,72,74] and the vibrational spectra have been interpreted in terms of the *cis*-isomer.[72] In a subsequent study, these workers have determined average Os-O and Os-F bond lengths for the compound they formulated as $[Cs]_2[$*cis*-$OsO_4F_2]$ using EXAFS spectroscopy.[74] Adduct formation between OsO_4 and weaker Lewis bases such as OH^- [52,63-67,69-71] and (R,R)-*trans*-1,2-bis(*N*-pyrrolidino)cyclohexane[59] was also shown to yield hexacoordinate osmium species. Although the composition was not reproducible, it was suggested that the $CsF \cdot OsO_4$ adduct, which was obtained from the reaction of CsF and OsO_4 in cold water, contains the OsO_4F^- anion and was characterized by elemental analyses and vibrational spectroscopy.[72]

The present work was undertaken to reinvestigate the formation and characterization of the OsO_4F^- and $OsO_4F_2^{2-}$ anions for which there is ambiguous and conflicting evidence in the literature and provides the first definitive structural studies of the OsO_4F^- and *cis*-$OsO_4F_2^{2-}$ anions in the solid state.

6.2. Results and Discussion

6.2.1. Syntheses of $[N(CH_3)_4][OsO_4F]$ and $[N(CH_3)_4]_2[OsO_4F_2]$

The compound, $[N(CH_3)_4][OsO_4F]$, was obtained as an orange solid from the reaction of stoichiometric amounts of $[N(CH_3)_4][F]$ and OsO_4 in CH_3CN solution according to eq. (6.1). The formation of the $[N(CH_3)_4][F]$ adducts of OsO_4 is instanta-

$$[N(CH_3)_4][F] + OsO_4 \xrightarrow{CH_3CN,\ RT} [N(CH_3)_4][OsO_4F] \qquad (6.1)$$

neous and initially yields a brown $[N(CH_3)_4]_2[OsO_4F_2]$ precipitate (*vide infra*) in sample regions where local concentrations of $[N(CH_3)_4][F]$ are high, but is reversible upon thorough mixing, yielding an orange precipitate of $[N(CH_3)_4][OsO_4F]$. The $[N(CH_3)_4][OsO_4F]$ salt is slightly soluble in CH_3CN at -40 °C giving an orange solution whereas no significant solubility was found for $[N(CH_3)_4][OsO_4F]$ in CHF_3 at temperatures as high as 0 °C. Attempts to observe a ^{19}F NMR signal for OsO_4F^- in CH_3CN solvent at -40 °C were unsuccessful, and is likely attributable to intermediate intermolecular exchange between the labile fluoride ligand of OsO_4F^- and low concentations of free fluoride ion (eq. (6.2)). Under these conditions, the ^{19}F NMR signal is likely to be broad

$$OsO_4F^- + CH_3CN \rightleftharpoons OsO_4{\cdot}CH_3CN + F^- \qquad (6.2)$$

and rendered indistinguishable from the baseline. This is consistent with the long Os-F bond observed in OsO_4F^- (see 6.2.3. X-ray Crystal Structure of $[N(CH_3)_4][OsO_4F]$) and with the low Os-F stretching frequency observed in the infrared spectrum of OsO_4F^- (see 6.2.4. Raman and Infrared Spectroscopy of $[N(CH_3)_4][OsO_4F]$).

The compound, $[N(CH_3)_4]_2[OsO_4F_2]$, was initially obtained in admixture with $[N(CH_3)_4][OsO_4F]$ and $[N(CH_3)_4][F]$ by reaction of OsO_4 with a stoichiometric amount of $[N(CH_3)_4][F]$ in CH_3CN solution according to eq. (6.3). Under CH_3CN solvent, $[N(CH_3)_4]_2$

$$2\ [N(CH_3)_4][F] + OsO_4 \xrightarrow{CH_3CN,\ -20\ °C} [N(CH_3)_4]_2[OsO_4F_2] \qquad (6.3)$$

$[OsO_4F_2]$ is dark brown but is light brown-ochre in color when dry. The reaction does not go to completion, presumably because $[N(CH_3)_4][OsO_4F]$ has a low solubility in CH_3CN at -20 °C and is occluded by $[N(CH_3)_4]_2[OsO_4F_2]$. Repeated washing with CH_3CN at -30 °C produced $[N(CH_3)_4]_2[OsO_4F_2]$ having only a minor $[N(CH_3)_4][OsO_4F]$ impurity.

6.2.2. Reaction of OsO_4 with NOF and NO_2F

Osmium tetroxide reacts with excess liquid NOF at -78 °C yielding a deep brown suspension after intermediate formation of a yellow solid, which presumably corresponds to a mixture of $[NO]_2[OsO_4F_2]$ and $[NO][OsO_4F]$, respectively (eq. (6.4)). Removal of

$$n\text{NOF} + \text{OsO}_4 \xrightarrow{\text{NOF}} [\text{NO}]_n[\text{OsO}_4\text{F}_n]\ ;\ n = 1,2 \qquad (6.4)$$

excess NOF yields a dark brown solid which is unstable above -40 °C and which decomposes by oxidation of the NO^+ cation. The latter oxidation is assumed based on the observation of a brown gas (NO_2) at -40 °C and a blue liquid (N_2O_3) at -78 °C. The exact nature of the brown solid could not be confirmed, since it readily decomposed in the beam of a YAG laser (1064-nm) and only Raman bands at 932 ($\nu_s(OsO_3)$), 919 ($\nu_{as}(OsO_3)$) and 2318 cm^{-1} ($\nu(NO)$) were observed indicating the presence of $[NO][OsO_4F]$ (see 6.2.4. Raman and Infrared Spectroscopy of $[N(CH_3)_4][OsO_4F]$ and $[N(CH_3)_4]_2[OsO_4F_2]$). However, the absence of Raman signals associated with the $OsO_4F_2^{2-}$ anion does not indicate a composition of predominantly $[NO][OsO_4F]$, since $[NO]_2[OsO_4F_2]$ most likely decomposes instantaneously in the laser beam and could, therefore, not be observed by Raman spectroscopy. The ^{19}F NMR spectrum of the red supernatant in the reaction between OsO_4 and excess, liquid NOF at -65 °C gave rise to an intense signal at 4.65 ppm that resembles a triplet with a splitting of 65 Hz, two broad signals (24.7 ppm, $\Delta\nu_{1/2}$ = 3000 Hz; -22.6 ppm, $\Delta\nu_{1/2}$ = 23000 Hz), two weak doublets

(6.77 ppm, J = 110 Hz; 10.5 ppm, J = 90 Hz) and a weak quartet at 15.45 ppm (J = 101 Hz). The origins of these signals are presently not understood.

No reaction of OsO_4 was observed with excess liquid NO_2F at -78 °C and with *ca.* 5.5 atm of NO_2F at temperatures as high as 55 °C. The difference in reactivity between NOF and NO_2F is consistent with the longer and more ionic N-F bond length in NOF (152 pm)[210] than that in NO_2F (135 pm).[211]

6.2.3. X-ray Crystal Structure of $[N(CH_3)_4][OsO_4F]$

Details of the data collection parameters and other crystallographic information for $[N(CH_3)_4][OsO_4F]$ are given in Table 6.1. Important bond lengths, contacts and angles for $[N(CH_3)_4][OsO_4F]$ are listed in Table 6.2.

The crystal structure consists of well-separated $N(CH_3)_4^+$ cations and OsO_4F^- anions. The tetrahedral $N(CH_3)_4^+$ cation lies on a C_2-axis giving rise to two crystallographically independent N-C bond lengths which are equal within experimental error and which have the expected values. The OsO_4F^- anion exhibits a distorted trigonal bipyramidal geometry (C_s point symmetry) (Figure 6.1) in which Os(1), F(1), O(1) and O(2) lie on a crystallographic mirror plane and the two equatorial oxygens, O(3) and O(3A), are symmetry related. The packing can be viewed as an approximate primitive cubic array of $N(CH_3)_4^+$ cations with OsO_4F^- anions occupying all cubic sites (distorted CsCl structure) (Figure 6.1). The OsO_4F^- anions exhibit long contacts to four $N(CH_3)_4^+$ cations forming one face of the cation cube. The equatorial O(3) and O(3A) atoms point and the O(1)-Os-F(1) bond angle bend towards this face as a consequence of contacts

Table 6.1 Summary of Crystal Data and Refinement Results for $[N(CH_3)_4][OsO_4F]$

	$[N(CH_3)_4][OsO_4F]$
formula	$C_4H_{12}FNO_4Os$
space group	*Abm2* (No. 39)
a [pm]	701.74(14)
b [pm]	1140.1(2)
c [pm]	1092.5(2)
α [deg]	90
β [deg]	90
γ [deg]	90
V [10^6 pm^3]	874.1(3)
Z [molecules/unit cell]	4
mol. wt	347.35
calcd density [g cm^{-3}]	2.639
colour, morphology	orange plate
size [mm^3]	0.400×0.442×0.0084
μ [mm^{-1}]	7.894
data/restraints/parameters	1214/1/57
final agreement factors	R^a = 0.0282
	$R_w{}^b$ = 0.0748
GOOF	1.135
Extinction coefficient	
$\Delta\delta_{max}/\Delta\delta_{min}$ [e 10^{-6}pm^{-3}]	2.081/-1.458

[a] $R = \Sigma||F_o| - |F_c||/\Sigma|F_o|$.

[b] $R_w = \Sigma|(|F_o| - |F_c|)w^{1/2}|/\Sigma(|F_o|w)$ where $w = 1/[\sigma^2(F) + (0.0344)^2 + 4.94]$.

Table 6.2 Experimental Bond Lengths, Contacts and Bond Angles in $[N(CH_3)_4][OsO_4F]$

$[N(CH_3)_4][OsO_4F]$			
Bond Lengths and Contacts [pm]			
Os(1)-F(1)	207.5(9)	Os(1)-O(1)	171.5(9)
Os(1)-O(2)	167.4(12)	Os(1)-O(3)	171.1(8)
N(1)-C(1)	148.4(11)	N(1)-C(2)	147.3(11)
O(1)···C(2A)	281.6(10)	O(1)···C(2B)	281.6(10)
O(3)···C(2D)	282.7(16)	F(1)···C(2)	328.0(14)
F(1)···C(2C)	328.7(14)		
Bond Angles [deg.]			
O(1)-Os(1)-F(1)	156.9(4)	O(1)-Os(1)-O(2)	101.4(5)
O(1)-Os(1)-O(3)	98.5(4)	O(2)-Os(1)-O(3)	118.4(4)
O(3)-Os(1)-O(3A)	115.2(8)	O(2)-Os(1)-F(1)	101.7(5)
O(3)-Os(1)-F(1)	70.2(4)	C(1)-N(1)-C(1A)	109.4(10)
C(1)-N(1)-C(2)	110.6(6)	C(1)-N(1)-C(2A)	108.3(8)
C(2)-N(1)-C(2A)	109.6(11)		

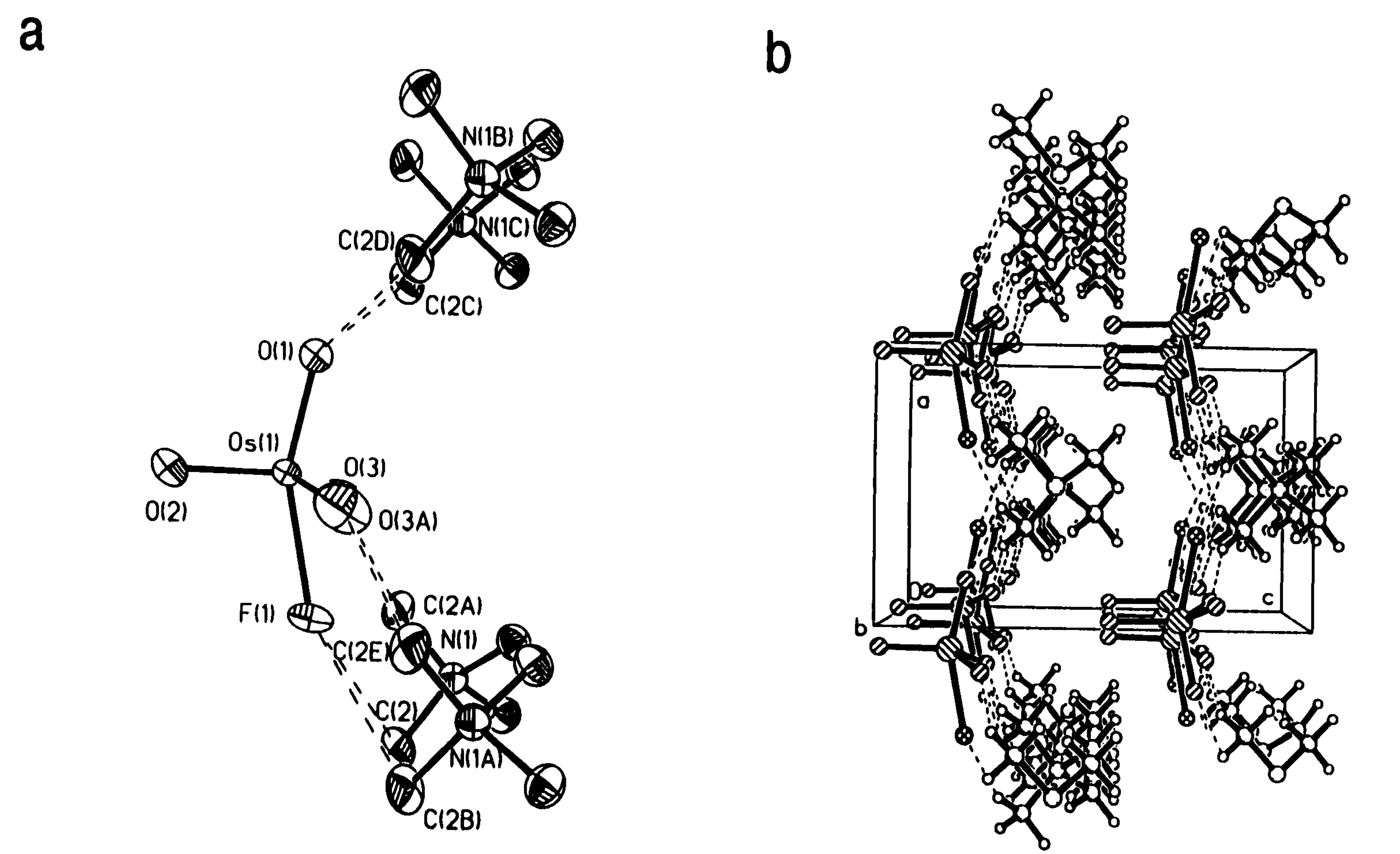

Figure 6.1 Views of (a) the $[N(CH_3)_4][OsO_4F]$ unit cell showing the packing along the *b*-axis and (b) the OsO_4F^- anion and its contacts to $N(CH_3)_4^+$ cations (thermal ellipsoids are shown at the 50% probability level).

between the axial O(1) and the symmetry-equivalent O(3) and O(3A) atoms of OsO_4F^- and the methyl groups of the $N(CH_3)_4^+$ cations. These O···H_3C contacts range from 281.6(10) to 282.7(16) pm and are significantly shorter than the sum of the CH_3 and O van der Waals radii (340 pm).[212,213] Significantly weaker F···H_3C contacts of 328.0(14) pm and 328.7(14) pm (van der Waals sum, 335 to 350 pm)[212,213] also exist in $[N(CH_3)_4][OsO_4F]$. The O···H_3C and F···H_3C contacts result in zig-zag layers in the *ab*-plane consisting of alternating $N(CH_3)_4^+$ and OsO_4F^- rows (Figure 6.1).

The equatorial Os-O(3)/Os-O(3A) bond lengths (171.1(8) pm/171.1(8) pm) and the axial Os-O(1) bond length (171.5(9) pm) are identical within experimental error and are equal, within 3σ, to that determined by EXAFS for $OsO_4F_2^{2-}$ (170.1(2) pm).[74] Based on the present study (see 6.2.4. Raman and Infrared Spectroscopy of $[N(CH_3)_4][OsO_4F]$ and $[N(CH_3)_4]_2[OsO_4F_2]$), the reported vibrational spectrum of the anion studied by EXAFS has been shown to be that of the OsO_4F^- anion. The Os-O(2) bond length of 167.4(12) pm is significantly shorter and can be explained by packing effects (*vide infra*). The Os-O(1), Os-O(3), and Os-O(3A) bond lengths are in good agreement with the mean Os-O bond length of 171.3(8) pm reported for OsO_4.[214] The short Os-O(2) bond length is still in the range found for the terminal Os-O bond lengths in the adducts, OsO_4·quinuclidine (169.7 to 172.2 pm)[57] and $OsO_4(OH)OsO_4^-$ (162(4) to 177(3); 164(4) to 171(3) pm).[71] The contacts between O(1), O(3), O(3A), and F(1) and the $N(CH_3)_4^+$ cations occur only on one side of the cubic hole occupied by the anion (*vide supra* and Figure 6.1) leaving O(2) without long contacts and sterically less crowded, resulting in a significantly shorter Os-O(2) bond. The Os-F bond (207.5(9) pm) in the OsO_4F^- anion is very long compared to the Os-F bond lengths in *cis*-OsO_2F_4 (188.3(3) pm and 184.3(3) pm)[6] and the terminal Os-F bond in $(OsO_3F_2)_\infty$ (187.9(1) pm),[7] and is in excellent agreement with that reported by EXAFS for OsO_4F^- (204.8(29) pm), which has been previously mistaken for the $OsO_4F_2^{2-}$ anion.[74] This bond is, however, considerably shorter than O_4Os-donor atom bond lengths found in the literature, which range from 2.21(2) Å in $OsO_4(OH)OsO_4^-$ [71] to 2.760(2) Å in OsO_4Cl^-,[55] reflecting the strong Lewis base character of the fluoride ion.

The two crystallographically independent O_{ax}-Os-O_{eq} angles, O(1)-Os-O(2) and O(1)-Os-O(3), are 101.4(5)° and 98.5(4)°, respectively. This comparatively small difference in O-Os-O bond angles is in agreement with the O_{ax}-Os-O_{eq} angles found in previously characterized OsO_4 adducts and is reflected in the similarity of the vibrational spectra of the adducts (see 6.2.4. Raman and Infrared Spectroscopic Characterization of $[N(CH_3)_4][OsO_4F]$) and indicative of the rigidity of the OsO_4 moiety. Surprisingly, the O(1)-Os-F(1) angle (156.9(4)°) is highly distorted from the O_{ax}-Os-X angle (X = donor atom) found in other Lewis base adducts of OsO_4 where the reported O_{ax}-Os-X angles range from 180.0° in OsO_4· quinuclidine[57] to 175.1(3)° in OsO_4· *N*-methylmorpholine *N*-oxide.[61]

The VSEPR model[120] predicts that the most energetically favoured geometry for OsO_4F^- is a distorted trigonal bipyramid with one oxygen and the fluorine in the axial positions and the remaining three oxygen atoms in the equatorial positions bent towards the fluorine. This was also the optimized geometry found using local density functional theory (LDFT) calculations.[215] In the crystal structure of $[N(CH_3)_4][OsO_4F]$, the geometry of the OsO_4F^- anion is, however, found to be a distorted trigonal bipyramid with the fluorine displaced towards one edge of the trigonal plane of the three equatorial oxygens. As a consequence of the rigidity of the OsO_4 moiety, the Os-F bond is quite ionic and can be easily distorted by close contacts with the cations. Because of the greater spatial requirements of Os–O double bond domains, the OsO_4-unit essentially retains its geometrical integrity with the O_{ax}–Os–F angle distorted by 23.14° from the ideal 180° bond angle of a regular trigonal bipyramid. In light of the computational findings, the distortion of the O_{ax}–Os–F angle is soley attributed to packing and is the consequence of strong O···H_3C and somewhat weaker F···H_3C anion-cation contacts (*vide supra*).

6.2.4. Raman and Infrared Spectroscopy of $[N(CH_3)_4][OsO_4F]$ and $[N(CH_3)_4]_2[OsO_4F_2]$

The $[N(CH_3)_4][OsO_4F]$ and $[N(CH_3)_4]_2[OsO_4F_2]$ salts were characterized by Raman (Figures 6.2 and 6.3) and infrared spectroscopy. The observed vibrational frequencies and their assignments for $[N(CH_3)_4][OsO_4F]$ and $[N(CH_3)_4]_2[OsO_4F_2]$ are given in Table 6.3 and 6.4, respectively. The anion mode assignments are based on recent LDFT calculations.[215] The $N(CH_3)_4^+$ cation mode assignments are those of Berg[201] and Kabisch[202] and are not further discussed.

The OsO_4F^- anion (C_s point symmetry) possesses 12 fundamental modes of vibration belonging to the irreducible representations 8A′ + 4A″, which are all infrared and Raman active. The room temperature Raman spectrum of $[N(CH_3)_4][OsO_4F]$ consists of seven bands assigned to OsO_4F^- and those attributed to the $N(CH_3)_4^+$ cation, while several anion bands were split at -115 °C resulting in 14 anion bands. Correlation of the

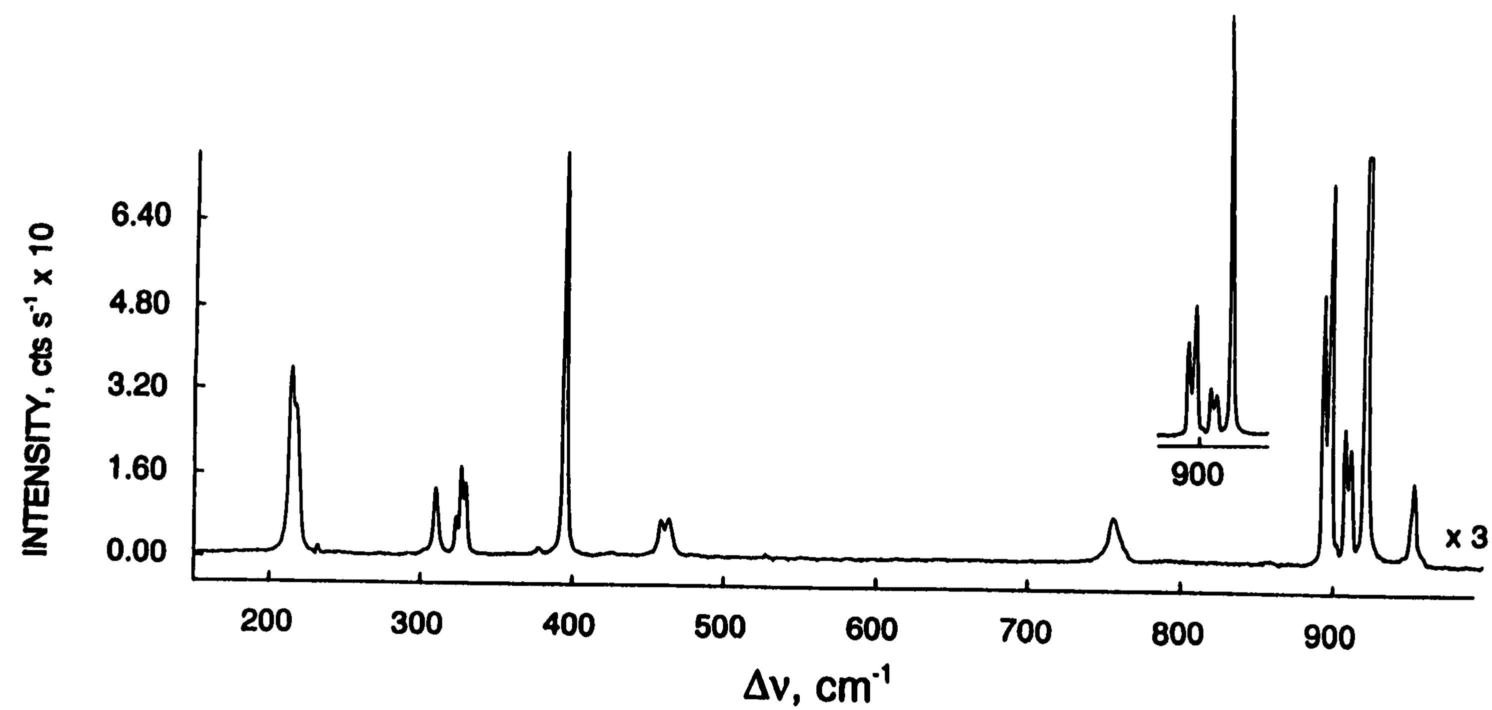

Figure 6.2 Raman spectrum (low-frequency range) of microcrystalline $[N(CH_3)_4][OsO_4F]$ in a Pyrex capillary at -115 °C using 647.1-nm excitation.

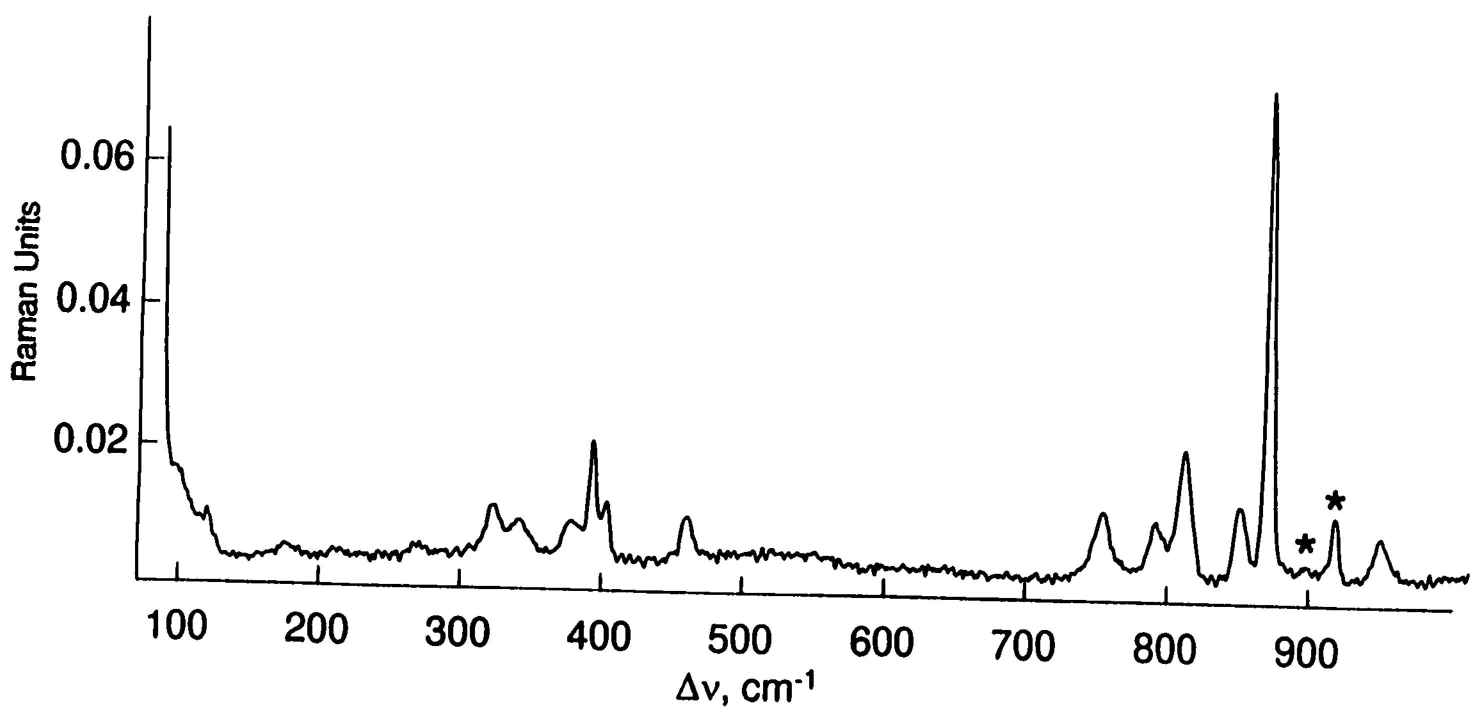

Figure 6.3 Raman spectrum (low-frequency range) of microcrystalline $[N(CH_3)_4]_2[OsO_4F_2]$ in a Pyrex capillary at -164 °C using 1064-nm excitation. Asterisks (*) denote bands arising from the OsO_4F^- anion.

Table 6.3 Experimental Vibrational Frequencies and Their Assignments for $[N(CH_3)_4][OsO_4F]$ and Calculated Vibrational Frequencies for OsO_4F^- (C_{3v})[215]

Frequency[a] [cm^{-1}]				Assignments for OsO_4F^- under C_s [C_{3v}] pt sym
IR[b,c], 25 °C	Raman[d,e], 25 °C	Raman[d,f], -115 °C	Calc.(LDFT)[g]	
956 vs[h]	951 (13)[h]	954 (7)[h]	918 (372)	$\nu_1(A')$ [$\nu_5(E)$], $\nu_{as}(OsO_{3eq})$
922 sh	921 (100)	921 (100)	931 (18)	$\nu_2(A')$ [$\nu_1(A_1)$], $\nu_s(OsO_{3eq} + OsO_{ax})$
910 sh	903 (19)	912 (10) 908 (11) 902 (2)	918 (372)	$\nu_9(A'')$ [$\nu_5(E)$], $\nu_{as}(OsO_{3eq})$
893 vs	893 (40)	898 (32) 893 (23)	893 (167)	$\nu_3(A')$ [$\nu_2(A_1)$], $\nu_s(OsO_{3eq} - OsO_{ax})$
858 w 855 w 723 w 472 w				
427 s			471 (49)	$\nu_4(A')$ [$\nu_3(A_1)$], $\nu(OsF)$
394 m[*]	395 (32)	395 (34)	397 (8)	$\nu_5(A')$ [$\nu_6(E)$], $\delta_{as}(O_{ax}$-Os-$O_{eq})$
340 m[*]			397 (8)	$\nu_{10}(A'')$ [$\nu_6(E)$], $\delta_{as}(O_{ax}$-Os-$O_{eq})$
326 s[*]	327 (7)	330 (6) 327 (7) 324 (3)	338 (68)	$\nu_6(A')$ [$\nu_4(A_1)$], $\delta_{inv}(OsO_{3eq})$
307 s[*]	311 (5)	310 (6)	322 (22)	$\nu_7(A')$ [$\nu_7(E)$], $\delta_{as}(OsO_{2eq} + O_{ax}$-Os-$O_{eq})$

Table 6.3 continued...

Frequency [cm^{-1}][a]				Assignments for OsO_4F^- under C_s [C_{3v}] pt sym
IR[b,c], 25 °C	Raman[d,e], 25 °C	Raman[d,f], -115 °C	Calc.(LDFT)[g]	
231 w*		232 (<0.5)	322 (22)	$\nu_{11}(A'')$ [$\nu_7(E)$], $\delta_{as}(OsO_{2eq} + O_{ax}\text{-}Os\text{-}O_{eq})$
215 m*	215 (14)	217 (13) 214 (16)	183 (9)	$\nu_8(A')$ [$\nu_8(E)$], $\delta_{as}(OsO_{2eq} - O_{ax}\text{-}Os\text{-}O_{eq})$
198 w*			183 (9)	$\nu_{12}(A'')$ [$\nu_8(E)$], $\delta_{as}(OsO_{2eq}\text{-}O_{ax}\text{-}Os\text{-}O_{eq})$
	83 (1)			lattice mode

[a] Abbreviations denote: shoulder (sh), very strong band (vs), strong (s), medium (m), weak (w), very weak (vw). [b] Intensities for far IR are denoted with (*). [c] The $N(CH_3)_4^+$ cation modes were observed in the infrared spectrum at 373 w*, $\nu_8(E)$; 465 s, $\nu_{19}(T_2)$; 956 vs, $\nu_{18}(T_2)$; 1293 w, $\nu_{17}(T_2)$; 1420 m, $\nu_{16}(T_2)$; 1453 w, $\nu_2(A_1)$; 1494 s, $\nu_6(E)$; and 1699 w, 1802 w, 1829 w, 2171 vw, 2367 w, 2490 w, 2528 w, 2589 w, 2818 w, 2865 w, 2926 w, 2963 w, 3032 m, 3337 vw, 3404 vw, 3492 vw cm^{-1}, ν_{CH_3} and binary bands (see ref. (201,202)). [d] Values in parentheses denote relative Raman intensities. [e] The spectrum was recorded on microcrystalline solid in Pyrex glass melting point capillary using the 647.1-nm excitation. The $N(CH_3)_4^+$ cation modes were observed in the Raman spectrum (25 °C) at 462 (6), $\nu_{19}(T_2)$; 756 (10), $\nu_3(A_1)$; 951 (13), $\nu_{18}(T_2)$; 1182 (1), $\nu_7(E)$; 1287 (2), $\nu_{17}(T_2)$; 1416 (5), $\nu_{16}(T_2)$; 1461 (7), $\nu_2(A_1)$; 1475 (9), $\nu_6(E)$; and 2815 (10), 2877 sh, 2893 sh, 2922 (20), 2952 (31), 2982 (16), 3029 (50) cm^{-1}, ν_{CH_3} and binary bands (see ref. (201,202)). [f] The spectrum was recorded on microcrystalline solid in Pyrex glass melting point capillary using the 1064-nm excitation. The $N(CH_3)_4^+$ cation modes were observed in the Raman spectrum (-115 °C) at 379 (1), $\nu_8(E)$; 458 (4), 463 (3), $\nu_{19}(T_2)$; 756 (4), $\nu_3(A_1)$; 954 (7), $\nu_{18}(T_2)$; 1175, 1182, 1188, $\nu_7(E)$; 1290, $\nu_{17}(T_2)$; 1414, $\nu_{16}(T_2)$; 1464, $\nu_2(A_1)$; 1483, $\nu_6(E)$; and 2813, 2963, 3028 cm^{-1}, ν_{CH_3} and binary bands (see ref.(201,202)); relative intensities are not reported for the high frequency bands due to slow decomposition of the sample in the laser beam (647.1-nm line of Kr^+ laser). [g] Infrared intensities, in km mol^{-1}, are given in parentheses. [h] This band overlaps with $\nu_{18}(T_2)$ of $N(CH_3)_4^+$.

Table 6.4 Experimental Vibrational Frequencies and Their Assignments for $[N(CH_3)_4]_2[OsO_4F_2]$ and Calculated Vibrational Frequencies for *cis*-$OsO_4F_2^{2-}$ [215]

Frequency[a] [cm^{-1}]			Assignments for *cis*-$OsO_4F_2^{2-}$ under C_{2v} pt sym[b]
IR,[c] 25 °C	Raman,[d,e] -164 °C	Calc.(LDFT)[f]	
872 s	872 (100)	881 (79)	$\nu_1(A_1)$, $\nu_s(OsO_{2cis} + OsO_{2trans})$
852 vs	852 (15)	854 (256)	$\nu_9(B_1)$, $\nu_{as}(OsO_{2trans})$
813 vs	813 (27)	842 (342)	$\nu_{13}(B_2)$, $\nu_{as}(OsO_{2cis})$
793 s 774 m	792 (12)	833 (121)	$\nu_2(A_1)$, $\nu_s(OsO_{2cis} - OsO_{2trans})$
428 s		415 (50)	$\nu_3(A_1)$, $\nu_s(OsF_2)$
403 s	403 (12)	392 (24)	$\nu_{10}(B_1)$, $\nu_{as}(OsF_2)$
	393 (24)	381 (14)	$\nu_{14}(B_2)$, $\delta_{rock}(OsO_{2trans}$ o.p.) + $\delta_{rock}(OsO_{2cis}$ i.p.)
	378 (8)[g]	380 (0)	$\nu_7(A_2)$, $\delta_{rock}(OsO_{2cis}$ o.p.)
	340 (8)	355 (41)	$\nu_4(A_1)$, $\delta(OsO_{2trans}$ i.p.)
	322 (11)	325 (9)	$\nu_{15}(B_2)$, $\delta_{wag}(OsO_{2trans} + OsF_2$ o.p.)
		301 (88)	$\nu_{11}(B_1)$, $\delta(OsO_{2cis}$ o.p. + O_{trans}-Os-F i.p.)
	268 (3)	292 (40)	$\nu_5(A_1)$, $\delta(OsO_{2cis}$ i.p.+ OsF_2 i.p.)
		239 (0)	$\nu_8(A_2)$, $\delta_{rock}(OsO_{2trans} + OsF_2$ o.p.)
	175 (3)	182 (1)	$\nu_{12}(B_1)$, $\delta(OsO_{2cis}$ o.p. - O_{trans}-Os-F i.p.)
	119 (6)	122 (1)	$\nu_6(A_1)$, $\delta(OsF_2$ i.p. - OsO_{2cis} i.p.)
	97 (3)		

[a] Abbreviations denote: shoulder (sh), very strong band (vs), strong (s), medium (m), weak (w), very weak (vw).

[b] Abbreviations denote: in-plane (i.p.), out-of-plane (o.p.).

[c] The $N(CH_3)_4^+$ cation modes were observed in the infrared spectrum at 465 s, $\nu_{19}(T_2)$; 961 vs, $\nu_{18}(T_2)$; 1061

w, 1084 w, 1187 w, 1255 w, 1266 w, 1300 m, $\nu_{17}(T_2)$; 1378 w, 1426 m, $\nu_{16}(T_2)$; 1452 m, 1459 m, $\nu_2(A_1)$; 1498 vs, $\nu_6(E)$; and 1549 w, 1644 w, 1725 w, 1945 w, 2247 w, 2379 w, 2543 w, 2610 w, 2772 w, 2833 w, 2856 w, 2875 w, 2927 m, 2969 m, 3025 s, 3124 w cm^{-1}, ν_{CH_3} and binary bands (see ref. (201,202)). Bands associated with the OsO_4F^- impurity were observed in the Raman spectrum at 901 s, $\nu_3(A')$ and 921 w, $\nu_2(A')$ cm^{-1}.

[d] Values in parentheses denote relative Raman intensities.

[e] The spectrum was recorded on microcrystalline solid in Pyrex glass melting point capillary using the 1064-nm excitation. The $N(CH_3)_4^+$ cation modes were observed in the Raman spectrum (-164 °C) at 378, $\nu_8(E)$; 460 (9), $\nu_{19}(T_2)$; 755 (15), $\nu_3(A_1)$; 953 (9), $\nu_{18}(T_2)$; 1290 (4), $\nu_{17}(T_2)$; 1470 sh (9), 1478 (17), $\nu_2(A_1)$, $\nu_6(E)$; and 2830 (14), 2898 (14) sh, 2923 (23), 2966 (23), 3017 (41) cm^{-1}, ν_{CH_3} and binary bands (see ref. (201,202)). Bands associated with OsO_4F^- impurity were observed in the Raman spectrum at 893 (3), $\nu_3(A')$ and 920 (14), $\nu_2(A')$ cm^{-1}.

[f] Infrared intensities, in km mol^{-1}, are given in parentheses.

[g] This band overlaps with $\nu_8(E)$ of $N(CH_3)_4^+$.

Table 6.5 Correlation Diagram for the Vibrational Modes of the $N(CH_3)_4^+$ Cation in $[N(CH_3)_4][OsO_4F]$[a]

	Cation Symmetry, T_d	Site Symmetry, C_2	Crystal Symmetry, C_{2v}[b]	

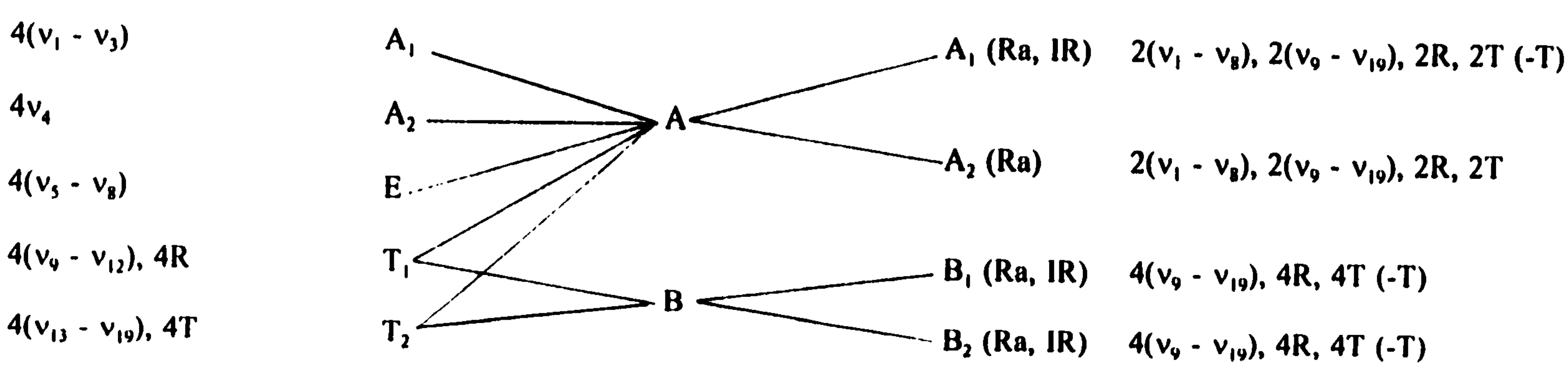

[a] The symbols T and R denote translatory and rotatory (external) modes, respectively, and Ra and IR in parentheses denote Raman and infrared activity, respectively.

[b] Space group *Abm2*, Z = 4.

free anion symmetry of OsO_4F^- (C_s) to the anion site symmetry (C_s) and the unit cell symmetry (C_{2v}, space group *Abm2*) predicts that the A′ modes of the free anion are each split into A_1 and B_1 components in the Raman and infrared spectra (Table 6.5). The A″ modes are expected to split into A_2 and B_2 components in the Raman spectrum while they are not split in the infrared spectrum. Correlation of the free cation symmetry of $N(CH_3)_4^+$ (T_d) to the cation site symmetry (C_2) and the unit cell symmetry (C_{2v}) predicts that all bands (ν_1 - ν_{19}) are Raman and infrared active (Table 6.6). In the Raman spectrum, ν_1 -ν_8 and ν_9 - ν_{19} are expected to be factor-group split into A_1 and A_2 and into A_1, A_2, B_1, and B_2 components, respectively. In the infrared spectrum, ν_1 - ν_8 are not expected to be split while ν_9 - ν_{19} are expected to split into A_1, B_1, and B_2 components. Only the cation bands, ν_7(E) and $\nu_{19}(T_2)$, were split into three and two components, respectively, in the low-temperature Raman spectrum. No formally inactive bands of the free cation were visible as a result of activity under the factor-group.

Three bands in the room-temperature Raman spectrum at 921, 903, and 893 cm^{-1} were assigned to the Os-O stretching modes, ν_2(A′), ν_3(A′), ν_9(A″), respectively. The fourth stretching mode, ν_1(A′), is presumably hidden under the cation band at 951 cm^{-1}. The Os-O stretches of the adducts OsO_4·1,8-naphthyridine,[56] OsO_4·*N*-methylmorpholine *N*-oxide,[61] and OsO_4·*N*-methylmorpholine[61] were found near 950 cm^{-1} and do not exhibit a strong dependence on the nature of the donor molecule presumably as a result of the rigidity of the OsO_4 moiety. The strongest Raman band at 921 cm^{-1} corresponds to the totally symmetric stretching mode ν_2(A′) while the bands at 954 and 912 cm^{-1} can be assigned to the asymmetric stretching modes ν_1(A′) and ν_3(A′), respectively. The band

Table 6.6 Correlation Diagram for the Vibrational Modes of the OsO_4F^- Anion in $[N(CH_3)_4][OsO_4F]$[a]

	Anion Symmetry, C_s	Site Symmetry, C_s	Crystal Symmetry, C_{2v}[b]	
$4(\nu_1 - \nu_8)$, 8T, 4R	A′	A′	A_1 (Ra, IR)	$2(\nu_1 - \nu_8)$, 2R, 4T (-T)
			A_2 (Ra)	$2(\nu_9 - \nu_{12})$, 4R, 2T
$4(\nu_9 - \nu_{12})$, 4T, 8R	A″	A″	B_1 (Ra, IR)	$2(\nu_1 - \nu_8)$, 2R, 4T (-T)
			B_2 (Ra, IR)	$2(\nu_9 - \nu_{12})$, 4R, 2T (-T)

(Correlation lines: A′ (site) → A_1, B_1; A″ (site) → A_2, B_2.)

[a] The symbols T and R denote translatory and rotatory (external) modes, respectively, and Ra and IR in parentheses denote Raman and infrared activity, respectively.

[b] Space group *Abm2*, Z = 4.

at 893 cm^{-1}, with its intense infrared counterpart, is assigned to the asymmetric stretching mode $\nu_9(A'')$ which mainly involves motion of the equatorial oxygen atoms O(3) and O(3A). The bands at 912 and 893 cm^{-1} are factor-group split in the low-temperature Raman spectrum into A_1 and B_1 and into A_2 and B_2 components, respectively. As expected, the Os-O bonds of the OsO_4F^- anion are more polar and the stretching bands are shifted to lower frequencies relative to those of OsO_4,[48] *i.e.*, the totally symmetric stretch is shifted from 965.2 cm^{-1} ($\nu_1(A_1)$ in OsO_4) to 921 cm^{-1} ($\nu_2(A')$ in OsO_4F^-), while the degeneracy of the asymmetric stretch of OsO_4, $\nu_3(T_2)$, at 960.1 cm^{-1} is removed and the frequencies are shifted to 951, 903, and 893 cm^{-1} in the OsO_4F^- anion. No Os-F stretch was observed in the Raman spectrum of OsO_4F^-, which is in agreement with the apparent absence of Os-X stretches reported for the Raman spectra of other OsO_4· Lewis base adducts in the literature. The Raman intensity of Os-X stretches is expected to be low because of the rather ionic character of the Os-X dative bond. However, the strong band at 427 cm^{-1} assigned to the Os-F stretching mode, $\nu_4(A')$, can be observed in the infrared spectrum. This frequency is also in accord with the assigned Os-OH stretching frequencies in OsO_4OH^- and $(OsO_4)_2OH^-$ which range from 485 to 490 cm^{-1}.[71] The vibrational bands below 400 cm^{-1} correspond to bending modes and their assignments are based on density functional theory calculations.

Two geometries are possible for the $OsO_4F_2^{2-}$ anion, the *cis*- and the *trans*-arrangements. A total of 15 vibrational modes spanning the irreducible representations $6A_1 + 2A_2 + 4B_1 + 3B_2$ under C_{2v} point symmetry (the plane of *cis*-OsF_2 is taken as the xz-plane) are expected for the *cis*-isomer with all modes Raman active and A_1, B_1, and

B_2 infrared active, while 11 vibrational bands belonging to the symmetry species $2A_{1g}$ + $2A_{2u}$ + B_{1g} + B_{2g} + B_{2u} + E_g + $3E_u$ are expected for *trans*-$OsO_4F_2^{2-}$ under D_{4h} symmetry with A_{1g}, B_{1g}, B_{2g}, and E_g Raman active and A_{2u} and E_u infrared active. This results in four (Raman and infrared active) and three Os-O (mutually exclusive infrared (E_u) and Raman active (A_{1g}, B_{2g})) stretching bands for *cis*- and *trans*-$OsO_4F_2^{2-}$, respectively. The Raman and infrared spectra of $[N(CH_3)_4]_2[OsO_4F_2]$ show four vibrational bands at 872, 852, 813, and 792 cm^{-1} which are attributed to Os-O stretches and are indicative of the *cis*-arrangement, which was found to be the stable arrangement based on density functional theory calculations.[215] The preference of the *cis*-isomer over the *trans*-isomer for pseudo-octahedral d^0 transition metal oxide fluoride has previously been shown for other dioxo species, *e.g.*, *cis*-OsO_2F_4,[6] *cis*-$TcO_2F_4^-$,[92] and *cis*-$ReO_2F_4^-$.[94] The Os-O stretching frequencies of *cis*-$OsO_4F_2^{2-}$, reported in the present work occur in the range found for the well characterized $OsO_4(OH)_2^{2-}$ anion[64,65,70,71] and agree well with those obtained from LDFT calculations. As in the case of the OsO_4F^- anion, no Os-F stretching bands were observed in the Raman spectrum. In the infrared spectrum, however, bands at 428 and 403 cm^{-1} were assigned to the symmetric and asymmetric Os-F stretch which are only 13 and 11 cm^{-1} higher than the calculated frequencies, respectively. The vibrational bands below 400 cm^{-1} were tentatively assigned to bending modes based on LDFT calculations.

The vibrational frequencies obtained for *cis*-$OsO_4F_2^{2-}$ in the present work are in total disagreement with the vibrational frequencies previously reported and assigned to this anion.[65,72] Rather, the previously reported frequencies are shown to belong to the

OsO_4F^- anion, and the EXAFS data attributed to the $OsO_4F_2^{2-}$ [74] must now be ascribed to the OsO_4F^- anion (see 6.2.3. X-ray Crystal Structure of $[N(CH_3)_4][OsO_4F]$).

6.3. Conclusion

The X-ray crystal structure of $[N(CH_3)_4][OsO_4F]$ extends the number of structurally well characterized Lewis acid-base adducts of OsO_4. The OsO_4F^- anion exhibits an unprecedented distortion from trigonal bipyramidal VSEPR geometry[120] with an O_{ax}-Os-F angle of 156.9(4)° instead of the expected 180° that is observed in the related OsO_4· Lewis base adducts. The vibrational frequencies assigned to $[N(CH_3)_4]_2[OsO_4F_2]$ are consistent with the *cis*-arrangement for the $OsO_4F_2^{2-}$ anion, however, they are in complete disagreement with those previously reported for the *cis*-$OsO_4F_2^{2-}$ anion,[65,72] proving the presence of the OsO_4F^- anion in the previously reported Lewis acid-base adducts of OsO_4 with fluoride ion.

CHAPTER 7

LEWIS-ACID PROPERTIES OF OsO_3F_2

7.1. Introduction

The Lewis acidity of OsO_3F_2 has been demonstrated by the synthesis of the $OsO_3F_3^-$ anion as the Na^+, K^+, Cs^+, Rb^+, and Ag^+ salts.[72,85] The K^+, Cs^+, and Ag^+ salts are formed by reaction of OsO_4 with BrF_3 and KBr, CsBr, and [Ag][IO_3], respectively, in excess BrF_3 at room temperature[85] and the Cs^+, Rb^+, K^+, and Na^+ salts by reaction of OsO_3F_2 with the corresponding alkali metal fluorides.[72] The facial geometry was suggested for the $OsO_3F_3^-$ anion based on the vibrational spectra of the Cs^+, K^+, Rb^+, and Na^+ salts[65,72,88]. Bond lengths for the $OsO_3F_3^-$ anion in [K][OsO_3F_3] have been estimated from EXAFS spectroscopy.[74] Other than the $OsO_3F_3^-$ anion, no other Lewis acid-base adducts of OsO_3F_2 have been reported. The facial arrangement is most frequently encountered for trioxo transition metal species, *e.g.*, *fac*-$ReO_3Cl_3^{2-}$,[116] *fac*-$WO_3F_3^{3-}$,[117] and has been explained in terms of the *trans*-influence of the doubly bonded oxygen ligand (see 1.5. The *Trans*-Influence). The vibrational spectra of the $ReO_3F_3^{2-}$,[216] $MoO_3F_3^{3-}$,[217] and $WO_3F_3^{3-}$ [217] anions, however, have been assigned in terms of the *mer*-isomer.

The present study provides the first detailed structural study of the *fac*-$OsO_3F_3^-$ anion in the solid state and in solution by single crystal X-ray diffraction, vibrational and

NMR spectroscopy. The first nitrogen base adduct of OsO_3F_2, $OsO_3F_2(CH_3CN)$ has been characterized by NMR and Raman spectroscopy.

7.2. Results and Discussion

7.2.1. Fuoride Ion Acceptor Properties of OsO_3F_2

7.2.1.1. Syntheses of the $[N(CH_3)_4][OsO_3F_3]$ and $[NO][OsO_3F_3]$. Osmium trioxide difluoride reacts with excess NOF over a period of *ca.* 90 min according to eq. (7.1) to

$$NOF + OsO_3F_2 \xrightarrow{\text{NOF, -78 to -60 °C}} [NO][OsO_3F_3] \quad (7.1)$$

give light orange to ochre colored $[NO][OsO_3F_3]$ at temperatures between -78 and -60 °C. The $[NO][OsO_3F_3]$ salt was insoluble in liquid NOF up to its boiling point (-56 °C) and is unstable at ambient temperature. The compound, $[N(CH_3)_4][OsO_3F_3]$, was obtained as a solid orange product by the reaction of stoichiometric amounts of $[N(CH_3)_4][F]$ and OsO_3F_2 in HF solution followed by removal of HF under dynamic vacuum (eq. (7.2)).

$$[N(CH_3)_4][F] + OsO_3F_2 \xrightarrow{\text{HF, RT}} [N(CH_3)_4][OsO_3F_3] \quad (7.2)$$

Although OsO_3F_2 is insoluble in anhydrous HF, it rapidly dissolves in the presence of $[N(CH_3)_4][F]$ to give a pale orange solution of $[N(CH_3)_4][OsO_3F_3]$ at room temperature which has a high solubility in HF even at -78 °C. The salt is moderately soluble in

CH_3CN at room temperature.

7.2.1.2 Attempted Synthesis of $[N(CH_3)_4]_2[OsO_3F_4]$. The reaction of OsO_3F_2 and $[N(CH_3)_4][F]$ in a 1:2 ratio in CH_3CN solvent yielded a brown solid, which exhibited no significant solubility in CH_3CN, presumably according to eq. (7.3). Solvent removal gave

$$2[N(CH_3)_4][F] + OsO_3F_2 \xrightarrow{CH_3CN,\ -40\ °C} [N(CH_3)_4]_2[OsO_3F_4] \qquad (7.3)$$

rise to a grey solid product, which was unstable at room temperature. The presence of $[N(CH_3)_4]_2[OsO_3F_4]$ could not be verified, since the grey solid product decomposed readily in the beam of the YAG laser (1064 nm) and no Raman band could be detected even at -160 °C using laser powers as low as 50 mW.

7.2.1.3. NMR Spectroscopic Characterization of the $OsO_3F_3^-$ Anion. The ^{19}F NMR spectrum of $[N(CH_3)_4][OsO_3F_3]$ in CH_3CN solvent at -20 °C consists of a singlet at -116.8 ppm ($\Delta\nu_{½}$ = 23 Hz) with ^{187}Os (I = ½, 1.64% natural abundance) satellites which is assigned to the $OsO_3F_3^-$ anion. The magnitude of the coupling ($^1J(^{187}Os-^{19}F)$ = 32 Hz) is consistent with those found in *cis*-OsO_2F_4 (35.1 and 59.4 Hz for coupling with the fluorines *trans* and *cis* to the oxygens).[6] A broad, weak singlet at -170.0 ppm ($\Delta\nu_{½}$ = 125 Hz) indicates the presence of small amounts of HF_2^- exchanging with HF that was not completely removed during the preparation of $[N(CH_3)_4][OsO_3F_3]$. In addition to the HF solvent signal at -194.1 ppm (singlet, $\Delta\nu_{½}$ = 10 Hz), the ^{19}F NMR spectrum of $[N(CH_3)_4][OsO_3F_3]$ in HF solvent at -80 °C shows a broad singlet at -164.0 ppm ($\Delta\nu_{½}$ = 270 Hz) corresponding to the $OsO_3F_3^-$ anion undergoing slow chemical exchange with HF solvent.

7.2.1.4. X-ray Crystal Structure of $[N(CH_3)_4][OsO_3F_3]$. Details of the data collection parameters and other crystallographic information for $[N(CH_3)_4][OsO_3F_3]$ are given in Table 7.1. Important bond lengths and angles for $[N(CH_3)_4][OsO_3F_3]$ are listed in Table 7.2.

The $N(CH_3)_4^+$ cations pack in an approximate cubic primitive array with the $OsO_3F_3^-$ anions occupying all cubic sites (distorted CsCl structure) (Figure 7.1). The anions and cations in the crystal structure are well separated and exhibit only weak contacts between the oxygen and the methyl groups (O---H_3C: 306(2) to 336(2) pm) and between the fluorines and the methyl groups (F---H_3C: 321(2) to 335(2) pm).

The nitrogen of the $N(CH_3)_4^+$ cation is located on a special position (*2*) and has an arrangement of carbon atoms that is tetrahedral within experimental error. The bond lengths in both independent cations are the same within experimental error and have the expected values. The environment around the osmium atom is hexacoordinate with Os-O bond lengths (170(1) to 173(1) pm) significantly shorter than the Os-F bond lengths (191(1) to 197(1) pm). The oxygen and fluorine atoms exhibit a facial arrangement about Os with O-Os-O bond angles that are considerably larger than 90°, *i.e.*, 102.8(8) to 101.2(7)°, and F-Os-F bond angles that are considerably smaller than 90°, *i.e.*, 79.9(4) to

Table 7.1 Summary of Crystal Data and Refinement Results for $[N(CH_3)_4][OsO_3F_3]$

	$[N(CH_3)_4][OsO_3F_3]$
formula	$C_4H_{12}F_3NO_3Os$
space group	*C2/c* (No. 15)
a [pm]	1634.7(4)
b [pm]	1347.5(3)
c [pm]	1143.6(3)
α [deg]	90
β [deg]	134.128(4)
γ [deg]	90
V [10^6 pm^3]	1808.1(7)
Z [molecules/unit cell]	8
mol. wt	369.35
calcd density [g cm^{-3}]	2.714
colour, morphology	orange plates
size [mm^3]	0.30×0.15×0.01
μ [mm^{-1}]	14.125
data/restraints/parameters	1727/0/111
final agreement factors	R^a = 0.0614
	$R_w{}^b$ = 0.1508
GOOF	1.005
Extinction coefficient	0.00043(12)
$\Delta\delta_{max}/\Delta\delta_{min}$ [e 10^{-6} pm^{-3}]	3.681/-3.919

[a] $R = \Sigma||F_o| - |F_c||/\Sigma|F_o|$.

[b] $R_w = \Sigma|(|F_o| - |F_c|)w^{1/2}|/\Sigma(|F_o|w)$ where $w = 1/[\sigma^2(F) + (0.0344)^2 + 4.94]$.

Table 7.2 Experimental Bond Lengths, Contacts and Bond Angles in $[N(CH_3)_4][OsO_3F_3]$

$[N(CH_3)_4][OsO_3F_3]$			
Bond Lengths and Contacts [pm]			
Os(1)-F(1)	197(1)	Os(1)-F(2)	191(1)
Os(1)-F(3)	194(1)	Os(1)-O(1)	170(1)
Os(1)-O(2)	172(1)	Os(1)-O(3)	173(1)
N(1)-C(1)	151(2)	N(1)-C(2)	148(2)
N(2)-C(3)	150(2)	N(2)-C(4)	149(2)
Bond Angles [deg.]			
F(1)-Os(1)-F(2)	80.4(5)	F(1)-Os(1)-F(3)	79.9(4)
F(2)-Os(1)-F(3)	80.4(5)	O(1)-Os(1)-O(2)	102.8(8)
O(1)-Os(1)-O(3)	101.3(7)	O(2)-Os(1)-O(3)	101.2(7)
F(1)-Os(1)-O(1)	87.4(6)	F(1)-Os(1)-O(2)	87.2(6)
F(2)-Os(1)-O(1)	87.8(7)	F(2)-Os(1)-O(3)	89.0(5)
F(3)-Os(1)-O(2)	86.5(6)	F(2)-Os(1)-O(3)	89.4(5)
C(1)-N(1)-C(1A)	109(2)	C(1)-N(1)-C(2)	110(1)
C(2)-N(1)-C(2A)	111(2)	C(3)-N(2)-C(3A)	110(2)
C(3)-N(2)-C(4)	110(1)	C(4)-N(2)-C(4A)	108(2)

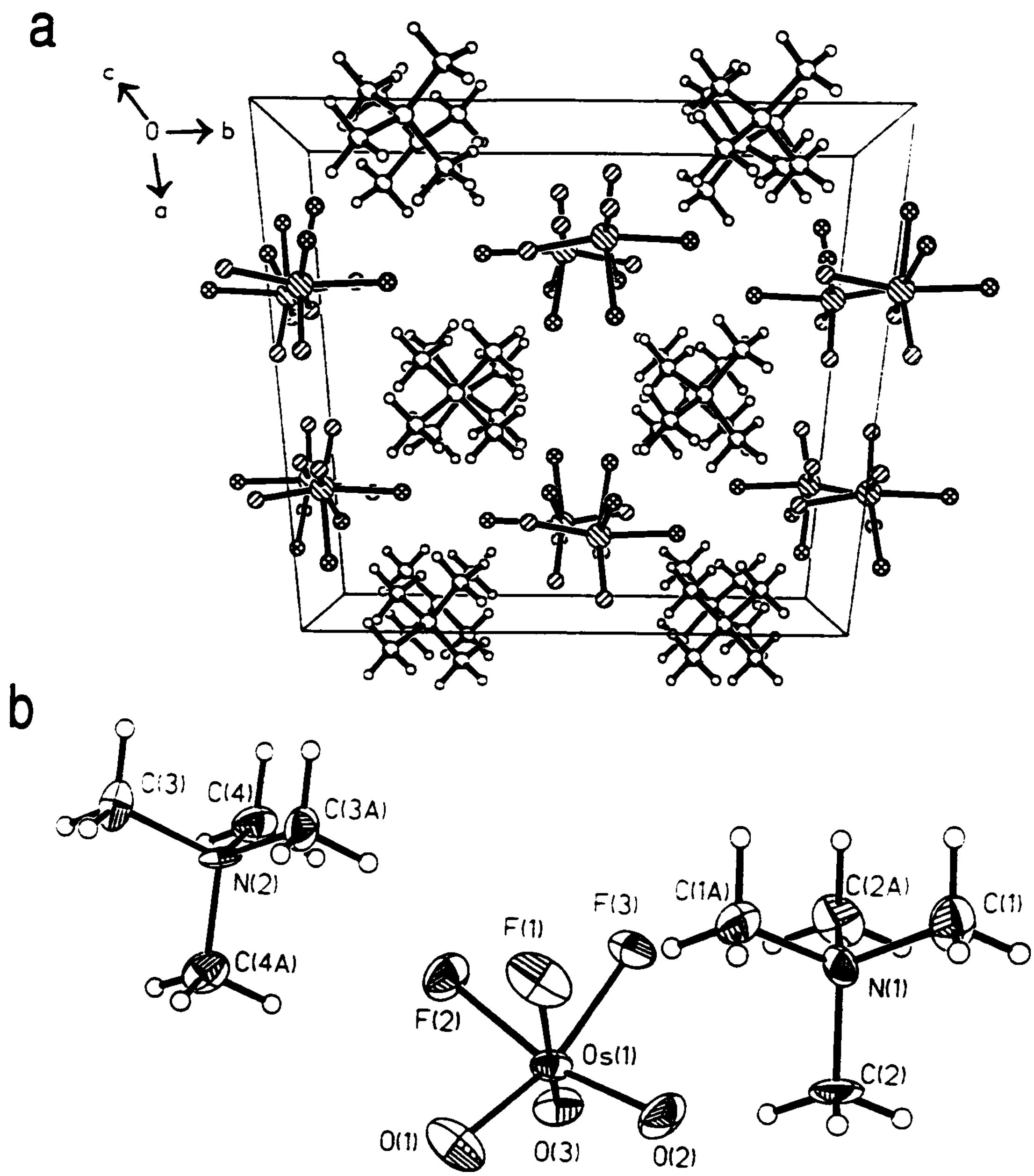

Figure 7.1 Views of (a) the $[N(CH_3)_4][OsO_3F_3]$ unit cell showing the packing along the *c*-axis and (b) the *fac*-$OsO_3F_3^-$ anion and the two crystallographically independent $N(CH_3)_4^+$ cations (thermal ellipsoids are shown at the 50% probability level).

80.4(5)° (Figure 7.1). This is in agreement with the greater repulsion of the Os=O double bond domains when compared to the Os-F single bond domains. The Os-O and Os-F bond lengths in $[N(CH_3)_4][OsO_3F_3]$ agree well with those determined by EXAFS $[K][OsO_3F_3]$, *i.e.*, 169.8(2) and 191.9(15) pm, respectively.[74] The Os-O bond lengths in $[N(CH_3)_4][OsO_3F_3]$ are larger compared to those of the neutral parent compound, $(OsO_3F_2)_\infty$, which has a polymeric fluorine-bridged chain structure in the solid state, with Os-O bond lengths of 172.7(1), 168.8(1), and 167.8(1) pm.[7] The terminal Os-F bond length of 187.9(1) pm in $(OsO_3F_2)_\infty$[7] is shorter than those in $[N(CH_3)_4][OsO_3F_3]$, which is in accord with the greater polarities of the Os-O and Os-F bonds in the anion.

The *fac*-isomer of $OsO_3F_3^-$ is expected to be more stable than the *mer*-isomer because each filled p orbital on an oxygen competes for the three available empty $d_{t_{2g}}$ orbitals on the osmium. An alternative view involves charge concentrations in the outer electron core of osmium located opposite to the doubly bonded oxygens.[119] Additional doubly bonded oxygens avoid the positions of these charge concentrations, disfavouring the *trans*-dioxo and *mer*-trioxo arrangements. Similar arguments have been advanced to account for *cis*-dioxo arrangements (see 6.2.4. Raman and Infrared Spectroscopic Characterization of $[N(CH_3)_4][OsO_4F]$ and $[N(CH_3)_4]_2[OsO_4F_2]$). The preference for the facial arrangement in MO_3F_3 (M = transition metal having a d^0 configuration) moieties has also been demonstrated by the X-ray crystal structures of $[Li]_2[Ta_2O_3F_6]$,[218] $(OsO_3F_2)_\infty$,[7] $[Ba]_4[Mo_2O_5F_7][HF_2]_3{\cdot}H_2O$,[219] and $Pb_5W_3O_9F_{10}$.[117]

7.2.1.5. Raman and Infrared Spectroscopy of $[N(CH_3)_4][OsO_3F_3]$ and $[NO][OsO_3F_3]$. The $[N(CH_3)_4][OsO_3F_3]$ and $[NO][OsO_3F_3]$ salts were characterized by low-temperature Raman spectroscopy and, in the case of $[N(CH_3)_4][OsO_3F_3]$, by room-temperature infrared spectroscopy. The Raman spectra are shown in Figures 7.2a and 7.2b, and the assignments made using frequencies calculated from LDFT[215] and are listed in Table 7.3.

Assignments are based on the *fac*-$OsO_3F_3^-$ anion (C_{3v} point symmetry). The 15 vibrational modes have the symmetries $4A_1 + A_2 + 5E$ with A_1 and E vibrations being Raman and infrared active and the A_2 vibration being inactive. The present assignments for $OsO_3F_3^-$ are in agreement with those previously reported by Griffith,[65] Jezowska-Trzebiatowska *et al.*,[88] and Levason *et al.*,[72] except for $\nu_s(OsO_3)$ which is assigned to bands at 920 ($N(CH_3)_4^+$) and 934 (NO^+) cm^{-1} in the present work. This mode was assigned to an infrared band at 950 cm^{-1} by Griffith[65] and Jezowska-Trzebiatowska,[88] but was not observed in the present work and was suspected by Levason *et al.*[72] to arise from the hydrolysis product, OsO_4. All vibrational modes with E symmetry but one (ν_8) are split in two components in the low-temperature Raman spectrum of $[N(CH_3)_4][OsO_3F_3]$. Correlation of the free anion symmetry of $OsO_3F_3^-$ (C_{3v}) to the anion site symmetry (C_1) and the unit cell symmetry (C_{2h}) (space group *C2/c*) predicts that all the vibrational bands are Raman and infrared active and are split into A_g and B_g components and into A_u and B_u components in the Raman and infrared spectrum, respectively (Table 7.4). Correlation of the free cation symmetry of $N(CH_3)_4^+$ (T_d) to the cation site symmetry (C_2) and the unit cell symmetry (C_{2h}) predicts that all bands are Raman and infrared active (Table 7.5). In the Raman and infrared spectra, ν_1 - ν_8 are not expected to show factor-group splitting,

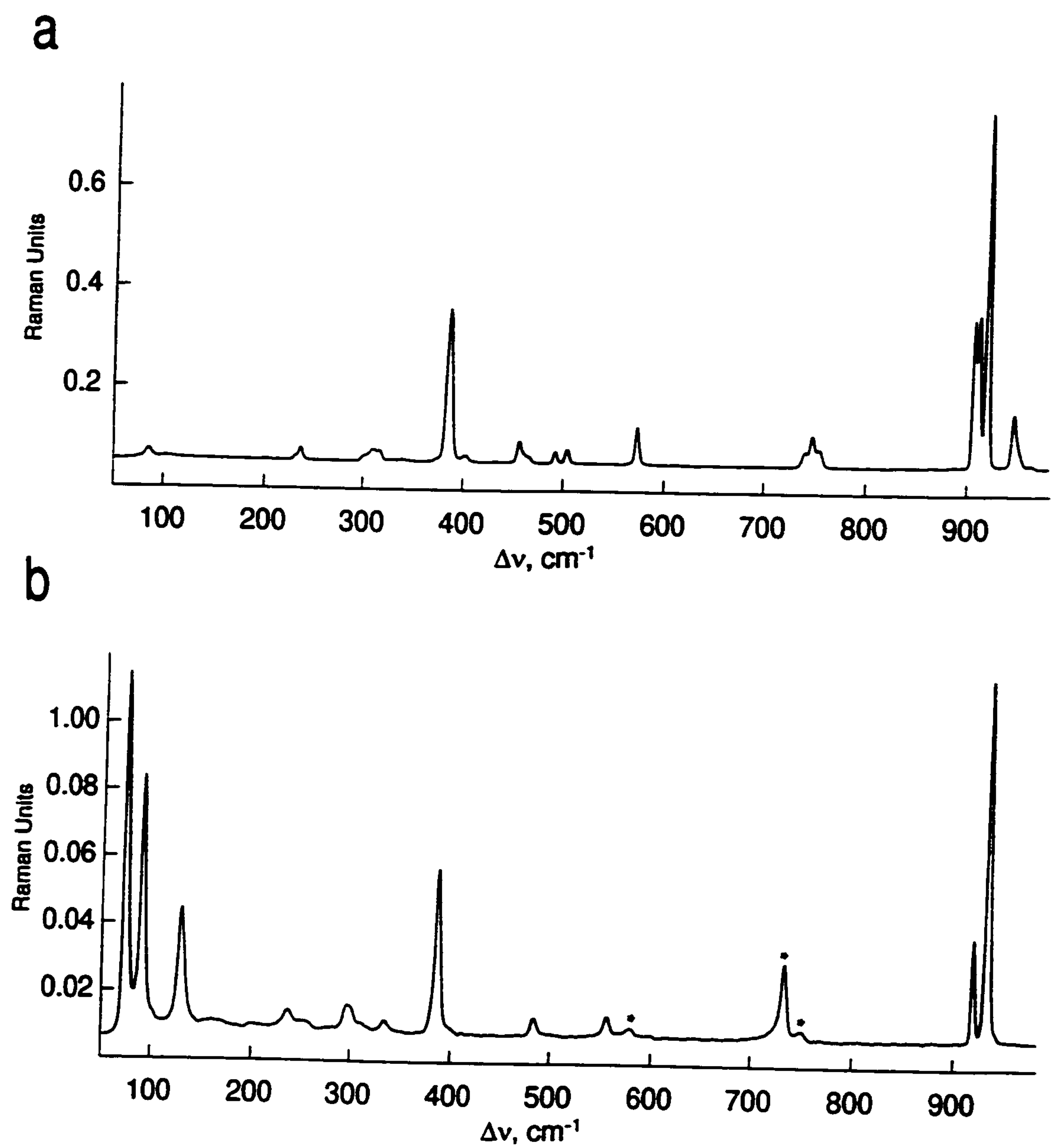

Figure 7.2 (a) Raman spectrum (low-frequency range) of microcrystalline $[N(CH_3)_4][OsO_3F_3]$ recorded in a Pyrex glass capillary at -160 °C using 1064-nm excitation; (b) Raman spectrum (low-frequency range) of microcrystalline $[NO][OsO_3F_3]$ recorded in a 4-mm FEP tube at -160 °C using 1064-nm excitation. Asterisks (*) denote FEP sample tube lines.

Table 7.3 Experimental Vibrational Frequencies and Their Assignments for $[N(CH_3)_4][OsO_3F_3]$ and $[NO][OsO_3F_3]$ and Calculated Vibrational Frequencies for *fac*-$OsO_3F_3^-$ [215]

Frequency[a] [cm^{-1}]				Assignment (C_{3v})
$[N(CH_3)_4][OsO_3F_3]$		$[NO][OsO_3F_3]$		
IR[b]	Raman[c,d]	Raman[c,e]	Calc.(LDFT)[f]	*fac*-$OsO_3F_3^-$
25 °C	-160 °C	-160 °C		
920 m	920 (100)	934 (100)	941 (76)	$\nu_1(A_1)$, $\nu_s(OsO_3)$
909 vs	912 (43) 908 (42)	920 (29)	930 (350)	$\nu_6(E)$, $\nu_{as}(OsO_3)$
609 w				
567 s	573 (11)	555 (6)	599 (128)	$\nu_2(A_1)$, $\nu_s(OsF_3)$
506 s 494 s	504 (4) 493 (3)	483 (5)	526 (115)	$\nu_7(E)$, $\nu_{as}(OsF_3)$
	402 (2) 385 (43)	386 (45)[g]	374 (8) 371 (8)	$\nu_8(E)$, $\delta_{as}(OsO_3)$ $\nu_3(A_1)$, $\delta_s(OsO_3)$
	339 (<0.5) 328 (<0.5)	332 (4)	323 (55)	$\nu_9(E)$, $\delta_{as}(OsF_3)$ + δ_{as}(F-Os-O)
	316 (3) 310 (3) 301 (2)	307 (2) 295 (7)[g]	321 (16)	$\nu_4(A_1)$, $\delta_s(OsF_3)$
	235 (3) 230 (1)	249 (2) 234 (5)	233 (3)	$\nu_{10}(E)$, $\delta_{as}(OsF_3)$-δ_{as}(F-Os-O)
			190 (0)	$\nu_5(A_2)$, $\tau(OsF_3)$ wrt OsO_3
	102 (<0.5) 84 (2)	128 (32) 89 (69) 72 (100)		lattice modes

[a] Symbols denote: shoulder (sh), very strong band (vs), strong (s), medium (m), weak (w), very weak (vw).

[b] The $N(CH_3)_4^+$ cation modes were observed in the infrared spectrum at 464 w, $\nu_{19}(T_2)$; 953 m, $\nu_{18}(T_2)$;

Table 7.3 continued...

1291 w, $\nu_{17}(T_2)$; 1381 vw, 1421 w, $\nu_{16}(T_2)$; 1453 w, 1461 m, $\nu_2(A_1)$, 1492 w, $\nu_6(E)$; and 1828 w, 2365 vw, 2856 m, 2926 m, 2957 m, 3041 m cm^{-1}, ν_{CH_3} and binary bands (see ref.(201,202)).

[c] Values in parentheses denote relative Raman intensities.

[d] Spectrum recorded on microcrystalline solid in a Pyrex glass melting point capillary using the 1064-nm excitation. The $N(CH_3)_4^+$ cation modes were observed in the Raman spectrum (-160 °C) at 457 (6), 467 (2), $\nu_{19}(T_2)$; 742 (2), 749 (9), 756 (5), $\nu_3(A_1)$; 948 (15), 965 (1), $\nu_{18}(T_2)$; 1175 (2), 1181 (2), $\nu_1(E)$; 1290 (2), $\nu_{17}(T_2)$; 1410 sh, 1414 (2), $\nu_{16}(T_2)$; 1445 (<0.5), 1460 (7), $\nu_2(A_1)$; 1472 (9), $\nu_6(E)$; and 1501 (1), 2808 (4), 2816 (4), 2868 (1), 2876 (1), 2889 (3), 2908 (4), 2913 (4), 2922 (7), 2931 (5), 2962 (18), 2979 (6), 2986 (6), 2997 (5), 3002 (5), 3024 (9), 3035 (27), 3046 (10) cm^{-1}, ν_{CH_3} and binary bands (see ref. (201,202)).

[e] Spectrum recorded on microcrystalline solid in a 4-mm FEP sample tube using the 1064-nm excitation. The NO^+ cation mode was observed in the Raman spectrum (-160 °C) at 2319 (37) cm^{-1}, $\nu(NO)$; Bands arising from the FEP sample tube were observed at 295 (7), 386 (45), 578 (3), 733 (21), and 750 (3) cm^{-1}.

[f] Infrared intensities, in km mol^{-1}, are given in parentheses.

[g] This band overlaps with a band arising from the FEP sample tube.

Table 7.4 Correlation Diagram for the Vibrational Modes of the $OsO_3F_3^-$ Anion in $[N(CH_3)_4][OsO_3F_3]$[a]

	Anion Symmetry, C_{3v}	Site Symmetry, C_1	Crystal Symmetry, C_{2h}[b]	
$8(\nu_1 - \nu_4)$, 8T	A_1	A	A_g (Ra)	$2(\nu_1 - \nu_5)$, $4(\nu_6 - \nu_{11})$, 6R, 6T
			B_g (Ra)	$2(\nu_1 - \nu_5)$, $4(\nu_6 - \nu_{11})$, 6R, 6T
$8\nu_5$, 8R	A_2		A_u (IR)	$2(\nu_1 - \nu_5)$, $4(\nu_6 - \nu_{11})$, 6R, 6T (-T)
$8(\nu_6 - \nu_{11})$, 8R, 8T	E		B_u (IR)	$2(\nu_1 - \nu_5)$, $4(\nu_6 - \nu_{11})$, 6R, 6T (-2T)

[a] The symbols T and R denote translatory and rotatory (external) modes, respectively, and Ra and IR in parentheses denote Raman and infrared activity, respectively.

[b] Space group *C2/c*, Z = 8.

Table 7.5 Correlation Diagram for the Vibrational Modes of the $N(CH_3)_4^+$ Cation in $[N(CH_3)_4][OsO_3F_3]$[a]

	Cation Symmetry, T_d	Site Symmetry, C_2	Crystal Symmetry, C_{2h}[b]	
$4(\nu_1 - \nu_3)$	A_1		A_g (Ra)	$2(\nu_1 - \nu_8)$, $2(\nu_9 - \nu_{19})$, 2R, 2T
$4\nu_4$	A_2	A	B_g (Ra)	$4(\nu_9 - \nu_{19})$, 4R, 4T
$4(\nu_5 - \nu_8)$	E			
$4(\nu_9 - \nu_{12})$, 4R	T_1		A_u (IR)	$2(\nu_1 - \nu_8)$, $2(\nu_9 - \nu_{19})$, 2R, 2T (-T)
$4(\nu_{13} - \nu_{19})$, 4T	T_2	B	B_u (IR)	$4(\nu_9 - \nu_{19})$, 4R, 4T (-2T)

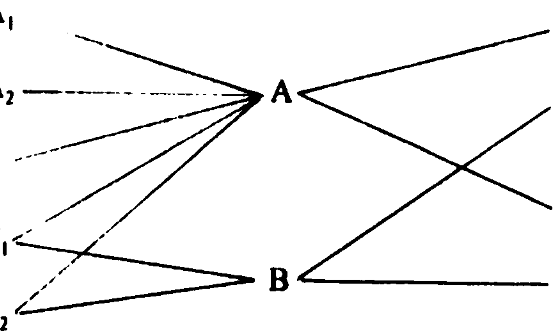

[a] The symbols T and R denote translatory and rotatory (external) modes, respectively, and Ra and IR in parentheses denote Raman and infrared activity, respectively.

[b] Space group $C2/c$, Z = 8.

while ν_9 - ν_{19} are expected to be factor-group split into A_g and B_g components and into A_u and B_u components in the Raman and infrared spectrum, respectively. Splittings were observed for the $N(CH_3)_4^+$ cation modes ν_{16}, ν_{18}, and ν_{19} in the low- temperature Raman spectrum. Fewer bands are split in the low-temperature Raman spectrum of $[NO][OsO_3F_3]$ and may result from a higher site symmetry for the $OsO_3F_3^-$ anion in the crystal lattice of $[NO][OsO_3F_3]$ salt. While the Os-O stretches appear at lower frequencies in the Raman spectrum of $[N(CH_3)_4][OsO_3F_3]$ than in that of $[NO][OsO_3F_3]$, the opposite trend is observed for the Os-F stretches. This suggests stronger cation---F contacts in the structure of $[NO][OsO_3F_3]$ and is supported by the splitting of the Raman bands associated with fluorine ligand motions.

The Os-O stretches in $OsO_3F_3^-$ anion appear at considerably lower frequencies when compared to those of its neutral parent compound $(OsO_3F_2)_\infty$[7] and is corroborated by longer, more polar Os-O bonds in the anion (see 7.2.1.4. X-ray Crystal Structure of $[N(CH_3)_4][OsO_3F_3]$).

7.2.2. Lewis Acid Behaviour of OsO_3F_2 Towards Nitrogen Bases

7.2.2.1. Synthesis of $OsO_3F_2(CH_3CN)$. Osmium trioxide difluoride dissolves in CH_3CN at -40 °C to give an orange solution according to eq. (7.3). Removal of excess CH_3CN

$$OsO_3F_2 + CH_3CN \xrightarrow{CH_3CN} OsO_3F_2(CH_3CN) \qquad (7.3)$$

initially yielded a wet, red-brown solid. Complete solvent removal yields yellow-ochre $OsO_3F_2(CH_3CN)$, which is stable at room temperature for several days and does not release CH_3CN under dynamic vacuum at room temperature. The $OsO_3F_2(CH_3CN)$ adduct is very soluble in CH_3CN at -40 °C and is slightly soluble in SO_2ClF at -80 °C.

7.2.2.2. Multi-NMR Spectroscopic Characterization $OsO_3F_2(CH_3CN)$. The ^{19}F NMR spectrum of $OsO_3F_2(CH_3CN)$ in CH_3CN solvent at -40 °C consists of a singlet at -99.6 ppm, which is less shielded than the ^{19}F resonance of the $OsO_3F_3^-$ anion (-116.8 ppm) and which is consistent with the neutrality of the $OsO_3F_2(CH_3CN)$ adduct. A singlet corresponding to complexed CH_3CN was found at higher frequency (2.55 ppm) in the ^1H NMR spectrum than the ^1H resonance for uncomplexed CH_3CN solvent (2.06 ppm, $^1J(^{13}C-^1H)$ = 136 Hz).

The ^{19}F NMR spectrum of $OsO_3F_2(CH_3CN)$ in SO_2ClF solvent at -80 °C comprises a singlet at -97.61 ppm with ^{187}Os satellites (^{187}Os: $I = ½$, natural abundance = 1.64%), $^1J(^{187}Os-^{19}F)$, of 39 Hz. The $^{187}Os-^{19}F$ coupling constant of the $OsO_3F_2(CH_3CN)$ is larger than that of the $OsO_3F_3^-$ anion (32 Hz), corresponding to more covalent Os-F bonds in the neutral adduct. Nitrogen-15 enrichment of CH_3CN in SO_2ClF resulted in a doublet splitting of the signal at -96.84 ppm, $^2J(^{19}F-^{15}N)$ = 21 Hz (Figure 7.3) which is consistent with the *fac*-$OsO_3F_2(CH_3CN)$ (structure I) in which one CH_3CN is coordinated to the osmium centre and the two fluorine ligands are chemically equivalent. Facial trioxo arrangements have also been found for the *fac*-$OsO_3F_3^-$ anion (see 7.2.1.4. X-ray Crystal Structure of $[N(CH_3)_4][OsO_3F_3]$) and for $(OsO_3F_2)_\infty$.[7]

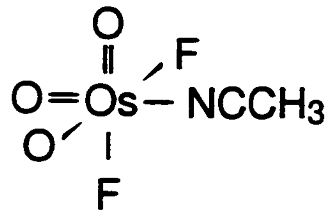

I

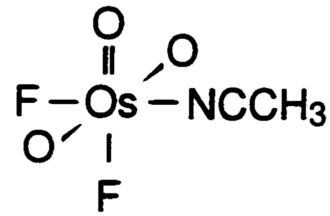

II

In addition to the singlet at -97.61 ppm, two weak doublets at -17.91 ppm and -47.95 ppm, $^2J(^{19}F-^{19}F)$ = 134 Hz and weak singlets at -68.87, -71.91, -72.84, and -72.87 ppm were observed in SO_2ClF solvent, but not in CH_3CN. The ^{15}N-enriched sample gave rise to an additional doublet splitting on the high-frequency doublet, $^2J(^{19}F-^{15}N)$ = 20 Hz (Figure 7.3). These splitting patterns are consistent with *mer*-$OsO_3F_2(CH_3CN)$ (structure II), which is unexpected, since the facial arrangement of the oxygen atoms is anticipated to be more stable. A $^{19}F-^{15}N$ coupling was not resolved for the second doublet. Two-bond couplings involving fluorine, $^2J(^{19}F-X)$, were found to exhibit no consistent dependency on the F-M-X bond angle. Therefore, an unambiguous assignment of the two doublet resonances could not be based on the expected magnitudes of the *cis* and *trans* $^{19}F-^{15}N$ coupling. The low-frequency doublet was, however, assigned to the fluorine *cis* to the CH_3CN ligand based on the *trans*-influence of the doubly bonded oxygen and the steric crowding in the plane of the three Os=O double bond domains. This results in a more ionic Os-F bond and in a more shielded fluorine environment than that of the fluorine *trans* to the oxygens. The weak singlets, which did not split upon ^{15}N enrichment could not be assigned.

The ^1H NMR spectrum of $OsO_3F_2(CH_3CN)$ in the presence of excess CH_3CN in SO_2ClF at -80 °C comprises an intense signal at 1.51 ppm, $^1J(^{13}C-^1H)$ = 136 Hz, for

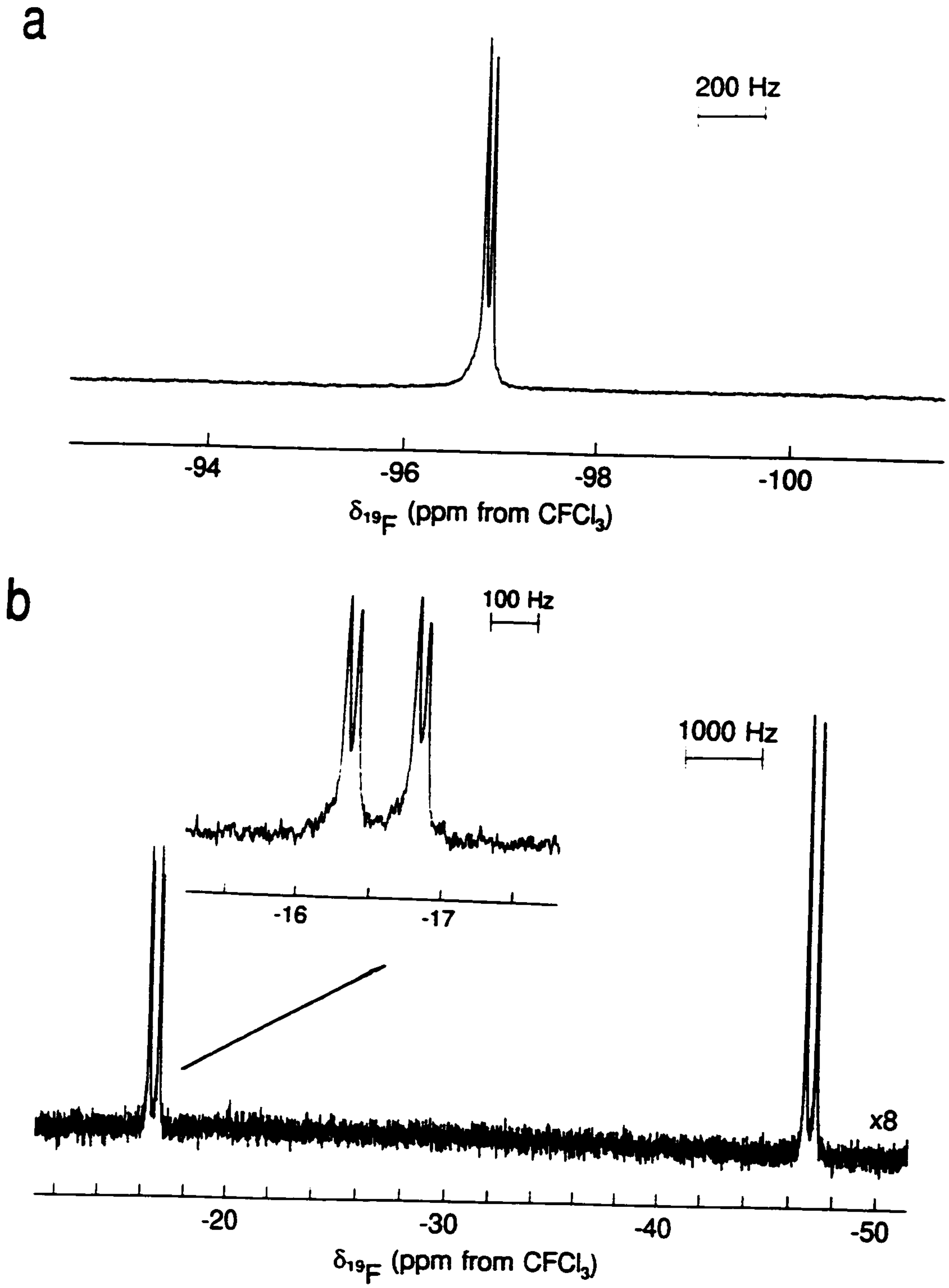

Figure 7.3 ^{19}F NMR spectrum (282.409 MHz) of ^{15}N-enriched *fac*-$OsO_3F_2(CH_3CN)$ (a) and *mer*-$OsO_3F_2(CH_3CN)$ (a) in SO_2ClF solvent at - 80 °C.

uncomplexed CH_3CN, a singlet at 2.02 ppm with ^{13}C satellites, $^1J(^{13}C-^1H)$ = 139 Hz assigned to *fac*-$OsO_3F_2{\cdot}CH_3CN$ (structure I), a singlet at 3.04 ppm assigned to *mer*-$OsO_3F_2(CH_3CN)$ (structure II), an unassigned broad signal at 2.33 ppm and a weak doublet at 7.19 ppm, $^1J(^{19}F-^1H)$ = 479 Hz corresponding to an HF impurity. The assignment of the ^1H resonances at 3.04 and 2.02 ppm to the *mer*-$OsO_3F_2(CH_3CN)$ and *fac*-$OsO_3F_2(CH_3CN)$ isomers, respectively, is supported by the ratio of their integrated intensities which matches the ratio of the combined intensities of the ^{19}F doublet resonances (-17.91 and -47.95 ppm) and the ^{19}F singlet resonance at -97.61 ppm. The complexation shift for *fac*-$OsO_3F_2{\cdot}CH_3CN$ in SO_2ClF (0.51 ppm) agrees well with that observed in CH_3CN solvent (0.49 ppm) and is consistent with the complexation shifts of $TcO_2F_3{\cdot}CH_3CN$ (0.37 ppm)[92] and $ReO_2F_3{\cdot}CH_3CN$ (0.59 ppm).[94] The complexation shift of 1.53 ppm for *mer*-$OsO_3F_2(CH_3CN)$ is much larger than that for *fac*-$OsO_3F_2(CH_3CN)$ (0.51 ppm), which is in accord with the stronger Os-N bond anticipated for the ligand *trans* to a fluorine when compared to that of a ligand *trans* to an oxygen. This significantly stronger Os-N bond may be the driving force for the change in geometry from *fac*-trioxo to the *mer*-trioxo configuration. The approximate 1:1 intensity ratio between the broad ^1H resonance at 2.33 ppm and that of *mer*-$OsO_3F_2(CH_3CN)$ at 3.04 ppm was found in different NMR samples having different relative concentrations of the *mer*- and *fac*-$OsO_3F_2(CH_3CN)$ and suggests a second, labile CH_3CN molecule in the coordination sphere of the *mer*-$OsO_3F_2(CH_3CN)$ that exchanges with free CH_3CN solvent resulting in broadening of the ^1H resonance at 2.33 ppm. The $^{13}C\{^1H\}$ NMR spectrum contains signals at 117.50 ppm and 0.86 ppm for free CH_3CN and signals at 2.24 and 3.15 ppm for the methyl carbon in *fac*-$OsO_3F_2(CH_3CN)$ and *mer*-$OsO_3F_2(CH_3CN)$, respectively. In contrast to $TcO_2F_3{\cdot}CH_3CN$[92] and $ReO_2F_3{\cdot}CH_3CN$,[94] no complexation shifts for ^{13}CN were observed.

The ^{15}N NMR spectrum of ^{15}N-enriched $OsO_3F_2(CH_3CN)$ (Figure 7.4) in the presence of excess CH_3CN in SO_2ClF at -84 °C comprised a singlet at -138.34 ppm for free CH_3CN, a triplet at -197.28 ppm with $^2J(^{19}F-^{15}N)$ = 20 Hz for *fac*-$OsO_3F_2(CH_3CN)$ and a doublet at -258.62 ppm with $^2J(^{19}F-^{15}N)$ = 18 Hz for *mer*-$OsO_3F_2(CH_3CN)$. A broad singlet observed at -72.08 ppm may be attributed to a labile second CH_3CN ligand in the coordination sphere of *mer*-$OsO_3F_2(CH_3CN)$, which was suggested based on ^1H NMR spectroscopy.

Although only the *fac*-$OsO_3F_2(CH_3CN)$ isomer was observed in the ^1H and ^{19}F NMR spectra in CH_3CN solvent, a mixture of *fac*- and *mer*-$OsO_3F_2(CH_3CN)$ was observed in the solid state after removal of CH_3CN solvent (see 7.2.2.3. Raman Spectroscopy of $OsO_3F_2(CH_3CN)$). The absence of an NMR signal corresponding to the *mer*-$OsO_3F_2(CH_3CN)$ isomer (structure II) in CH_3CN solvent presumably is a consequence of an intermediate exchange of the CH_3CN ligand with free CH_3CN solvent, and therefore between the two fluorine environments. The apparent absence of the *mer*-$OsO_3F_2(CH_3CN)$ isomer (structure III) can be explained in terms of steric crowding in the plane containing three oxygens and one CH_3CN ligand, which is expected to destabilize the adduct.

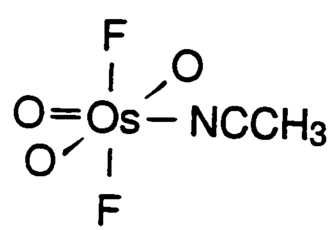

III

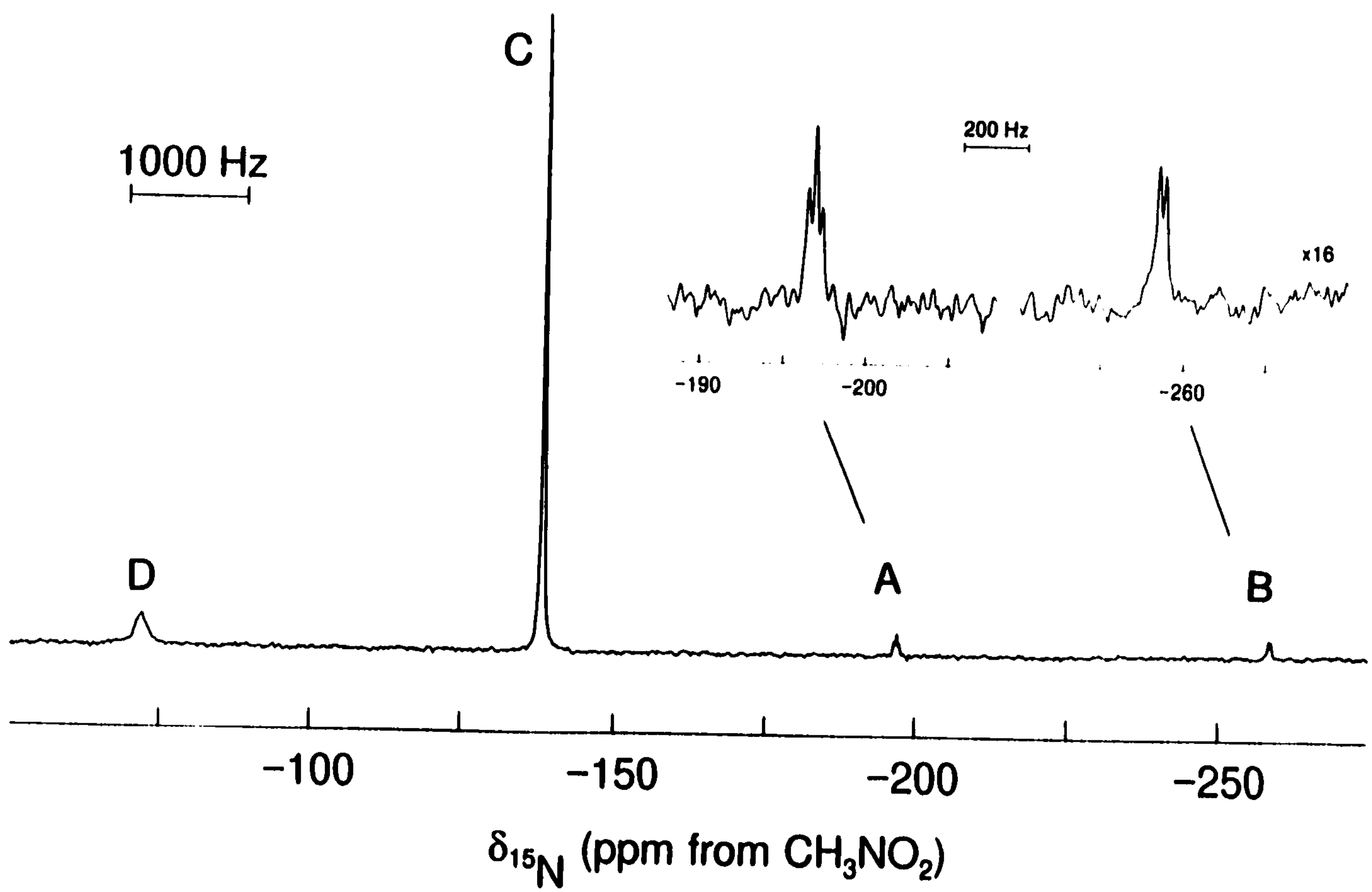

Figure 7.4 ^{15}N NMR spectrum (50.687 MHz) of ^{15}N-enriched *fac*-$OsO_3F_2(CH_3CN)$ (A), *mer*-$OsO_3F_2(CH_3CN)$ (B), free CH_3CN (C), and an unidentified species (D) in SO_2ClF solvent at - 84 °C.

Attempts to grow single crystals of $OsO_3F_2(CH_3CN)$ from SO_2ClF and a mixture of SO_2ClF and CH_3CN failed because of a very flat solubility curve for the CH_3CN adduct in these solvents.

7.2.2.3. Vibrational Spectroscopic Characterization of $OsO_3F_2(CH_3CN)$. The mixture of *fac*- and *mer*-$OsO_3F_2(CH_3CN)$ was characterized by infrared (25 °C) and low-temperature Raman spectroscopy (-163 °C). The Raman spectrum is shown in Figure 7.5 and the infrared and Raman frequencies with their tentative assignments are listed in Table 7.6. The Raman spectrum of $OsO_3F_2(CH_3CN)$, which was isolated from CH_3CN solvent, was the same as that of the precipitate in an NMR sample of $OsO_3F_2(CH_3CN)$ in SO_2ClF solvent indicating the presence of the same isomers in both solvents. The Raman spectrum of red-brown $OsO_3F_2(CH_3CN)$ in the presence of small amounts of free CH_3CN is shown in Figure 7.6 and the Raman frequencies are listed in Table 7.7.

The Raman spectrum of solid $OsO_3F_2(CH_3CN)$ isolated from CH_3CN solvent comprises eight bands between 900 and 970 cm^{-1}, the typical range for Os-O stretching modes and the C-C stretches of the CH_3CN ligands. The number of stretching bands in this region, three Os-O stretches and one C-C stretch for each isomer, confirms the existence of two $OsO_3F_2(CH_3CN)$ isomers and is in accord with the solution multi-NMR spectroscopic findings for solutions of OsO_3F_2 and CH_3CN in SO_2ClF solvent. The observation of four Os-F stretching bands in the Raman and infrared spectra provides further evidence for the presence of two $OsO_3F_2(CH_3CN)$ isomers.

The modes associated with the CH_3CN moiety exhibit complexation shifts

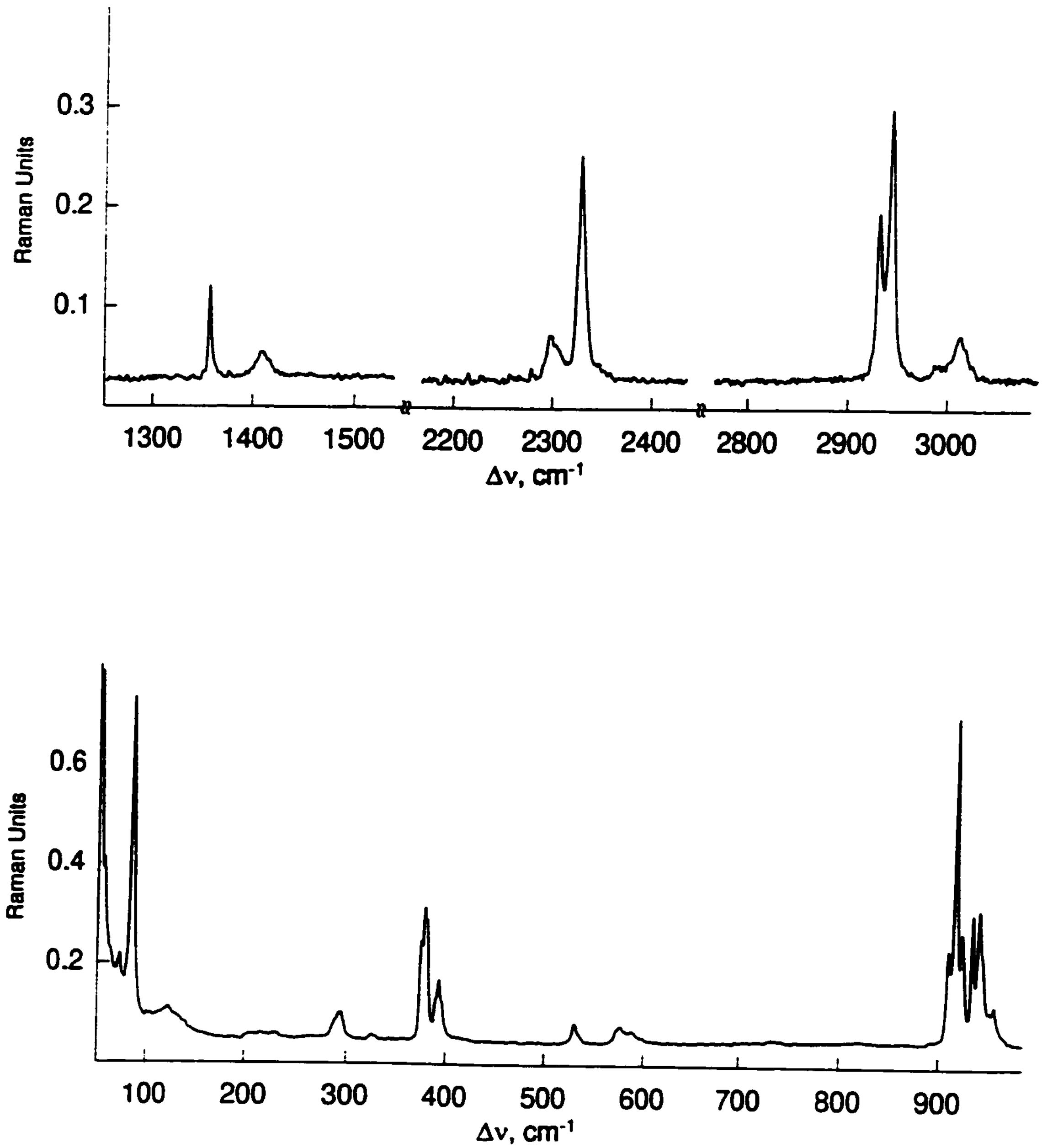

Figure 7.5 Raman spectrum of microcrystalline $OsO_3F_2(CH_3CN)$ recorded in a Pyrex glass capillary at -163 °C using 1064-nm excitation.

Table 7.6 Raman Frequencies and Their Assignments for *fac*-$OsO_2F_3(CH_3CN)$ and *mer*-$OsO_2F_3(CH_3CN)$

Frequency[a] [cm^{-1}]		Assignment[c]	
IR, 25 °C	Raman,[b] -165 °C	*fac*-$OsO_2F_3(CH_3CN)$ (C_s)	*mer*-$OsO_2F_3(CH_3CN)$ (C_s)
3286 vw		$(\nu_2+\nu_4)$	$(\nu_2+\nu_4)$
3015 w	3013 (5)	$\nu_{as}(CH_3)$ $(\nu_5(E))$	$\nu_{as}(CH_3)$ $(\nu_5(E))$
	2990 (2)		
2957 sh			
2942 m	2943 (28)	$\nu_s(CH_3)$ $(\nu_1(A_1))$	$\nu_s(CH_3)$ $(\nu_1(A_1))$
2935 m			
2928 sh	2930 (17)		
2873 vw			
2856 w			
2334 s	2330 (23)	$\nu(CN)$ $(\nu_2(A_1))$	$\nu(CN)$ $(\nu_2(A_1))$
2304 w	2299 (5)		
2264 vw		$(2\nu_4+\nu_8)$	$(2\nu_4+\nu_8)$
2055 vw			
1879 vw			
1836 vw			
1822 vw			
1731 vw			
1701 vw			
1524 vw			
1457 w			
1414 w	1410 (3)	$\delta_{as}(CH_3)$ $(\nu_6(E))$	$\delta_{as}(CH_3)$ $(\nu_6(E))$
1360 m	1357 (10)	$\delta_s(CH_3)$ $(\nu_3(A_1))$	$\delta_s(CH_3)$ $(\nu_3(A_1))$
1290 vw			
1176 vw			
1123 vw			
1076 vw			
1035 m	1038 (<0.5)	$(\nu_7(E))$	$(\nu_7(E))$
955 sh	955 (12)	$\nu(CC)$ $(\nu_4(A_1))$	$\nu(CC)$ $(\nu_4(A_1))$
	951 (10)		
944 vs	944 (28)sh	$\nu(OsO_3)$	
937 sh	940 (42)	$\nu(OsO_3)$	
	934 (40)	$\nu(OsO_3)$	
	923 (34)		$\nu(OsO_3)$

Table 7.6 continued...

Frequency[a] [cm^{-1}]		Assignment[c]	
IR, 25 °C	Raman,[b] -165 °C	*fac*-$OsO_2F_3(CH_3CN)$ (C_s)	*mer*-$OsO_2F_3(CH_3CN)$ (C_1)
918 vs	917 (100)		$\nu_s(OsO_3)$
910 vs	909 (29)		$\nu(OsO_3)$
867 m			
826 w		$(2\nu_8)$	$(2\nu_8)$
667 vw			
620 sh			
599 sh	599 (2)	$\nu(OsF_2)$	$\nu(OsF_2)$
589 vs	587 (4)		
	575 (5)		
532 vs	530 (6)		
419 m		$\delta(CCN)$ ($\nu_8(E)$)	$\delta(CCN)$ ($\nu_8(E)$)
413 m	411 (1)		
	395 (12)	$\delta(OsO_3)$	$\delta(OsO_3)$
	392 (18)		
	389 (13)		
	380 (38)		
	377 (42)		
	374 (31)		
	323 (1)	bending modes	
	292 (8)		
	288 (6)sh		
	228 (2)		
	216 (2)		
	204 (1)		
	120 (5)		
	84 (92); laser line		
	71 (7)		

[a] Abbrevations denote: shoulder (sh), very strong band (vs), strong (s), medium (m), weak (w), very weak (vw).

[b] Spectrum recorded on microcrystalline solid in a Pyrex glass melting point capillary using the 1064-nm excitation. Values in parentheses denote relative Raman intensities.

[c] Assignments in parentheses refer to the free CH_3CN ligand (C_{3v}) (see ref. (200)).

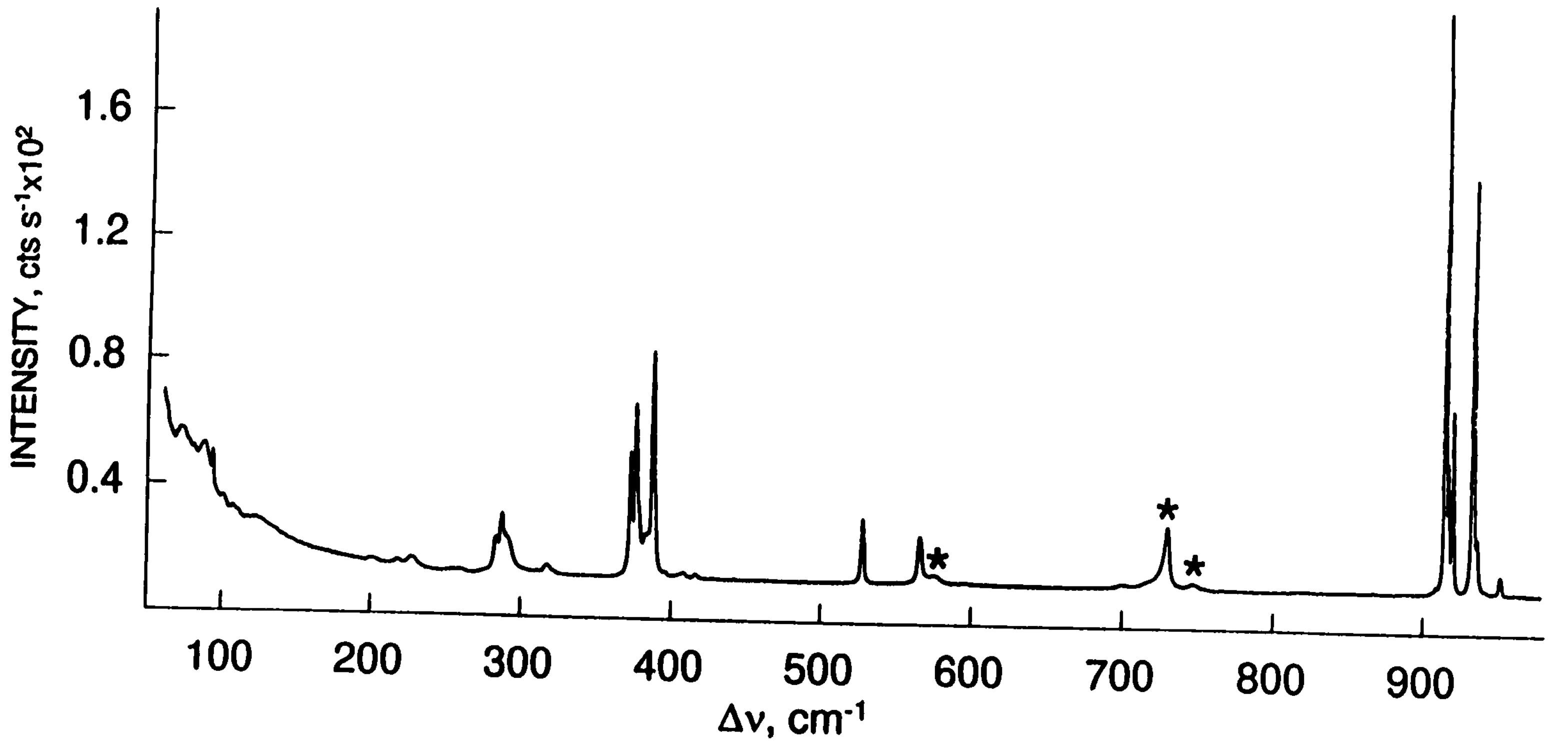

Figure 7.6 Raman spectrum (low-frequency region) of solid $OsO_3F_2(CH_3CN)$ in the presence of residual CH_3CN recorded in a ¼-in. FEP sample tube at -145 °C using 647.1-nm excitation.

Table 7.7 Raman Frequencies and Their Assignments for *fac*-$OsO_2F_3(CH_3CN)$ and *mer*-$OsO_2F_3(CH_3CN)$ in the Presence of Small Amounts of CH_3CN Solvent

Frequency[a] [cm^{-1}]	Assignment		
Raman,[b] -145 °C	*fac*-$OsO_2F_3(CH_3CN)$[c] (C_s)	*mer*-$OsO_2F_3(CH_3CN)$[c] (C_s)	CH_3CN (C_{3v})
3008 (1)	$\nu_{as}(CH_3)$ ($\nu_5(E)$)	$\nu_{as}(CH_3)$ ($\nu_5(E)$)	
3001 (1)			$\nu_5(E)$, $\nu_{as}(CH_3)$
2943 (6)	$\nu_s(CH_3)$ ($\nu_1(A_1)$)	$\nu_s(CH_3)$ ($\nu_1(A_1)$)	$\nu_1(A_1)$, $\nu_s(CH_3)$
2937 (2)sh			
2304 (1)	$\nu(CN)$ ($\nu_2(A_1)$)	$\nu(CN)$ ($\nu_2(A_1)$)	
2293 (<0.5)			$\nu_3+\nu_4$
2286 (<0.5)			
2252 (10)			$\nu_2(A_1)$, $\nu(CN)$
2249 (2)			
1456 (<0.5)			$\nu_6(E)$, $\delta_{as}(CH_3)$
1423 (<0.5)	$\delta_{as}(CH_3)$ ($\nu_6(E)$)	$\delta_{as}(CH_3)$ ($\nu_6(E)$)	
1369 (2)			$\nu_3(A_1)$, $\delta_s(CH_3)$
1356 (4)	$\delta_s(CH_3)$ ($\nu_3(A_1)$)	$\delta_s(CH_3)$ ($\nu_3(A_1)$)	
955 (3)	$\nu(CC)$ ($\nu_4(A_1)$)	$\nu(CC)$ ($\nu_4(A_1)$)	
939 (9)	$\nu(OsO_2)$		
936 (71)	$\nu(OsO_2)$		
923 (31)		$\nu(OsO_2)$	
920 (22)		$\nu(OsO_2)$	
917 (100)		$\nu(OsO_2)$	$\nu_4(A_1)$, $\nu(CC)$
702 (1)			
567 (8)	$\nu(OsF_2)$	$\nu(OsF_2)$	
529 (11)			
417 (1)	$\delta(CCN)$ ($\nu_8(E)$)	$\delta(CCN)$ ($\nu_8(E)$)	
408 (1)			
396 (1)	$\delta(OsO_2)$	$\delta(OsO_2)$	
388 (39)			
385 (7)[d]			
382 (7)[d]			
376 (39)			
373 (21)			
317 (2)			
291 (6)sh[d]			
387 (10)			
283 (6)			
258 (1)			
227 (2)			
217 (1)			
199 (1)			
122 (1)			

Table 7.7 continued...

Frequency[a] [cm^{-1}]	Assignment		
Raman,[b] -145 °C	*fac*-$OsO_2F_3(CH_3CN)$[c] (C_s)	*mer*-$OsO_2F_3(CH_3CN)$[c] (C_s)	CH_3CN (C_{3v})
106 (1)			
99 (1)			
93 (5); laser line			
87 (5)			
72 (3)			

[a] Abbreviation (sh) denotes shoulder.

[b] Spectrum recorded on microcrystalline solid in a ¼-in. FEP sample tube using the 647.1-nm excitation. Values in parentheses denote relative Raman intensities. Bands arising from the FEP sample tube were observed at 576 (2), 733 (11), 749 (1), 1307 (1), and 1384 (2) cm^{-1}.

[c] Assignments in parentheses refer to the free CH_3CN ligand (C_{3v}).

[d] This band overlaps with a band arising from the FEP sample tube.

comparable to those found for $TcO_2F_3(CH_3CN)$[92] and $ReO_2F_3(CH_3CN)$,[94] indicating a similar Lewis acid strengths for monomeric OsO_3F_2, TcO_2F_3 and ReO_2F_3, which all have polymeric structures in the solid state. The bands assigned to ν_5 (3004 cm^{-1}), ν_1 (2945 cm^{-1}), ν_2 (2254 cm^{-1}), ν_6 (1447 cm^{-1}), ν_3 (1375 cm^{-1}), ν_4 (918 cm^{-1}), and ν_8 (379 cm^{-1}) of free CH_3CN are shifted to 3015/2990 [3015], 2943/2930 [2942/2935/2978], 2330/2300 [2334/2304], 1409 [1414], 1357 [1360], 955/951 [955], and [419/413] cm^{-1}, respectively, in the Raman [infrared] spectrum of *fac*-$OsO_3F_2(CH_3CN)$ and *mer*-$OsO_3F_2(CH_3CN)$. Some CH_3CN bands are split which is in agreement with the presence of two $OsO_3F_2(CH_3CN)$ isomers.

The Os-O and Os-F stretching bands of the $OsO_3F_2(CH_3CN)$ adducts appear at lower frequencies than those of polymeric, fluorine-bridged $(OsO_3F_2)_\infty$,[7] which is a result of the stronger Lewis basicity for CH_3CN than that of the fluorine of a OsO_3F_2 moiety forming a bridge. Compared to the Os-O and Os-F stretching frequencies of the *fac*-$OsO_3F_3^-$ anion, the stretches in the $OsO_3F_2(CH_3CN)$ adducts occur at similar but somewhat higher frequencies which correlates with the greater base strength of the free fluoride ion.

The Raman spectrum of $OsO_3F_2(CH_3CN)$ in the presence of residual CH_3CN shows essentially the same Raman bands in the low-frequency region. The bands, however, have somewhat different intensities and slightly different frequencies. In addition to uncomplexed CH_3CN, the CH_3CN ligand Raman bands in the high-frequency region of $OsO_3F_2(CH_3CN)$ in the presence of residual CH_3CN appear at significantly different frequencies than those of $OsO_3F_2(CH_3CN)$ after complete removal of CH_3CN. The differences in the Raman spectra of $OsO_3F_2(CH_3CN)$ in the presence and absence of

CH_3CN are attributed to packing effects and increased vibrational coupling in the solid state after complete solvent removal.

7.3. Conclusion

The single crystal X-ray structure of $[N(CH_3)_4][OsO_3F_3]$ represents only the second X-ray structure containing an isolated $MO_3F_3^{n-}$ anion (M = d^0 transition metal) besides that of $WO_3F_3^{3-}$ [117] and unambiguously confirms the facial geometry of the $OsO_3F_3^-$ anion which has also been established in solution by ^{19}F NMR spectroscopy. The $OsO_3F_2(CH_3CN)$ adduct was shown to exist as both *mer*- and *fac*-isomers based on NMR and Raman spectroscopy. Other than the $ReO_3F_3^{2-}$,[216] $MoO_3F_3^{3-}$,[217] and $WO_3F_3^{3-}$ [217] anions whose assignments of their *mer*-trioxo-arrangements were based solely on vibrational spectroscopy, the *mer*-$OsO_3F_2(CH_3CN)$ isomer is one of the very few examples of transition metal d^0 species with a *mer*-trioxo arrangement.

CHAPTER 8

FLUORIDE ION DONOR PROPERTIES OF OsO_3F_2

8.1. Introduction

The cation chemistry of osmium(VIII) has thus far been restricted to cations derived from *cis*-OsO_2F_4.[91] The latter are formed by reaction of *cis*-OsO_2F_4 with the Lewis acids, AsF_5 and SbF_5. The dimeric fluorine-bridged $Os_2O_4F_7^+$ cation exhibits a pseudo-octahedral *cis*-dioxo arrangement about osmium in the crystal structure of $[Os_2O_4F_7][Sb_2F_{11}]$. Failure to obtain a crystal structure containing the trigonal bipyramidal $OsO_2F_3^+$ cation indicates the reluctance of osmium dioxo species to lower its coordination number below six. Rather, $[Os_2O_4F_7][Sb_2F_{11}]$ crystallized from SbF_5/HF mixtures instead of a $OsO_2F_3^+$ salt. The $OsO_2F_3^+$ cation has only been observed by ^{19}F NMR spectroscopy with the weakly nucleophilic, polymeric $Sb_nF_{5n+1}^-$ anion as the counteranion in SbF_5 solvent.

The Lewis acid properties of OsO_3F_2 have been well established by the formation of the *fac*-$OsO_3F_3^-$ anion in the salts, $[K][OsO_3F_3]$,[72,85] $[Rb][OsO_3F_3]$,[72] $[Cs][OsO_3F_3]$,[72,85] $[Ag][OsO_3F_3]$,[72,85] $[NO][OsO_3F_3]$, and $[N(CH_3)_4][OsO_3F_3]$ (see Chapter 7). The preferred coordination number of osmium(VIII) trioxo species appears to be six, which has been found in the *fac*-$OsO_3F_3^-$ (see Chapter 7) anion as well as the low-temperature phase of the neutral parent compound, $(OsO_3F_2)_\infty$,[7] which exists as a fluorine bridged polymeric chain in the solid state. The Lewis base properties of OsO_3F_2 have not been investigated prior to this study, although ReO_3F, which is isoelectronic with the OsO_3F^+ cation, has been prepared[220] and characterized by vibrational,[221-223] mircowave,[224] and UV spectroscopy.[223]

8.2. Results and Discussion

8.2.1. Syntheses of the OsO_3F^+ and $Os_2O_6F_3^+$ Cations and Solution Characterization of the OsO_3F^+ Cation by ^{19}F NMR Spectroscopy

Osmium trioxide difluoride, which is insoluble in HF, reacts with excess AsF_5 according to eq. (8.1), yielded a yellow-orange solution of solvated $[OsO_3F][AsF_6]$. Stoichiometric amounts of AsF_5 did not result in complete dissolution of OsO_3F_2, presumably because of the competing reaction with HF solvent (eq. (8.2)). Slow removal

$$OsO_3F_2 + PnF_5 \xrightarrow{HF,\ RT} [OsO_3F][PnF_6]_{(HF)} \quad ; Pn = As, Sb \tag{8.1}$$

$$2HF + AsF_5 \rightleftharpoons [H_2F][AsF_6] \tag{8.2}$$

of the HF solvent at -78 °C under certain conditions that are not entirely understood, initially yielded orange crystals having the composition $[OsO_3F][HF]_2[AsF_6]$ (see 8.2.2.2. X-ray Crystallography; Structure of $[OsO_3F][HF]_2[AsF_6]$). Further pumping at -78 °C resulted in the loss of the two HF solvent molecules and straw yellow $[OsO_3F][AsF_6]$

which was unstable at ambient temperatures. With excess AsF_5, crystals of solvent-free $[OsO_3F][AsF_6]$ were grown from HF solvent at -78 °C.

Attempts to redissolve $[OsO_3F][AsF_6]$ in fresh HF solvent resulted in loss of AsF_5 and precipitation of orange $[Os_2O_6F_3][AsF_6]$ according to eq. (8.3). Subsequent removal of HF solvent gave a mixture of solid $[OsO_3F][AsF_6]$, OsO_3F_2, and small amounts of $[Os_2O_6F_3][AsF_6]$, which was identified by Raman spectroscopy and resulted from dissociation according to eq. (8.4). The formation of the dinuclear $Os_2O_6F_3^+$ cation from $[OsO_3F][AsF_6]$ can be reversed by addition of excess AsF_5 to the HF solution (eq. (8.5)).

$$2[OsO_3F][AsF_6] \xrightarrow{HF} [Os_2O_6F_3][AsF_6] + AsF_5 \quad (8.3)$$

$$[Os_2O_6F_3][AsF_6] \xrightarrow{HF,\ RT} [OsO_3F][AsF_6] + OsO_3F_2 \quad (8.4)$$

$$[Os_2O_6F_3][AsF_6] + AsF_5 \xrightarrow{HF} 2[OsO_3F][AsF_6] \quad (8.5)$$

The very low solubility of $[Os_2O_6F_3][AsF_6]$ in HF solvent prevented crystal growth. Solutions of $[OsO_3F][AsF_6]$ in HF solvent are unstable towards dissociation to OsO_3F_2 and AsF_5 at room temperature. The ^{19}F NMR spectrum of OsO_3F_2 in the presence of a 13-fold molar excess of AsF_5 in HF sovlent at -80 °C showed a broad singlet at -132.2 ppm ($\Delta\nu_{1/2}$ = 500 Hz) which is attributed to fast fluorine exchange among the OsO_3F^+ cation, AsF_5 and HF solvent.

At room temperature, OsO_3F_2 is highly soluble in HF solutions containing stoichiometric amounts of SbF_5 and yields $[OsO_3F][SbF_6]$ as a yellow solution (eq. (8.1)) and at -78 °C, yellow $[OsO_3F][HF][SbF_6]$ slowly crystallizes (see 8.2.2.3. X-Ray Crystallography, Structure of $[OsO_3F][HF][SbF_6]$). Removal of HF solvent at -78 °C yielded yellow $[OsO_3F][HF][SbF_6]$, which melts at approximately 45 °C. Pumping at room temperature resulted in the removal of only small amounts of HF giving $[OsO_3F][SbF_6]$. Complete conversion to $[OsO_3F][SbF_6]$ was not successful, presumably because the dissociation pressure of coordinated HF is very low at room temperature and the competing decomposition of $[OsO_3F][SbF_6]$ occurs at temperatures close to and higher than room temperature. Pumping at 45 °C led to a decrease in the relative Raman intensities of the symmetric Os-O stretching band assigned to $[OsO_3F][SbF_6]$ compared to that of $[OsO_3F][HF][SbF_6]$. No evidence for the $Os_2O_6F_3^+$ cation was found using the Lewis acid SbF_5. Upon slow removal of HF solvent, orange $[OsO_3F][HF]_2[SbF_6]$ crystallizes at high concentration. One solvent molecule is readily lost under dynamic vacuum at -78 °C, yielding $[OsO_3F][HF][SbF_6]$.

At 55 °C, OsO_3F_2 dissolved in neat SbF_5 giving a yellow solution according to eq. (8.6). Below 55 °C, the solubility of $[OsO_3F][Sb_nF_{5n+1}]$ decreased dramatically and straw-

$$OsO_3F_2 + nSbF_5 \xrightarrow{SbF_5,\ 55\ °C} [OsO_3F][Sb_nF_{5n+1}] \qquad (8.6)$$

yellow $[OsO_3F][Sb_3F_{16}]$ crystallized from SbF_5 solvent. The empirical formula was established by mass balance ($OsO_3F_2 : SbF_5 = 1 : 3.1$) after removal of excess SbF_5 at room temperature and was confirmed by the X-ray crystallography (see 8.2.2.4. X-Ray

Crystallography; Structure of [OsO_3F][Sb_3F_{16}]). The weakly fluoro-basic $Sb_3F_{16}^-$ anion is required to stabilize the unsolvated OsO_3F^+ cation and is indicative of the weak fluoride ion donor properties of OsO_3F_2 and the high electrophilicity of the OsO_3F^+ cation. Dissolution of [OsO_3F][Sb_3F_{16}] in HF solvent resulted in precipitation of [OsO_3F][HF][SbF_6] at -78 °C, which was identified by Raman spectroscopy. Although [OsO_3F][AsF_6] was isolated from HF solutions in the presence of excess AsF_5, solvent free [OsO_3F][SbF_6] does not form from an HF solution containing a 2-fold molar excess of SbF_5. This is likely a consequence of the lower nucleophilicity of SbF_6^- compared to that of AsF_6^- leaving the OsO_3F^+ cation coordinatively less saturated in the solvent free SbF_6^- salt, so that the vacant coordination site is occupied by an HF solvent molecule.

The ^{19}F NMR spectrum of OsO_3F_2 dissolved in neat SbF_5 at 55 °C gives rise to a broad singlet for the OsO_3F^+ cation at 70.9 ppm ($\Delta\nu_{1/2}$ = 360 Hz) and to broad $Sb_nF_{5n+1}^-$ /$(SbF_5)_n$ resonances at -91.5 (shoulder), -105.7 ppm ($\Delta\nu_{1/2} \approx$ 5400 Hz), and -128.1 ($\Delta\nu_{1/2} \approx$ 5800 Hz). The ^{19}F resonance of the OsO_3F^+ cation is significantly more shielded than those of the $OsO_2F_3^+$ cation (122.4 and 129.5 ppm), which is consistent with the decrease in the number of strongly electron withdrawing fluorine ligands. This trend, however, is opposite to that observed for xenon oxide fluorides.[148] The ^{19}F NMR spectrum of [OsO_3F][Sb_3F_{16}] dissolved in SO_2ClF solvent at -100 °C showed a singlet at 77.1 ppm ($\Delta\nu_{1/2}$ = 140 Hz) corresponding to the OsO_3F^+ cation. Resonances for the *cis*-fluorine-bridged $Sb_3F_{16}^-$ and $Sb_2F_{11}^-$ anions and for $SO_2ClF{\cdot}SbF_5$ were observed in the F-on-Sb region (Table 8.1). The NMR parameters of the anions and the SO_2ClF adduct are in good agreement with the previously reported values.[225] Approximately 70% of the $Sb_3F_{16}^-$

Table 8.1 ^{19}F NMR parameters of $SO_2ClF{\cdot}SbF_5$, $Sb_2F_{11}^-$, and $Sb_3F_{16}^-$ at 100 °C in SO_2ClF solvent

$SO_2ClF{\cdot}SbF_5$[a]	chemical shift [ppm][b]	$^2J(^{19}F-^{19}F)$ [Hz]
F-on-S (1)	94.40 (s)	
F_{trans} (1)	-143.08 (q)	96
F_{cis} (4)	-105.63 (d)	95

$Sb_2F_{11}^-$[a]	chemical shift [ppm][b]	$^2J(^{19}F-^{19}F)$ [Hz]
F_b (1)	-90.99 (m)	60
F_{trans} (2)	-136.04 (q)	104
F_{cis} (8)	-113.79 (dd)	102, 62

$Sb_3F_{16}^-$[a]	chemical shift [ppm][b]	$^2J(^{19}F-^{19}F)$ [Hz]
F_{trans} (2)	-140.32 (q)	60
F_{cis} (8)	-112.18 (dd)	99, 53
F_b (2)	-89.66 (s,br)	
$F_{trans'}$ (2)	-128.19 (dt)	134, 37
$F_{cis'}$ (2)	-108.23 (m)	

[a] Values in parentheses denote relative intensies. Symbols denote: bridging fluorine (F_b), fluorines *trans/cis* to F_b in a terminal SbF_5 moiety (F_{trans}/F_{cis}), fluorine *trans/cis* to F_b in a bridging SbF_4 moiety ($F_{trans'}/F_{cis'}$).

[b] Abbreviations denote: singlet (s), doublet (d), quintet (q), multiplet (m), doublet of doulbets (dd), doublet of triplets (dt), and broad (br).

anions were dissociated in SO_2ClF solution according to eq. (8.7). In view of the small

$$Sb_3F_{16}^- + SO_2ClF \xrightarrow{SO_2ClF,\ -100\ ^\circ C} Sb_2F_{11}^- + SO_2ClF{\cdot}SbF_5 \qquad (8.7)$$

magnitudes of the one-bond ^{187}Os-^{19}F coupling constants found for *cis*-OsO_2F_4 (35.1 and 59.4 Hz)[6] and *fac*-$OsO_3F_3^-$ (32 Hz) (see Chapter 7) and the low abundance of ^{187}Os (1.64%), the ^{187}Os satellites are expected to be hidden by the breath of the central ^{19}F signal.

8.2.2. X-ray Crystallography

Details of the data collection parameters and other crystallographic information for $[OsO_3F][AsF_6]$, $[OsO_3F][HF]_2[AsF_6]$, $[OsO_3F][HF][SbF_6]$, and $[OsO_3F][Sb_3F_{16}]$ are given in Table 8.2. Important bond lengths, angles and contacts are listed in Table 8.3.

8.2.2.1. Structure of $[OsO_3F][AsF_6]$. The crystal structure of $[OsO_3F][AsF_6]$ consists of OsO_3F^+ cations and AsF_6^- anions which are bridged through a fluorine of the AsF_6^- anion. Two cation-anion pairs are connected to each other by two additional Os---F-As bridges forming a cyclic dimer. The dimers are, in turn, stacked in columns parallel to the *a*-axis (Figure 8.1).

The OsO_3F^+ cation is distorted form the expected C_{3v} point symmetry with one Os-O bond being significantly longer (171.1(8) pm) than the other two (167.4(9) and 167.9(9)

Table 8.2 Summary of Crystal Data and Refinement Results for $[OsO_3F][AsF_6]$, $[OsO_3F][HF]_2[AsF_6]$, $[OsO_3F][HF][SbF_6]$, and $[OsO_3F][Sb_3F_{16}]$

	$[OsO_3F][AsF_6]$	$[OsO_3F][HF]_2[AsF_6]$	$[OsO_3F][HF][SbF_6]$	$[OsO_3F][Sb_3F_{16}]$
formula	AsF_7O_3Os	$H_2AsF_9O_3Os$	HF_8O_3OsSb	$F_{17}O_3OsSb_3$
space group	$P2_1/n$ (No. 14)	$P2_1/n$ (No. 14)	Pc (No. 7)	$P\bar{4}2_1m$ (No. 113)
a [pm]	700.01(11)	514.91(9)	524.4(4)	1007.6(6)
b [pm]	1106.20(11)	812.9(2)	964.6(6)	1007.6(6)
c [pm]	886.29(13)	1963.6(7)	1526.9(10)	758.5(8)
α [deg]	90	90	90	90
β [deg]	92.270(7)	95.099(7)	97.154(13)	90
γ [deg]	90	90	90	90
V [10^6 pm^3]	685.8(2)	818.7(4)	766.4(10)	770.1(10)
Z [molecules/unit cell]	4	4	4	2
mol. wt. [g mol^{-1}]	446.12	486.14	512.96	926.45
colour	yellow	orange	yellow	straw-yellow

Table 8.2 continued...

	$[OsO_3F][AsF_6]$	$[OsO_3F][HF]_2[AsF_6]$	$[OsO_3F][HF][SbF_6]$	$[OsO_3F][Sb_3F_{16}]$
size $[mm^3]$	0.12×0.10×0.10	0.25×0.20×0.05	0.08×0.04×0.03	0.14×0.10×0.005
calcd density $[g\ cm^{-3}]$	4.321	3.944	4.446	3.995
μ $[mm^{-1}]$	23.494	19.730	20.215	13.617
data/restraints/parameters	1535/0/110	1887/0/130	3278/2/127	620/0/49
final agreement factors	$R^a = 0.0401$	$R^a = 0.0348$	$R^a = 0.0558$	$R^a = 0.0858$
	$R_w^b = 0.0797$	$R_w^b = 0.0864$	$R_w^b = 0.1198$	$R_w^b = 0.1871$
GOOF	1.075	1.030	1.046	1.038
Extinction coefficient	0.0013(3)	0.0057(4)	0.0012(2)	0.0001(7)
$\Delta\delta_{max}/\Delta\delta_{min}$ $[e\ 10^{-6}\ pm^{-3}]$	1.636/-1.397	1.446/-1.280	2.598/-2.327	2.209/-2.610

[a] $R = \Sigma||F_o| - |F_c||/\Sigma|F_o|$.

[b] $R_w = \Sigma|(|F_o| - |F_c|)w^{1/2}|/\Sigma(|F_o|w)$ where $w = 1/[\sigma^2(F) + (0.0344)^2 + 4.94]$.

Table 8.3 Bond Lengths, Selected Bond Angles, and Contacts in $[OsO_3F][AsF_6]$, $[OsO_3F][HF]_2[AsF_6]$, $[OsO_3F][HF][SbF_6]$, and $[OsO_3F][Sb_3F_{16}]$.

$[OsO_3F][AsF_6]$

Bond Lengths and Contacts [pm]			
Os(1)-O(1)	171.2(8)	Os(1)-O(2)	167.3(9)
Os(1)-O(3)	167.8(9)	Os(1)-F(1)	178.2(7)
Os(1)-F(2)	245.1(7)	As(1)-F(2)	177.6(7)
As(1)-F(3)	167.7(7)	As(1)-F(4)	174.6(7)
As(1)-F(5)	169.5(8)	As(1)-F(6)	168.5(8)
As(1)-F(7)	169.3(7)	Os(1)---F(4)	266.6(7)
Os(1)---F(5)	307.2(8)		
Bond Angles [deg.]			
O(1)-Os(1)-O(2)	105.1(4)	O(1)-Os(1)-O(3)	108.4(4)
O(2)-Os(1)-O(3)	104.6(4)	O(1)-Os(1)-F(1)	120.4(4)
O(1)-Os(1)-F(2)	75.6(3)	O(2)-Os(1)-F(1)	105.6(4)
O(3)-Os(1)-F(1)	111.4(4)	O(2)-Os(1)-F(2)	179.0(4)
O(3)-Os(1)-F(2)	75.8(3)	F(1)-Os(1)-F(2)	73.5(3)
As(1)-F(2)-Os(1)	138.4(4)	F(2)-As(1)-F(3)	89.9(4)
F(2)-As(1)-F(4)	87.3(3)	F(2)-As(1)-F(5)	88.3(4)
F(2)-As(1)-F(6)	89.7(4)	F(2)-As(1)-F(7)	177.0(4)

$[OsO_3F][HF]_2[AsF_6]$

Bond Lengths and Contacts [pm]			
Os(1)-O(1)	169.4(6)	Os(1)-O(2)	166.6(6)
Os(1)-O(3)	172.0(6)	Os(1)-F(1)	180.4(5)

Table 8.3 continued...

Os(1)-F(2)	228.2(5)	Os(1)-F(3)	223.1(4)
As(1)-F(3)	182.3(4)	As(1)-F(4)	173.5(5)
As(1)-F(5)	170.3(5)	As(1)-F(6)	169.5(5)
As(1)-F(7)	170.5(5)	As(1)-F(8)	168.9(4)
F(2)---F(9)	242.9(8)	F(9)---F(4A)	251.2(8)
		Bond Angles [deg.]	
O(1)-Os(1)-O(2)	102.9(3)	O(1)-Os(1)-O(3)	102.4(3)
O(2)-Os(1)-O(3)	103.5(3)	O(1)-Os(1)-F(1)	100.0(3)
O(2)-Os(1)-F(1)	101.3(3)	O(3)-Os(1)-F(1)	141.6(3)
O(2)-Os(1)-F(3)	87.5(2)	O(1)-Os(1)-F(3)	169.0(2)
O(3)-Os(1)-F(3)	78.2(2)	F(1)-Os(1)-F(3)	74.1(2)
O(2)-Os(1)-F(2)	169.1(2)	O(1)-Os(1)-F(2)	87.1(3)
O(3)-Os(1)-F(2)	78.0(2)	F(1)-Os(1)-F(2)	72.4(2)
F(3)-Os(1)-F(2)	82.3(2)	As(1)-F(3)-Os(1)	138.8(2)
F(3)-As(1)-F(4)	86.1(2)	F(3)-As(1)-F(5)	86.5(2)
F(3)-As(1)-F(6)	88.2(2)	F(3)-As(1)-F(7)	87.0(2)
F(3)-As(1)-F(8)	178.5(2)		

$[OsO_3F][HF][SbF_6]$

Bond Lengths and Contacts [pm]

Os(1)-O(12)	166(2)	Os(1)-O(13)	168(2)
Os(1)-O(11)	170(2)	Os(1)-F(11)	184.7(13)
Os(1)-F(13)	223(2)	Os(1)-F(12)	223.6(14)
Os(2)-O(21)	168(2)	Os(2)-O(23)	170(2)
Os(2)-O(22)	176(2)	Os(2)-F(21)	182(2)
Os(2)-F(23)	224.0(14)	Os(2)-F(22)	227(2)

Table 8.3 continued...

Sb(1)-F(13)	196(2)	Sb(1)-F(14)	187(2)
Sb(1)-F(15)	186(2)	Sb(1)-F(16)	191.3(14)
Sb(1)-F(17)	185(2)	Sb(1)-F(18)	184.6(14)
Sb(2)-F(23)	197.7(14)	Sb(2)-F(24)	186(2)
Sb(2)-F(25)	185.0(14)	Sb(2)-F(26)	193(2)
Sb(2)-F(27)	187(2)	Sb(2)-F(28)	184(2)
F(12)---F(26)	238(2)		
	Bond Angles [deg.]		
O(11)-Os(1)-O(12)	103.1(9)	O(11)-Os(1)-O(13)	102.9(8)
O(11)-Os(1)-F(11)	101.2(8)	O(11)-Os(1)-F(12)	168.7(7)
O(11)-Os(1)-F(13)	87.1(8)	O(12)-Os(1)-O(13)	103.8(8)
O(12)-Os(1)-F(11)	98.0(7)	O(12)-Os(1)-F(12)	87.4(7)
O(12)-Os(1)-F(13)	167.8(7)	O(13)-Os(1)-F(11)	142.7(7)
O(13)-Os(1)-F(12)	78.2(7)	O(13)-Os(1)-F(13)	80.1(7)
F(11)-Os(1)-F(12)	72.9(5)	F(11)-Os(1)-F(13)	73.1(5)
F(12)-Os(1)-F(13)	82.0(5)	O(21)-Os(2)-O(22)	101.4(9)
O(21)-Os(2)-O(23)	102.7(9)	O(21)-Os(2)-F(21)	100.0(8)
O(21)-Os(2)-F(22)	87.5(7)	O(21)-Os(2)-F(23)	170.1(7)
O(22)-Os(2)-O(23)	102.4(9)	O(22)-Os(2)-F(21)	143.4(8)
O(22)-Os(2)-F(22)	77.9(7)	O(22)-Os(2)-F(23)	79.8(7)
O(23)-Os(2)-F(21)	101.3(8)	O(23)-Os(2)-F(22)	169.5(7)
O(23)-Os(2)-F(23)	86.5(7)	F(21)-Os(2)-F(22)	73.8(7)
F(21)-Os(2)-F(23)	74.3(6)	F(23)-Os(2)-F(22)	83.2(5)
Sb(1)-F(13)-Os(1)	151.8(7)	Sb(2)-F(23)-Os(2)	137.7(7)
F(13)-Sb(1)-F(18)	179.2(6)	F(13)-Sb(1)-F(17)	86.5(6)
F(13)-Sb(1)-F(15)	89.1(6)	F(13)-Sb(1)-F(14)	87.8(7)
F(13)-Sb(1)-F(16)	87.1(6)	F(23)-Sb(2)-F(28)	175.1(6)

Table 8.3 continued...

F(23)-Sb(2)-F(25)	86.4(6)	F(23)-Sb(2)-F(24)	88.1(6)
F(23)-Sb(2)-F(27)	85.3(6)	F(23)-Sb(2)-F(26)	84.6(6)

$[OsO_3F][Sb_3F_{16}]$

Bond Lengths and Contacts [pm]			
Os(1)-FOA	168(3)	Sb(1)-F(2)	184(4)
Sb(1)-F(1)	187(3)	Sb(1)-F(3)	188(4)
F(1)-Sb(2)	219(3)	Sb(2)-F(10A)	177(6)
Sb(2)-F(12)	178(4)	Sb(2)-F(11B)	180(5)
Sb(2)-F(10B)	187(6)	Sb(2)-F(11A)	191(5)
Os(1)···F(10A)	285(6)	Os(1)···F(10B)	283(6)
Bond Angles [deg.]			
FOA#1-Os(1)-OFA	104(2)	OFA-Os(1)-FOA#2	112.5(10)
F(1)-Sb(1)-F(2)	85(2)	F(1)-Sb(1)-F(3)	90.8(14)
F(2)-Sb(1)-F(3)	78(2)	Sb(1)-F(1)-Sb(2)	146(2)
F(1)-Sb(2)-F(10B)	81(2)	F(1)-Sb(2)-F(11A)	83(2)
F(1)-Sb(2)-F(12)	173.8(14)	F(1C)-Sb(2)-F(10A)	87(2)
F(1C)-Sb(2)-F(11B)	91(2)		

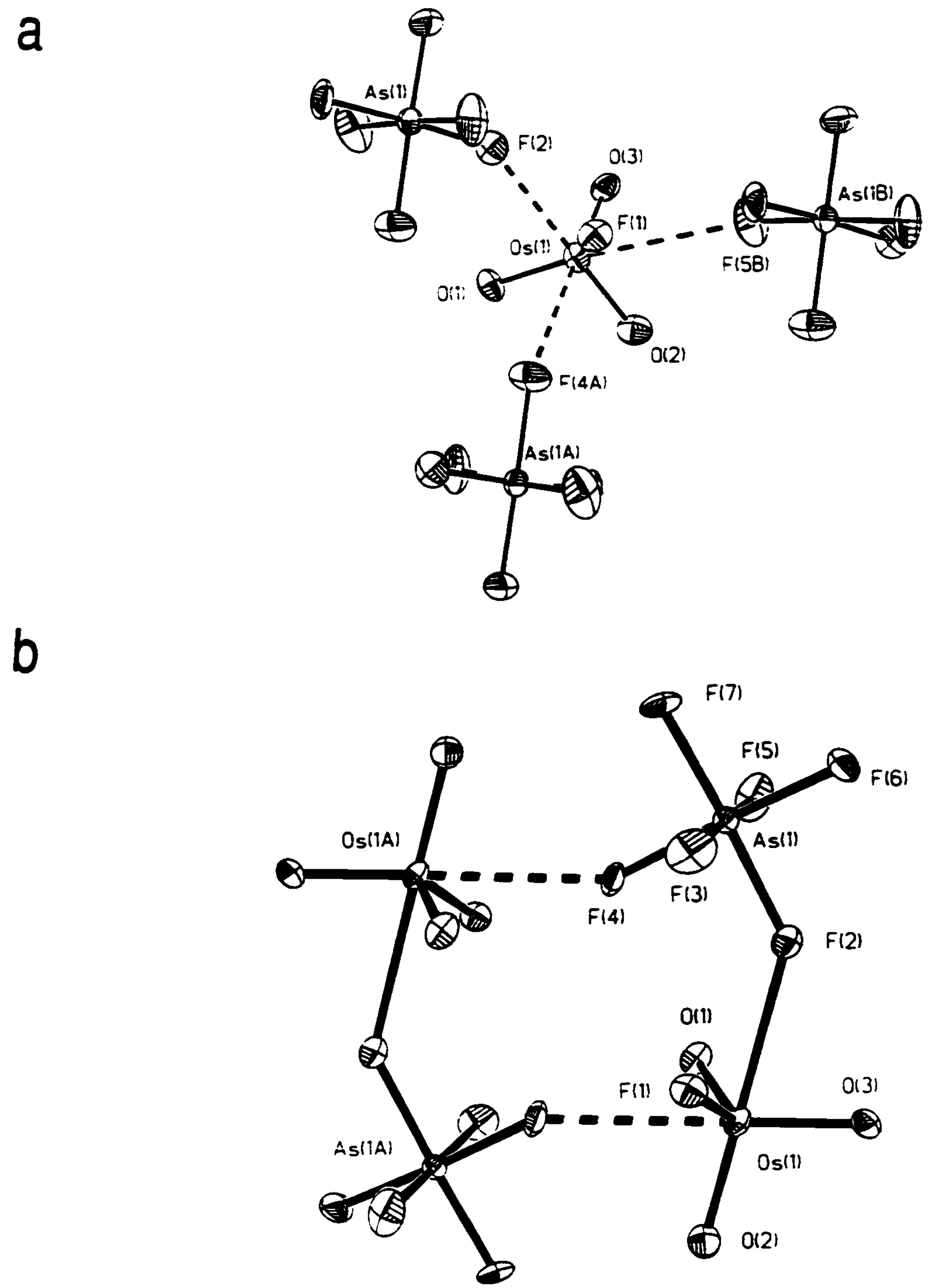

Figure 8.1 Views of (a) the OsO_3F^+ cation and its contacts to AsF_6^- anions in the $[OsO_3F][AsF_6]$ structure and (b) the $([OsO_3F][AsF_6])_2$ dimer (thermal ellipsoids are shown at the 50% probability level).

pm). Each cation forms two strong (245.0(7) and 266.6(7) pm) Os---F contacts and one weak (307.2(8) pm) Os---F contact to the fluorines of AsF_6^- anions. The fluorine contacts are directed through three trigonal faces of the OsO_3F^+ pseudo-tetrahedron, such that they are located on the side opposite to the Os=O bonds. Extension of the coordination sphere by inclusion of the Os---F contacts results in a monocapped trigonal prismatic geometry about Os with the three oxygen atoms *cis* to each other (Figure 8.1). The longer Os-O(1) bond is opposite to the weakest Os---F contact and is likely a consequence of the steric crowding caused by the two close Os---F contacts in the vinicity of O(1). Two fluorines of the AsF_6^- anion that are *cis* to each other form two strong contacts to the cation resulting in elongation of the two As-F bonds (177.6(7) and 174.6(7) pm) compared to the remaining four As-F bonds (169.5(8) to 167.7(7) pm) and in lowering of the anion symmetry of C_{2v} point symmetry or lower.

8.2.2.2. Structure of $[OsO_3F][HF]_2[AsF_6]$. The crystal structure of $[OsO_3F][HF]_2[AsF_6]$ consists of cyclic dimers of AsF_6^- anions fluorine bridged to the OsO_3F^+ cations, both bridged through two $(HF)_2$ moieties to a second anion-cation pair (Figure 8.2). These cyclic dimers are alligned parallel to the (10½) plane and are stacked in columns parallel to the *a*-axis (Figure 8.2).

The OsO_3F^+ cation deviates significantly from the ideal C_{3v} structure with one short (166.6(6) pm) and two long (169.4(6) and 170.4(6) pm) Os-O bonds. The Os-F bond length in the cation (180.4(5) pm) is similar to that in $[OsO_3F][AsF_6]$ (178.2(7) pm), however, unlike the latter structure the O-Os-F bond angles in $[OsO_3F][HF]_2[AsF_6]$

a

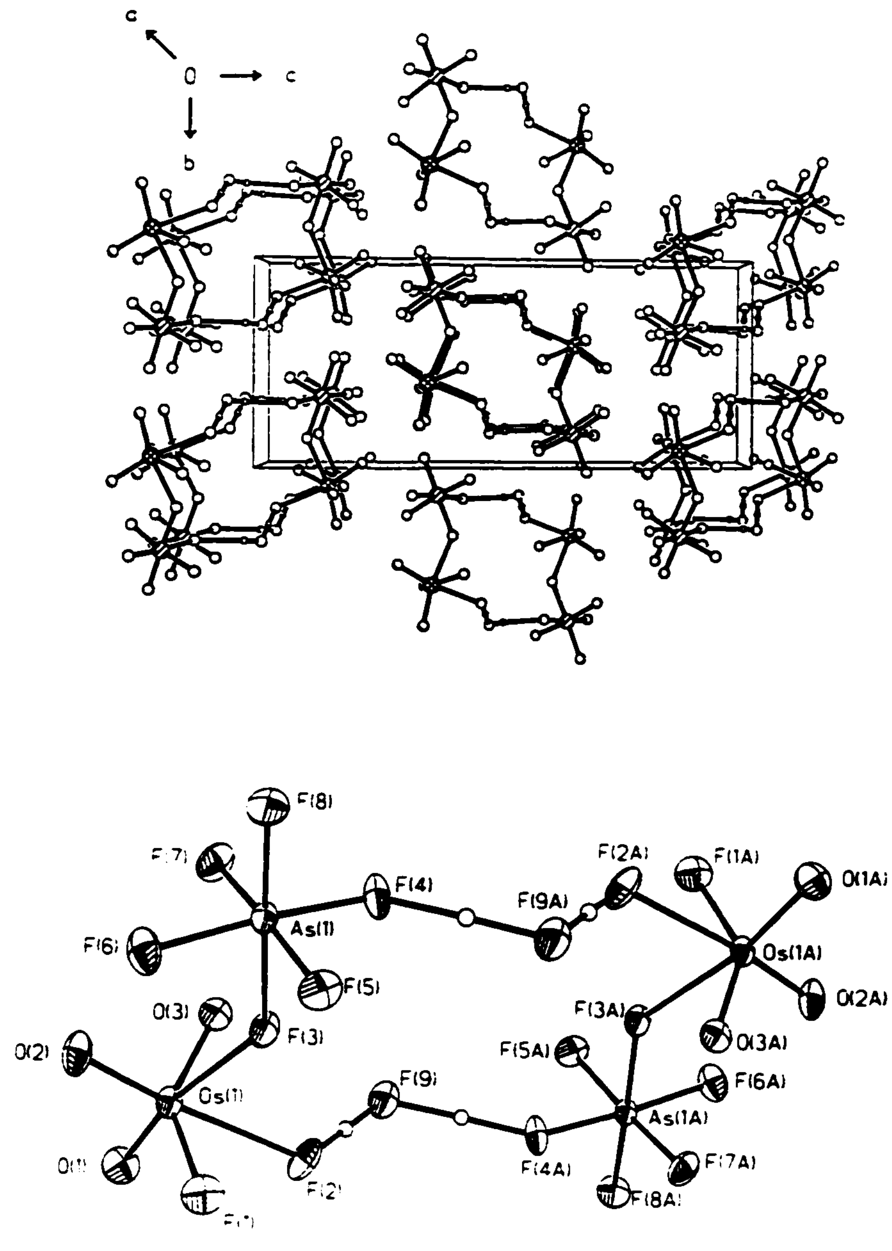

Figure 8.2 Views of (a) the $[OsO_3F][HF]_2[AsF_6]$ unit cell showing the packing along the *a*-axis and (b) the $([OsO_3F][HF]_2[AsF_6])_2$ dimer (thermal ellipsoids are shown at the 50% probability level).

(100.0(3), 102.4(3), and 141.6(3)°) are significantly distorted from C_{3v} symmetry as a result of the coordination of one fluorine from an AsF_6^- anion and one fluorine from an HF solvent molecule. The resulting OsO_3F_3 moiety exhibits a facial arrangement of the oxygen and fluorine atoms as found for the *fac*-$OsO_3F_3^-$ anion in $[N(CH_3)_4][OsO_3F_3]$ (see 7.2.1.4. X-ray Crystal Structure of $[N(CH_3)_4][OsO_3F_3]$). The Os-F contacts with 223.0(4) and 227.9(5) pm are much stronger than those found in $[OsO_3F][AsF_6]$ (245.0(7) pm). This structure, together with that of $[OsO_3F][HF][SbF_6]$ (*vide infra*), represents a rare example of an HF molecule coordinated to a metal centre. The only other reported examples are $[La][HF]_2[AsF_6]_3$[226] and $[(\eta^5\text{-}C_5Me_5)NbF_4(HF)AsF_3]_2$.[227] In the latter structure, HF also bridges two metal centers. The F(2)---F(9) and F(9)---F(4A) distances in $[OsO_3F][HF]_2[AsF_6]$ of 242.9(8) and 251.2(8) pm, respectively, are shorter than the F---F distance in $[(\eta^5\text{-}C_5Me_5)NbF_4(HF)AsF_3]_2$ (268.6 pm),[227] indicating stronger hydrogen-bonding in the $[OsO_3F][HF]_2[AsF_6]$ structure. The F---F distances in $[OsO_3F][HF]_2[AsF_6]$ are, however, much larger than that found for bifluoride in $[N(CH_3)_4][HF_2]$ (221.3(4) pm)[228] and are also significantly larger than the F---F distances in $NiF(HF)(C_4N_2F_2H)(PEt_3)_2$ (240.0(6) pm),[229] *trans*-[Ru(dmpe)$_2$(H)(FHF)] (227.6(8) pm),[230] $Mo(PMe_3)_4(H)_2F(FHF)$ (235.1(8) pm),[331] and in $WF(H)_2(FHF)(PMe_3)_4$ (238.9(6) pm),[232] where one HF molecule is hydrogen-bridged to a fluorine ligand of the metal centre. Similarly, one HF molecule is bridged to the fluorine on As in $[OsO_3F][HF]_2[AsF_6]$. The previously reported structures, however, contain a terminal HF molecule and can, alternatively, be described as an HF_2^- ligand coordinated to the metal.

The symmetry of the AsF_6^- anion is lowered to C_{2v} point symmetry or lower by formation of As-F---Os and As-F---HF bridges, which are *cis* to each other, producing significantly elongated As-F bonds of 182.3(4) and 173.5(5) pm, respectively, compared to the remaining four As-F bonds (168.9(4) to 170.5(5) pm).

8.2.2.3. Structure of $[OsO_3F][HF][SbF_6]$. The $[OsO_3F][HF][SbF_6]$ salt crystallizes in the non-centrosymmetric *Pc* space group as a 2:1 twin preventing a proper absorption correction. As a consequence it was not possible to refine the fluorine and oxygen atoms anisotropically. The relatively large errors in the bond lengths and bond angles prevents a detailed structural comparison with related structures. Two fluorine-bridged OsO_3F^+/SbF_6^- ion pairs defined in the asymmetric unit (Figure 8.3). One HF molecule bridges the osmium centre and a fluorine of the SbF_6^- anion of another OsO_3F^+/SbF_6^- ion pair resulting in a helical arrangement comprising alternating OsO_3F^+ and SbF_6^- ions running parallel to the *a*-axis (Figure 8.3). The bond lengths and angles in both crystallographically independent anion-cation pairs are the same within 3σ.

As in the crystal structure of $[OsO_3F][HF]_2[AsF_6]$, the coordination sphere of the OsO_3F^+ cation is expanded by fluorine bridge formation with an SbF_6^- and an HF molecule, resulting in *fac*-OsO_3F_3 coordination. One F-Os-O bond angle of the OsO_3F^+ cation is also significantly larger (142.7(7)/143.4(8)°) than the other two (98.0(7)/100.0(8)° and 101.2/101.3(8)°). All the bond lengths and bond angles in $[OsO_3F][HF][SbF_6]$ are the same, within 3σ, as those in $[OsO_3F][HF]_2[AsF_6]$.

8.2.2.4. Structure of $[OsO_3F][Sb_3F_{16}]$. The crystal structure of $[OsO_3F][Sb_3F_{16}]$ consists

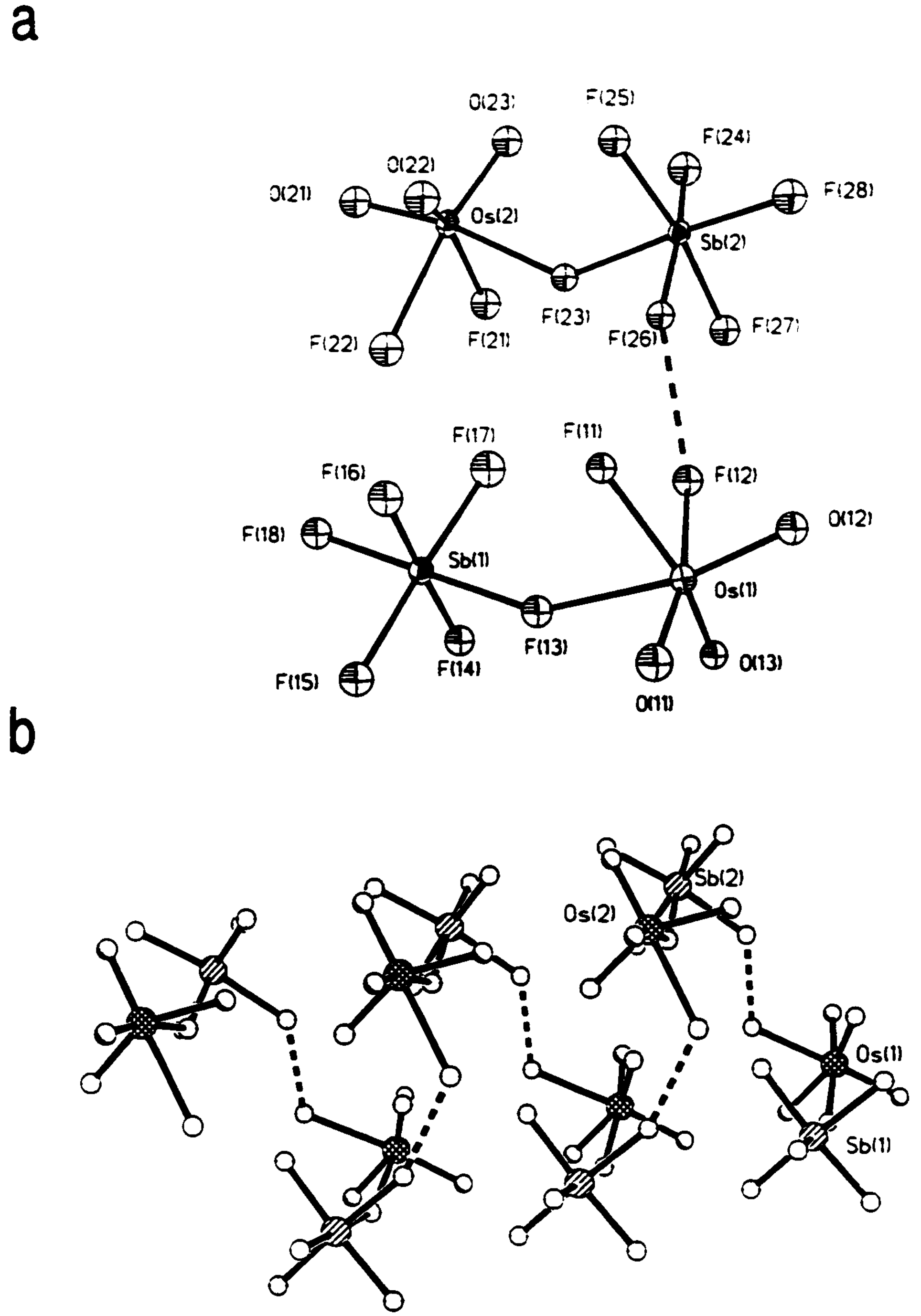

Figure 8.3 Views of (a) the asymmetric unit of $[OsO_3F][HF][SbF_6]$ and (b) the $([OsO_3F][HF][SbF_6])_n$ helix along the *a*-axis (thermal ellipsoids are shown at the 50% probability level).

of separate OsO_3F^+ and *cis*-fluorine-bridged $Sb_3F_{16}^-$ ions. The OsO_3F^+ cation is located on a special position ($\bar{4}$..) resulting in a positional disorder of the symmetry-related oxygen and fluorine atoms. A disorder between two different orientations could be resolved for the $Sb_3F_{16}^-$ anion. The disorder in the cation and anion prevented the anisotropic refinement of all the fluorine and oxygen atoms giving rise to a relatively large R-factor. The *cis*-fluorine-bridged $Sb_3F_{16}^-$ anions pack in the (110) and (-110) planes in such a way that they form square-based channels parallel to the *c*-axis which are filled with rows of OsO_3F^+ cations (Figure 8.4).

The first coordination sphere around osmium is essentially tetrahedral with an average Os-O/F bond length of 168(3) pm which is the same as the average of the Os-O and Os-F bond lengths in $[OsO_3F][AsF_6]$, $[OsO_3F][HF]_2[AsF_6]$, and $[OsO_3F][HF][SbF_6]$. The osmium atom also has long contacts to a fluorine of each of the four $Sb_3F_{16}^-$ anions (Os···F(10B/10A); 283(6)/285(6) pm) with the trajectory through the centre of each trigonal face of the tetrahedral cation, forming a second tetrahedral coordination sphere. The $Sb_3F_{16}^-$ anion adopts a *cis*-fluorine-bridged geometry as found for the $Sb_3F_{16}^-$ and $Sb_4F_{21}^-$ anions in the crystal structures of $[XeN(SO_2F)_2][Sb_3F_{16}]$,[233] and $[Xe_2][Sb_4F_{21}]$,[234] respectively. This geometry was also found in SO_2ClF solutions of $[OsO_3F][Sb_3F_{16}]$ by ^{19}F NMR spectroscopy and contrasts with the structure of $[Br_2][Sb_3F_{16}]$ in which $Sb_3F_{16}^-$ was found to contain a *trans*-fluorine-bridged $Sb_3F_{16}^-$ anion.[235] The high standard deviations in the bond lengths and bond angles of $[OsO_3F][Sb_3F_{16}]$ prevent a detailed comparison to related anion structures.

a

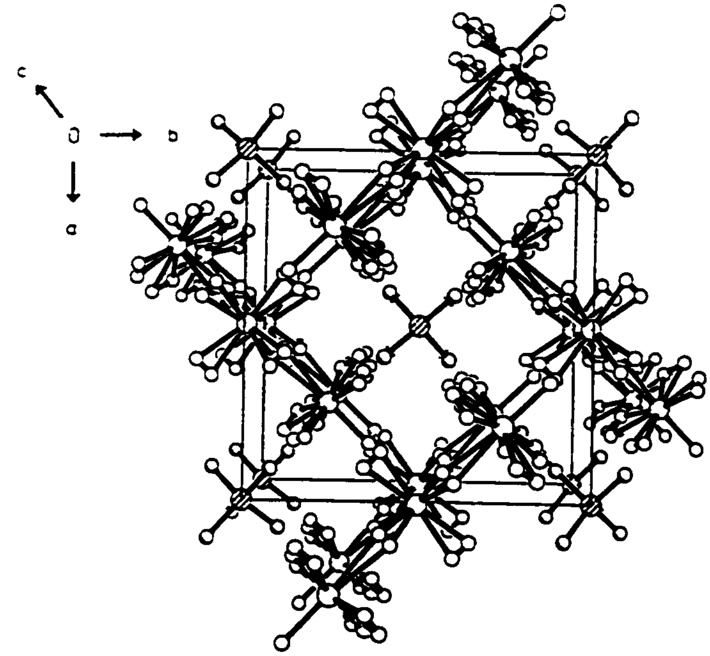

b

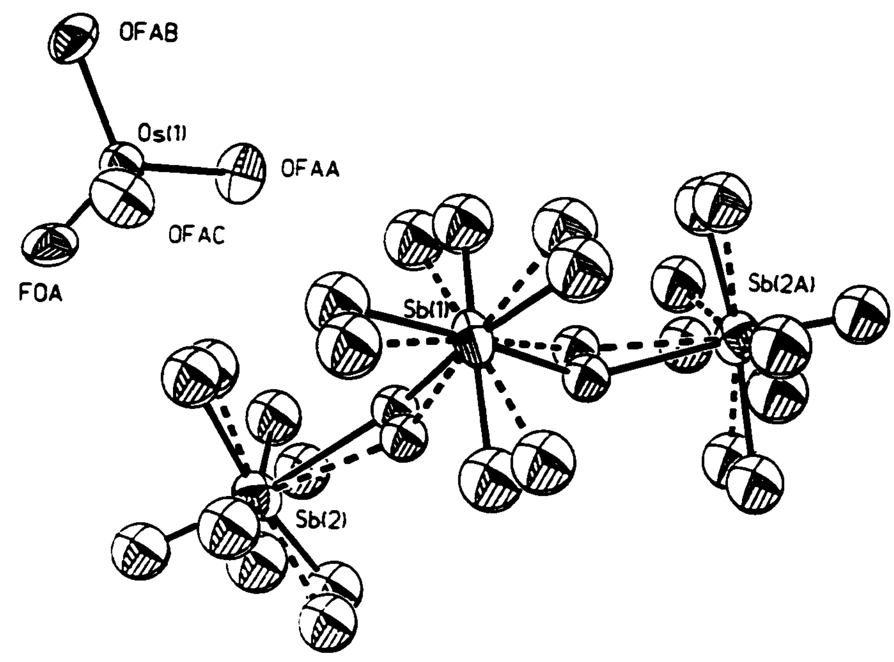

Figure 8.4 Views of (a) the $[OsO_3F][Sb_3F_{16}]$ unit cell showing the packing along the *c*-axis and (b) the OsO_3F^+ and $Sb_3F_{16}^-$ ions (thermal ellipsoids are shown at the 50% probability level).

8.2.3. Raman Spectroscopy

The $[OsO_3F][Sb_3F_{16}]$, $[OsO_3F][PnF_6]$ (Pn = As, Sb), $[OsO_3F][HF][SbF_6]$, $[OsO_3F][HF]_2[PnF_6]$ (Pn = As, Sb), and $[Os_2O_6F_3][AsF_6]$ salts were characterized by low temperature Raman spectroscopy (Figures 8.5 to 8.8) and the observed Raman frequencies and their assignments are given in Tables 8.4 to 8.8. The free OsO_3F^+ cation is expected to have C_{3v} point symmetry and the vibrational modes span the irreducible representations $3A_1 + 3E$ where all modes are infrared and Raman active.

8.2.3.1. $[OsO_3F][Sb_3F_{16}]$. The low-temperature Raman spectrum of $[OsO_3F][Sb_3F_{16}]$ contains at least five bands attributed to the OsO_3F^+ cation and anion bands in the Sb-F stretching and F-Sb-F bending regions. The frequencies and intensities of the Raman bands for the $Sb_3F_{16}^-$ anion reported in the literature vary significantly depending on the nature of the countercation. Among the three known $Sb_3F_{16}^-$ salts that have been characterized by Raman spectroscopy, *i.e.*, $[PF_4][Sb_3F_{16}]$,[236] $[XeN(SO_2F)_2][Sb_3F_{16}]$,[233] and $[ReF_6][Sb_3F_{16}]$,[237] the Raman frequencies and intensities attributed to the $Sb_3F_{16}^-$ anion in $[PF_4][Sb_3F_{16}]$ show the best agreement with those of $[OsO_3F][Sb_3F_{16}]$.

The presence of only two Os-O stretching bands ($\nu_1(A_1)$ and $\nu_4(E)$) is consistent with the C_{3v} point symmetry of the OsO_3F^+ cation and is confirmed by the high symmetry of the disordered cation in the crystal structure of $[OsO_3F][Sb_3F_{16}]$ (see 8.2.2.4. X-ray Crystallography; Structure of $[OsO_3F][Sb_3F_{16}]$). The Os-O stretches of the OsO_3F^+ cation (1002 and 992 cm^{-1}) appear at significantly higher frequencies than those of the neutral parent compound, monomeric OsO_3F_2 (946.5 and 929.0 cm^{-1}),[86] which is in accord with

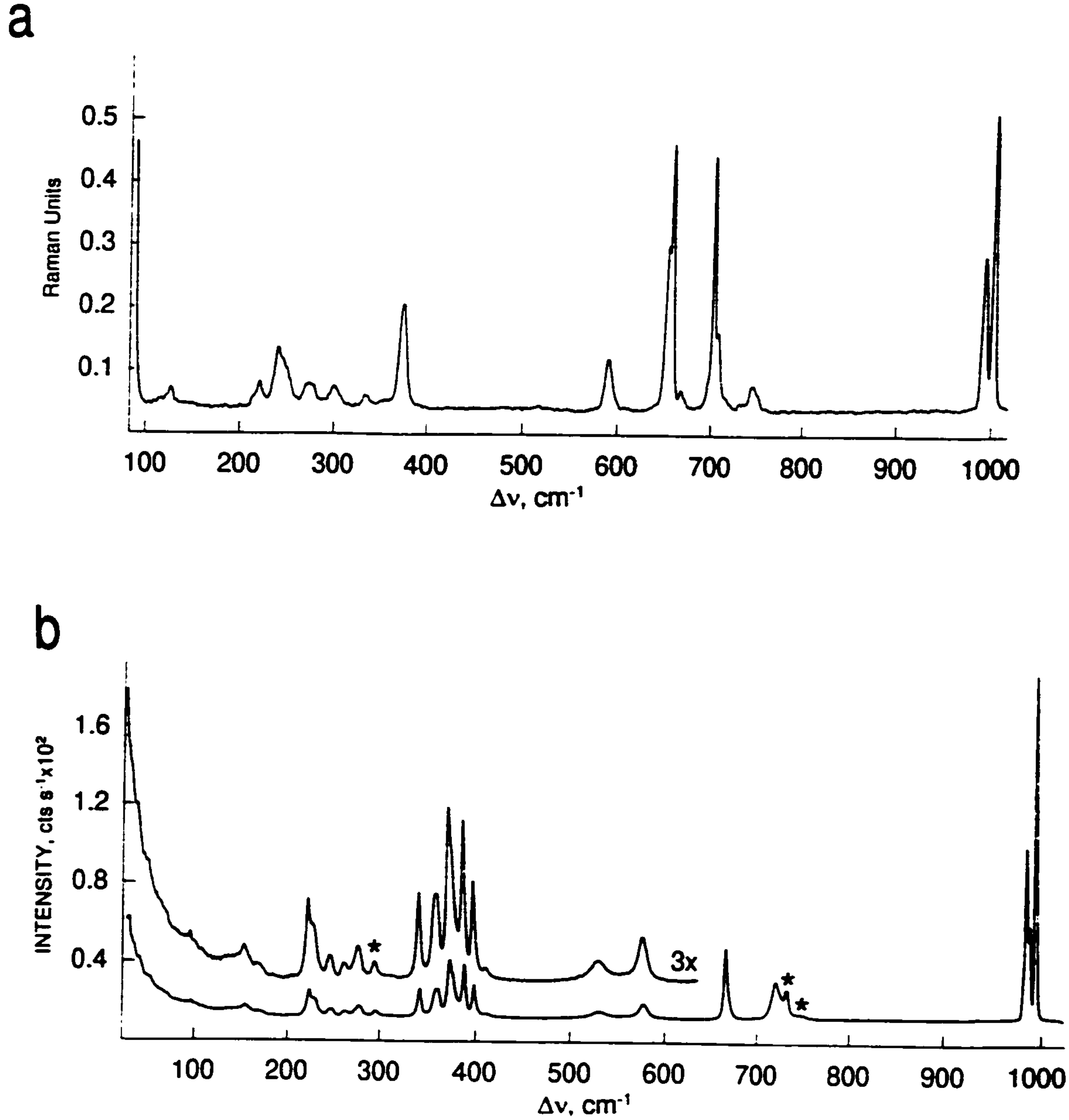

Figure 8.5 Raman spectra of (a) microcrystalline $[OsO_3F][Sb_3F_{16}]$ recorded in a Pyrex glass capillary at -165 °C using the 1064-nm excitation and (b) microscrystalline $[OsO_3F][AsF_6]$ recorded in a ¼-in. FEP sample tube at -150 °C using the 647.1-nm excitation. Asterisks (*) denote FEP sample tube lines.

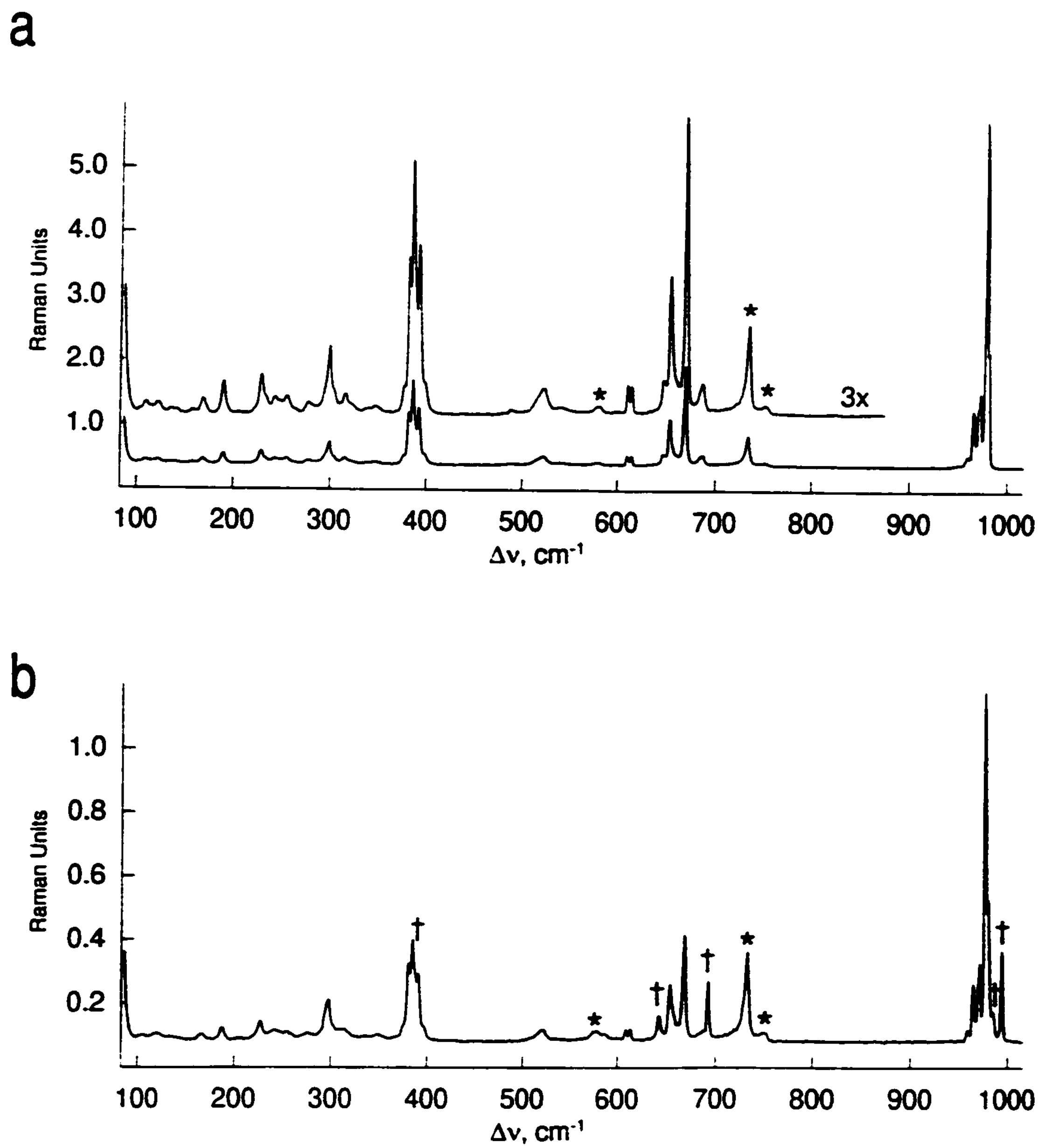

Figure 8.6 Raman spectra of (a) microcrystalline $[OsO_3F][HF][SbF_6]$ at -165 °C and (b) microcrystalline $[OsO_3F][HF][SbF_6]$ containing $[OsO_3F][SbF_6]$ at -150 °C recorded in ¼-in. FEP sample tubes using the 647.1-nm excitation. Asterisks (*) denote FEP sample tube lines. Daggers (†) denote bands arising from $[OsO_3F][SbF_6]$.

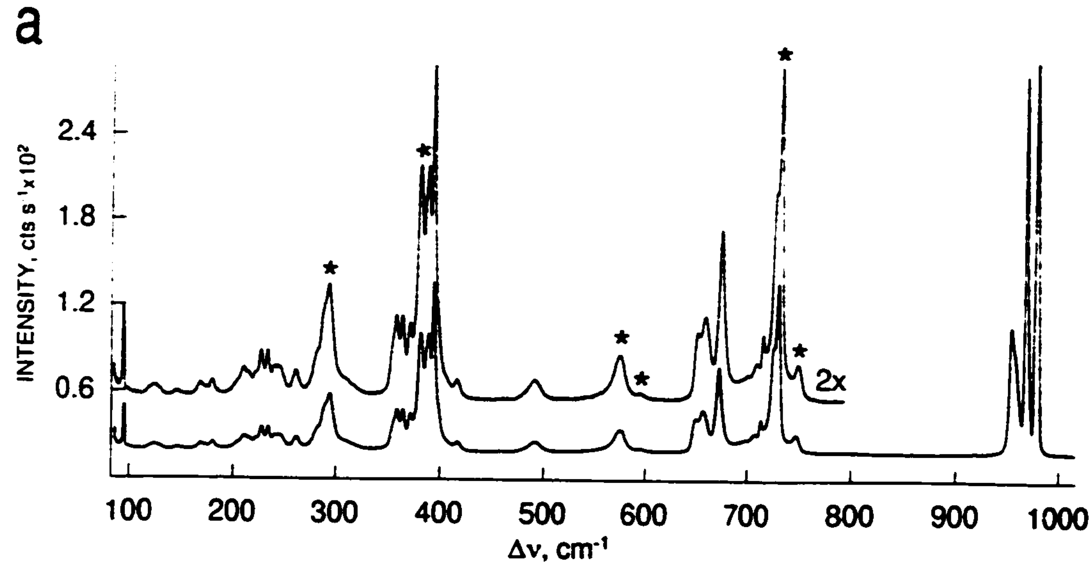

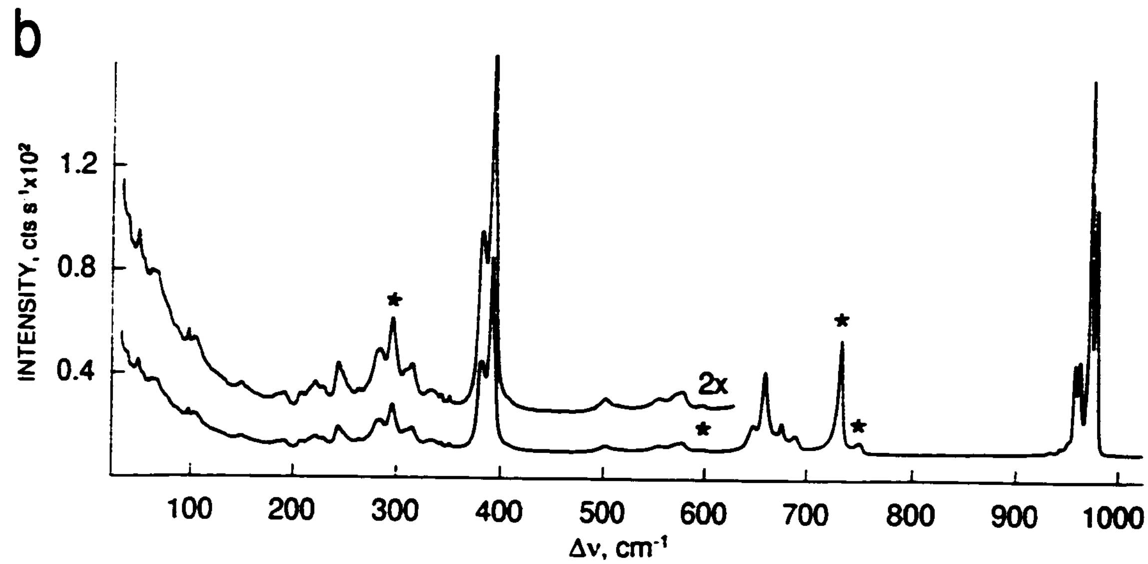

Figure 8.7 Raman spectra of (a) microcrystalline $[OsO_3F][HF]_2[AsF_6]$ recorded in a ¼-in. FEP sample tube at -140 °C using the 647.1-nm excitation and (b) microcrystalline $[OsO_3F][HF]_2[SbF_6]$ under HF solvent recorded in a ¼-in. FEP sample tube at -80 °C using the 647.1-nm excitation. Asterisks (*) denote FEP sample tube lines.

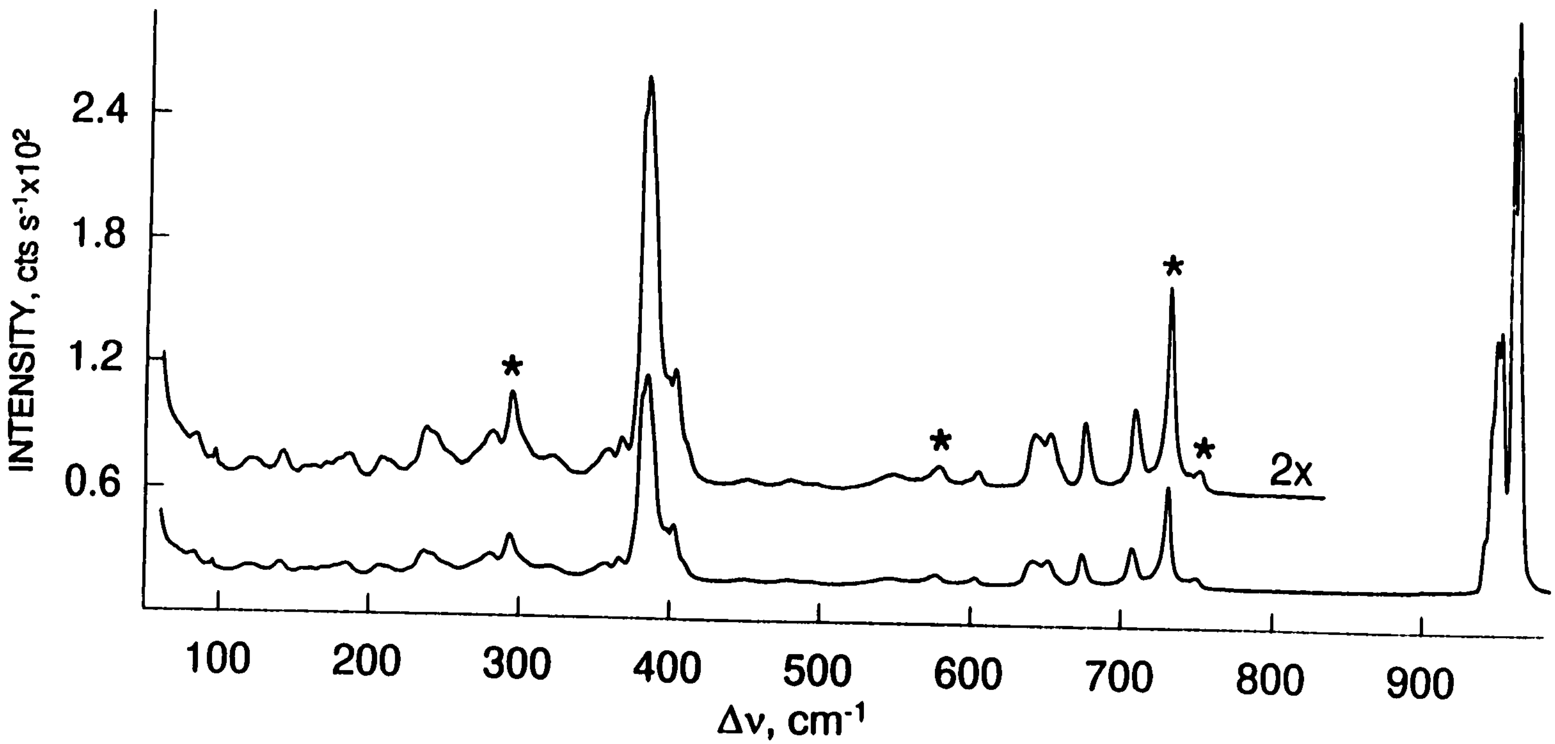

Figure 8.8 Raman spectra of microcrystalline [μ-F($OsO_3F)_2$][AsF_6] under HF solvent recorded in a ¼-in. FEP sample tube at -80 °C using the 647.1-nm excitation. Asterisks (*) denote FEP sample tube lines.

Table 8.4 Raman Frequencies and Their Assignments for $[OsO_3F][Sb_3F_{16}]$

Frequency,[a] cm^{-1}	Assignment	
	OsO_3F^+ (C_{3v})	$Sb_3F_{16}^-$
1002 (100)	$\nu_1(A_1)$; $\nu_s(OsO_3)$	
992 (53)	$\nu_4(E)$; $\nu_{as}(OsO_3)$	
745 (9)	$\nu_2(A_1)$; $\nu_s(OsF)$	
731 (3)		$\nu(SbF)$
707 (25)		
701 (87)		
696 sh(10)		
666 (7)		
656 (92)		
652 (56)		
588 (18)		
372 (36)	$\nu_3(A_1)$; $\delta(OsO_3)$	
333 (4)	$\nu_5(E)$	
298 (7)		$\delta(SbF)$
271 (9)		
248 (13)		
242 (16)		
238(21)		
218 (9)		
212 (3)		
125 (6)		
84 (86)		
71 (7)		
60 (6)		

[a] Spectrum recorded on microcrystalline solid in a Pyrex glass capillary at -165 °C using the 1064-nm excitation. Values in parentheses denote relative intensities. Abbreviation (sh) denotes a shoulder.

Table 8.5 Raman Frequencies and Their Assignments for $[OsO_3F][PnF_6]$, Pn = As, Sb

Frequency,[a] cm^{-1}		Assignment		
$[OsO_3F][AsF_6]$[b]	$[OsO_3F][SbF_6]$[c]	OsO_3F^+	AsF_6^- (C_{4v})	SbF_6^- (C_{4v})
996 (100)	995 (100)	$\nu_s(OsO_3)$		
990 (27)		$\nu_{as}(OsO_3)$		
986 (50)	986 (32)	$\nu_{as}(OsO_3)$		
984 (14)sh				
725 (8)sh			$\nu_8(E)$	
721 (11)				
	692 (65)			$\nu_8(E)$
666 (21)	656 sh		$\nu_1(A_1)$	$\nu_1(A_1)$
	642 (28)			$\nu_2(A_1)$
576 (5)[a]			$\nu_5(B_1)$	
529 (2)			$\nu_4(A_1)$	
410 (1)			$\nu_3(A_1)$	
397 (10)		$\delta(OsO_3)$		
387 (16)	386 sh			
374 (13)sh			$\nu_9(E)$	
372 (17)				
358 (8)			$\nu_7(B_2)$	
341 (8)				
276 (3)			$\nu_{11}(E)$	
259 (2)				
244 (3)				
225 (5)				
221 (8)				
167 (1)				
152 (3)				

[a] Values in parentheses denote relative intensities. Abbreviation (sh) denotes a shoulder.

[b] Spectrum recorded on microcrystalline solid in a ¼-in. FEP sample tube at -150 °C using the 647.1-nm excitation. Bands arising from FEP sample tube were observed at 293 (2), 733 (9), and 746 (2) cm^{-1}.

[c] Spectrum recorded on solid in admixture with $[OsO_3F][HF][SbF_6]$ in a ¼-in. FEP sample tube at -165 °C using the 1064-nm excitation.

[d] This band overlaps with a band arising from the FEP sample tube.

Table 8.6 Raman Frequencies and Their Assignments for $[OsO_3F][HF][SbF_6]$

Frequency,[a] cm^{-1}	Assignment	
	OsO_3F^+ (C_{3v})	SbF_6^- (C_{4v})
981 (33)	$\nu_s(OsO_3)$	
977 (100)		
972 (21)	$\nu_{as}(OsO_3)$	
970 (17)		
965 (16)	$\nu_{as}(OsO_3)$	
960 (3)		
685 (3)		$\nu_8(E)$
668 (29)		$\nu_1(A_1)$
652 (13)	$\nu_s(Os\text{-}F)$	
645 (3)		$\nu_2(A_1)$
613 (3)		$\nu_5(B_1)$
609 (3)		
537 (1)		
520 (3)		
515 (2)sh		
487 (<0.5)		$\nu_4(A_1)$
397 (3)		
390 (17)		
384 (25)	$\delta_s(OsO_3)$	
380 (16)		
375 (3)		
345 (<0.5)		
312 (2)		
297 (6)[b]		$\nu_9(E)$
275 (1)		
254 (2)		
239 (1)		
226 (4)		
187 (3)		
165 (1)		
155 (<0.5)		
135 (<0.5)		
120 (1)		
106 (1)		
84 (12)	laser line	

[a] Spectrum recorded on microcrystalline solid in a ¼-in. FEP sample tube at -150 °C using the 1064-nm

excitation. Values in parentheses denote relative intensities. Abbreviation (sh) denotes a shoulder. Bands arising from FEP sample tube were observed at 297 (6), 579 (1), 734 (8), and 751 (1) cm^{-1}.

[b] This band overlaps with a band arising from the FEP sample tube.

Table 8.7 Raman Frequencies and Their Assignments for $[OsO_3F][HF]_2[PnF_6]$ (Pn= As, Sb)

Frequency,[a] cm^{-1}		Assignment		
$[OsO_3F][HF]_2[AsF_6]$[b]	$[OsO_3F][HF]_2[SbF_6]$[c]	OsO_3F^- (C_{3v})	AsF_6^- (C_{4v})	SbF_6^- (C_{4v})
981 (100)	979 (65)	$\nu_s(OsO_3)$		
971 (97)	973 (100)			
959 (26)sh	963 (25)	$\nu_{as}(OsO_3)$		
957 (33)	960 (24)			
	954 (4)			
	945 (3)			
728 (26)sh[a]	688 (5)		$\nu_8(E)$	$\nu_8(E)$
716 (9)	675 (8)			
710 (5)				
674 (22)	658 (22)		$\nu_1(A_1)$	$\nu_1(A_1)$
659 (11)	646 (8)		$\nu_2(A_1)$	$\nu_2(A_1)$
651 (9)				
596 (1)				
576 (6)[d]	572 (3)		$\nu_5(B_1)$	$\nu_5(B_1)$
	555 (2)			
491 (6)	501 (2)		$\nu_4(A_1)$	$\nu_4(A_1)$
417 (3)			$\nu_3(A_1)$	
	391 (31)sh			$\nu_7(B_2)$
398 (11)sh	388 (51)[d]			
393 (42)	378 (24)[d]	$\delta(OsO_3)$		
371 (10)				
364 (10)			$\nu_9(E)$	
358 (10)			$\nu_7(B_2)$	
354 (7)sh	348 (2)			
	340 (2)			
	330 (3)			
	311 (6)			
289 (10)sh[d]	306 (5)			
282 (5)sh				
	292 (12)			$\nu_9(E)$
	281 (8)			$\nu_3(A_1)$
261 (3)	260 (3)			
245 (3)				

Table 8.7 continued...

Frequency,[a] cm^{-1}		Assignment		
$[OsO_3F][HF]_2[AsF_6]$[b]	$[OsO_3F][HF]_2[SbF_6]$[c]	OsO_3F^+ (C_{3v})	AsF_6^- (C_{4v})	SbF_6^- (C_{4v})
240 (3)				
	240 (6)			ν_{11}(E)
234 (6)				
227 (6)	225 (3)			
221 (3)	218 (3)			
215 (3)				
210 (3)	204 (2)			
	188 (1)			
179 (2)	180 (1)			
167 (2)				
144 (1)	145 (1)			
123 (1)				
	101 (2)			
	93 (2)			

[a] Values in parentheses denote relative intensities. Abbreviation (sh) denotes a shoulder.

[b] Spectrum recorded on microcrystalline solid in a ¼-in. FEP sample tube at -140 °C using the 647.1-nm excitation. Bands arising from FEP sample tube were observed at 293 (14), 381 (30), 389 (30), 576 (6), 596 (1), 733 (43), and 750 (5) cm^{-1}.

[c] Spectrum recorded on solid under HF solvent in a ¼-in. FEP sample tube at -80 °C using the 647.1-nm excitation. Bands arising from FEP sample tube were observed at 292 (12), 576 (3), 596 (1), 732 (31), and 749 (3) cm^{-1}.

[d] This band overlaps with a band arising from the FEP sample tube.

Table 8.8. Raman Frequencies and Their Assignments for $[Os_2O_6F_3][AsF_6]$

Frequency, cm^{-1} [a]	Assignment	
$[Os_2O_6F_3][AsF_6]$	$Os_2O_6F_3^+$	AsF_6^- (O_h)
967 (100)	$\nu_s(OsO_3)$ in-phase	
963 (91)	$\nu_s(OsO_3)$ out-of-phase	
956 (45)	$\nu_{as}(OsO_3)$ in-phase	
953 (44)	$\nu_{as}(OsO_3)$ out-of-phase	
949 (29)sh	$\nu_{as}(OsO_3)$ in-phase	
944 (10)sh	$\nu_{as}(OsO_3)$ out-of-phase	
744 (2)		
708 (8)		$\nu_3(T_{1u})$
675 (6)		$\nu_1(A_{1g})$
651 (5)	ν_s(Os-F)	
641 (5)		
603 (2)		
545 (1)		
493 (<1)		
478 (1)		
448 (1)		
408 (3)sh		
402 (10)		
397 (10)		
384 (36)	$\delta(OsO_3)$	
381 (32)sh		
365 (4)		$\nu_5(T_{2g})$
356 (3)		
320 (2)		
250 (2)		
240 (4)		
235 (4)		
182 (2)		
176 (1)		
167 (1)		

Table 8.8. continued...

Frequency, cm^{-1} [a]	Assignment	
$[Os_2O_6F_3][AsF_6]$	$Os_2O_6F_3^+$	AsF_6^- (O_h)
159 (1)		
152 (1)		
139 (2)		
117 (1)		
81 (2)		

[a] Spectrum recorded on the solid under liquid HF solvent in a ¼-in. FEP sample tube at -80 °C using the 647.1-nm excitation. Values in parentheses denote relative intensities. Abbreviation (sh) denotes a shoulder. Bands arising from FEP sample tube were observed at 292 (8), 576 (2), 732 (18), and 751 (2) cm^{-1}.

stronger and less polar Os-O bonds. The Re-O stretching frequencies of isoelectronic ReO_3F agree well with those of the cationic Os analogue and differ by less than 15 cm^{-1}. The Raman band at 745 cm^{-1} is tentatively assigned to the Os-F stretch which is at significantly higher frequency than those of matrix-isolated monomeric OsO_3F_2 (646.0, 619.0 cm^{-1})[86] and ReO_3F (666 cm^{-1})[221] and is in accord with the positive charge of OsO_3F^+ and a correspondingly less polar Os-F bond. The symmetric OsO_3 bend appears at 370 cm^{-1} which is between the ReO_3 bending frequencies in ReO_3F obtained from an HF solution[221] and a N_2 matrix.[223] The unambiguous assignment of the Os-F stretching mode and the $\nu_6(E)$ cation bending mode was not possible because of the large number of anion modes in that region of the spectrum.

The $[OsO_3F][Sb_3F_{16}]$ salt represents the best approximation to a free OsO_3F^+ cation as evidenced by the absence of splitting for the degenerate modes and the fact that the stretches appear at the highest frequencies when compared to those of other OsO_3F^+ salts (*vide infra*).

8.2.3.2. $[OsO_3F][AsF_6]$ and $[OsO_3F][SbF_6]$. The Raman spectrum of $[OsO_3F][AsF_6]$ is far more complex than suggested by its simple ionic formulation. The observation of 13 cation bands and 10 anion bands indicates a significant reduction of symmetry from the ideal C_{3v} point symmetry of the OsO_3F^+ cation and O_h symmetry of the AsF_6^- anion, and is corroborated by the crystallographic findings. The Raman frequencies of only the most intense bands of $[OsO_3F][SbF_6]$ have been observed, since it could only be obtained as a minor component in admixture with $[OsO_3F][HF][SbF_6]$ (*vide supra*) but the cation bands correspond to those of $[OsO_3F][AsF_6]$.

The Os-O stretching frequencies in $[OsO_3F][AsF_6]$ are approximately 6 cm^{-1} lower than those in $[OsO_3F][Sb_3F_{16}]$, resulting from the higher nucleophilicity of the AsF_6^- anion, which forms stronger contacts to the OsO_3F^+ cation in the solid state to five the $(OsO_3F{\cdots}FAsF_5)_2$ dimer (see 8.2.2.1. X-Ray Crystallography; Structure of $[OsO_3F][AsF_6]$). These contacts distort the OsO_3F^+ cation, resulting in splitting of the degenerate $\nu_4(E)$ mode and the observation of three Os-O stretching bands. A shoulder at 984 cm^{-1} may arise from vibrational coupling of the OsO_3 modes in the dimer. The Os-F stretching frequency could not be assigned, because the intense anion modes in that region of the spectrum obscure the weak Os-F stretching band which is expected to occur at significantly lower frequency than that of $[OsO_3F][Sb_3F_{16}]$ (745 cm^{-1}). Detailed assignments of the bending modes were not possible because of the high degree of vibrational coupling between the two bridged $OsO_3F{\cdots}FAsF_5$ units.

8.2.3.3. $[OsO_3F][HF]_2[PnF_6]$ (Pn = As, Sb) and $[OsO_3F][HF][SbF_6]$. As in the case of $[OsO_3F][AsF_6]$, the Raman spectra of $[OsO_3F][HF]_2[PnF_6]$ and $[OsO_3F][HF][SbF_6]$ indicate lowering of the symmetry of the cation and anion from their ideal C_{3v} and O_h point symmetries, respectively. The AsF_6^- and SbF_6^- anion bands were assigned under C_{4v} point symmetry based on previous assignements,[238] however, the crystal structure shows that the anion symmetries are C_{2v} or lower.

The Raman spectra of $[OsO_3F][HF]_2[PnF_6]$ (Pn = As, Sb) are very similar suggesting that the two compounds are isostructural. Three Os-O stretching modes appear

16 to 20 cm^{-1} lower in the Raman spectrum of $[OsO_3F][HF]_2[AsF_6]$ than those of $[OsO_3F][AsF_6]$. The band splittings are consistent with the distorted OsO_3F^+ cation found in the crystal structure of $[OsO_3F][HF]_2[AsF_6]$. A shoulder at 959 cm^{-1} and the observed splittings of the Os-O stretching bands in the Raman spectra of $[OsO_3F][HF]_2[AsF_6]$ and $[OsO_3F][HF]_2[SbF_6]$, respectively, are likely a result of vibrational coupling between two $OsO_3F{\cdots}FPnF_5$ moieties which are found to be bridged by two HF molecules in the structure of $[OsO_3F][HF]_2[AsF_6]$. The Os-O stretches of $[OsO_3F][HF][SbF_6]$ have frequencies similar to those of $[OsO_3F][HF]_2[PnF_6]$. However, all three Os-O stretches are split by ca. 3 cm^{-1} which can be explained by the stronger vibrational coupling that results from the shorter HF bridge in the helical solid state structure of $[OsO_3F][HF][SbF_6]$ (see 8.2.2.3. X-Ray Crystallography; Structure of $[OsO_3F][HF][SbF_6]$). The Os-F stretches and the bending modes in the Raman spectra could not be unambiguously assigned due to strong vibrational coupling and overlap with the anion bands.

8.2.3.4. $[Os_2O_6F_3][AsF_6]$. The Raman spectrum of $[Os_2O_6F_3][AsF_6]$ contains six Os-O stretching bands consistent with a fluorine-bridged μ-$F(OsO_3F)_2^+$ cation in which the two OsO_3F moieties are vibrationally coupled to each other. The splittings of the Os-O stretching bands range from 5 to 3 cm^{-1} and agree very well with the degree of coupling observed for μ-$F(\textit{cis}\text{-}OsO_2F_3)^+$ cation.[91] The bands at 651 and 641 cm^{-1} are tentatively assigned to the two Os-F stretching bands and appear at much lower frequencies than that in $[OsO_3F][Sb_3F_{16}]$ (745 cm^{-1}), which is consistent with a lower charge density in the dinuclear cation and a correspondingly lower Os-F polarity. Contacts between the cation and the AsF_6^- anion are likely, becauce the pentacoordinate osmium in μ-$F(OsO_3F)_2^+$ is coordinatively unsaturated and because formally Raman inactive anion modes are observed in the Raman spectrum.

8.3. Conclusion

The fluoride ion donor properties of OsO_3F_2 were studied and the new compounds, $[OsO_3F][PnF_6]$, $[OsO_3F][HF][SbF_6]$, $[OsO_3F][HF]_2[PnF_6]$, and $[Os_2O_6F_3][AsF_6]$ have been prepared from HF solutions of OsO_3F_2 and the Lewis acids, AsF_5 or SbF_5, and have been characterized by Raman spectroscopy. The OsO_3F^+ cations in the crystal structures of $[OsO_3F][AsF_6]$, $[OsO_3F][HF][SbF_6]$, and $[OsO_3F][HF]_2[AsF_6]$ extend their coordination spheres by fluorine bridging with the PnF_6^- anions and HF molecules to the Os centre and therefore deviate significantly from the ideal point symmetry of an isolated OsO_3F^+ cation. The closest approximation to a free OsO_3F^+ cation was found in the crystal structure of $[OsO_3F][Sb_3F_{16}]$ which was isolated from neat SbF_5 solvent.

CHAPTER 9

LEWIS-ACID PROPERTIES OF OsO_2F_4

9.1. Introduction

The highest, and most common, coordination number for osmium in the +8 oxidation state that has been reported to date is six. In the presence of four oxygen double-bond domains, coordination numbers of four (OsO_4)[214] and five (OsO_4F^-) (see Chapter 6) are well established. Monomeric, pentacoordinate OsO_3F_2 has only been isolated in a matrix[86] and polymerizes to form a fluorine-bridged chain structure in which Os(VIII) exhibits hexacoordination.[7] Only the strong Lewis acid, neat SbF_5, can stabilize the pentacoordinate $OsO_2F_3^+$ [91] and tetracoordinate OsO_3F^+ cations (see Chapter 8). Their coordinatively unsaturated nature is documented by failed attempts to obtain crystals containing the $OsO_2F_3^+$ cation,[91] isolation of the fluorine-bridged $Os_2O_4F_7^+$ cation in the solid state, and by the strong anion-cation contacts in crystal structures containing the OsO_3F^+ cation (see Chapter 8). The present work investigates the Lewis acidity of *cis*-OsO_2F_4 yielding Lewis acid-base adducts having an Os(VIII) coordination number of seven.

9.2. Results and Discussion

9.2.1. Fluoride Ion Acceptor Properties of *cis*-OsO_2F_4

9.2.1.1. Synthesis of $OsO_2F_5^-$. Purple *cis*-OsO_2F_4 reacts with CsF at 150 °C according to equation (9.1) yielding light brown [Cs][OsO_2F_5], which was characterized by Raman

$$CsF + OsO_2F_4 \xrightarrow{150\ °C} [Cs][OsO_2F_5] \qquad (9.1)$$

spectroscopy. Osmium dioxide tetrafluoride is moderately soluble in liquid NOF at -78 °C yielding a deep red solution and exists in equilibrium (9.2) with [NO][OsO_2F_5] in the

$$NOF + OsO_2F_4 \overset{NOF}{\rightleftharpoons} [NO][OsO_2F_5] \qquad (9.2)$$

precipitate and in solution based on the Raman and ^{19}F NMR spectra. Removal of the NOF solvent at -78 °C results in dissociation of [NO][OsO_2F_5] to OsO_2F_4 and NOF. Tetramethylammonium fluoride reacts vigorously and exothermally with OsO_2F_4 in liquid NOF solvent according to equation (9.3), in which [$N(CH_3)_4$][F] was found to be very

$$[N(CH_3)_4][F] + OsO_2F_4 \xrightarrow{NOF} [N(CH_3)_4][OsO_2F_5] \qquad (9.3)$$

soluble at -78 °C. Vigorous boiling of NOF at -59.9 °C provides a means to absorb the heat of reaction. The [$N(CH_3)_4$][OsO_2F_5] salt exhibits a low solubility in NOF and is moderately soluble in CH_3CN and HF solvents. When the reaction of [$N(CH_3)_4$][F] with

OsO_2F_4 was carried out in HF solvent at -78 °C, immediate decomposition ensued, and is attributed to the exothermic nature of the reaction and the lack of a means sufficient dissipate the heat of reaction. An attempt to react OsO_2F_4 and $[N(CH_3)_4][F]$ in CHF_3 at -100 °C was unsuccessful based on Raman and ^{19}F NMR spectroscopy which showed only the starting materials and solvent signals. Failure to react is attributed to the low solubility of OsO_2F_4 in CHF_3. No reaction was observed between OsO_2F_4 and NO_2F at -78 °C in liquid NO_2F, in which OsO_2F_4 was insoluble, and at 55 °C under *ca.* 6 atms NO_2F gas. The difference in reactivity between NOF and NO_2F towards OsO_2F_4 is consistent with a more ionic N-F bond in NOF than that in NO_2F and was also observed with OsO_4 (see 6.2.2. Reaction of OsO_4 with NOF and NO_2F).[210,211]

9.2.1.2. NMR Spectroscopic Characterization of the $OsO_2F_5^-$ Anion. The ^{19}F NMR spectrum of OsO_2F_4 dissolved in NOF at -65 °C comprised a doublet at 37.06 ppm and a quintet at 79.29 ppm, $^2J(^{19}F-^{19}F)$ = 96 Hz, with a doublet:quintet intensity ration of approximately 4:1. An increase in the intensity of the ^{19}F resonance of NO_2F (395.30 ppm, $^1J(^{19}F-^{14}F)$ = 114 Hz) relative to that of the NOF_3 impurity indicated that some oxidation of NOF had occurred; the reduction product, however, was not identified. The absence of ^{19}F NMR signals associated with OsO_2F_4 despite its observation by Raman spectroscopy (see 9.2.1.3. Raman Spectroscopic Characterization of the $OsO_2F_5^-$ Anion) is presumably the result of fast exchange on the NMR time scale between the fluorine environments in OsO_2F_4 and that in NOF solvent (^{19}F: 487.91 ppm). The ^{19}F NMR spectrum of $[N(CH_3)_4][OsO_2F_5]$ dissolved in CH_3CN at -30 °C also shows a doublet at

46.70 ppm and a quintet at 93.20 ppm, $^2J(^{19}F-^{19}F)$ = 93 Hz (Figure 9.1). In HF solvent at -78 °C, the quintet and doublet in the ^{19}F NMR spectrum of $[N(CH_3)_4][OsO_2F_5]$ were shifted to -6.49 and -36.58 ppm, respectively, with $^2J(^{19}F-^{19}F)$ = 97 Hz (Figure 9.2). This extreme solvent dependence of the chemical shift indicates significant interactions between solvent and the $OsO_2F_5^-$ anion. A similar dependence has also been found for the $ReO_2F_4^-$ anion, whose low-frequency ^{19}F resonance shifted by *ca.* 70 ppm to lower frequency upon changing the solvent from CH_3CN ($N(CH_3)_4^+$ salt) to HF (Cs^+ salt);[94] the nature of the countercation is unlikely to have such a large influence.

The heptacoordinate $OsO_2F_5^-$ anion can potentially exhibit structures based on three geometries, namely, the pentagonal bipyramid, the monocapped octahedron, and the monocapped trigonal prism, which are shown in Figures 9.3 and 9.4 together with their expected splittings in the ^{19}F NMR spectrum. Only one structure gives rise to the observed doublet and quintet splittings, *i.e.*, the monocapped trigonal prismatic structure with a *cis*-arrangement of the two oxygen atoms and four fluorine atoms forming the square face, which is capped by a unique fluorine atom (structure I). The $OsO_2F_5^-$ anion

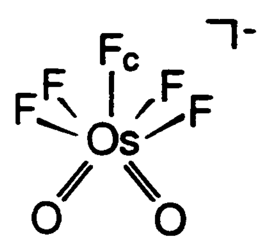

I

retains the *cis*-dioxo arrangement from its neutral precursor *cis*-OsO_2F_4 and provides the first example of an $AO_2F_5^{n-}$ system that, unlike $IO_2F_5^{2-}$ (see Chapter 10) and $UO_2F_5^{3-}$,[136,137] is not based on a pentagonal bipyramid. The capping fluorine in $OsO_2F_5^-$ is significantly

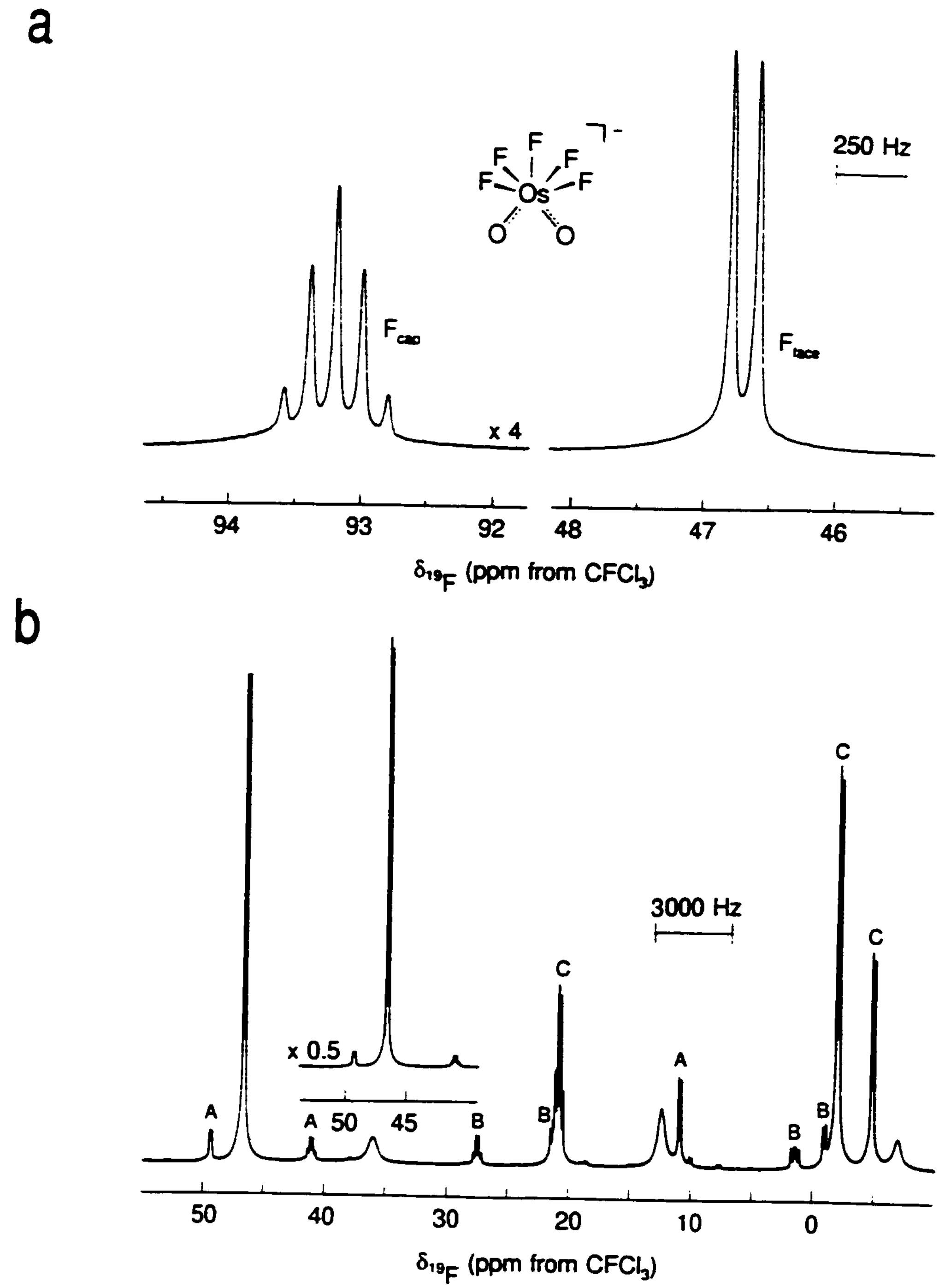

Figure 9.1 ^{19}F NMR spectrum (470.592 MHz) of $[N(CH_3)_4][OsO_2F_5]$ in CH_3CN solvent at -30 °C; (a) multiplets corresponding to the $OsO_2F_5^-$ and (b) low-frequency region.

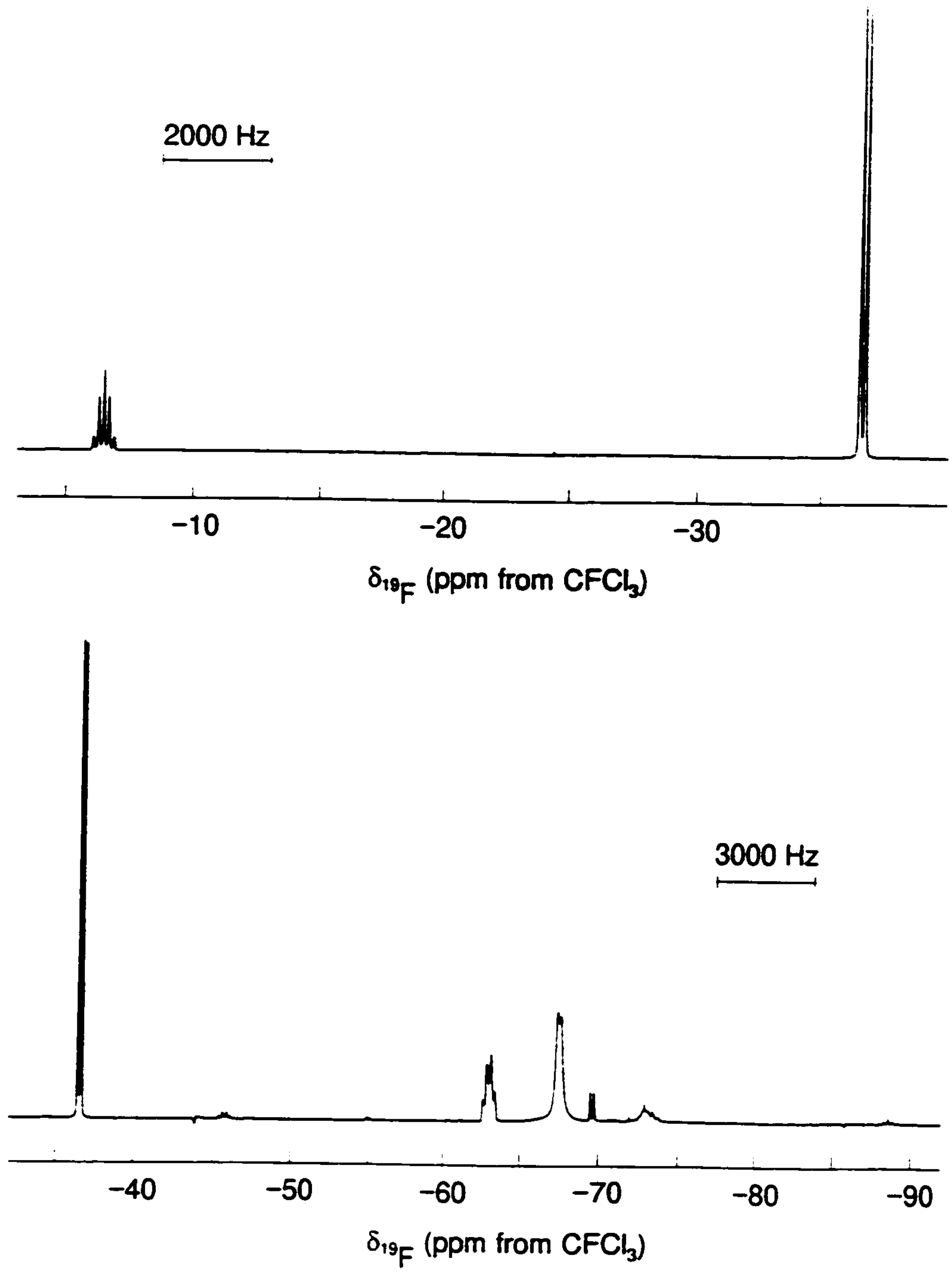

Figure 9.2 ^{19}F NMR spectra (470.592 MHz) of $[N(CH_3)_4][OsO_2F_5]$ in HF solvent at -80 °C.

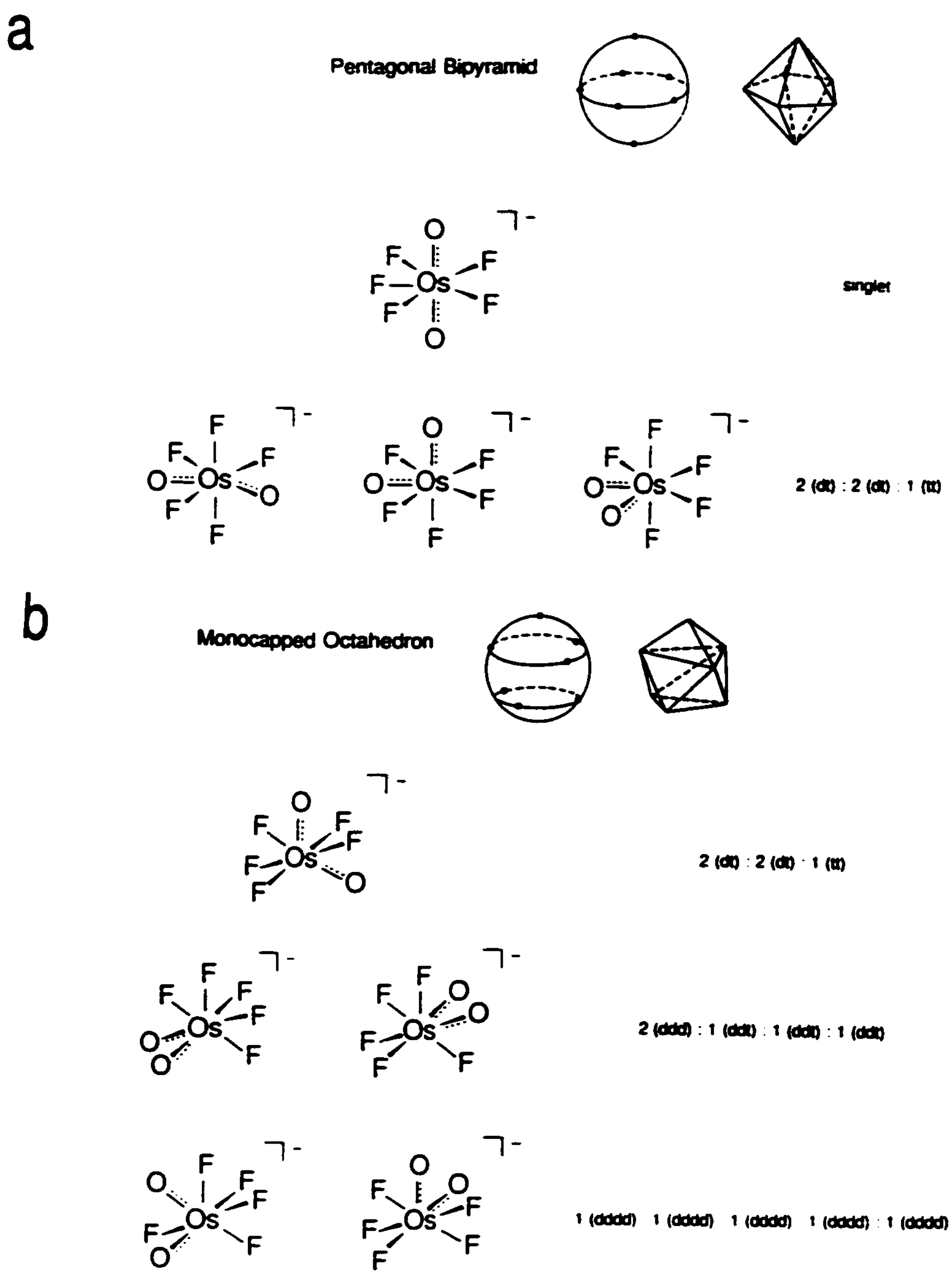

Figure 9.3 Possible structures for the $OsO_2F_5^-$ anion based on (a) a pentagonal bipyramid and (b) a monocapped octahedron together with their expected ^{19}F NMR multiplicities and relative intensities. Abbreviations d and t denote doublet and triplet.

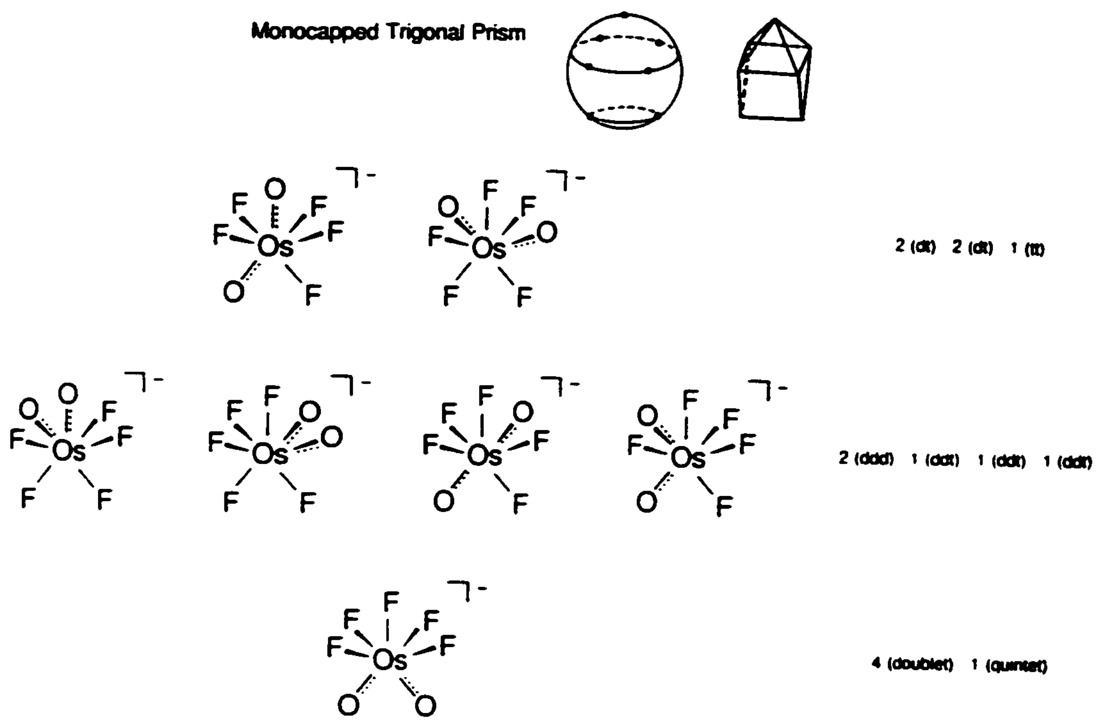

Figure 9.4 Possible structures for the $OsO_2F_5^-$ anion based on a monocapped trigonal prism, together with their expected ^{19}F NMR multiplicities and relative intensities. Abbreviations d and t denote doublet and triplet.

less shielded than the four fluorine atoms which form the equatorial square face, suggesting a strong, relatively covalent Os-F_{cap} bond and four, more ionic Os-F_{face} bonds in the sterically crowded plane. Structure I can be rationalized in terms of charge concentrations in the outer electron core opposite the doubly bonded oxygens, as was found in *cis*-$CrO_4F_2^{2-}$ by Bader and Gillespie (see 1.5. The *Trans*-Influence).[119] In the monocapped trigonal prismatic structure I, the repulsion between the fluorine ligands and the two expected charge concentrations is minimized with the latter located in the two trigonal faces which comprise the capping fluorine and two equatorial fluorine atoms.

In addition to the doublet and quintet for $[N(CH_3)_4][OsO_2F_5]$ dissolved in CH_3CN, a number of weaker, multiplets were observed in CH_3CN solvent at lower frequency (Figure 9.1 and Table 9.1). A ^{19}F-COSY spectrum identified three major groups of signals (Figure 9.5). The approximate relative intensities of the signals within at least two groups suggests the coupling of four, or multiples of four, fluorine atoms to each other. The magnitudes of the couplings are consistent with a two-bond coupling through osmium. The nature of these species could not be determined. The species likely arise from a reaction between $[N(CH_3)_4][OsO_2F_5]$ and CH_3CN and not from the preparation of $[N(CH_3)_4][OsO_2F_5]$ in NOF, since solid $[N(CH_3)_4][OsO_2F_5]$ did not show any significant amounts of impurities in its Raman spectrum. The ^1H NMR spectrum of $[N(CH_3)_4][OsO_2F_5]$ dissolved in CH_3CN at -30 °C contained signals at 2.41 and 3.55 ppm for CH_3CN solvent and $N(CH_3)_4^+$, respectively, and only weak singlets at 4.16, 4.91 (broad), and 11.21 ppm, showing that the bulk of the CH_3CN solvent and the cation remained intact. A possible reaction is provided by the replacement of a fluoride ion with

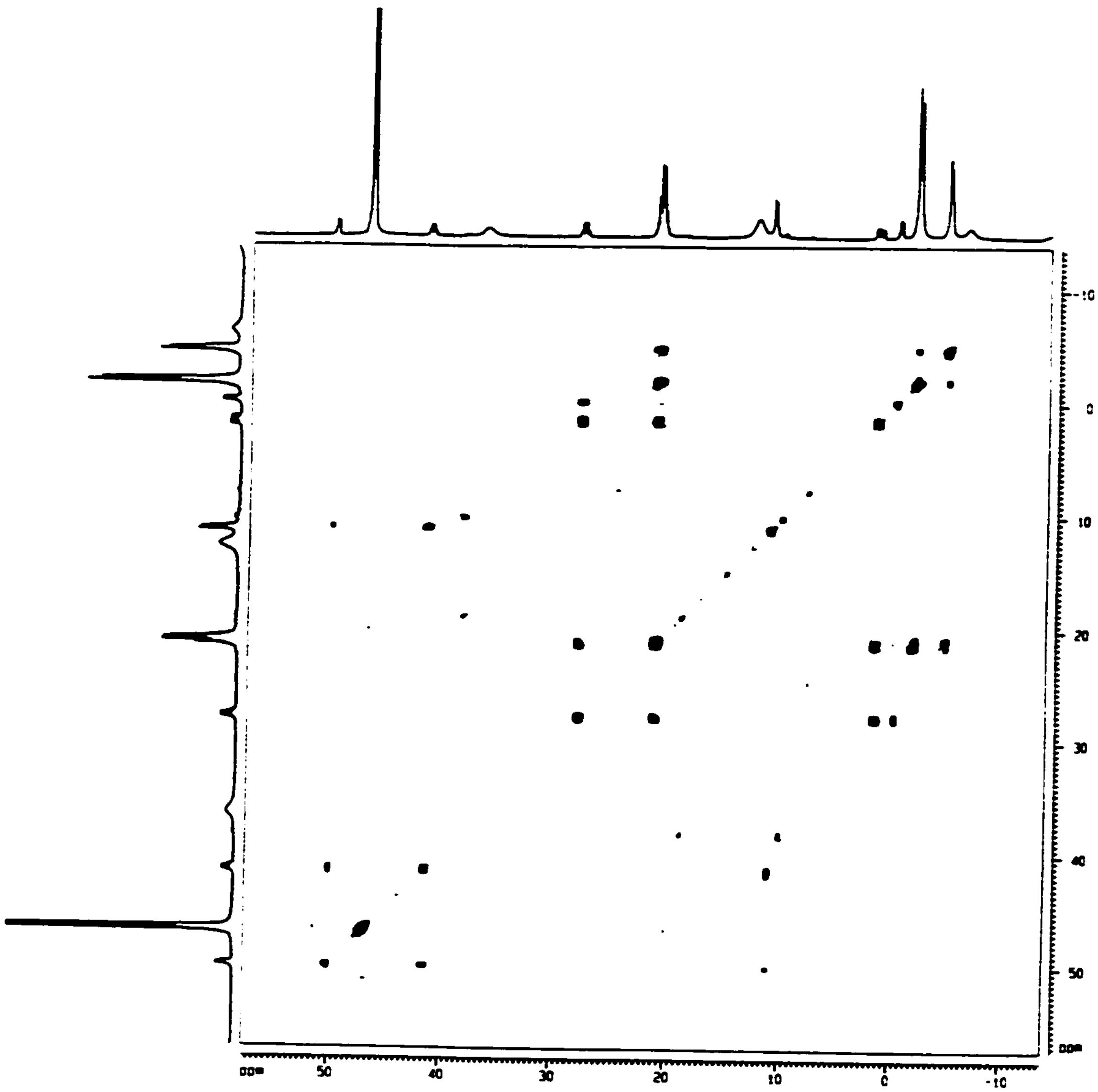

Figure 9.5 ^{19}F COSY-45 (470.592 MHz) of $[N(CH_3)_4][OsO_2F_5]$ in CH_3CN solvent at -30 °C.

CH_3CN yielding different isomers of the $OsO_2F_4(CH_3CN)$ adduct. Such an adduct should, however, coincide with the observation of the same isomer by NMR spectroscopy in a solution of OsO_2F_4 in CH_3CN solvent (see 9.2.2.2. NMR Spectroscopic Characterization of $OsO_2F_4(CH_3CN)$). The ^{19}F NMR spectrum of $[N(CH_3)_4][OsO_2F_5]$ dissolved in HF also contained several additional weak multiplets that could not be assigned (Table 9.1)

The ^{19}F NMR spectrum of the orange-brown supernatant that occurred above the large amounts of precipitate that resulted from the reaction of OsO_2F_4 and $[N(CH_3)_4][F]$ in liquid NOF contained a number of weak, very broad signals: doublet (-92.65 ppm, J = 123 Hz); singlets (-72.20, -70.81, 67.91, 63.94, 48.38 ppm); doublet (-40.06 ppm, J = 104 Hz); multiplet (-35.4 ppm); doublet (-28.22 ppm, J = 102 Hz); triplet (-24.8 ppm, J = 102 Hz); multiplets (between -5 to -14 ppm); doublet (4.8 ppm, J = 102 Hz); doublet (10.6 ppm, J = 105 Hz); multiplets (16.3, 21.5, 35 ppm); doublets (39.5 ppm, J = 86 Hz; 40.2 ppm, J = 80 Hz); multiplet (85.0 ppm). The origins of these lines is presently not well understood; they are, however, believed to be associated with volatile compounds or have a low concentration since the Raman spectrum of solid $[N(CH_3)_4][OsO_2F_5]$ did not contain major impurities. The unambiguous identification of the doublet and quintet corresponding to the $OsO_2F_5^-$ anion was not possible, because of the broadness and the possible overlap with a large number of multiplets present in the spectrum. The strong solvent dependence of the chemical shift associated with the $OsO_2F_5^-$ also complicates the assignment.

In spite of the side reactions, the assignment of the doublet and quintet to the $Os(VIII)O_2F_5^-$ anion is unambiguous. The reversability of eq. (9.2) in NOF solvent clearly

Table 9.1 Chemical Shifts and Spin-Spin Coupling Constants Observed in the ^{19}F NMR Spectra of $[N(CH_3)_4][OsO_2F_5]$ in CH_3CN and HF Solvents

Species[a]	$\delta(^{19}F)$ [ppm]	multiplicity	$J(^{19}F-^{19}F)$ [Hz]	rel. intensity
		CH_3CN Solvent		
$OsO_2F_5^-$	93.20	quintet	93	1
	46.69	doublet	93	4
A	49.39	doublet	77	1
	41.13	quartet	93	1
	11.00	doublet	101	3
B	27.58	quartett	103	
	ca. 21.5	doublet	100	
	1.49	doublet of doublets	112, 193	
	-0.93	doublet	100	
C	*ca.* 20.9	multiplet		1
	-1.95	doublet	107	2
	-4.80	doublet	89	1
	36.11	broad singlet		
	12.49	broad singlet		
	-6.85	broad singlet		
		HF Solvent		
$OsO_2F_5^-$	-6.49	quintet	97	1
	-36.58	doublet	97	4
	-45.76	quartet	112	
	-63.04	quartet	117	
	-67.54	doublet	88	
	-69.65	doublet	105	
	-72.89	overlapping multiplet		
	-88.58	triplet	134	
	-96.21	triplet	141	
	-123.02	doublet	118	

[a] Three groups of signals, A, B, and C, were identified by ^{19}F-COSY.

shows the absence of a possible redox reaction that generates a species associated with the doublet and quintet, such as the $OsOF_5^-$ anion and $OsOF_5$. The latter species is paramagnetic and has been shown to give rise to no observable ^{19}F NMR signals.[239] The possibility of the $OsOF_5^-$ anion or $OsOF_5$ is also eliminated by the observation of two distinct Os-O stretching bands in the Raman spectrum (*vide infra*).

9.2.1.3. Raman Spectroscopic Characterization of the $OsO_2F_5^-$ Anion.

The $[Cs][OsO_2F_5]$ and $[N(CH_3)_4][OsO_2F_5]$ salts were characterized by low-temperature Raman spectroscopy. The latter salt is a poor scatterer and readily decomposes in the YAG laser beam at power levels of 90 mW at -165 °C. The Raman spectra of $[Cs][OsO_2F_5]$ and $[N(CH_3)_4][OsO_2F_5]$ are shown in Figure 9.6. The major bands for the $OsO_2F_5^-$ anion in $[NO][OsO_2F_5]$ were observed in the Raman spectra of the precipitate under NOF solvent (Figure 9.7) and in that of the NOF solution in admixture with OsO_2F_4. The Raman frequencies for the $OsO_2F_5^-$ anion are listed in Table 9.2.

A total of 18 vibrational modes is expected for monocapped trigonal prismatic $OsO_2F_5^-$ (C_{2v}) belonging to the irreducible representations $6A_1 + 3A_2 + 4B_1 + 5B_2$. All modes are Raman active, while A_1, B_1, and B_2 are infrared active. Two Os-O stretches ($A_1 + B_2$) and five Os-F stretches ($2A_1 + A_2 + B_1 + B_2$) are expected for the $OsO_2F_5^-$ anion. The spectrum of $[Cs][OsO_2F_5]$ ($[N(CH_3)_4][OsO_2F_5]$) contains two Os-O stretching frequencies at 959 (977) and 921 (921) cm^{-1}, which is consistent with a *cis*-OsO_2 arrangement, since the symmetric and asymmetric *trans*-OsO_2 stretching modes would be mutually exclusive in the Raman and infrared spectra. The average of the symmetric and

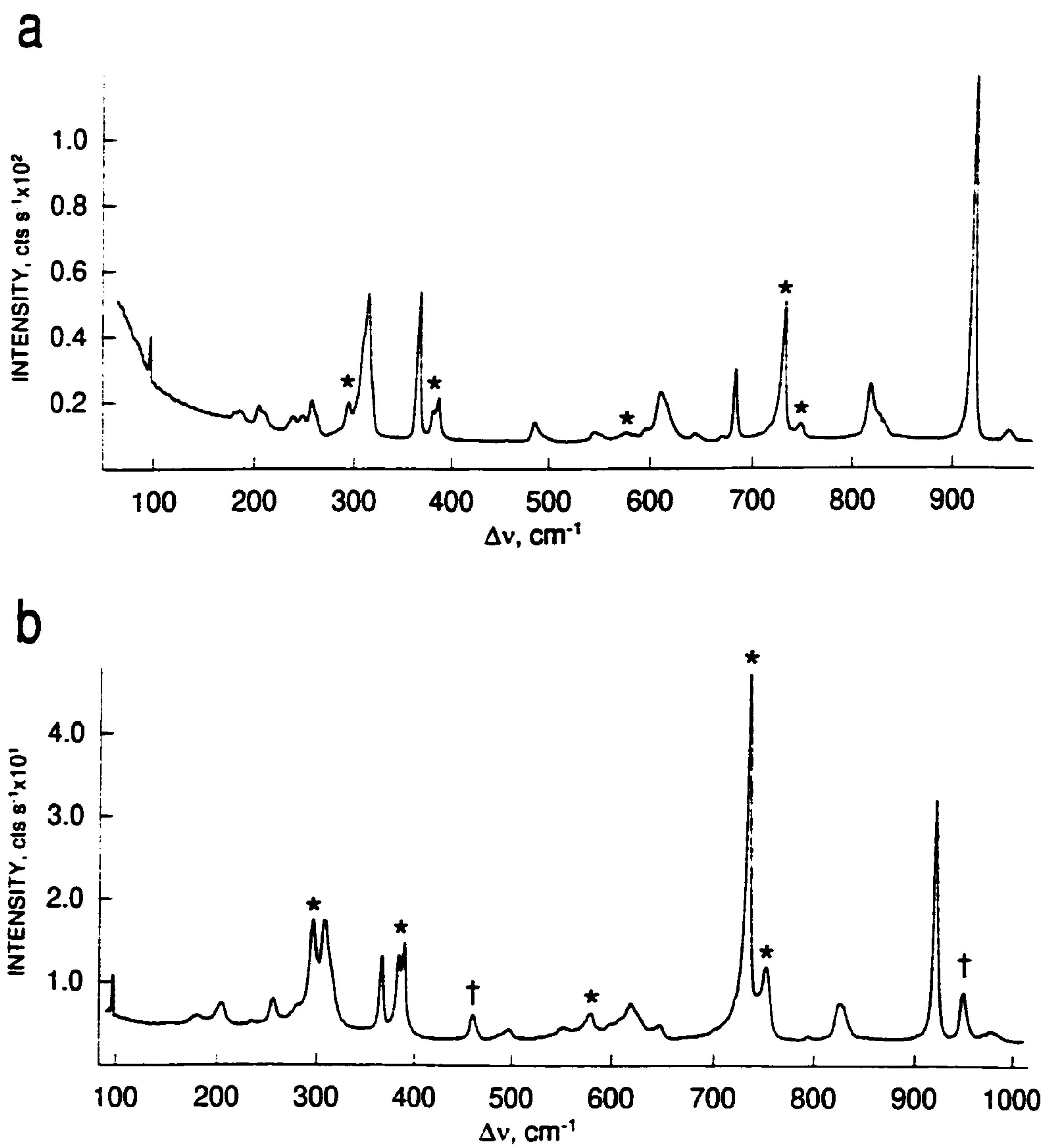

Figure 9.6 Raman spectra of (a) [Cs][OsO_2F_5] and (b) [$N(CH_3)_4$][OsO_2F_5] recorded in a 4-mm FEP tube at -145 °C using the 671.4-nm excitation. Asterisks (*) denote FEP bands. Daggers (†) denote bands arising from the $N(CH_3)_4^+$ cation.

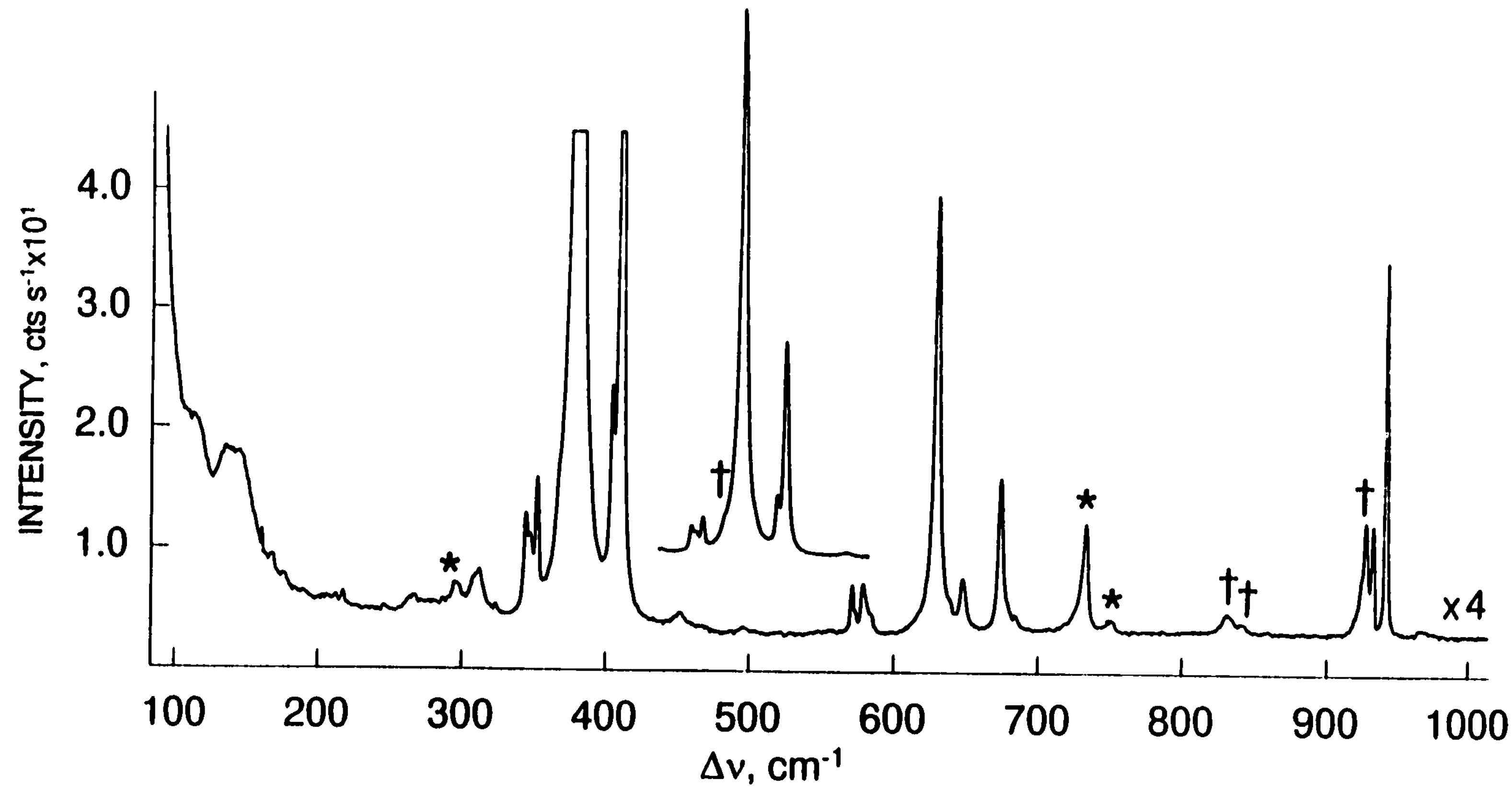

Figure 9.7 Raman spectrum of a $[NO][OsO_2F_5]/OsO_2F_4$ mixture under frozen NOF recorded in a 4-mm FEP tube at -150 °C using the 671.4-nm excitation. Asterisks (*) and daggers (†) denote FEP bands and signals arising from the $OsO_2F_5^-$ anion, respectively.

Table 9.2 Vibrational Frequencies and Assignments for $[M][OsO_2F_5]$, M = Cs^+, $N(CH_3)_4^+$, and NO^+

Frequeny,[a] [cm^{-1}]			Assignment
$[Cs][OsO_2F_5]$[b]	$[N(CH_3)_4][OsO_2F_5]$[c]	$[NO][OsO_2F_5]$[d]	$OsO_2F_5^-$ (C_{2v})
959 (4)	977 (4)	967 (7)	$\nu_{14}(B_2)$, $\nu_{as}(OsO_2)$
921 (100)	921 (100)	929 (100) 926 (53)sh	$\nu_1(A_1)$, $\nu_s(OsO_2)$
829 (7)sh	826 (15)	841 (10) 832 (20)	
819 (16)	795 (2)		$\nu_2(A_1)$, $\nu_s(OsF_{cap})$
684 (21) 670 (2)			$\nu_s(OsF_4)$
645 (2)	645 (7)		$\nu_{as}(OsF_4)$
609 (14) 595 (4)	617 (16)		$\nu_{as}(OsF_4)$
545 (4)	552 (7)		$\nu_{as}(OsF_4)$
485 (6)	496 (5)	494 (7)	$\delta_{sciss}(OsO_2)$
365 (40) 311 (40) 307 (26)sh 260 (6)sh 255 (10) 246 (5) 236 (4) 207 (4) 202 (6) 183 (4) 177 (2)	364 (33) 310 (27)sh 304 (46) 254 (12) 232 (3) 201 (10) 177 (5)	366 sh	bending modes

[a] Relative Raman intensities are given in parentheses. The abbreviation (sh) denotes a shoulder.

[b] Spectrum recorded on microcrystalline solid in a 4-mm FEP sample tube at -145 °C using the 647.1-nm excitation. Bands arising from FEP sample tube were observed at 292 (10), 380 (8), 386 (12), 576 (3), 732 (38), and 750 (5) cm^{-1}.

[c] Spectrum recorded on microcrystalline solid in a 4-mm FEP sample tube at -145 °C using the 647.1-nm excitation. Bands arising from FEP sample tube were observed at 293 (46), 381 (34), 387 (39), 579 (12), 733 (152), and 751 (30) cm^{-1}.

[d] Spectrum recorded on the solid under frozen NOF in a 4-mm FEP sample tube at -150 °C using the 647.1-nm excitation. Bands arising from *cis*-OsO_2F_4 were observed at 264 (17), 310 (40), 321 (13), 342 (97), 347 (77), 350 (127), 402 (213), 571 (45), 573 (20)sh, 578 (47), 584 (20)sh, 673 (137), 683 (18), 934 (97), and 943 (330) cm^{-1}; bands arising from NOF solvent were observed at 111 (27), 131 (47), 141 (60), 377 (1920), 408 (747), 628 (390), 638 (33)sh, 647 (50) cm^{-1}; bands arising from FEP sample tube were observed at 293 (30), 734 (97), and 751 (13) cm^{-1}.

asymmetric stretching frequency of 940 (949) cm^{-1} is slightly higher than that for OsO_2F_4 (938 cm^{-1})[6] indicating somewhat weaker Os-O bonds in the anion.

In the Raman spectrum of $[Cs][OsO_2F_5]$, the band at 822 cm^{-1} is assigned to the strong symmetric OsF_5 stretch, $\nu_2(A_1)$, while the bands at 684, 645, 609, and 545 cm^{-1} correspond to the other four Os-F stretches, which appear in the same Os-F stretching region as those of OsO_2F_4.[6] The signal at 485 cm^{-1} is tentatively assigned to the scissoring motion of the OsO_2 unit, which is at much higher frequency than $\delta_{sciss}(OsO_2)$ in OsO_2F_4 (402 cm^{-1})[6] reflecting the higher degree of ligand crowding in the $OsO_2F_5^-$ anion. A more complete assignment of the Os-F stretching and the bending modes awaits DFT calculations of vibrational frequencies.

9.2.2. Lewis Acid Behaviour of *cis*-OsO_2F_4 Towards CH_3CN

9.2.2.1. Synthesis of $OsO_2F_4(CH_3CN)$. Osmium dioxide tetrafluoride readily dissolves in CH_3CN solvent according to equation (9.4) yielding an intense red-brown solution.

$$OsO_2F_4 + CH_3CN \xrightarrow{CH_3CN} OsO_2F_4(CH_3CN) \qquad (9.4)$$

In addition to $OsO_2F_4(CH_3CN)$, significant concentrations of the $OsO_2F_5^-$ have been observed by ^{19}F NMR spectroscopy (see 9.2.2.2. NMR Spectroscopic Characterization of $OsO_2F_4(CH_3CN)$). The formation of the anion cannot be conclusively explained, but may be generated by a CH_3CN-assisted dissociation of OsO_2F_4 (eq. (9.5)). No evidence for the

$$2OsO_2F_4 + CH_3CN \rightleftharpoons OsO_2F_3(CH_3CN)^+ + OsO_2F_5^- \quad (9.5)$$

$OsO_2F_3(CH_3CN)^+$ cation was found by the ^{19}F NMR spectroscopy which is consistent with a possible attack of the CH_3CN solvent by the highly electrophilic $OsO_2F_3(CH_3CN)^+$ cation, as a possible secondary reaction. Removal of the CH_3CN solvent at -30 °C initially produces a concentrated, nearly black solution, which changes into a black glassy solid upon complete solvent removal, that did not give rise to any Raman lines. In the presence of excess CH_3CN, OsO_2F_4 slowly reacts with CH_3CN in SO_2ClF solvent yielding a pale red solution of $OsO_2F_4(CH_3CN)$.

9.2.2.2. Multi-NMR Spectroscopic Characterization of $OsO_2F_4(CH_3CN)$. The ^{19}F NMR spectrum of OsO_2F_4 dissolved in CH_3CN contains two major osmium oxide fluoride species, *i.e.*, $OsO_2F_5^-$ and $OsO_2F_4(CH_3CN)$. The spectrum of $OsO_2F_4(CH_3CN)$ at -40 °C consists of an AMX_2 spin system with $\delta(^{19}F_A)$ = 108.26 ppm, $\delta(^{19}F_M)$ = 23.08 ppm, $\delta(^{19}F_X)$ = 5.26 ppm, $^2J(^{19}F_A-^{19}F_M)$ = 111 Hz, $^2J(^{19}F_A-^{19}F_X)$ = 20 Hz, $^2J(^{19}F_M-^{19}F_X)$ = 65 Hz (Figure 9.8). A ^{19}F COSY spectrum confirmed that these three signals are coupled to each. Since the monocapped trigonal prism was shown to be the preferred geometry of the heptacoordinate dioxo species, $OsO_2F_5^-$, $OsO_2F_4(CH_3CN)$ is likely based on the same geometry. The AMX_2 spin system is consistent with structure II which is based on a

II 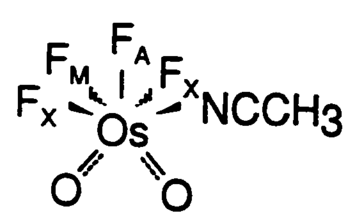

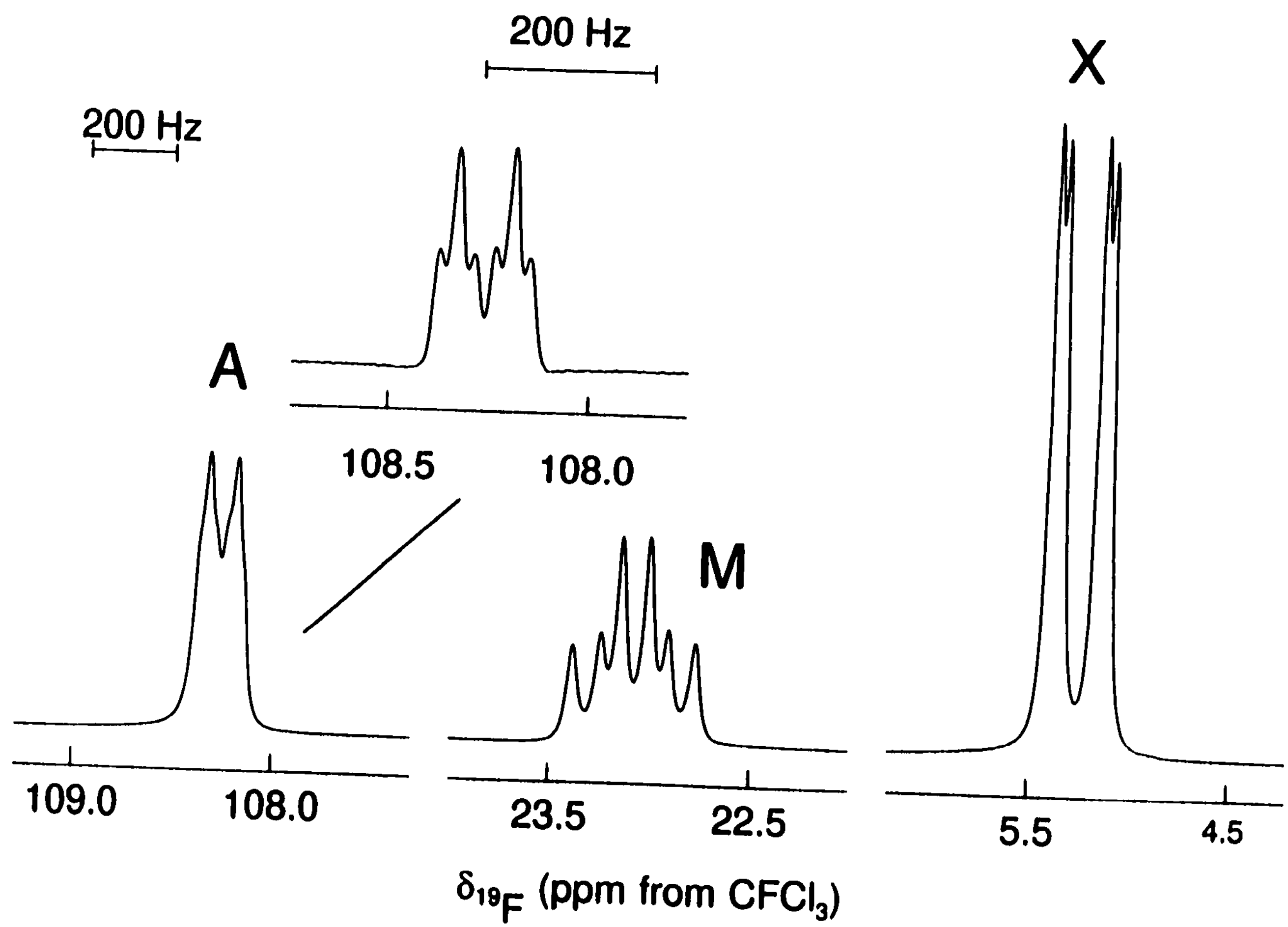

Figure 9.8 ^{19}F NMR spectrum (470.592 MHz) of $OsO_2F_4(CH_3CN)$ in CH_3CN solvent at -40 °C. Insert shows resolution enhanced signal.

monocapped trigonal prism with one fluorine in the square face replaced by a CH_3CN molecule. The high-frequency signal (108.26 ppm) corresponds to the capping fluorine and is even more deshielded than the capping fluorine in $OsO_2F_5^-$, which is consistent with the neutrality of the CH_3CN adduct. The three fluorine atoms in the equatorial squareface of the $OsO_2F_4(CH_3CN)$ adduct are more shielded than the four fluorine atoms that form the square face in the $OsO_2F_5^-$ anion. The higher steric demand of the CH_3CN ligand compared to a fluorine apparently results in weaker, more ionic Os-F bonds causing an larger shielding of the equatorial fluorine environments. The preference of the CH_3CN ligand for the equatorial site, instead of the capping position, is a consequence of the strong Os-F_{cap} bond which is evidenced by its deshielded ^{19}F resonance. Furthermore, the trajectory of CH_3CN attack likely points through the trigonal face in *cis*-OsO_2F_4 which involves the two oxygen atoms *cis* to each other as depicted in Figure 9.9. Fluorine ligand rearrangement yields structure II, while a non-dissociative isomerization to a $OsO_2F_4(CH_3CN)$ geometry with a capping CH_3CN is kinetically unfavourable.

Besides ^{19}F NMR signals associated with $OsO_2F_4(CH_3CN)$, $OsO_2F_5^-$, and HF (-178.29 ppm; $^1J(^{19}F-^1H) = 477$ Hz), several weak signals were observed which have not been assigned thus far: singlets at 50.3, -59.36, -79.56, and -98.89 ppm; a quartet at 15.39 ppm ($J = 101$ Hz); and a doublet at 8.36 ppm ($J = 88$ Hz). The ^1H NMR spectrum at -40 °C of the CH_3CN solution is far more complex than expected for $OsO_2F_4(CH_3CN)$ dissolved in CH_3CN. Besides the intense CH_3CN solvent signal at 2.75 ppm, small amounts of HF (8.37 ppm, $^1J(^{19}F-^1H) = 478$ Hz), a singlet at 5.29 ppm and several weaker signals between 3 and 4 ppm were observed. The complexity of the ^1H NMR spectrum

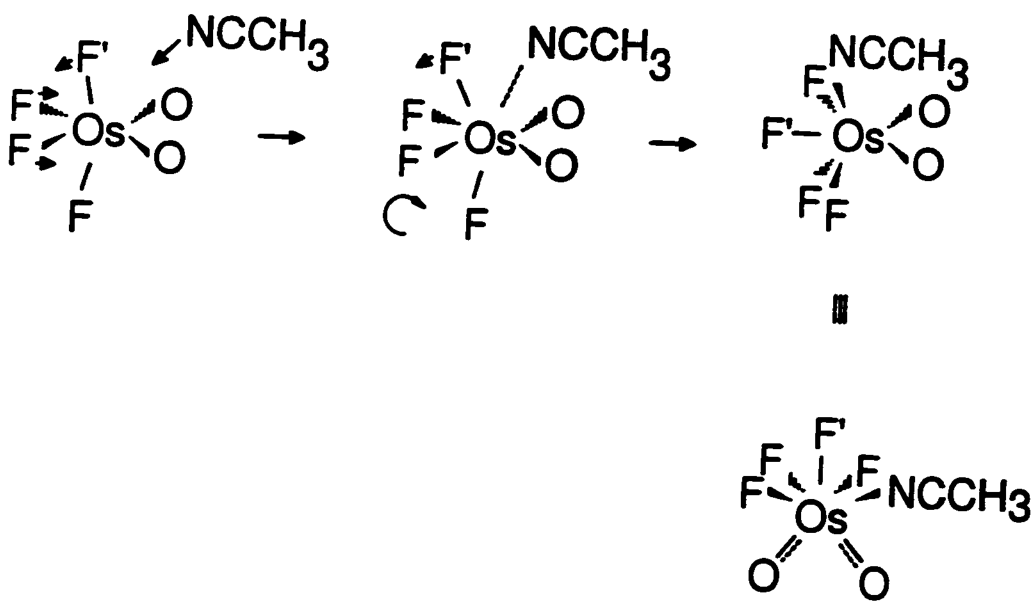

Figure 9.9 Proposed trajectory of CH_3CN attack at *cis*-OsO_2F_4.

suggest that attack of the CH_3CN solvent has occurred.

The ^{19}F NMR spectrum of the reaction of OsO_2F_4 with CH_3CN in SO_2ClF solvent at -80 °C showed two triplets for OsO_2F_4 (48.66 and 33.38 ppm, $^2J(^{19}F-^{19}F)$ = 137 Hz), which decreased in intensity over the course of the reaction, while signals for $OsO_2F_4(CH_3CN)$ increased in intensity. The ^{19}F NMR parameters for $OsO_2F_4(CH_3CN)$ in SO_2ClF solvent $\delta(^{19}F_A)$ = 108.26 ppm, $\delta(^{19}F_M)$ = 23.91 ppm, $\delta(^{19}F_X)$ = 6.65 ppm, $^2J(^{19}F_A-^{19}F_M)$ = 108 Hz, $^2J(^{19}F_A-^{19}F_X)$ = 19 Hz, $^2J(^{19}F_M-^{19}F_X)$ = 62 Hz agree very well with those obtained in CH_3CN solvent. Additional signals indicate side reactions: sharp singlets at 175.6, 48.91, -61.07, -71.61, -81.51 ppm, broad signals at 39.4 and 13.3 ppm, and a doublet at 11.84 ppm (J = 94 Hz). The complex ^1H NMR spectrum with signals at 1.75 ppm (CH_3CN); doublet at 7.42 ppm, $^1J(^{19}F-^1H)$ = 479 Hz (HF); singlets at 2.03, 2.39, 2.68, 3.57, and 4.26 ppm support the suggestion of CH_3CN attack by OsO_2F_4.

9.3. Conclusion

The Os(VIII) oxide fluoride, *cis*-OsO_2F_4, was shown to behave as a Lewis acid towards F^- and CH_3CN yielding the $OsO_2F_5^-$ anion and $OsO_2F_4(CH_3CN)$ adducts, respectively. Fluorine-19 NMR spectroscopy provides the conclusive structural characterization of $OsO_2F_5^-$ which has the unprecedented monocapped trigonal prismatic *cis*-dioxo structure with one fluorine capping the equatorial square face of four fluorine atoms. The AMX_2 spin system observed for $OsO_2F_4(CH_3CN)$ is consistent with a structure derived from the $OsO_2F_5^-$ anion by replacement of one equatorial fluorine atom by a CH_3CN molecule.

CHAPTER 10

FLUORIDE ION ACCEPTOR PROPERTIES OF $IO_2F_4^-$

10.1. Introduction

Iodine in the +7 oxidation state usually has the coordination number six, as in $IO_2F_4^-$,[102,103] $(IO_2F_3)_2$,[96] IOF_5,[97] and H_5IO_6.[1] It is well documented, however, that I(VII) can expand its coordination number to seven, as in IF_7[104-107] and IOF_6^-.[110] In the wake of recent successes in the synthesis of heptacoordinate oxide fluoride and fluoride main-group anions with doubly negative charges, *e.g.*, $TeOF_6^{2-}$,[113], IF_5^{2-},[140] SbF_7^{2-},[135] BiF_7^{2-},[135] the fluoride ion acceptor properties of the $IO_2F_4^-$ anion were investigated in order to obtain the first heptacoordinate main-group dioxide pentafluoride species. All four doubly charged anions have been prepared using anhydrous $[N(CH_3)_4][F]$,[172] commonly referred to as called 'naked fluoride', as the fluoride ion source. Tetramethylammonium fluoride is very soluble in CH_3CN and CHF_3 solvents. However, the latter solvent has not been used as extensively because of its low boiling point (-82.1 °C). On the other hand, CH_3CN is not inert towards fluoride ions at room temperature (*vide infra*), but solutions are stable at low temperatures (<-30 °C).[172,173]

10.2. Results and Discussion

10.2.1. Synthesis of $[N(CH_3)_4]_2[IO_2F_5]$

A mixture of $[N(CH_3)_4]$[*trans*-IO_2F_4] and $[N(CH_3)_4]$[*cis*-IO_2F_4] was allowed to react with one mole equivalent of $[N(CH_3)_4][F]$ in CH_3CN at -30 °C and in CHF_3 at 0 °C followed by removal of the solvent under dynamic vacuum. The white product mixture contained $[N(CH_3)_4]_2[IO_2F_5]$ and $[N(CH_3)_4]$[*cis*-IO_2F_4] based on Raman spectroscopy. In the case of CHF_3 solvent, small amounts of $[N(CH_3)_4]$[*trans*-IO_2F_4] were also present.

It is apparent from the Raman spectrum of the novel $IO_2F_5^{2-}$ anion prepared in CH_3CN, where the most intense bands of *cis*-$IO_2F_4^-$ were observed and none were observed for the *trans*-isomer, that the *trans*-$IO_2F_4^-$ selectively acts as a Lewis base towards $[N(CH_3)_4][F]$ yielding the $IO_2F_5^{2-}$ anion, structure I (eq. (10.1)), while $[N(CH_3)_4]$

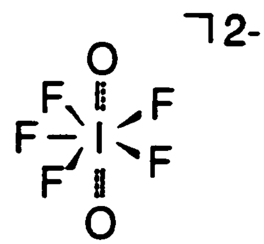

I

[*cis*-IO_2F_4] is inert towards F^- (eq. (10.2)). Even addition of excess $[N(CH_3)_4][F]$ to

$$[N(CH_3)_4][trans\text{-}IO_2F_4] + [N(CH_3)_4][F] \xrightarrow{CH_3CN/CHF_3} [N(CH_3)_4]_2[IO_2F_5] \quad (10.1)$$

$$[N(CH_3)_4][cis\text{-}IO_2F_4] + [N(CH_3)_4][F] \xrightarrow{CH_3CN/CHF_3} \text{no reaction} \quad (10.2)$$

$[N(CH_3)_4]_2[IO_2F_5]$/$[N(CH_3)_4]$[*cis*-IO_2F_4] mixtures and prolonged reaction times do not result in reduction of the relative intensities of the Raman bands for *cis*-$IO_2F_4^-$. The reaction between $[N(CH_3)_4][F]$ and *trans*-$IO_2F_4^-$ proceeds *via* the proposed trajectory for fluoride attack though one of the eight equivalent trigonal faces of the pseudo-octahedron as depicted in Figure 10.1. In the case of the *cis*-$IO_2F_4^-$ anion the trajectory of the attacking fluorine likely favours one of the two trigonal faces containing the O-O edge, since the O-I-O bond angle is expected to be larger than the other bond angles in the *cis*-$IO_2F_4^-$ anion (Figure 10.1). The addition of fluoride ion to the plane of the $IO_2F_4^-$ anion, which is already highly crowded by the larger oxygen double bond domain and three fluorine bond domains, is not favourable. The formation of the $IO_2F_5^{2-}$ anion (I) with a *trans*-IO_2 arrangement from *cis*-$IO_2F_4^-$ would require a ligand rearrangement that is kinetically unfavourable, which is documented by the apparent absence of a rapid *trans*/*cis*-isomerization of the $IO_2F_4^-$ anion. A reaction time of 2 h in CH_3CN at -30 °C resulted in complete reaction with respect to *trans*-$IO_2F_4^-$, whereas a longer reaction time (12 h) in CHF_3 at 0 °C failed to result in complete conversion of *cis*-$IO_2F_4^-$ to $IO_2F_5^{2-}$, presumably because of the low solubility of *trans*-$IO_2F_4^-$ in CHF_3.

Most of the unreacted $[N(CH_3)_4]$[*cis*-IO_2F_4] salt was extracted from the product mixture with CH_3CN. However, not all of the $[N(CH_3)_4]$[*cis*-IO_2F_4] could be removed even after numerous washings.

10.2.2. Raman Spectroscopic Characterization of $[N(CH_3)_4]_2[IO_2F_5]$

Raman spectra of the $[N(CH_3)_4]_2[IO_2F_5]$/$[N(CH_3)_4]$[*cis*-IO_2F_4] product mixtures obtained from CH_3CN and CHF_3 solvents are shown in Figures 10.2 and 10.3, respectively. The observed frequencies and their assignments for the product mixtures

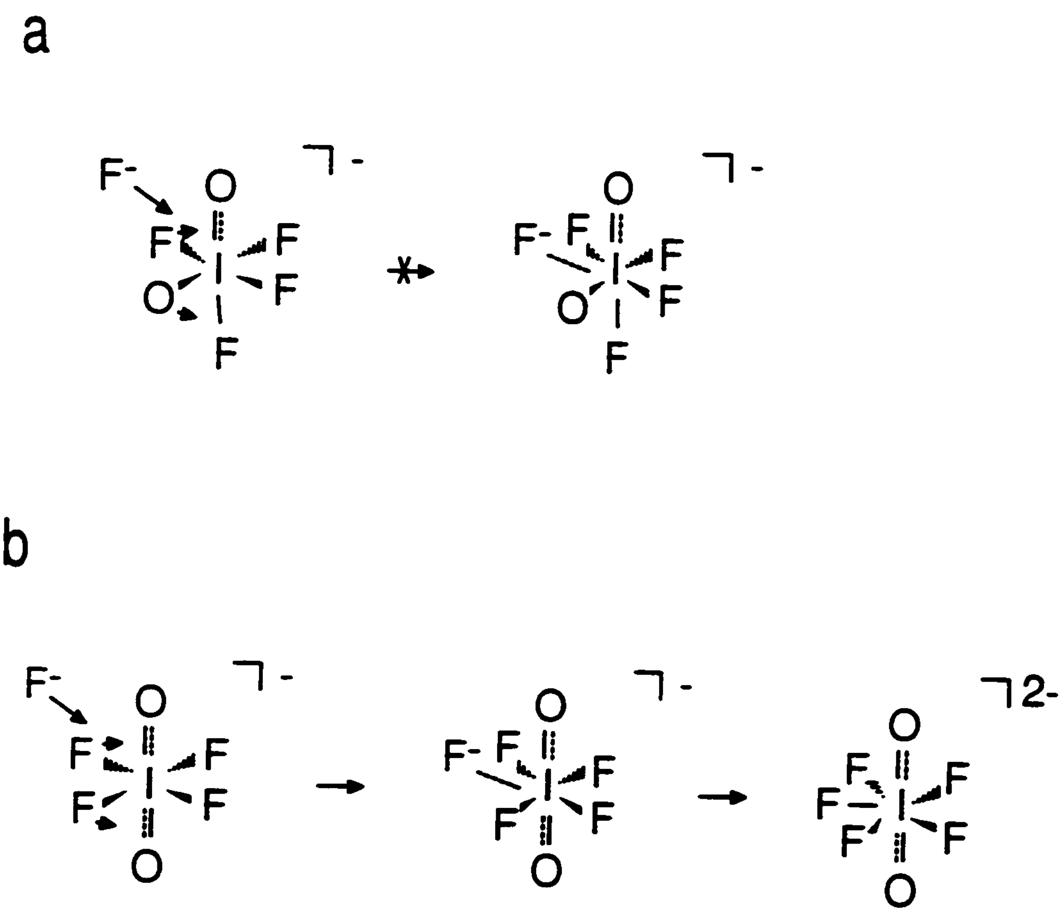

Figure 10.1 Proposed trajectories for fluoride attack on (a) *cis*-$IO_2F_4^-$ and (b) *trans*-$IO_2F_4^-$.

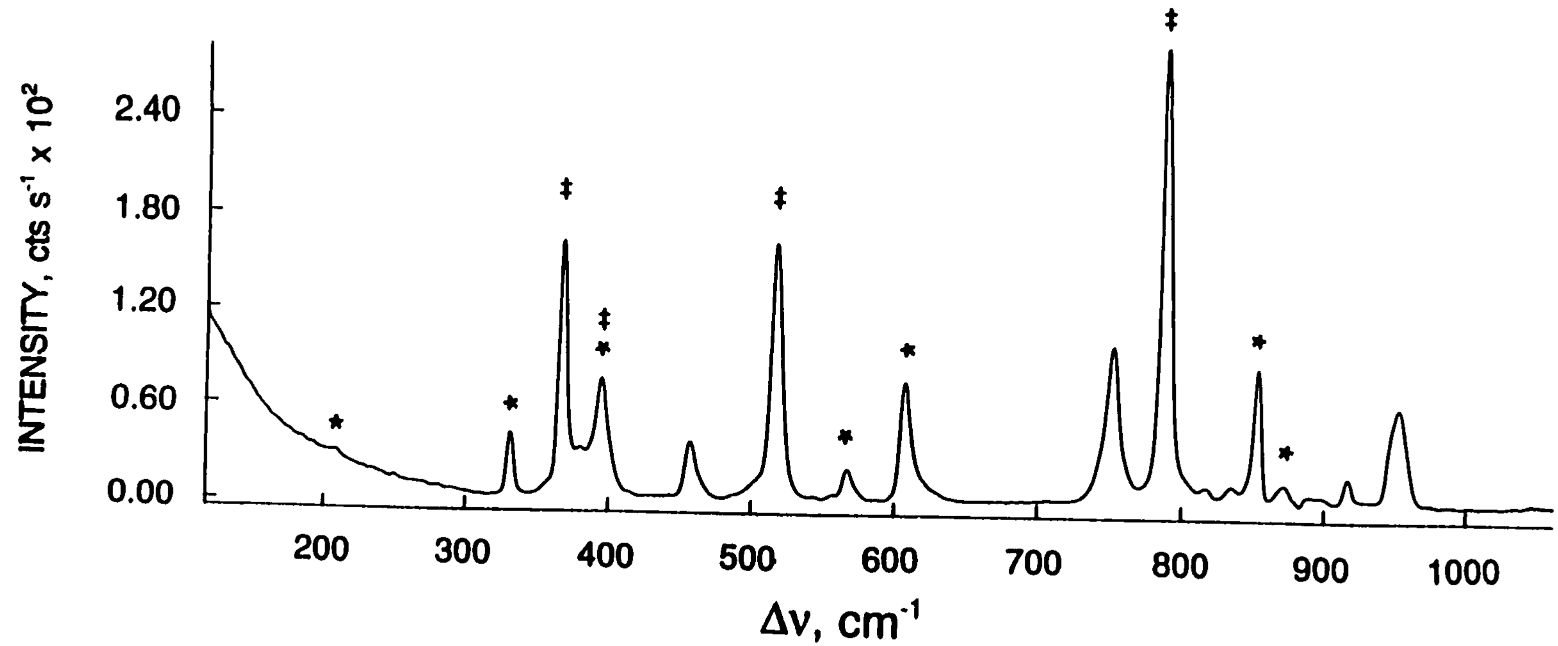

Figure 10.2 The Raman spectrum of a $[N(CH_3)_4]_2[IO_2F_5]/[N(CH_3)_4][IO_2F_4]$ mixture prepared from CH_3CN, recorded at -113 °C using 514.5-nm excitation. The $IO_2F_5^{2-}$ and *cis*-$IO_2F_4^-$ bands are indicated by ‡ and *, respectively.

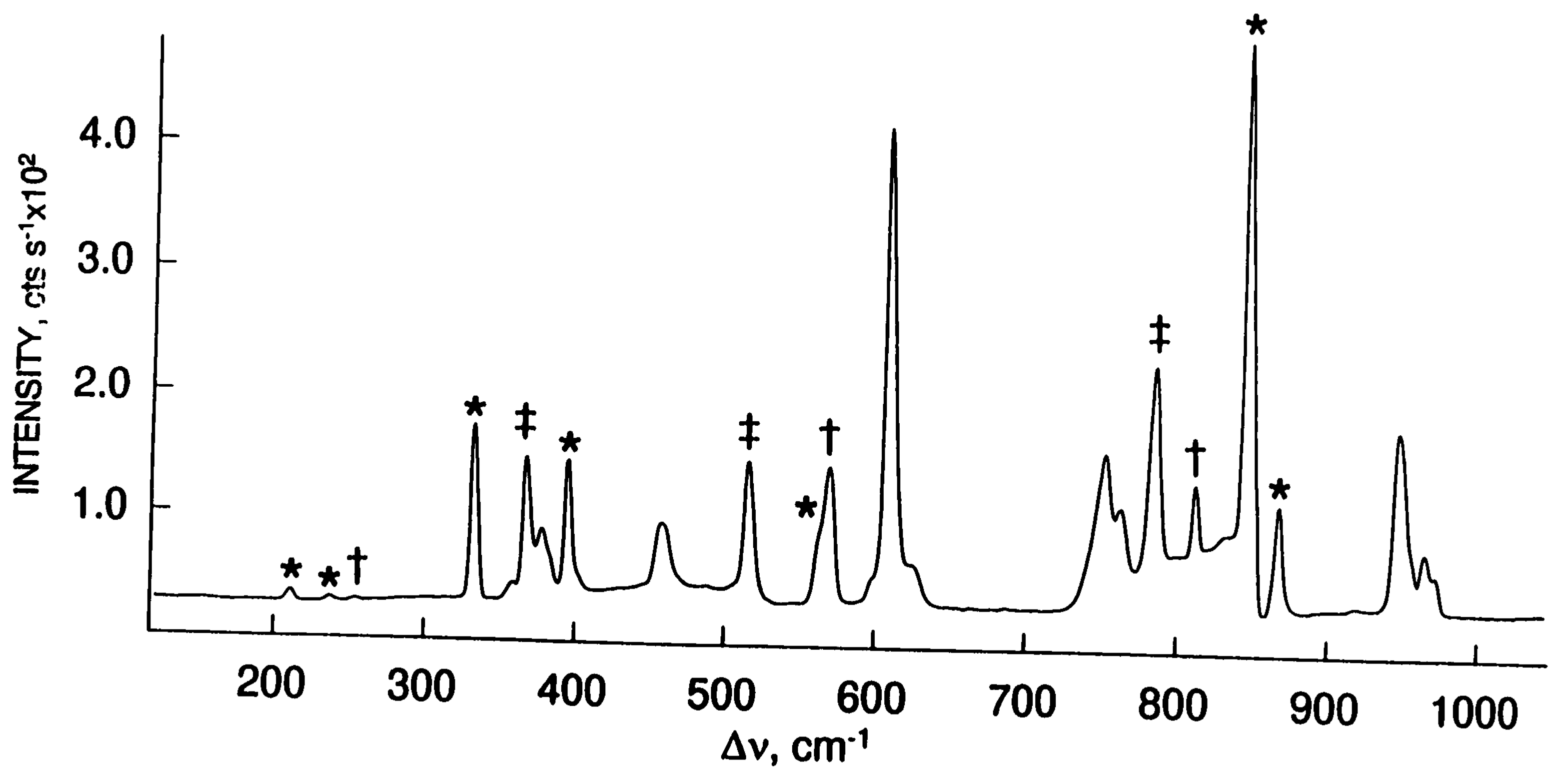

Figure 10.3 The Raman spectrum of a $[N(CH_3)_4]_2[IO_2F_5]/[N(CH_3)_4][cis\text{-}IO_2F_4]$ mixture prepared in CHF_3, recorded at room temperature using 514.5-nm excitation. The $IO_2F_5^{2-}$, *cis*-$IO_2F_4^-$, and *trans*-$IO_2F_4^-$ bands are indicated by ‡, *, and †, respectively.

prepared from CH_3CN and CHF_3 are summarized in Tables 10.1 and 10.2, respectively.

In addition to bands assigned to the $N(CH_3)_4^+$ cation, the *cis*- and *trans*-$IO_2F_4^-$ anions, and CH_3CN, four new Raman bands at 789, 517, 395, and 368 cm^{-1} were observed and are assigned to the novel pentagonal bipyramidal $IO_2F_5^{2-}$ anion (D_{5h}) with the oxygen atoms in the axial position (structure I).

A total of 18 vibrational modes are expected for the $IO_2F_5^{2-}$ anion (D_{5h}) which span the irreducible representations $\Gamma = 2A_1' + 3E_1' + 2E_2' + 2A_2'' + E_1'' + E_2''$. Of these, five bands corresponding to the A_1', E_2', and E_1'' modes are Raman active, five bands corresponding to the A_2'' and E_1' modes are infrared active, and the E_2'' mode is inactive. Of the five Raman active bands, three were observed in the Raman spectrum of $[N(CH_3)_4]_2[IO_2F_5]$. The most intense band observed at 789 cm^{-1} is assigned to $\nu_1(A_1')$, the symmetric stretching band for the axial IO_2 unit. The IO_2 stretching band for the *trans*-$IO_2F_4^-$ anion was observed at 813 cm^{-1} in the Raman spectrum. The higher frequency observed for *trans*-$IO_2F_4^-$ compared to that of $IO_2F_5^{2-}$ is consistent with the anticipated greater I–O bond polarity in the $IO_2F_5^{2-}$ anion resulting from increased negative charge localization on the oxygen atom. The predicted *trans*-arrangement of the oxygen atoms in the $IO_2F_5^{2-}$ anion was confirmed by the absence of an intense frequency around 800 cm^{-1}, where the asymmetric stretching frequency of *cis*-$IO_2F_4^-$ occurs. For the monocapped octahedral and monocapped trigonal prismatic geometries, the symmetric as well as the asymmetric I-O stretches would be Raman active. A second intense Raman band observed at 517 cm^{-1} is associated with the $IO_2F_5^{2-}$ anion and was assigned to $\nu_2(A_1')$. This band, which corresponds to the symmetric stretching mode of the five equatorial I–F bonds, is

Table 10.1 Raman Frequencies and Assignments for a $[N(CH_3)_4]_2[IO_2F_5]$/ $[N(CH_3)_4][cis\text{-}IO_2F_4]$ Mixture Prepared in CH_3CN

Frequency[a,b] [cm^{-1}]	Assignment	
	$IO_2F_5^{2-}$ (D_{5h})	*cis*-$IO_2F_4^-$ (C_{2v})
889 (2)		
871 (5)		$\nu_{12}(B_2)$, $\nu_{as}(IO_2)$
854 (31)		$\nu_1(A_1)$, $\nu_s(IO_2)$
834 (4)		
817 (4)		
789 (100)	$\nu_1(A_1')$,$\nu_s(IO_2)$	
620 (2)sh		
608 (26)		$\nu_2(A_1)$, $\nu_s(IF_2)_{eq}$
567 (7)		$\nu_3(A_1)$, $\nu_s(IF_2)_{ax}$
517 (57)	$\nu_2(A_1')$, $\nu_s(IF_5)$	
500 (4)sh		
395 (26)	$\nu_{10}(E_2')$, $\nu_{as}(IF_5)$	$\nu_4(A_1)$, $\delta_{sciss}(IO_2)$
368 (57)	$\nu_8(E_1'')$, $\delta_{rock}(IO_2)$	
356 (3)sh		bending modes
331 (14)		
209 (1)		

[a] Spectrum recorded on microcrystalline solid in a Pyrex glass capillary at -113 °C using the 514.5-nm excitation. Values in parentheses denote relative intensities; sh: shoulder.

[b] The $N(CH_3)_4^+$ cation modes were observed t 380 (11), $\nu_8(E)$; 457 (13), $\nu_{19}(T_2)$; 752 (35), $\nu_3(A_1)$; 953 (22), $\nu_{18}(T_2)$; 1187 (3), $\nu_7(E)$; 1294 (3), $\nu_{17}(T_2)$; 1418 (5), $\nu_{16}(T_2)$; 1465 sh, $\nu_2(A_1)$; 1476 (31), $\nu_6(E)$; 2818 (4), 2828 (5), 2836 (5), 2899 sh, 2934 (16), 2970 (25), 2995 (15), 3038 (33) cm^{-1}, ν_{CH_3} and binary bands (see ref. (201,202)). Bands arising from residual CH_3CN were observed at 916 (7), $\nu_4(A_1)$; 1378 (1), $\nu_3(A_1)$; 2247 (14), $\nu_2(A_1)$; 2944 (16) cm^{-1}, $\nu_1(A_1)$ (see ref. (200)).

Table 10.2 Raman Frequencies and Assignments for a $[N(CH_3)_4]_2[IO_2F_5]$/ $[N(CH_3)_4][cis\text{-}IO_2F_4]$ Mixture Prepared in CHF_3

Frequency[a,b] [cm^{-1}]	Assignment		
	$IO_2F_5^{2-}$ (D_{5h})	*cis*-$IO_2F_4^-$ (C_{2v})	*trans*-$IO_2F_4^-$ (D_{4h})
870 (19)		$\nu_{12}(B_2)$, $\nu_{as}(IO_2)$	
849 (100)		$\nu_1(A_1)$, $\nu_s(IO_2)$	
839 (14)sh			
815 (22)			$\nu_1(A_{1g})$,$\nu_s(IO_2)$
787 (43)	$\nu_1(A_1')$, $\nu_s(IO_2)$		
754 (28)			
629 (8)sh		$\nu_2(A_1)$, $\nu_s(IF_2)_{eq}$	
611 (84)			
599 (5)sh			
571 (25)			$\nu_2(A_{1g})$, $\nu_s(IF_4)$
563 (12)sh		$\nu_3(A_1)$, $\nu_s(IF_2)_{ax}$	
517 (26)	$\nu_2(A_1')$, $\nu_s(IF_5)$		
396 (25)	$\nu_{10}(E_2')$, $\nu_{as}(IF_5)$	$\nu_4(A_1)$, $\delta_{sciss}(IO_2)$	
377 (13)			$\nu_8(E_g)$, $\delta(OIF_4O)$
368 (25)	$\nu_8(E_1'')$, $\delta_{rock}(IO_2)$		
359 (3)		bending modes	
333 (32)			
253 (1)			$\nu_6(B_{2g})$, $\delta_s(IF_4)$ in plane
235 (1)		bending modes	
209 (2)			

[a] Spectrum recorded on microcrystalline solid in a Pyrex glass capillary at room temperature using the 514.5-nm excitation. Values in parentheses denote relative intensities; sh: shoulder.

[b] The $N(CH_3)_4^+$ cation modes were observed at 458 (15), $\nu_{19}(T_2)$; 765 (20), $\nu_3(A_1)$; 951 (32), 967 (11), 974 (8), $\nu_{18}(T_2)$; 1178 (5), 1193 (3), $\nu_7(E)$; 1208 (3), 1288 (3), $\nu_{17}(T_2)$; 1416 (6), $\nu_{16}(T_2)$; 1464 (19), $\nu_2(A_1)$; 1471 (26), 1480 (29), 1489 (6), $\nu_6(E)$: 1516 (1), 2816 (11), 2834 (10), 2885 (12), 2927 (20), 2940 (20), 2966 (43), 2978 (32), 3004 (24), 3040 (67) cm^{-1}, ν_{CH_3} and binary bands (see ref. (201,202)).

much lower in frequency than the corresponding band found at 571 cm^{-1} for the four I-F bonds in *trans*-$IO_2F_4^-$. The Raman active asymmetric IF_5 stretching mode, $\nu_9(E_2')$, overlaps with the IO_2 scissoring mode of *cis*-$IO_2F_4^-$, $\nu_4(A_1)$, and was identified by the increase in relative intensity compared to a Raman spectrum of the *cis*-$IO_2F_4^-$ (see 2.2.8. Preparation of $[N(CH_3)_4][IO_4]$ and $[N(CH_3)_4][IO_2F_4]$). The band at 368 cm^{-1} was assigned to the $\nu_8(E_1'')$ mode of the $IO_2F_5^{2-}$ anion, and corresponds to the rocking of the axial atoms. The assignment is based on the fact that for the known pentagonal bipyramidal molecules, $TeOF_6^{2-}$,[113] $UO_2F_5^{3-}$,[240] and IOF_6^-,[110] the rocking mode is the most intense band among the bending modes and is more intense than the $\nu_{10}(E_2')$ mode in species with axial oxygen atoms in the Raman spectrum. The absence of the remaining $\nu_9(E_2')$ mode corresponding to scissoring motion of the IF_5 unit is a consequence of its expected low intensity and its likely overlap with the *cis*-$IO_2F_5^{2-}$ and $N(CH_3)_4^+$ bands. The equatorial scissoring mode also has a low intensity in the Raman spectra of SbF_7^{2-},[135] BiF_7^{2-},[135] TeF_7^-,[145] IF_7,[106] IOF_6^-,[110] $TeOF_6^{2-}$,[113] and $UO_2F_5^{2-}$.[240]

The pentagonal bipyramidal geometry for $IO_2F_5^{2-}$ cannot be unequivocally explained by VSEPR rules using the "repelling points on a sphere model".[120] The geometry of the $IO_2F_5^{2-}$ anion is, however, consistent with the structures of other main-group heptacoordinated species, such as IOF_6^-,[110] IF_7,[104-107] SbF_7^{2-},[135] BiF_7^{2-},[135] TeF_7^-,[113] $TeOF_6^{2-}$,[113] $ROTeF_6^-$,[111] and $(RO)_2TeF_5^-$ (where R is an alkyl group).[111] In particular, a close analogy can be made with the XeF_5^- anion.[90] The XeF_5^- anion has a pentagonal planar structure with five equatorial fluorines and two axial free valence electron pairs. As with the XeF_5^- anion, which maintains the large lone pair electron domains as far apart as possible, the large doubly bonded oxygen domains of the $IO_2F_5^{2-}$ anion are expected to be comparatively far apart. The pentagonal bipyramidal structure is the only geometry that affords this.

The observed frequencies of the modes for $IO_2F_5^{2-}$ are consistent with the expected trend in the isoelectronic sequence: $IO_2F_5^{2-}$, IOF_6^-,[110] IF_7.[106] The symmetric stretching frequency of the equatorial IF_5 bonds is much lower for $IO_2F_5^{2-}$ (517 cm^{-1}) than for IOF_6^- (584 cm^{-1})[110] and IF_7 (635 cm^{-1}),[106] but is very similar to the symmetric XeF_5 stretching frequency of XeF_5^- (502 cm^{-1}).[141] Similarly, the asymmetric IF_5 stretching frequency of 395 cm^{-1} for $IO_2F_5^{2-}$ is much lower than those IOF_6^- (457 cm^{-1})[110] and IF_7 (510 cm^{-1}),[106] but occurs in the same range as $\nu_{as}(XeF_5)$ in XeF_5^- (423 cm^{-1}).[141] The symmetric and asymmetric IF_5 stretching frequencies of these pentagonal bipyramidal species decrease in the order $IF_7 > IOF_6^- > IO_2F_5^{2-}$, consistent with substitution of the fluorine single bond domain by the larger oxygen double bond domain and with the increase of negative charge, resulting in weaker, more ionic IF bonds over this series. These factors are also responsible for the observed decrease in energy for the I–O stretching modes from IOF_6^- (873 cm^{-1})[110] to $IO_2F_5^{2-}$ (789 cm^{-1}). The rocking frequencies of the axial atoms in these isoelectronic species follow the reverse sequence IF_7 (319 cm^{-1})[106] < IOF_6^- (341 cm^{-1})[110] < $IO_2F_5^{2-}$ (368 cm^{-1}). This trend is expected since the I–O bond domains result in increased steric crowding and a decrease in the flexibility of the axial atoms. The similarity of the symmetric and asymmetric equatorial stretching frequencies of the $IO_2F_5^{2-}$ and XeF_5^- anions suggests a bonding description for $IO_2F_5^{2-}$ which is closely related to that of the XeF_5^- which involves two sp-hybrid orbitals bonding to two axial oxygens/containing two lone pairs and two semiionic multicentre four-electron bonds involving two 5p orbitals of the central atom.[141] The analogy between the two anions, implies that one negative charge is delocalized over the four equatorial fluorines in $IO_2F_5^{2-}$, while the second charge is located on the two axial oxygen atoms.

10.2.3. Formation of $[N(CH_3)_4]_2[IO_2F_2][HF_2]$

Crystals of $[N(CH_3)_4]_2[IO_2F_2][HF_2]$ containing the $IO_2F_2^-$ anion were grown in the CH_3CN extract of the $[N(CH_3)_4]_2[IO_2F_5]$/$[N(CH_3)_4]$[*cis*-IO_2F_4] mixture, which contained $[N(CH_3)_4][F]$, $[N(CH_3)_4]$[*cis*-IO_2F_4], and presumably some $[N(CH_3)_4]$[*trans*-IO_2F_4] arising from the dissociation of the $IO_2F_5^{2-}$ anion (eq. (10.3)). Raman bands of $[N(CH_3)_4]_2[IO_2F_2]$

$$[N(CH_3)_4]_2[IO_2F_5] \rightarrow [N(CH_3)_4][\textit{trans}\text{-}IO_2F_4] + [N(CH_3)_4][F] \qquad (10.3)$$

$[HF_2]$ were observed in the isolated white solid from a sample of a $[N(CH_3)_4]_2[IO_2F_5]$/ $[N(CH_3)_4]$[*cis*-IO_2F_4] mixture kept at room temperature for one week. Tetramethylammonium fluoride apparently plays a crucial role in the reduction of $IO_2F_4^-$ to $IO_2F_2^-$ since the autodecomposition of $IO_2F_4^-$ has never been reported. At room temperature, anhydrous $[N(CH_3)_4][F]$ readily abstracts a H^+ from CH_3CN solvent (eq (10.4)) yielding the CH_2CN^- anion, which reacts with CH_3CN to form 3-amino-2-butenenitrile (eq (10.5)).[172] The oxidation product resulting from the observed reduction

$$2[N(CH_3)_4][F] + CH_3CN \xrightarrow{CH_3CN} [N(CH_3)_4][HF_2] + [N(CH_3)_4][CH_2CN] \qquad (10.4)$$

$$CH_2CN^- + H^+ + CH_3CN \xrightarrow{CH_3CN} H_2N(CH_3)C{=}CHCN \qquad (10.5)$$

of I(VII)$O_2F_4^-$ to I(V)$O_2F_2^-$ has not been identified yet. However, the fluorination of the double bond in 3-amino-2-butenenitrile according to eq. (10.6) is a possible route, which

$$IO_2F_4^- + H_2N(CH_3)C{=}CHCN \xrightarrow{CH_3CN} IO_2F_2^- + H_2N(CH_3)FC\text{-}CF(H)CN \qquad (10.6)$$

has to be verified by NMR spectroscopy in the future.

10.2.4. X-ray Crystal Structure of $[N(CH_3)_4]_2[IO_2F_2][HF_2]$

Details of the data collection parameters and other crystallographic information for $[N(CH_3)_4]_2[IO_2F_2][HF_2]$ are given in Table 10.3. Important bond lengths, angles, and contacts for $[N(CH_3)_4]_2[IO_2F_2][HF_2]$ are listed in Table 10.4.

The crystal structure of $[N(CH_3)_4]_2[IO_2F_2][HF_2]$ contains alternating layers of $N(CH_3)_4^+$ cations and $IO_2F_2^-$ and HF_2^- anions in the (10-1) plane (Figure 10.4). The two crystallographically independent $N(CH_3)_4^+$ cations are tetrahedral about the nitrogen within 3σ and have the expected bond lengths. The I-O (177.4(2) pm) and I-F (202.5(2), 202.7(2) pm) bond lengths for $IO_2F_2^-$ anion in $[N(CH_3)_4]_2[IO_2F_2][HF_2]$ are in good agreement with those for the previously reported crystal structure of $[K][IO_2F_2]$ (I-O: 176.2(8), 177.5(13) pm; I-F: 201.5(8), 198.5(8) pm).[241] As in the structure of the K^+ salt, the two fluorine atoms in the $IO_2F_2^-$ are in the axial positions, while the two oxygens and

Table 10.3 Summary of Crystal Data and Refinement Results for $[N(CH_3)_4]_2[IO_2F_2][HF_2]$

	$[N(CH_3)_4]_2[IO_2F_2][HF_2]$
formula	$C_8H_{25}F_4IN_2O_2$
space group	*C2/m* (No. 12)
a [pm]	1467.65(2)
b [pm]	860.490(10)
c [pm]	1395.72(2)
α [deg]	90
β [deg]	120.2040(10)
γ [deg]	90
V [10^6 pm^3]	1523.35(3)
Z [molecules/unit cell]	4
mol. wt	384.20
calcd density [g cm^{-3}]	1.675
colour, morphology	colourless needles
size [mm^3]	0.8×0.08×0.02
μ [mm^{-1}]	2.139
data/restraints/parameters	1584/0/146
final agreement factors	R^a = 0.0192
	R_w^b = 0.0455
GOOF	1.099
Extinction coefficient	0.0013(2)
$\Delta\delta_{max}/\Delta\delta_{min}$ [e 10^{-6} pm^{-3}]	0.680/-0.561

[a] $R = \Sigma||F_o| - |F_c||/\Sigma|F_o|$.

[b] $R_w = \Sigma|(|F_o| - |F_c|)w^{1/2}|/\Sigma(|F_o|w)$ where $w = 1/[\sigma^2(F) + (0.0344)^2 + 4.94]$.

Table 10.4 Important Bond Lengths, Contacts, and Bond Angles in $[N(CH_3)_4]_2[IO_2F_2][HF_2]$

$[N(CH_3)_4]_2[IO_2F_2][HF_2]$

Bond Lengths and Contacts [pm]

I(1)–O(1)	177.4(2)	I(1)-F(1)	202.5(2)
I(1)–F(2)	202.5(2)	N(1)-C(1)	150.0(4)
N(1)-C(2)	149.3(4)	N(1)-C(3)	149.5(3)
N(2)-C(4)	150.0(4)	N(2)-C(5)	148.8(4)
N(2)-C(6)	149.9(3)	F(3)--F(3A)	227.7(5)
I(1)--F(3)	280.6(2)		

Bond Angles [deg.]

O(1)–I(1)–O(1A)	101.98(12)	O(1)-I(1)–F(1)	91.01(7)
O(1)–I(1)–F(2)	91.00(7)	F(1)–I(1)–F(2)	176.73(8)
C(1)-N(1)-C(2)	110.1(3)	C(1)-N(1)-C(3)	109.3(2)
C(2)-N(1)-C(3)	109.4(2)	C(4)-N(2)-C(5)	110.0(3)
C(4)-N(2)-C(6)	109.5(2)	C(5)-N(2)-C(6)	109.6(2)
F(3)---I(1)---F(3A)	84.63(8)		

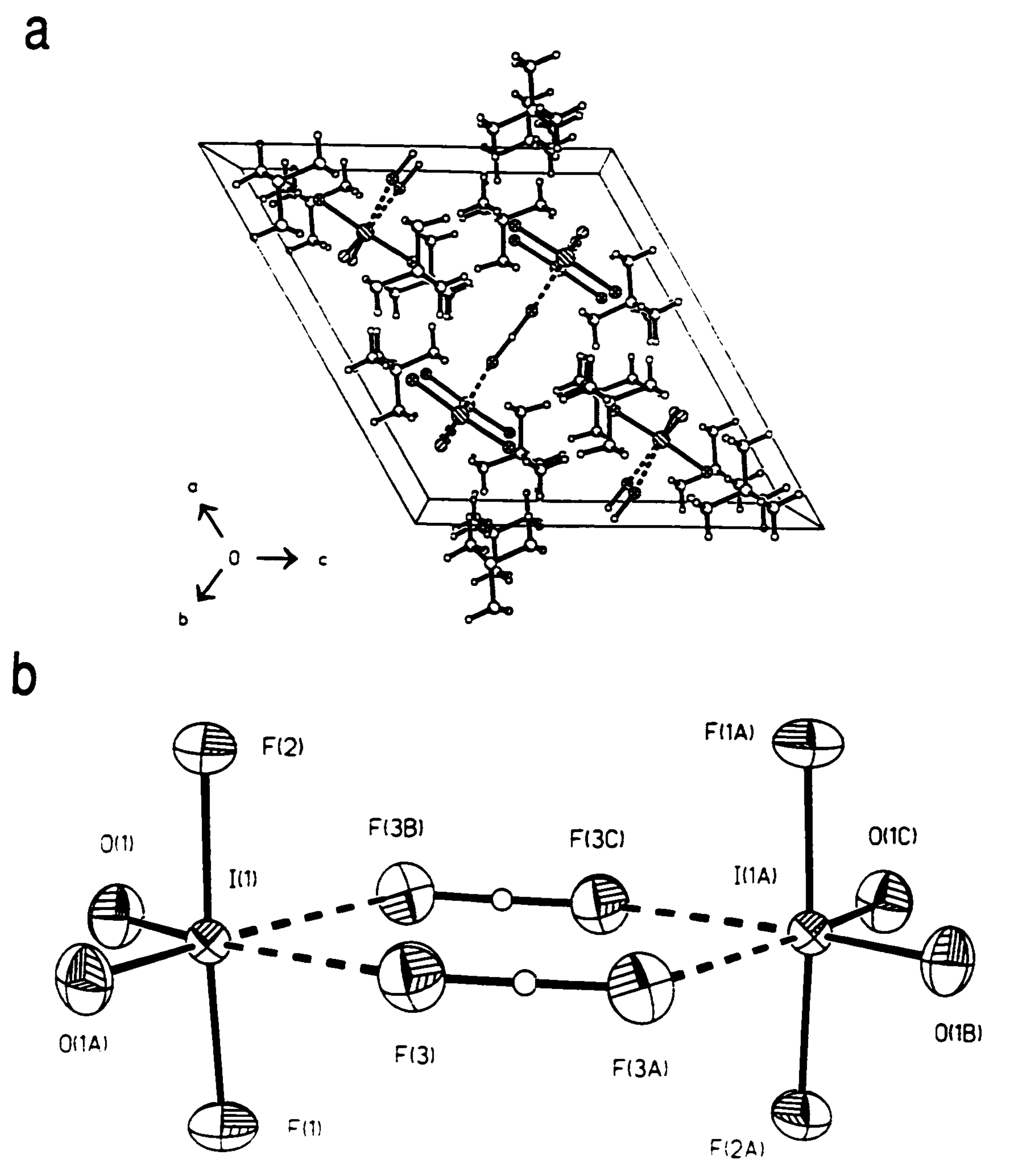

Figure 10.4 View of (a) the $[N(CH_3)_4]_2[IO_2F_2][HF_2]$ unit cell showing the packing along the *b*-axis and (b) the $IO_2F_2^-$ HF_2^- arrangement (thermal ellipsoids are drawn at the 50% probability level).

the lone pair are in the equatorial plane, which is predicted by VSEPR rules for an AX_2Y_2E structure.[120] The axial F-I-F angle is slightly bent (176.73(8)°) towards the lone pair position, away from the two I=O double bond domains, and is in contrast to the essentially linear F-I-F arrangement (179.1(5)°) in the K^+ salt.[241] The bending of the axial ligands in the pseudo-trigonal bipyramidal AX_2Y_2E structures towards the lone pair position has also been found in the crystal structures of XeO_2F_2 (174.7(4)°),[162] XeO_2F_2···TcO_2F_3 (175.7(6)°),[93] and $XeO_2(OTeF_5)_2$ (163.7(2)°),[242] and has been attributed to a non-spherical charge distribution of the lone pair, which is more extended in the equatorial plane and reduces the repulsion with the axial ligands.[243] The axial angle in $IO_2F_2^-$, however, is significantly larger than that in the neutral xenon analogues, reflecting the decreased steric demand of O-I bonds, which are more ionic in an anionic species. The smaller I-O bond domain in $IO_2F_2^-$ is also evidenced by the smaller O-I-O bond angles in $[N(CH_3)_4]_2[IO_2F_2][HF_2]$ (101.98(12)°) and $[K][IO_2F_2]$ (102.0(6)°)[241] when compared to those in XeO_2F_2 (105.7(3)°),[162] XeO_2F_2···TcO_2F_3 (105.6(6)°),[93] and $XeO_2(OTeF_5)_2$ (106.5(2)°).[242]

The two fluorine atoms of the HF_2^- anion are related through a crystallographic 2-fold axis and the hydrogen was refined on the special position (*2*). The F(3)···F(3A) distance (227.7(5) pm) is longer than that in the crystal structure of $[N(CH_3)_4][HF_2]$ (221.3 pm)[228], because of the strong I(1)···F(3) contacts in the $[N(CH_3)_4]_2[IO_2F_2][HF_2]$ structure (*vide infra*). The F···F distance in the present structure is the same as that in the HF_2^- in *trans*-$[Ru(dmpe)_2(H)(HF_2)]$ (227.6(8) pm);[230] it is, however, significantly smaller than the F···F distances found in the transition metal complexes, $[Ni(FHF)(C_4N_2F_2H)(PEt_3)_2]$

(240.0(6) pm),[229] $Mo(PMe_3)_4(H)_2F(FHF)$ (235.1(8) pm),[231] $W(PMe_3)_4(H)_2F(FHF)$ (238.9(6) pm),[232] and $[(\eta^5\text{-}C_5Me_5)NbF_4(HF)AsF_3]_2$ (268.6 pm),[227] indicating that the latter four structures can better be described as an HF molecule hydrogen-bonded to the metal-F group.

The $IO_2F_2^-$ and HF_2^- anions form strong contacts (280.6(2) pm; sum of van der Waals radii: 350 to 346 pm)[212,213] with F(3) of two symmetry related bifluoride ions, which coordinate to I(1) and avoid the lone pair position, resulting in a pseudo-octahedral coordination sphere around iodine. Such an extension of the coordination sphere of iodine to a pseudo-octahedron has also been found in $[K][IO_2F_2]$[241] where two oxygen atoms from two adjacent $IO_2F_2^-$ anions form contacts with the iodine (287.6(8), 288.7(12) pm), which are, however, significantly weaker than the I--F contacts in the $[N(CH_3)_4]_2[IO_2F_2][HF_2]$. Such a pseudo-octahedral coordination environment for the Xe^{VI} atom has also been found in the crystal structure of XeO_2F_2.[162]

10.2.5. Raman Spectroscopic Characterization of $[N(CH_3)_4]_2[IO_2F_2][HF_2]$

A Raman spectrum of the single crystal of $[N(CH_3)_4]_2[IO_2F_2][HF_2]$ used for X-ray diffraction (*vide supra*) was recorded at room temperature (Figure 10.5). The frequencies and their assignments are listed in Table 10.5. The assignments for the Raman bands of $IO_2F_2^-$ are based on those given for KIO_2F_2[244] and those of isoelectronic XeO_2F_2.[163,164]

The vibrations of the $IO_2F_2^-$ anion span the irreducible representations $\Gamma = 4A_1 + A_2 + 2B_1 + 2B_2$ under C_{2v} point symmetry (IO_2 in the *xz*-plane). While all modes are Raman active, $4A_1 + 2B_1 + 2B_2$ are infrared active. The band at 838 cm^{-1} corresponds to

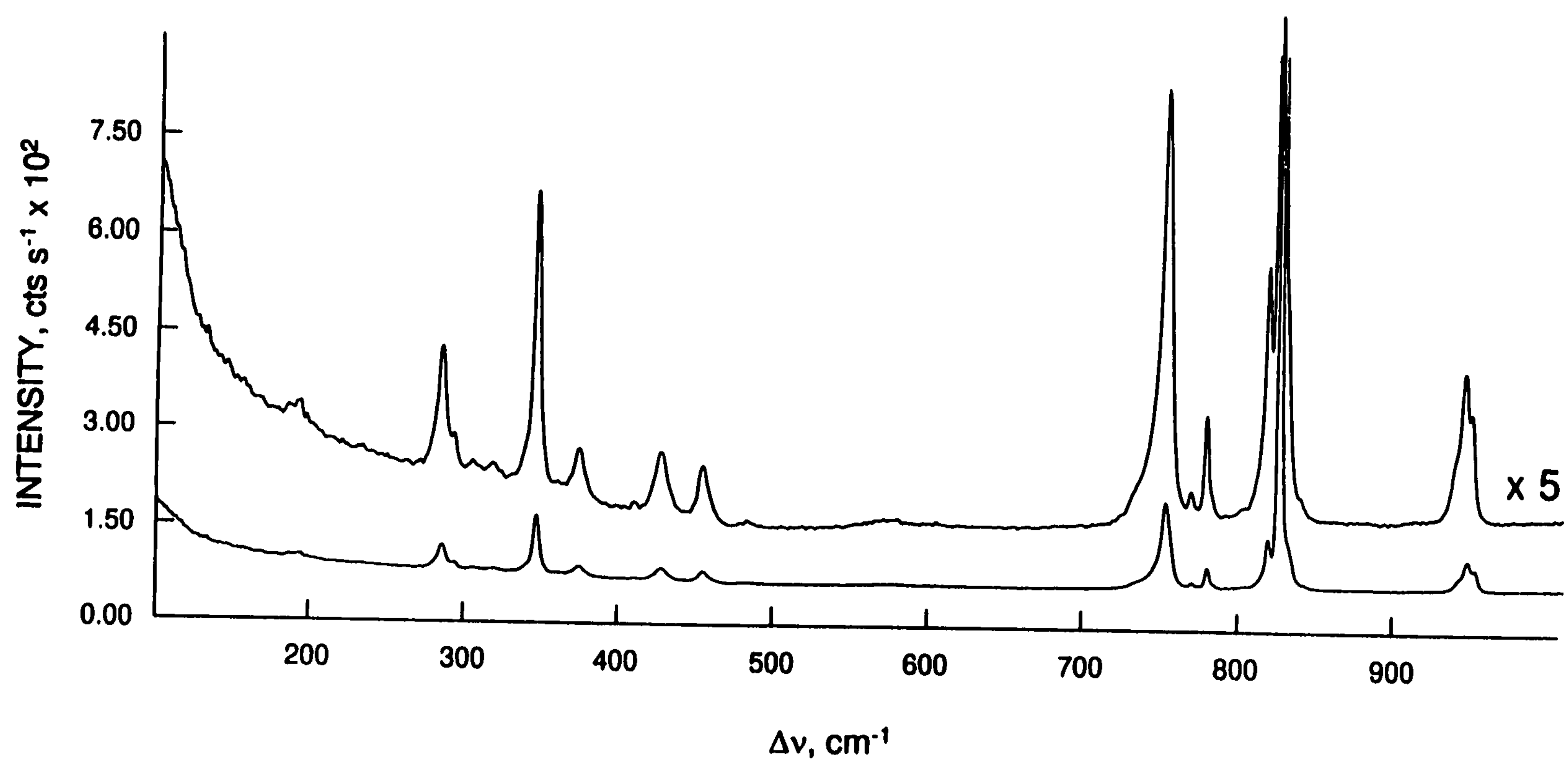

Figure 10.5 Raman spectrum of a single crystal of $[N(CH_3)_4]_2[IO_2F_2][HF_2]$ recorded in a glass Lindemann capillary at room temperature using the 514.5-nm excitation.

Table 10.5 Vibrational Frequencies and Assignments for $[N(CH_3)_4]_2[IO_2F_2][HF_2]$.

Frequency[a] [cm^{-1}]	Assignment		
	$N(CH_3)_4^+$ (T_d)	$IO_2F_2^-$ (C_{2v})	HF_2^- ($D_{\infty h}$)
3041 (12)sh	ν_{CH3} and binary bands		
3034 (14)			
3020 (19)			
2968 (16)			
2933 (13)			
2897 (7)			
2837 (11)			
1479 (24)	$\nu_6(E)$, $\nu_2(A_1)$		
1473 (10)sh			
1420 (1)	$\nu_{16}(T_2)$		
1293 (1)	$\nu_{17}(T_2)$		
1189 (2)	$\nu_7(T_2)$		
960 (4)	$\nu_{18}(T_2)$		
955 (6)			
950 (2)sh			
847 (1)		$\nu_6(B_1)$, $\nu_{as}(IO_2)$	
838 (10)sh			
832 (100)		$\nu_1(A_1)$, $\nu_s(IO_2)$	
825 (9)			
811 (<0.5)			
785 (4)			
775 (1)			
758 (16)	$\nu_3(A_1)$		
741 (1)sh			
581 (<0.5)			$\nu_1(\Sigma_g^+)$, ν_s
487 (<0.5)		$\nu_8(B_2)$, $\nu_{as}(IF_2)$	
458 (1)	$\nu_{19}(T_2)$		
430 (3)		$\nu_2(A_1)$, $\nu_s(IF_2)$	

Table 10.5 continued ...

Frequency[a] [cm^{-1}]	Assignment		
	$N(CH_3)_4^+$ (T_d)	$IO_2F_2^-$ (C_{2v})	HF_2^-
413 (<0.5)			
378 (2)	ν_8(E)		
349 (10)		$\nu_3(A_1)$, $\delta_s(IO_2)$	
344 (1)sh		$\nu_7(B_1)$, $\delta(IF_2)$	
321 (1)			
308 (1)			
296 (1)			
288 (5)		$\nu_9(B_2)$, $\delta_{rock}(IO_2)$	
197 (1)		$\nu_4(A_1)$, $\delta(IF_2)$	

[a] Spectrum recorded on a single crystal in a glass Lindemann capillary at room temperature using the 514.5-nm excitation. Values in parentheses denote relative Raman intensities; and sh a shoulder.

the symmetric I-O stretch $\nu_1(A_1)$, which is shifted to slightly higher frequency with respect to $\nu_s(IO_2)$ in $[K][IO_2F_2]$ (808 cm^{-1}).[244] The symmetric and asymmetric IF_2 stretching modes were assigned to the bands at 430 and 487 cm^{-1} based on their intensities. The ordering of $\nu_s(IF_2)$ and $\nu_{as}(IF_2)$ modes is opposite to that for $[K][IO_2F_2]$,[244] but is in the same order as the $\nu_s(XeF_2)$ and $\nu_{as}(XeF_2)$ modes in XeO_2F_2.[164] The weak band at 581 cm^{-1} can be assigned to the symmetric stretch of the bifluoride ion and is slightly lower in frequency than in $[N(CH_3)_4][HF_2]$ (596 cm^{-1}),[228] which is consistent with the strong I···F contacts in the crystal structure (see 10.2.4 X-ray Crystal Structure of $[N(CH_3)_4]_2[IO_2F_2][HF_2]$).

10.3. Conclusion

The fluoride ion acceptor properties of *cis*-$IO_2F_4^-$ and *trans*-$IO_2F_4^-$ have been studied. Because of steric crowding in the intermediate derived from *cis*-$IO_2F_4^-$, only the *trans*-$IO_2F_4^-$ anion acts as a fluoride ion acceptor towards naked fluoride ion, while the addition of a fluoride ion to the *cis*-isomer is kinetically unfavourable. The novel $IO_2F_5^{2-}$ anion that results from the addition of F^- to *trans*-$IO_2F_4^-$ has been prepared and is presently the only known main-group $AO_2F_5^{n-}$ species. Based on Raman spectroscopy, the $IO_2F_5^{2-}$ anion was found to have a pentagonal bipyramidal geometry, that is consistent with general preference of main-group fluorides and oxide fluorides for geometries based on a pentagonal bipyramid. A crystal structure of $[N(CH_3)_4]_2[IO_2F_2][HF_2]$, a decomposition product in the preparation of $[N(CH_3)_4]_2[IO_2F_5]$, provides a rare example of coordination of a bridging HF_2^- ligand and more precise X-ray crystal structure for the $IO_2F_2^-$ anion.

CHAPTER 11

XENON(II) OXIDE FLUORIDES

11.1. Introduction

Minkwitz and Nowicki[1,245] reported that the protonated hypofluorous acid cation, H_2OF^+ results from the oxidative fluorination of H_2O by $[XeF][MF_6]$ (M = As, Sb) in HF solvent at -60 °C according to eq. (11.1). The resulting pale red product was formulated

$$[XeF][MF_6] + H_2O \xrightarrow{HF} Xe + [H_2OF][MF_6], M = As, Sb \quad (11.1)$$

as $[H_2OF][MF_6]$ and was characterized by infrared and ^1H and ^{19}F NMR spectroscopy. Renewed interest in the preparative use of the protonated hypofluorous acid prompted the attempt to repeat the work of Minkwitz and Nowicki, but the observation that xenon is retained in HF solutions of XeF^+ and H_2O as well as the failure to reproduce the reported NMR and vibrational spectra sparked a reinvestigation of the reaction between $[XeF][AsF_6]$ and H_2O in HF solvent.

Controlled hydrolysis of xenon fluorides is one possible preparative route to xenon oxide fluorides. Neutral xenon oxide fluorides with xenon in the +4 ($XeOF_2$)[147-150], +6 ($XeOF_4$,[156-160] XeO_2F_2[92,162-164]), and +8 (XeO_3F_2,[8] XeO_2F_4[10]) oxidation states are known and cationic xenon oxide fluorides have been prepared for xenon in the +6 oxidation state ($XeOF_3^+$,[151-155] XeO_2F^+,[152,153,156,161] and $Xe_2O_4F_3^+$ [156,161]). All the oxide fluorides of Xe(VI) and that of Xe(IV) have been prepared by hydrolysis of XeF_6 and XeF_4 in HF solvent. Prior to this work, no systematic study of the hydrolytic behaviour of a Xe(II) fluoride species had been reported and no examples of neutral or ionic xenon(II) oxide fluorides have been reported.

11.2. Results and Discussion

11.2.1. Reaction of [XeF][AsF$_6$] with H_2O in HF and BrF_5 Solvents and Multi-NMR Spectroscopic Characterization

At -78 °C, [XeF][AsF$_6$] and H_2O slowly react in anhydrous HF to form XeF_2 and [H$_3$O][AsF$_6$] according to eq. (11.2). Xenon difluoride was identified at -75 °C by ^{19}F and

$$[XeF][AsF_6] + H_2O + HF \overset{HF}{\rightleftharpoons} XeF_2 + [H_3O][AsF_6] \qquad (11.2)$$

^{129}Xe NMR spectroscopy ($\delta(^{129}Xe) = 1516.3$ ppm, $\delta(^{19}F) = -200.68$ ppm, $^1J(^{129}Xe-^{19}F) = 5670$ Hz). In addition to the XeF_2 resonance and the HF solvent line (-193.66 ppm, $\Delta\nu_{1/2} = 38$ Hz), only a broad singlet at -68.5 ppm ($\Delta\nu_{1/2} = 1560$ Hz) corresponding to the AsF_6^- anion was observed in the ^{19}F NMR spectrum. The ^{17}O NMR spectrum of a sample prepared from ^{17}O-enriched H_2O (64.6% ^{16}O, 21.9% ^{17}O, and 42.7% ^{18}O) showed a singlet at -0.47 ppm ($\Delta\nu_{1/2} = 177$ Hz) at -75 °C, which is assigned to H_3O^+ and which presumably undergoes rapid proton exchange with HF and residual H_2O preventing the observation of $^1J(^{17}O-^1H)$ coupling.[246]

The reaction of XeF_2 with $[H_3O][AsF_6]$ in HF solution successively yields three cationic xenon species according to eqs. (11.3) - (11.9). The reaction of XeF_2 with the

$$[H_3O][AsF_6] + XeF_2 \xrightarrow{\text{HF, -78 °C}} [H_2OXeF][AsF_6] + HF \qquad (11.3)$$

$$2[H_2OXeF][AsF_6]_{(HF)} \xrightarrow{\text{HF, < -78 °C}} [H_2OXeF]_2[F][AsF_6]_{(s)} + AsF_5 \qquad (11.4)$$

strong protic acid H_3O^+ yields the protonated fluorohypoxenous acid cation, H_2OXeF^+, upon HF elimination according to (11.3) and is analogous to the reaction of XeF_2 with neutral and cationic, protic acids, such as $HOTeF_5$,[247] HSO_3F,[248,249] $HClO_4$,[248,249] $HN(SO_2F)_2$,[250] $C_5F_5NH^+$,[251] and $CF_3C(OH)NH_2^+$ [252] yielding neutral and cationic (adduct) species formulated as L-XeF^+, where L is the deprotonated acid. The new species, $[H_2OXeF][AsF_6]$, exhibits moderate solubility and precipitates from HF solution close to the freezing point of the solvent. Colorless to pale orange crystals of $[H_2OXeF]_2[F][AsF_6]$ crystallize from HF solution between -78 °C and the freezing point of HF (-83 °C) (see 11.2.3.1. X-ray Crystal Structures, $[H_2OXeF]_2[F][AsF_6]$). The strong hydrogen-bonding interaction between the H_2OXeF^+ cations and AsF_6^- anions apparently results in dissociation of half of the AsF_6^- anions into fluoride ions and AsF_5 upon crystallization/precipitation according to eq. (11.4). Failure to observe the H_2OXeF^+ cation by NMR spectroscopy in HF solvent is presumably the result of rapid exchange between the fluorine environments of the H_2OXeF^+ cation and HF solvent.

Free AsF_5 generated from reaction (11.4) reacts with dissolved XeF_2 to yield $[XeF][AsF_6]$ (eq. (11.5)) which subsequently reacts with XeF_2 at low temperature to form the trigonal modification of $[Xe_2F_3][AsF_6]$ (eq. (11.6)) which is soluble in HF solvent at

$$XeF_2 + AsF_5 \xrightarrow{HF,\ -78\ °C} [XeF][AsF_6] \qquad (11.5)$$

$$[XeF][AsF_6] + XeF_2 \xrightarrow{HF,\ -78\ °C} [Xe_2F_3][AsF_6] \qquad (11.6)$$

-30 °C, and which crystallized from a very concentrated HF solution of $[XeF][AsF_6]$ and H_2O (3 : 1 ratio; *ca.* 2.8 M with respect to XeF^+) at *ca.* -30 °C (see 11.2.3.2. X-ray Crystal Structures, trigonal $[Xe_2F_3][AsF_6]$). When an excess of H_2O with respect to $[XeF][AsF_6]$ is used (*i.e.*, 2:1 and 4:1 H_2O:$[XeF][AsF_6]$ molar ratios), the AsF_5 is consumed by formation of additional $[H_3O][AsF_6]$ without formation of $[Xe_2F_3][AsF_6]$. However, insufficient mixing of the initial reaction mixture can result in $[XeF][AsF_6]$ which reacts with XeF_2 according to eq. (11.6) even if an excess of H_2O is used.

The reaction of an additional mole of XeF_2 with the protic acid, $[H_2OXeF][AsF_6]$, presumably yields $[FXe(OH)XeF][AsF_6]$ according to eq. (11.7). Elimination of HF according to eq. (11.8) gives rise to $FXeOXe^+$ as an intermediate which subsequently reacts with XeF_2 to give the intense red $[Xe_3OF_3][AsF_6]$ salt (eq. (11.9)) as the final

$$[H_2OXeF][AsF_6] + XeF_2 \xrightarrow{HF,\ -78\ °C} [FXe(OH)XeF][AsF_6] + HF \qquad (11.7)$$

$$[FXe(OH)XeF][AsF_6] \xrightarrow{HF,\ -78\ ^{\circ}C} [FXeOXe][AsF_6] + HF \quad (11.8)$$

$$[FXeOXe][AsF_6] + XeF_2 \xrightarrow{HF,\ -78\ ^{\circ}C} [FXeOXeFXeF][AsF_6] + HF \quad (11.9)$$

product in the reaction sequence for the XeF^+/H_2O system. The $[Xe_3OF_3][AsF_6]$ salt does not react further in HF solvent at -78 °C. However, the slow growth (several weeks) of intense red-magenta colored dendrimeric crystal clusters in the colorless HF solution above the red-orange precipitate at -78 °C suggests that equilibrium (11.10) is operative.

$$[FXeOXe\cdots FXeF][AsF_6]_{(s)} \rightleftharpoons FXeOXe^+_{(HF)} + AsF^-_{6\,(HF)} + XeF_{2\,(HF)} \quad (11.10)$$

At H_2O concentrations of 0.26 M, $[H_2OXeF][AsF_6]$ was formed within approximately one day, while $[Xe_2F_3][AsF_6]$ was the major species in the solid precipitate after approximately two days. Upon standing for a further five days, $[Xe_3OF_3][AsF_6]$ became the major species. Crystalline $[Xe_3OF_3][AsF_6]$ has also been obtained by dissolution of a mixture of $[XeF][AsF_6]$ and H_2O in HF at -30 °C (*ca.* 0.50 M with respect to XeF^+), which had been maintained at -78 °C for *ca.* 48 h. Slow cooling of the clear colorless solution resulted in crystallization of red-orange needles between -46 and -54 °C which were shown to be $[Xe_3OF_3][AsF_6]$ by a unit cell determination.

The reaction rate is strongly dependent on the concentration, reaction temperature, and the degree of initial mixing. Without initial agitation, small amounts of $[XeF][AsF_6]$ were detected in the Raman spectrum of the precipitate for at least a week. After thorough mixing at an initial concentration of 1.77 M H_2O, $[H_2OXeF][AsF_6]$ and $[Xe_2F_3][AsF_6]$ were formed after only 2 h with $[XeF][AsF_6]$ being completely reacted, and significant amounts of $[Xe_3OF_3][AsF_6]$ were present after 12 h.

Small amounts of $[Xe_3OF_3][AsF_6]$ likely are the cause of the beige and flesh colorations of $[H_2OXeF]_2[F][AsF_6]$ and $[Xe_2F_3][AsF_6]$, respectively, because $[H_2OXeF]_2[F][AsF_6]$ has been identified by Raman spectroscopy as a colorless precipitate from HF solution and $[Xe_2F_3][AsF_6]$ has been obtained as colorless single crystals below -30 °C. The reaction mixture (*ca.* 0.50 M with respect to XeF^+) was found to be soluble and stable up to -30 °C, decomposing above -30 °C with gas evolution (Xe gas; $\delta(^{129}Xe)$ = -5308.3 ppm at -30 °C). The direct reaction of XeF_2 and $[H_3O][AsF_6]$ in HF yielded the same reaction products, $[H_2OXeF][AsF_6]$, $[Xe_2F_3][AsF_6]$, and $[Xe_3OF_3][AsF_6]$ according to eqs. (11.3) - (11.9).

The products of the $[XeF][AsF_6]/H_2O$ reaction are relatively insensitive to small deviations from 1:1 stoichiometry. The reaction of $[XeF][AsF_6]$ with *n* moles of water H_2O (n = 2 and 4) initially yields XeF_2, $[H_3O][AsF_6]$, and (n-1) moles of H_2O according to eq. (11.11). In subsequent reactions $[H_2OXeF]_2[F][AsF_6]$ and $[Xe_3OF_3][AsF_6]$ are formed. The reaction of H_2O with a three-fold molar excess of $[XeF][AsF_6]$ (eq. (11.12))

$$[XeF][AsF_6] + nH_2O + HF \xrightarrow{HF} XeF_2 + [H_3O][AsF_6] + (n-1)H_2O \quad (11.11)$$

$$3[XeF][AsF_6] + H_2O + HF \xrightarrow{HF} 2[XeF][AsF_6] + XeF_2 + [H_3O][AsF_6] \longrightarrow [Xe_2F_3][AsF_6] + [H_3O][AsF_6] + [XeF][AsF_6] \quad (11.12)$$

yielded a white solid as the final product after *ca.* 7 months at -78 °C, which was identified by Raman spectroscopy and X-ray crystallography as the trigonal modification of $[Xe_2F_3][AsF_6]$ (see 11.2.3.2. X-ray Crystal Structures, trigonal $[Xe_2F_3][AsF_6]$). The formation of $[Xe_3OF_3][AsF_6]$ is prevented by the absence of XeF_2 in the reaction mixture, which is effectively removed by reaction with excess $[XeF][AsF_6]$ (eq. (11.6)) and the precipitation of $[Xe_2F_3][AsF_6]$.

In an attempt to characterize the H_2OXeF^+, $HO(XeF)_2^+$, and $Xe_3OF_3^+$ cations by solution NMR spectroscopy and circumvent rapid chemical exchange with the solvent, XeF_2 was allowed to react with $[H_3O][AsF_6]$ in BrF_5 solvent at -55 °C and was monitored by ^{19}F NMR spectroscopy at that temperature. The initial ^{19}F NMR spectrum of a sample of XeF_2 and $[H_3O][AsF_6]$ in BrF_5 solvent consisted of several resonances corresponding to XeF_2 (-183.25 ppm; $^1J(^{129}Xe-^{19}F)$ = 5737 Hz), AsF_6^- (-59.71 ppm), and BrF_5 (F_{ax}: 273.22 ppm; F_{eq}: 135.73 ppm; $^2J(^{19}F-^{19}F)$ = 76 Hz) solvent. After several minutes at -55 °C, resonances corresponding to $Xe_2F_3^+$ (F_t: -250.05 ppm, F_b: -183.48 ppm; $^2J(^{19}F-^{19}F)$ = 299 Hz, $^1J(^{129}Xe-^{19}F_t)$ = 6659 Hz; ^{129}Xe satellites of F_b overlapped with the resonances of XeF_2 and HF), HF (-192.33 ppm; $^1J(^{19}F-^1H)$ = 519 Hz) and BrO_2F (194.35 ppm, $\Delta\nu_{1/2}$ = 1950 Hz) were also observed and increased with time relative to the ^{19}F resonance for XeF_2. The formation of HF is consistent with eq. (11.13). In contrast to the analogous

$$2XeF_2 + 2[H_3O][AsF_6] + BrF_5 \xrightarrow{BrF_5} [Xe_2F_3][AsF_6] + BrO_2F + 6HF \quad (11.13)$$

reaction in HF solvent, where excess HF shifts equilibrium (11.2) completely to the side of XeF_2 and H_3O^+, XeF_2 and H_3O^+ are partially converted to XeF^+, H_2O, and HF in BrF_5 solvent. The interaction of XeF_2 and XeF^+ subsequently yields the $Xe_2F_3^+$ cation and H_2O reacts with BrF_5 solvent to form BrO_2F and HF. The ^{19}F NMR signals for HF and $Xe_2F_3^+$ become broader with time presumably because intermolecular exchange between HF and $Xe_2F_3^+$ increases with increasing concentration.

11.2.2. Raman Spectroscopy

The Raman spectra of $[H_2OXeF]_2[F][AsF_6]$, trigonal $[Xe_2F_3][AsF_6]$, and $[Xe_3OF_3][AsF_6]$ are shown in Figures 11.1, 11.2, and 11.3, respectively. The Raman frequencies and tentative assignments for $[H_2OXeF]_2[F][AsF_6]$ and $[Xe_3OF_3][AsF_6]$ are listed in Table 11.1. The frequencies and assignments for trigonal and monoclinic $[Xe_2F_3][AsF_6]$ are given in Table 11.2.

11.2.2.1. $[H_2OXeF]_2[F][AsF_6]$. Assuming C_s symmetry for the H_2OXeF^+ cation, a maximum of nine Raman and infrared active bands ($\Gamma = 6A' + 3A''$) is expected for the vibrational spectrum of the cation, and include the symmetric and asymmetric H_2O stretches which are expected above 3000 cm^{-1}. The Raman spectrum of solid $[H_2OXeF]_2[F][AsF_6]$ consists of nine vibrational bands between 760 and 70 cm^{-1} that are assigned to the H_2OXeF^+ cation and is dominated by the intense Xe-F stretching band at 552 cm^{-1}. The Xe-O stretch is assigned to a band at 470 cm^{-1} and only very weak, broad bands in the O-H stretching region (3292, 3160, and 3077 cm^{-1}) were observed in the

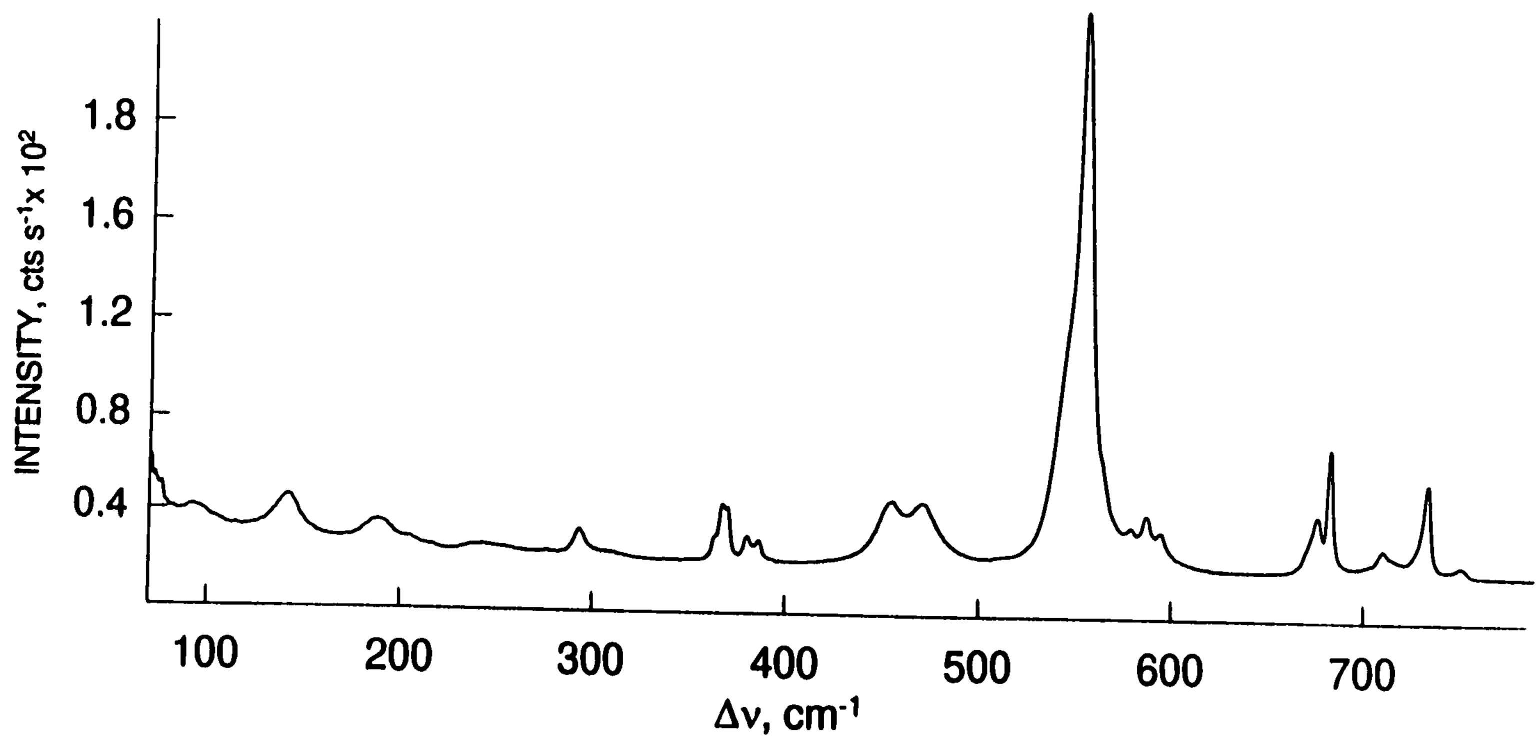

Figure 11.1 Raman spectrum of $2XeF_2 \cdot [H_3O][AsF_6]$ recorded under frozen HF in FEP at -145 °C using 514.5-nm excitation. Asterisks (*) denote FEP sample tube lines.

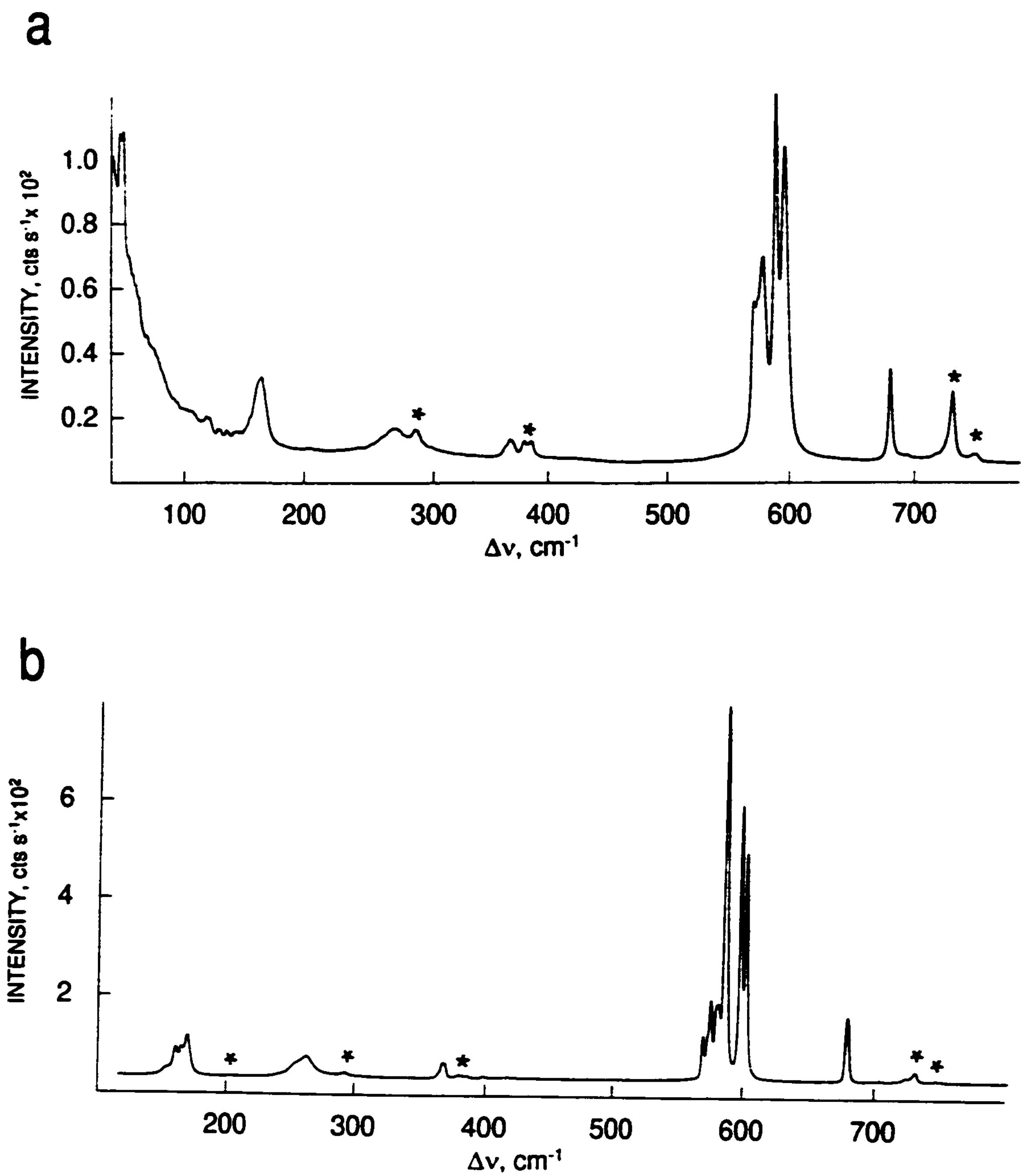

Figure 11.2 Raman spectra of (a) trigonal $[Xe_2F_3][AsF_6]$ under liquid HF at -85 °C and (b) monoclinic $[Xe_2F_3][AsF_6]$ at -150 °C recorded in FEP using 514.5-nm excitation. Asterisks (*) denote FEP sample tube lines.

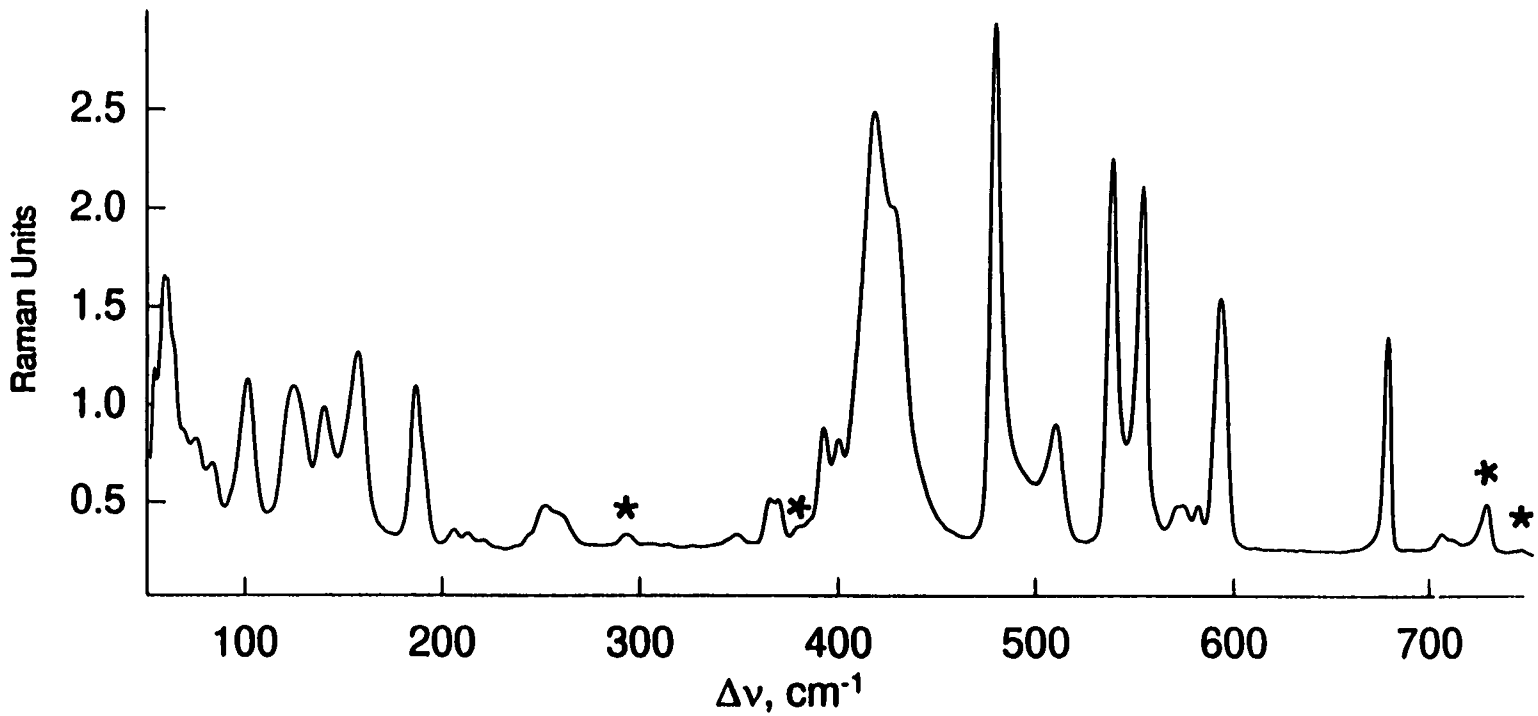

Figure 11.3 Raman spectrum of $[Xe_3OF_3][AsF_6]$ recorded under frozen HF in FEP at -155 °C using 1064-nm excitation. Asterisks (*) denote FEP sample tube lines.

Table 11.1 Raman Frequencies and Their Assignments for $[H_2OXeF]_2[F][AsF_6]$ (-145 °C) and $[Xe_3OF_3][AsF_6]$ (-155 °C)

Frequencies [cm^{-1}][a]	Assignments	Frequencies [cm^{-1}][a]	Assignments	
$[H_2OXeF]_2[F][AsF_6]$[b]	H_2OXeF^+	$[Xe_3OF_3][AsF_6]$[c]	$Xe_3OF_3^+$ [d]	AsF_6^- (C_{4v})
3292 (<0.5)	ν(O-H)	598 (37) sh	$\nu_{as}(F_1\text{-}Xe_1\text{-}F_2)$	
3160 (<0.5)		595 (48)		
3077 (<0.5)		555 (70)	$\nu(Xe_3\text{-}F_3)$	
561 (20) sh		539 (74)	$\nu_{as}(Xe_2\text{-}O\text{-}Xe_3)$	
552 (100)	ν(Xe-F)	511 (25)		
544 (41) sh		480 (100)	$\nu_s(F_1\text{-}Xe_1\text{-}F_2)$	
470 (11)	ν(Xe-O)	429 (55)	$\nu_s(Xe_2\text{-}O\text{-}Xe_3)$	
216 (1)		419 (83)		
204 (2)		349 (3)	δ modes	
188 (4)		258 (7)		
142 (7)	δ(OXeF)	252 (9)		
92 (2)		244 (2)		
		221 (1)		
		212 (2)		
		205 (3)		
		190 (15) sh		
		185 (30)	$\delta(F_1\text{-}Xe_1\text{-}F_2)$	
		156 (34)	$\delta(O\text{-}Xe_3\text{-}F_3)$	
		139 (23)		
		123 (26)		
		100 (26)		
710 (5)		715 (3),710 (4)		$\nu_8(E)$
682 (23)		681 (42)		$\nu_1(A_1)$
676 (11), 670 (4)sh				$\nu_2(A_1)$
594 (7), 587 (10)		584 (9), 576 (9), 573 (9)		$\nu_5(B_1)$
455 (11)				$\nu_4(A_1)$
		419 (83), 401 (22)		$\nu_3(A_1)$
370 (10)		393 (23)		$\nu_9(E)$
367 (11)				
363 (5)		370 (10), 366 (10)		$\nu_7(B_2)$
241 (1)				$\nu_{11}(E)$

[a] Spectra recorded on solid under HF solvent in a ¼-in. FEP sample tube using the 514.5-nm excitation. Values in paratheses denote relative Raman intensities. Abbreviations denote the following: shoulder (sh), broad (br). [b] Bands arising from FEP sample tube were observed at 293 (5), 380 (5), 386 (4), 578 (8) overlap, 733 (17), and 751 (2) cm^{-1}. [c] Bands arising from FEP sample tube were observed at 293 (2), 381 (5), 386 (6), 733 (11), and 751 (1) cm^{-1}. [d] The number of the atoms is the following: $F_1\text{-}Xe_1\text{-}F_2\cdots Xe_2\text{-}O\text{-}Xe_3\text{-}F_3$.

Table 11.2 Raman Frequencies and Their Assignments for Monoclinic and Trigonal $[Xe_2F_3][AsF_6]$

Frequencies $[cm^{-1}]$[a]			Assignments[b]	
mono. $[Xe_2F_3][AsF_6]$		trig. $[Xe_2F_3][AsF_6]$	$Xe_2F_3^+$ (C_{2v})	AsF_6^- (O_h)
RT	-150 °C[c,e]	-85 °C[d,e]		
598 (95)	604 (60)	596 (86)	$\nu_1(A_1)$, $\nu_s(F_t\text{-}Xe)$	
	600 (73)	589 (100)		
588 (100)	588 (100)	578 (55)	$\nu_6(B_1)$, $\nu_{as}(F_t\text{-}Xe)$	
417 (<1)	418 (1)		$\nu_7(B_1)$, $\nu_{as}(F_b\text{--}Xe)$	
401 (<1)	402 (<0.5)			
	399 (1)			
255 (5)	264 (6)	275 (7)	$\nu_2(A_1)$, $\nu_s(F_b\text{--}Xe)$+some bend	
	257 (4) sh			
163 (37)	169 (11)	164 (18)	$\nu_9(B_2)$, $\delta(F_t\text{-}Xe\text{--}F_b$ o.p.)	
	165 (8)			
	160 (8)			
	155 (2) sh			
	726 (1)	720 (1)		$\nu_3(T_{1u})$
	706 (1)			
	700 (1)	695 (1)		
678 (20)	682 (17)	681 (25)		$\nu_1(A_{1g})$
667 (4)				
580 sh	583 (20)			$\nu_2(E_g)$
	582 (21)			
	577 (22)			
	575 (12) sh			
	571 (12)			
	370 (4)			$\nu_5(T_{2g})$
367 (7)	369 (4)	368 (5)		
	366 (2) sh	365 sh		

[a] Values in parentheses denote relative Raman intensities. [b] The Raman spectrum has been recorded under HF solvent. [c] Spectrum recorded on microcrystalline solid in a ¼-in. FEP sample tube using the 514.5-nm excitation. Bands arising from FEP sample tube were observed at 204 (<0.5), 293 (2), 381 (1), 386 (1), 733 (3), and 750 (1) cm^{-1}. [d] Spectrum recorded on solid under HF solvent in a ¼-in. FEP sample tube using the 514.5-nm excitation. Bands arising from FEP sample tube were observed at 293 (7), 380 (5), 386 (5), 574 sh, 733 (19), and 751 (2) cm^{-1}. [e] Abbreviation denote: out-of-plane (o.p.).

Raman spectrum. The vibrational bands corresponding to the AsF_6^- anion indicate severe distortion from O_h to C_{4v} or lower symmetry arising from a strong fluorine bridge interaction between the cation and the anion. The distortion is similar to that found in the Raman spectra of $[KrF][AsF_6]$ and $[XeF][AsF_6]$[238] and is verified by the crystal structure of $[H_2OXeF]_2[F][AsF_6]$ (see 11.2.3.1. X-ray Crystal Structures, $[H_2OXeF]_2[F][AsF_6]$). Consequently, the anion bands were assigned under C_{4v} point symmetry. Oxygen isotope enrichment of H_2O (64.6% ^{16}O, 21.9% ^{17}O, and 42.7% ^{18}O) failed to show isotopic shifts on any of the cation bands below 600 cm^{-1} presumably because their line widths (10 to 18 cm^{-1}) prevented resolution and no significant differences in their line widths were discernable when compared to those of natural abundance $[H_2OXeF]_2[F][AsF_6]$.

The Xe-F stretching frequency at 552 cm^{-1} lies between the symmetric stretch of XeF_2 (497 cm^{-1})[253] and that of XeF^+ ($[XeF][AsF_6]$, 609 cm^{-1}),[174] *i.e.*, between that for a three-center four-electron bond and that of a two-center two-electron bond, respectively, and is similar to that in the cationic $LXeF^+$ adducts, $[s\text{-}C_3F_3N_2NXeF][AsF_6]$ (553, 544 cm^{-1}),[254] $[FXeFBrOF_2][AsF_6]$ (561, 550, 546 cm^{-1}),[255] $[(CF_3)_2S{=}OXeF][AsF_6]$ (552 cm^{-1}),[256] $CF_3C(OXeF)NH_2^+$ (543, 530 cm^{-1})[252] and $[F_3SNXeF][AsF_6]$ (554 cm^{-1})[252]. The Xe-O stretching frequency at 470 cm^{-1} is significantly higher in frequency than those of neutral FXeL species containing Xe-O linkages, *i.e.*, L = $OTeF_5$ (457 cm^{-1}),[257] $OIOF_4$ (438 cm^{-1}),[258] and OSO_2F (434 cm^{-1}),[174] and is consistent with a less polar xenon-ligand bond. The Xe-O stretches in the previously reported $FXeL^+$ cations, $CF_3C(OXeF)NH_2^+$ (508, 502 cm^{-1}),[252] $(CF_3)_2SOXeF^+$ (494 cm^{-1}),[256] also appear at higher frequencies and are somewhat higher than that of H_2OXeF^+. The lower Xe-O stretching frequency in

$[H_2OXeF]_2[F][AsF_6]$ is likely a result of strong hydrogen-bonding between the H_2OXeF^+ cations and the F^- anion, as found in the crystal structure of $[H_2OXeF]_2[F][AsF_6]$, which lowers the effective charge of the cation rendering the Xe-O bond more polar than in the isolated cation. The Raman band at 142 cm^{-1} is tentatively assigned to the δ(F-Xe-O) mode and is similar to that assigned to δ(FXeO) in $CF_3(OXeF)NH_2^+$ (141 cm^{-1}).[252] The δ(FXeF) modes have been found at somewhat higher frequencies in $Xe_2F_3^+$ (163 cm^{-1}),[174] $XeF_2{\cdots}MoOF_4$ (152 cm^{-1}),[259] and $XeF_2{\cdots}WOF_4$ (153 cm^{-1})[259] and at significantly higher frequency (213 cm^{-1}) in XeF_2.[253]

11.2.2.2. Trigonal $[Xe_2F_3][AsF_6]$. The Raman spectrum of trigonal $[Xe_2F_3][AsF_6]$ resembles that of the monoclinic modification. However, differences in the frequencies and intensities indicate the presence of two distinct phases, which has been confirmed by X-ray crystallography (see 11.2.3.2. X-Ray Crystal Structures, trigonal $[Xe_2F_3][AsF_6]$). The exact conditions for the phase transition from monoclinic to trigonal $[Xe_2F_3][AsF_6]$ are not, however, well understood, with HF solvent somehow assisting the phase transition. Suspending monoclinic $[Xe_2F_3][AsF_6]$ in HF solvent at -78 °C resulted in a white precipitate with a Raman spectum characteristic of trigonal $[Xe_2F_3][AsF_6]$.

The assignment of the $Xe_2F_3^+$ cation modes in Table 11.2 are based on recent density functional theory calculations.[260] The symmetric and asymmetric Xe-F_t stretching bands of the trigonal $[Xe_2F_3][AsF_6]$ (596/589 and 578 cm^{-1}) appear at lower frequencies than those of the monoclinic modification (604/600 and 588 cm^{-1}). The symmetric Xe---F_b stretching mode is shifted in the opposite direction, from 264 cm^{-1} in the monoclinic phase to 275 cm^{-1} in the trigonal phase. The higher symmetric Xe---F_b stretching frequency of the trigonal modification indicates a more covalent Xe---F_b---Xe bridge interaction in the $Xe_2F_3^+$ cation with a smaller Xe---F_b---Xe bridge angle that is closer to the expected for an AX_2E_2 VSEPR geometry.[120] A more covalent Xe---F_b bond weakens the Xe-F_t bond which, in turn, leads to the observed low-frequency shift of the Xe-F_t stretching modes. No signals associated with an asymmetric Xe---F_b stretch mode were observed in the Raman spectrum of the trigonal $[Xe_2F_3][AsF_6]$ under HF solvent.

11.2.2.3. $[Xe_3OF_3][AsF_6]$. The Raman spectrum of $[Xe_3OF_3][AsF_6]$ is complex. Assuming C_s symmetry for the free $Xe_3OF_3^+$ cation, a maximum of 15 Raman and infrared active bands (Γ = 11A′ + 4A″) is expected for the cation. Eleven Raman bands associated with the distorted AsF_6^- anion were observed and reflect the tetragonal anion distortion from the ideal O_h point symmetry. The anion bands were assigned under C_{4v} point symmetry based on previous assignments. Eight cation bands were observed in the Xe-F and Xe-O stretching regions. The strongly coupled Xe-F stretches for the XeF_2 moiety in FXeOXe---FXeF$^+$ are expected to occur at frequencies similar to the symmetric (497 cm^{-1}) and asymmetric (555 cm^{-1}) stretches in XeF_2.[253] The strongest Raman band at 480 cm^{-1} is tentatively assigned to the symmetric stretch of the XeF_2 moiety, while the weaker band at 595 cm^{-1} is assigned to the asymmetric XeF_2 stretch, which is Raman inactive in free, centrosymmetric XeF_2. The symmetric and asymmetric stretches of the strongly coupled Xe-O-Xe group are assigned to the 429 and 539 cm^{-1} bands, respectively, and are in the range of Xe-O stretches in other cationic xenon(II) species ($CF_3C(OXeF)NH_2^+$, 508, 502

cm^{-1};[252] $(CF_3)_2SOXeF^+$, 494 cm^{-1}).[256] The band at 555 cm^{-1} is tentatively assigned to the terminal Xe-F stretch of the FXeOXe moiety and is very similar to the frequency of the Xe-F stretch found for H_2OXeF^+. The band associated with the Xe---F stretch is expected to occur at significantly lower frequency and could not be unambiguously assigned. The intense bending modes at 185 and 156 cm^{-1} are assigned to the δ(FXeF) and δ(FXeO) modes, respectively. The contact with $FXeOXe^+$ likely lowers the frequency of the δ(FXeF) mode from 213 cm^{-1} in XeF_2 [253] to 185 cm^{-1}, while the δ(FXeO) mode appears at somewhat higher frequency than that in H_2OXeF^+ reflecting the stronger Xe-O bond in the $FXeOXe^+$ moiety.

11.2.3. X-ray Crystal Structures

Details of the data collection parameters and other crystallographic information for $[H_2OXeF]_2[F][AsF_6]$, trigonal $[Xe_2F_3][AsF_6]$, and $[Xe_3OF_3][AsF_6]$ are given in Table 11.3. Important bond lengths, angles, and contacts for $[H_2OXeF]_2[F][AsF_6]$, trigonal $[Xe_2F_3][AsF_6]$, and $[Xe_3OF_3][AsF_6]$ are listed in Table 11.4.

11.2.3.1. $[H_2OXeF]_2[F][AsF_6]$. The compound, $[H_2OXeF]_2[F][AsF_6]$, crystallizes in the tetragonal space group *I4/mcm* and consists of two H_2OXeF^+ cations and one F^- and one AsF_6^- anion. The xenon of the H_2OXeF^+ cation is located on a high-symmetry position (*..2/m*) resulting in a disorder between the fluorine and the oxygen ligands rendering it impossible to locate the two hydrogen atoms in the difference map. The AsF_6^- anions are located on special positions (*4/m*) and pack in chains along the *c*-axis. The thermal

Table 11.3. Summary of Crystal Data and Refinement Results for $[H_2OXeF]_2[F][AsF_6]$, Trigonal $[Xe_2F_3][AsF_6]$ and $[Xe_3OF_3][AsF_6]$

	$[H_2OXeF]_2[F][AsF_6]$	trigonal $[Xe_2F_3][AsF_6]$	$[Xe_3OF_3][AsF_6]$
formula	$H_4AsF_9O_2Xe_2$	AsF_9Xe_2	$As_2F_{18}O_2Xe_6$
space group	*I4/mcm* (No. 140)	*P3₂21* (No. 154)	*P2₁/c* (No. 14)
a [pm]	874.0(4)	860.2(5)	671.07(13)
b [pm]	874.0(4)	860.2(5)	911.5(2)
c [pm]	1307.8(9)	1066.5(9)	867.4(2)
α [deg]	90	90	90
β [deg]	90	90	96.85(3)
γ [deg]	90	120	90
V [10^6 pm^3]	999.1(9)	683.4(8)	526.8(2)
Z [molecules/unit cell]	4	3	2
mol. wt. [g mol^{-1}]	544.55	508.52	655.82
colour	pale orange	colourless	red
size [mm^3]	0.2×0.18×0.08	0.1×0.08×0.05	0.14×0.12×0.10
calcd density [g cm^{-3}]	3.620	3.707	4.135
μ [mm^{-1}]	10.182	11.135	12.808
data/restraints/parameters	327/0/26	800/12/58	1215/3/68
final agreement factors	R^a = 0.0222	R^a = 0.0385	R^a = 0.0571
	$R_w{}^b$ = 0.0633	$R_w{}^b$ = 0.1053	$R_w{}^b$ = 0.1388
GOOF	1.106	0.912	1.321
Extinction coefficient	0.0032(3)		0.0061(9)
$\Delta\delta_{max}/\Delta\delta_{min}$ [e $10^{-6}pm^{-3}$]	0.717/-0.811	1.446/-1.280	2.456/-1.942

[a] $R = \Sigma||F_o| - |F_c||/\Sigma|F_o|$.

[b] $R_w = \Sigma|(|F_o| - |F_c|)w^{1/2}|/\Sigma(|F_o|w)$ where $w = 1/[\sigma^2(F) + (0.0344)^2 + 4.94]$.

Table 11.4 Bond Lengths, Selected Bond Angles, and Contacts in $[H_2OXeF]_2[F][AsF_6]$, Trigonal $[Xe_2F_3][AsF_6]$, and $[Xe_3OF_3][AsF_6]$

$[H_2OXeF]_2[F][AsF_6]$

Bond Lengths and Contacts [pm]

Xe(1)-F(1)	198.6(4)	Xe(1)-O(1)	198.6(4)
As(1)-F(3)	172.5(5)	As(1)-F(4)	169.6(5)
O(1)---F(2)	259.0(4)		

Bond Angles [deg.]

O(1)-Xe(1)-F(1A)	180	F(3)-As(1)-F(4)	90
F(3)-As(1)-F(3A)	180		

Trigonal $[Xe_2F_3][AsF_6]$

Bond Lengths [pm]

Xe(1)-F(1)	209(2)	Xe(1)-F(1A)	226(2)
Xe(1)-F(2)	190.7(11)	As(1)-F(3)	177(2)
As(1)-F(7)	171(4)	As(1)-F(4)	172(2)
As(1)-F(8)	170(3)	As(1)-F(5)	175(2)
As(1)-F(9)	177(3)	As(1)-F(6)	170(2)

Bond Angles [deg.]

F(1)-Xe(1)-F(2)	167.7(6)	F(4)-As(1)-F(6)	91.6(6)
Xe(1)-F(1)-Xe(1A)	139.8(8)	F(5)-As(1)-F(6)	94.5(8)
F(3)-As(1)-F(4)	180.000(10)	F(7)-As(1)-F(8)	93(2)
F(3)-As(1)-F(5)	90.5(7)	F(7)-As(1)-F(9)	89(2)
F(3)-As(1)-F(6)	88.4(6)	F(8)-As(1)-F(9)	89.8(14)
F(4)-As(1)-F(5)	89.5(7)		

Table 11.4 continued...

[Xe_3OF_3][AsF_6]

	Bond Lengths [pm]		
Xe(1)-F(2)	251.0(8)	Xe(1)-O(1)	193.8(8)
Xe(2)-F(1)	198.4(8)	Xe(2)-O(1)	210.0(8)
Xe(2A)-F(1A)	198.4(8)	Xe(2A)-F(2)	210.0(8)
As(1)-F(3)	172.2(12)	As(1)-F(6)	172.4(12)
As(1)-F(4)	176.4(11)	As(1)-F(7)	176.2(11)
As(1)-F(5)	173.1(12)	As(1)-F(8)	172.9(12)
	Bond Angles [deg.]		
F(1)-Xe(2)-O(1)	177.6(4)	Xe(2)-O(1)-Xe(2)	122.8(5)
O(1)-Xe(1)-F(2)	177.5(2)	F(3)-As-F(4)	88.1(9)
F(3)-As-F(5)	90.2(10)	F(4)-As-F(5)	92.0(9)
F(6)-As-F(7)	91.9(9)	F(6)-As-F(8)	90.6(10)
F(7)-As-F(8)	90.9(9)		

ellipsoids of F(4) in the AsF_6^- anion are elongated in the *a,b*-plane indicating some residual rotational motion along the F(3)-As(1)-F(3A) axis which coincides with the *c*-axis. These anion chains fill square-based channels formed by a network of H_2OXeF^+ cations hydrogen-bonded to F^- anions (see Fig. (11.4)). The fluoride ion F(2) exhibits short contacts to two oxygen atoms, O(1), in four crystallographically related H_2OXeF^+ cations, (259.0(4) pm), which indicates the presence of hydrogen-bonding between H_2OXeF^+ and F^-. The F(2)---O(1) distance agrees well with the F---O distances of 255.1(6) to 255.8(5) pm and 261.9 to 266.7 pm found for hydrogen-bonding in $[H_3O][TiF_5]$[261] and $[H_3O][AsF_6]$,[262] respectively, and is significantly smaller than the sum of the van der Waals radii (275 to 300 pm)[212,213] of oxygen and fluorine. The interatomic distances between the four symmetry-related F(4) atoms of AsF_6^- anions to one F(2) atom (300.1(7) pm) are at the limit of the sum of the van der Waals radii (270 to 300 pm).[212,213]

The AsF_6^- anion exhibits a tetragonal distortion from the octahedral symmetry with the As(1)-F(3) bond length (172.5(5) pm) longer than As(1)-F(4) (169.6(5) pm), which is paralleled by the Raman spectroscopic observation of the lowering of the anion symmetry from O_h to C_{4v} (see 11.2.2.1. Raman Spectroscopy, $[H_2OXeF]_2[F][AsF_6]$). The Xe(1)-F(1)/O(1) bond lengths (198.6(4) pm) are similar to that found in the crystal structure of XeF_2 (200(1) pm),[253] but significantly shorter that those found for XeF_2 in $XeF_2{\cdot}IF_5$ (201.8(9) pm),[263] and in $XeF_2{\cdot}XeF_4$ (201.0(6) pm).[264] The shorter Xe-F/O bond lengths in H_2OXeF^+ are in agreement with its cationic nature and less polar XeF/O bonds.

An alternative interpretation of the X-ray crystal data as $2XeF_2{\cdot}[H_3O][AsF_6]$ was rejected primarily on the basis of the Raman spectroscopic characterization. In addition,

a

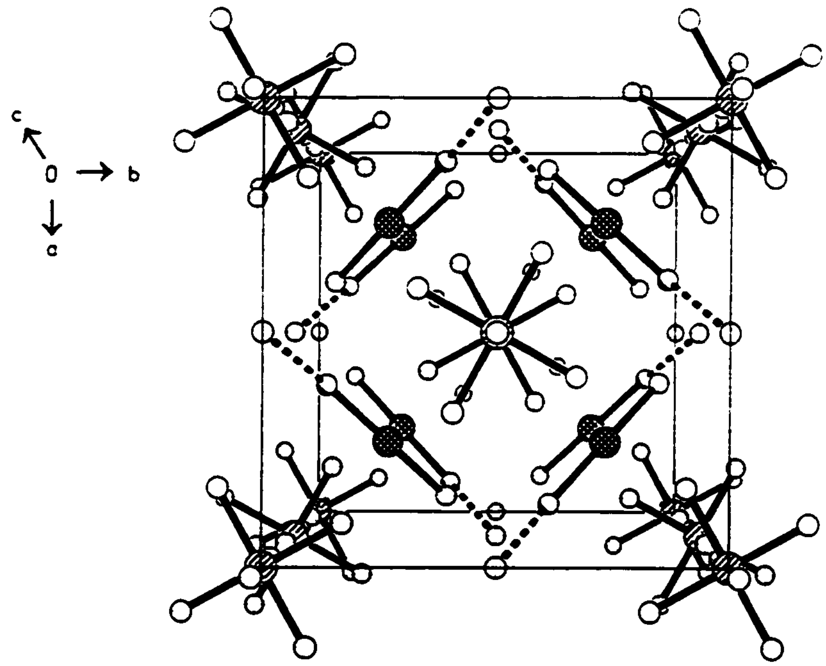

b

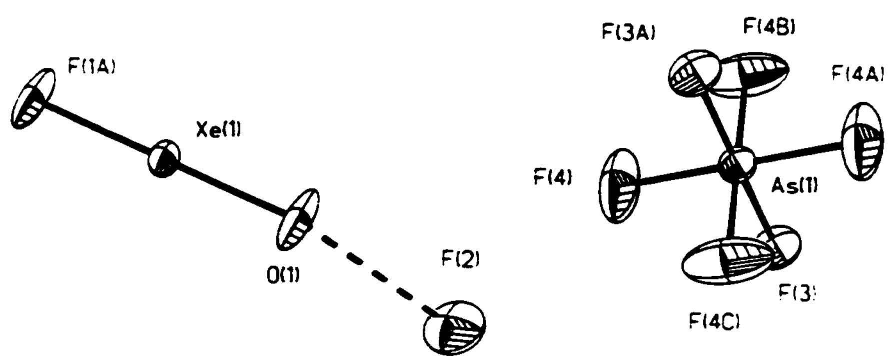

Figure 11.4. Views of (a) the $[H_2OXeF]_2[F][AsF_6]$ unit cell showing the packing along the *c*-axis and (b) the asymmetric unit of $[H_2OXeF]_2[F][AsF_6]$ (thermal ellipsoids are at the 50 % probability level); the disordered hydrogens of the H_2OXeF^+ cation are not shown.

the short Xe-ligand bond length and the strong interaction between the xenon-containing species and the species located at position (*m.mm*), *i.e.*, F^- or H_3O^+, is in better agreement with the presence of the H_2OXeF^+ cation.

11.2.3.2. Trigonal [Xe_2F_3][AsF_6]. The crystal structure of trigonal [Xe_2F_3][AsF_6], obtained by crystallization from HF between -30 and -40 °C, consists of isolated $Xe_2F_3^+$ cations and AsF_6^- anions (Figure 11.5). The packing along the *b*-axis is very similar to that in monoclinic [Xe_2F_3][AsF_6]. Unlike monoclinic [Xe_2F_3][AsF_6], the $Xe_2F_3^+$ cations and AsF_6^- anions of trigonal [Xe_2F_3][AsF_6] alternate along the *c*-axis with the bridging fluorine of the bent $Xe_2F_3^+$ cations in three adjacent anion/cation columns pointing towards the center of a C_3 symmetric channel parallel to the *c*-axis (Figure 11.5). Contacts between the fluorine atoms of the anion and the xenon atoms of the $Xe_2F_3^+$ cation range from 299(3) pm to the limit of the sum of their van der Waals radii (355 to 370 pm).[212,213]

The AsF_6^- anion exhibits a disorder between mainly two orientations (70%/30%) with As-F bond lengths ranging from 169(3) to 178(2) pm. The $Xe_2F_3^+$ cation is also disordered. The xenon atoms are the pivot points for the two orientations where only the positions of the F_b atoms can be defined, allowing for an accurate determination of the Xe···F_b···Xe angle. The terminal F atom positions, however, could not be split, giving rise to an underestimated F-Xe···F_b angle (Table 11.4). Unlike the bridge angle in monoclinic [Xe_2F_3][AsF_6] (149.5(4)° and 148.6(4)°), the average bridge angle in the $Xe_2F_3^+$ cation of the trigonal modification is significantly more closed (139.8(8)°). The Xe···F_b···Xe bridge in $Xe_2F_3^+$ is asymmetric with two different Xe(1)-F(1) bond lengths of 210(2) and 225(2)

a

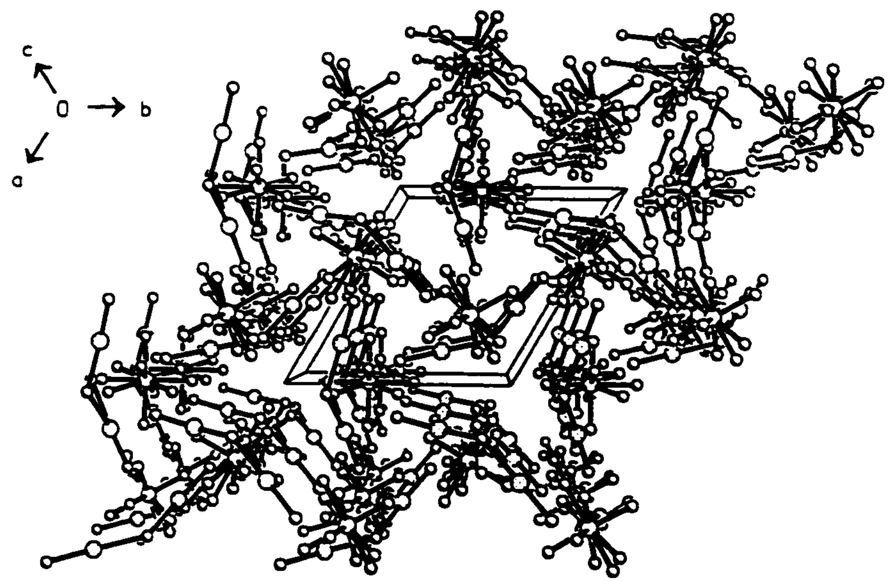

b

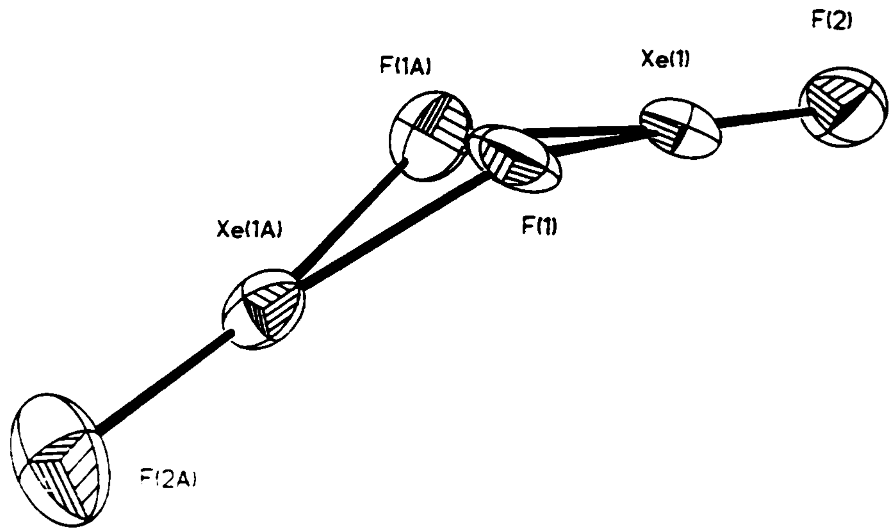

Figure 11.5. Views of (a) the trigonal $[Xe_2F_3][AsF_6]$ unit cell showing the packing along the *c*-axis and (b) the $Xe_2F_3^+$ cation (thermal ellipsoids are at the 50 % probability level).

pm and a positional disorder of the bridging fluorine. However, the average Xe···F_t bridge bond length is similar to those in monoclinic $Xe_2F_3^+$. The terminal Xe(1)-F(1) bond lengths in $Xe_2F_3^+$ of the trigonal modification (191(1) pm) are the same, within 3σ, as those of the monoclinic phase.

Similar to the monoclinic structure, terminal fluorines F(1) from two adjacent $Xe_2F_3^+$ cations approach the bridging fluorine of a third cation (281(2) pm) from opposite sides, bisecting the Xe···F_b···Xe angle and avoiding the fluorine lone pairs.

The difference in conditions leading to the formation of the monoclinic and trigonal $[Xe_2F_3][AsF_6]$ modifications is not well understood. Although the monoclinic modification has apparently been grown at somewhat higher temperatures than the trigonal phase, Bartlett *et al.* reported a trigonal high-temperature phase (>50 °C) of $[Xe_2F_3][AsF_6]$ with essentially the same unit cell parameters found in this work, but no detailed structural information has since been reported.[265]

11.2.3.2. $[Xe_3OF_3][AsF_6]$. The crystal structures of $[Xe_3OF_3][AsF_6]$ consist of isolated $Xe_3OF_3^+$ cations and AsF_6^- anions. The AsF_6^- anions are packed in chains along the *a*-axis and are located in channels which are formed by the $Xe_3OF_3^+$ cations (Figure 11.6).

The $Xe_3OF_3^+$ cation contains two terminal fluorines, one bridging fluorine, and one bridging oxygen and is nearly planar with a mean deviation from the plane of 1.7 pm. The bond angles around the xenon atoms of 177.6(4) and 177.5(2)° deviate only slightly from the ideal 180° angle. The bridging oxygen and fluorine positions are disordered as a result of a crystallographic inversion centre that also causes the bridging Xe(1) position

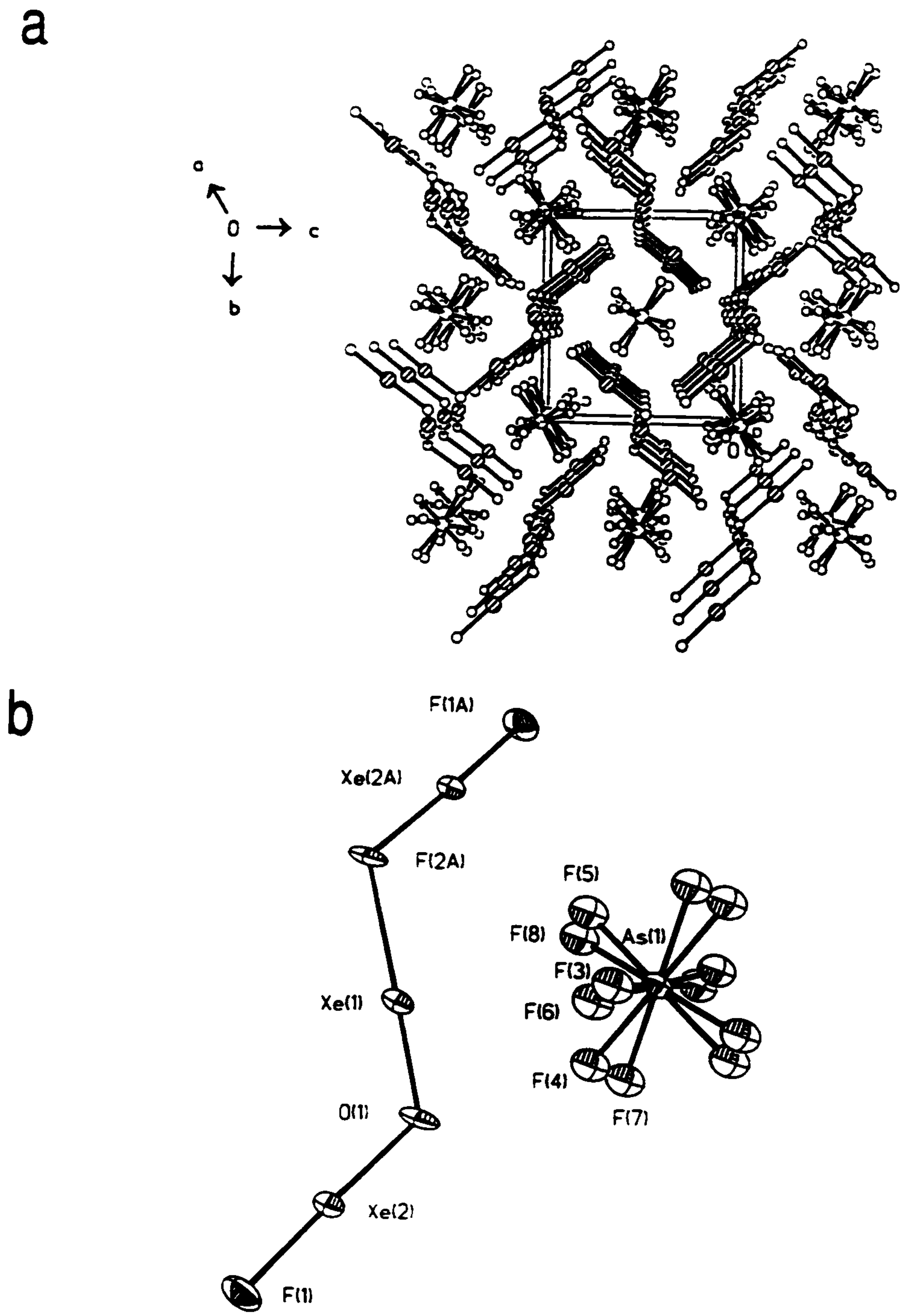

Figure 11.6. Views of (a) the $[Xe_2OF_3][AsF_6]$ unit cell showing the packing along the *a*-axis and (b) the $Xe_2OF_3^+$ cation (thermal ellipsoids are at the 50 % probability level).

to be split between a long (Xe---F) and a short (Xe-O) bond. The two disorder models, *i.e.*, (a) F-Xe-O-Xe---F-Xe-F and (b) F-Xe-F-Xe---O-Xe-F, are not distinguishable based solely on diffraction data. Model (a), which can be rationalized as the addition of XeF_2 to an $FXeOXe^+$ fragment, was chosen, since model (b) would impose an unlikely charge separation having double positive and negative fragments, $FXeFXe^{2+}$ and $OXeF^-$, respectively. The AsF_6^- anions are disordered between two orientations and exhibit contacts as close as 308.6(19) and 316.7(13) pm to Xe(1) and Xe(2) of the $Xe_3OF_3^+$ cation, respectively, which are significantly smaller than the sum of the van-der-Waals radii (355 to 370 pm).[212,213] The anion in both orientations was found to be tetragonally distorted from ideal O_h symmetry with two symmetry-related As-F bonds (2x 176.4(11){176.2(11)} pm) slightly longer than the other four As-F bonds (2x 172.2(12){172.4(12)} and 2x 173.1(12){172.9(12)} pm), which is paralleled by the number of anion modes in the Raman spectrum (see 11.2.2.3. Raman Spectroscopy; $[Xe_3OF_3][AsF_6]$).

The short contact between the $FXeFXeO^+$ and the FXeF moieties of the $Xe_3OF_3^+$ cation (251.0(8) pm) is significantly larger than the Xe---F_b bond in the $Xe_2F_3^+$ cation (214.2(7), 214.8(7), and 215.7(3) pm).[260] The absence of a stronger bonding interaction between these two fragments supports the assumption of a labile contact and the presence of an equilibrium between the $Xe_3OF_3^+$ cation in the solid state and the $FXeFXeO^+$ and FXeF fragments in solution (see Figure 11.6 and eq. (11.10)). The terminal Xe(2)-F(1) bond length of 198.4(8) pm is close to the Xe-F bond length in XeF_2 (*vide supra*) but is somewhat longer than the terminal Xe-F bonds in $Xe_2F_3^+$ (192.9(6) pm, 190.8(7), and

190.8(6) pm). The Xe(2a)-F(2a) bond length of 210.0(8) pm in the XeF_2 unit is elongated as the result of the strong Xe(1)···F(2a) contact. The O(1)-Xe(1) bond length (193.8(8) pm) represents one of the shortest and most covalent Xe(II)-O single bonds known and is similar to that found in HF·[$HOTeF_4OXe$][AsF_6] (196.2(9) pm).[266]

11.3. Conclusion

Contrary to an earlier report, no evidence was found for the formation of the H_2OF^+ cation[1,245] when XeF^+ is allowed to react with H_2O in HF. Instead of the previously proposed oxidative fluorination of H_2O by XeF^+ (eq. (11.1)), XeF_2, [H_3O][AsF_6] and H_2OXeF^+ are formed. Condensation reactions between XeF_2 and strong protic hydroxy acids, H_3O^+ and H_2OXeF^+, occur with HF elimination leading to Xe^{II}-O bond formation. The H_2OXeF^+ and $Xe_3OF_3^+$ cations represent the first examples of Xe^{II} oxide fluoride species. As an intermediate product, the trigonal modification of [Xe_2F_3][AsF_6] was isolated, which contains $Xe_2F_3^+$ cations with a significantly smaller Xe···F_b···Xe bridge angle than that in the monoclinic phase.

CHAPTER 12

CONCLUSIONS AND DIRECTIONS FOR FUTURE WORK

12.1. Conclusions

The chemistry of elements in the +8 oxidation state was significantly extended in the present work. The previously known Xe(VIII) species, XeO_4 and XeO_3F_2, were characterized by multi-NMR spectroscopy for the first time and four new Xe(VIII) species were synthesized and structurally characterized using NMR and Raman spectroscopy, $XeO_4(CH_3CN)$, *fac*-$XeO_3F_3^-$, *trans*- and *cis*-$XeO_4F_2^{2-}$. The study of the Lewis acid-base chemistry of the known neutral osmium(VIII) species, OsO_4, OsO_3F_2, and *cis*-OsO_2F_4 was completed with the preparation and characterization of the OsO_4F^-, *cis*-$OsO_4F_2^{2-}$, *fac*-$OsO_3F_3^-$, *mer*- and *fac*-$OsO_3F_2(CH_3CN)$, OsO_3F^+, $Os_2O_6F_3^+$, $OsO_2F_5^-$, and $OsO_2F_4(CH_3CN)$.

The *trans*-influence of the doubly bonded oxygen in the osmium(VIII) (d^0) species is well documented in the present work. The $OsO_4F_2^{2-}$ and $OsO_3F_3^-$ oxide fluoride anions were shown to exist exclusively as their *cis*- and *fac*-isomers, respectively. The facial trioxo-arrangement was also found in the crystal structures of $[OsO_3F][HF][SbF_6]$ and $[OsO_3F][HF]_2[AsF_6]$, in which osmium in the OsO_3F^+ cation is coordinated to one HF molecule and one fluorine of an adjacent PnF_6^- (Pn = As, Sb) anion. In this context, the finding that $OsO_3F_2(CH_3CN)$ exists as its *mer*- and *fac*-isomers in both, solution and solid state is surprising and indicates that the *trans*-influence of oxygen is not the only factor that determines the structure of a d^0 transition metal oxide fluoride. In main-group oxide fluorides, the *trans*-influence of the doubly bonded oxygen is not as strong as in d^0 transition metal species, resulting in a mixture of *trans*- and *cis*-$XeO_4F_2^{2-}$. However, only the *fac*-$XeO_3F_3^-$ isomer was observed in solution.

The coordination number seven was attained in the $OsO_2F_5^-$ and $IO_2F_5^{2-}$ anions, which are the only main-group and transition metal examples of the AO_2F_5 type species. The $IO_2F_5^{2-}$ anion has a pentagonal bipyramidal geometry with a *trans*-dioxo arrangement and was obtained by the reaction of *trans*-$IO_2F_4^-$ with F^-, while the transition metal analogue, $OsO_2F_5^-$, retains the *cis*-dioxo arrangement of its precursor, *cis*-OsO_2F_4, and exhibits a monocapped trigonal prismatic geometry, which is a consequence of the *trans*-influence of the oxygen ligands. The *cis*-$IO_2F_4^-$ anion does not react with fluoride ions showing the reluctance of I(VII) to form heptacoordinate compounds containing a *cis*-dioxo arrangement. The reduction of the $[N(CH_3)_4]_2[IO_2F_5]$/$[N(CH_3)_4]$[*cis*-IO_2F_4] mixture in CH_3CN solvent yielded the $IO_2F_2^-$ anion and may provide a means of a controlled fluorination of organic molecules.

The extension of the oxide fluoride chemistry to xenon in the +2 oxidation state is a significant contribution in noble-gas chemistry, especially since the hydrolysis of XeF_2 leading to its decomposition has been known for many years, but not well understood.

The present work has also served to correct two erroneous reports in the literature, which have now found their way into textbooks. Previous claims for the synthesis of *cis*-

$OsO_4F_2^{2-}$ were found to be erroneous and the species reported was found to be identical with the OsO_4F^- anion synthesized and characterized in the course of this work. Secondly, a report of the preparation of the H_2OF^+ cation by the reaction of XeF^+ and H_2O was proven to be wrong, instead, the novel $Xe_3OF_3^+$ and H_2OXeF^+ cations have been prepared and characterized. The latter cation is the protonated form of the presently unknown fluorohypoxenoneous acid, HOXeF.

12.2. Directions for Future Work

Vibrational frequencies for the $XeO_4F_2^{2-}$, OsO_3F^+, $OsO_2F_5^-$, and $IO_2F_5^-$ species should be calculated at the DFT level of theory to aid in making complete and unambiguous assignments of their vibrational spectra. Such a theoretical treatment has already been successfully performed on the OsO_4F^-, $OsO_4F_2^{2-}$ and $OsO_3F_3^-$ anions.

The generation of higher concentrations of XeO_3F_2 may be achieved by reacting XeO_4 and XeF_6 (eq. (5.1)) in the absence of a solvent, followed by dissolving and stabilizing XeO_3F_2 in the appropriate solvent medium. The dissolution of XeO_3F_2 in CH_3CN is likely to yield an $XeO_3F_2(CH_3CN)$ adduct according to eq. (12.1). As found for

$$XeO_3F_2 + CH_3CN \xrightarrow{CH_3CN} XeO_3F_2(CH_3CN) \qquad (12.1)$$

$OsO_3F_2(CH_3CN)$, the $XeO_3F_2(CH_3CN)$ adduct is expected to exist as a mixture of its *fac*- and *mer*-isomers which can easily be identified by ^{19}F, ^{129}Xe NMR spectroscopy. The reaction of XeO_3F_2 with CsF or $[N(CH_3)_4][F]$ in CH_3CN will result in the formation of larger amounts of $XeO_3F_3^-$ (eq. (12.2)), which should also be characterized in the solid

$$XeO_3F_2 + F^- \xrightarrow{CH_3CN} XeO_3F_3^- \quad (12.2)$$

state in light of the possible coexistence of its *fac*- and *mer*-isomers. Crystal growth of $[N(CH_3)_4][XeO_3F_3]$ and $[N(CH_3)_4]_2[XeO_4F_2]$, which was found to be remarkably stable, should be attempted from CH_3CN solvent. The reaction between XeO_3F_2 with the strong Lewis acids, AsF_5 and SbF_5, are expected to yield the XeO_3F^+ cation (eq. (12.3)), which

$$XeO_3F_2 + AsF_5 \xrightarrow{HF} [XeO_3F][AsF_6] \quad (12.3)$$

is the main-group analogue to the OsO_3F^+ cation that was studied in the present work.

Attempts should also be made to obtain a crystal structure of the $OsO_2F_5^-$ anion as its $N(CH_3)_4^+$ and Cs^+ salts from HF solvent at low temperature in order to confirm the anion geometry that was established in solution by NMR spectroscopy. A number of new, presently unknown species were observed in the ^{19}F NMR spectra of $[N(CH_3)_4][OsO_2F_5]$ in CH_3CN and HF solvents and of $OsO_2F_4(CH_3CN)$ in SO_2ClF solvent. Their structure should be investigated further by NMR spectroscopy. The preparation of lower oxidation state oxide fluorides of osmium, *e.g.*, $OsOF_5^-$, and their characterization by ^{19}F NMR spectroscopy may lead to their recognition as reduction products of $OsO_2F_5^-$ and

$OsO_2F_4(CH_3CN)$.

The reduction of $IO_2F_4^-$ to the $IO_2F_2^-$ anion is worth investigating further, since it possibly provides a means to a controlled fluorination of organic molecules.

Attempts should be made to isolate and characterize FXeOXeF, the first neutral Xe(II) oxide fluoride, from the FXeFXe--FXeF$^+$ cation by addition of a stoichiometric amount of fluoride ion, according to eq. (12.4), where NOF and CsF are the fluoride ion

$$[Xe_3OF_3][AsF_6] + F^- \xrightarrow{HF} O(XeF)_2 + XeF_2 + AsF_6^- \qquad (12.4)$$

sources. Crystal growth of FXeOXeF should be attempted in the event the fluoride ion displacement reaction is successful.

REFERENCES

1 (a) Holleman, A.F.; Wiberg, N.; Wiberg, E. *Lehrbuch der Anorganischen Chemie: 101. Auflage*; de Gruyter: Berlin, Germany, 1995; (b) Greenwood, N.N.; Earnshaw, A. *Chemistry of the Elements*, 2nd Edition; Butterworth-Heinemann: Oxford, 1997.

2 Wartenberg, H.V. *Annalen* **1924**, *440*, 97.

3 *Gmelins Handbuch der Anorganischen Chemie, 8. Aufl., Ergänzungsband, Ruthenium*; Verlag Chemie: Weinheim, Germany, 1970; pp. 88.

4 (a) *Gmelins Handbuch der Anorganischen Chemie, Ergänzungswerk zur 8. Aufl., Edelgasverbindungen, Bd. 1*; Verlag Chemie: Weinheim, Germany, 1970; (b) Holloway, J.H.; Hope, E.G. *Adv. Inorg. Chem.* **1999**, *46*, 51; (c) Schrobilgen, G.J.; Whalen, J.M. In *Kirk-Othmer Encyclopaedia of Chemical Technology*, 4th ed.; Wiley and Sons, Inc.: New York, 1994; Chapter 13, pp. 38; (d) Selig, H.: Holloway, J.H. *Top. Curr. Chem.* **1984**, *124*, 33; (e) Bartlett, N.; Sladky, F.O. In *Comprehensive Inorganic Chemistry*; Trotman-Dickenson, A.F., Ed.; Pergamon: Oxford, 1973; pp. 213; (f) Malm, J.G.; Appelman, E.H. *At. Energy Rev.* **1969**, *7*, 3.

5 Selig, H.; Claassen, H.H.; Chernick, C.L.; Malm, J.G.; Huston, J.L. *Science* **1964**, *143*, 1322.

6 Christe, K.O.; Dixon, D.A.; Mack, H.G.; Oberhammer, H.; Pagelot, A.; Sanders, J.C.P.; Schrobilgen, G.J. *J. Am. Chem. Soc.* **1993**, *115*, 11279.

7 Bougon, R.; Buu, B.; Seppelt, K. *Chem. Ber.* **1993**, *126*, 1331.

8 Claassen, H.H.; Huston, J.L. *J. Chem. Phys.* **1971**, *55*, 1505.

9 Huston, J.L. *Inorg. Chem.* **1982**, *21*, 685.

10 Huston, J.L. *J. Am. Chem. Soc.* **1971**, *93*, 5255.

11 Chernick, C.L.; Malm, J.G. *Inorg. Synth.* **1966**, *8*, 259.

12 Burns, R.C.; O'Donnell, T.A. *J. Inorg. Nucl. Chem.* **1980**, *42*, 1613.

13 Glemser, O.; Roesky, H.W.; Hellberg, K.-H.; Werther, H.-U. *Chem. Ber.* **1966**, *99*, 2652.

14 (a) Slivnik, J.; Volavšek, B.; Marsel, J.; Vrščaj, V.; Šmalc, A.; Frlec, B.; Zemljič, Z. In *Noble Gas Compounds*; Hyman, H.H., Ed.; The University of Chicago Press, Chicago: 1963; pp 64; (b) Slivnik, J.; Volavšek, B.; Marsel, J. Vrščaj, V.; Šmalc, A.; Frlec, B.; Zemljič, Z. *Croat. Chem. Acta* **1963**, *35*, 81.

15 Ruff, O.; Tschirch, F.W. *Ber.* **1913**, *46*, 929.

16 Weinstock, B.; Weaver, E.E.; Knop, E.P. *Inorg. Chem.* **1966**, *5*, 2189.

17 Weinstock, B.; Malm, J.G. *J. Am. Chem. Soc.* **1958**, *80*, 4466.

18 (a) Vossel, W. *Ann. Phys. (Leipzig) Ser. 4* **1916**, *49*, 229; (b) Antropoff, A.v. *Z. Angew. Chem.* **1924**, *37*, 217; (c) Pauling, L. *J. Am. Chem. Soc.* **1933**, *55*, 1895.

19 (a) Antropoff, A.v.; Weil, K.; Frauenhof, H. *Naturwissenschaften* **1932**, *20*, 688; (b) Yost, D.M.; Kaye, A.L. *J. Am. Chem. Soc.* **1933**, *55*, 3891.

20 Bartell, N. *Proc. Chem. Soc.* **1962**, 218.

21 Hoppe, R.; Dähne, W.; Mattauch, H.; Rödder, K. *Angew. Chem.* **1962**, *11*, 599.

22 Hamilton, W.C.; Ibers, J.A.; Mackenzie, D.R. *Science* **1963**, *141*, 532.

23 Peterson, J.L.; Claassen, H.H.; Appelman, E.H. *Inorg. Chem.* **1970**, *9*, 619.

24 Shustov, L.D.; Tolmacheva, N.S.; Nabiev, Sh.Sh.; Il'in, E.K.; Klimov, V.D.; Ushakov, V.P. *Russ. J. Inorg. Chem.* **1989**, *34*, 946; *Zh. Neorg. Khim.* **1989**, *34*, 1673.

25 Marcus, Y.; Cohen, D. *Inorg. Chem.* **1966**, *5*, 1740.

26 Isupov, V.K.; Oleinik, A.V.; Aleinikov, N.N. *Russ. J. Inorg. Chem.* **1989**, *34*, 1183; *Zh. Neorg. Khim.* **1989**, *34*, 2080.

27 Jørgensen, C.K.; Berthou, H. *Chem. Phys. Lett.* **1975**, *36*, 432.

28 Waard, H.D.; Bukshpan, S.; Schrobilgen, G.J.; Holloway, J.H.; Martin, D. *J. Chem. Phys.* **1979**, *70*, 3247.

29 Ibers, J.A.; Hamilton, W.C.; Mackenzie, D.R. *Inorg. Chem.* **1964**, *3*, 1412.

30 Zalkin, A.; Forrester, J.D.; Templeton, D.H.; Williamson, S.M.; Koch, C.W.

Science **1963**, *142*, 501.

31 Zalkin, A.; Forrester, J.D.; Templeton, D.H. *Inorg. Chem.* **1964**, *3*, 1417.

32 Zalkin, A.; Forrester, J.D.; Templeton, D.H.; Williamson, S.M.; Koch, C.W. *J. Am. Chem. Soc.* **1964**, *86*, 3569.

33 Hauck, J. *Z. Naturforsch.* **1970**, *25b*, 226.

34 Downey, G.D.; Claassen, H.H.; Appelman, E.H. *Inorg. Chem.* **1971**, *10*, 1817.

35 Schrobilgen, G.J; Holloway, J.H.; Granger, P.; Brevard, C. *Inorg. Chem.* **1978**, *17*, 980.

36 Appelman, E.H.; Malm, J.G. *J. Am. Chem. Soc.* **1964**, *86*, 2141.

37 Kläning, U.K.; Appelman, E.H. *Inorg. Chem.* **1988**, *27*, 3760.

38 Appelman, E.H.; Williamson, S.M. *Inorg. Synth.* **1968**, *11*, 205.

39 Appelman, E.H.; Williamson, S.M. *Inorg. Synth.* **1968**, *11*, 210.

40 Malm, J.G.; Appelman, E.H. *Chem. Abstr.* **1967**, *66*, 96989r.

41 Foropoulos, Jr., J.; DesMarteau, D.D. *Inorg. Chem.* **1982**, *21*, 2503.

42 Gruen, D.M. In *Noble Gas Compounds*; Hyman, H.H., Ed.; Chicago University Press: Chicago, Ill., 1963; p. 174.

43 Aleinikov, N.N.; Kashtanov, S.A.; Pomytkin, I.A.; Sipyagin, A.M. *Russ. Chem. Bulletin* **1995**, *44*, 180; *Izv. Akad. Nauk. Ser. Khim.* **1995**, *44*, 184.

44 Huston, J.L.; Studier, M.H.; Sloth, E.N. *Science* **1964**, *143*, 1161.

45 Selig, H.; Claassen, Chernick, C.L.; Malm, J.G.; Huston, J.L. *Science* **1964**, *143*, 1322.

46 Gunn, S.R. *J. Am. Chem. Soc.* **1965**, *87*, 2290.

47 Gunderson, G.; Hedberg, K.; Huston, J.L. *J. Chem. Phys.* **1970**, *52*, 812.

48 Huston, J.L.; Claassen, H.H. *J. Chem. Phys.* **1970**, *52*, 5646.

49 Huston, J.L. *Inorg. Nucl. Chem. Letters* **1968**, *4*, 29.

50 Aoyama, S.; Watanabe, K. *Nippon Kagaku Zasshi* **1955**, *76*, 970; ref. (2) in *Gmelin Handbuch der Anorganischen Chemie*, 8th Ed., Supplement Vol. 1; Springer-Verlag: Berlin, 1980; p.82.

51 Handbook of Chemistry and Physics, 74[th] Ed.;1993-1994, p.6-69.

52 Fritzmann, E. *Z. Anorg. Chem.* **1928**, *172*, 213.

53 Griffith, W.P.; Rossetti, R. *J. Chem. Soc., Dalton Trans.* **1972**, 1449.

54 Cleare, M.J.; Hydes, P.C.; Griffith, W.P.; Wright, M.J. *J. Chem. Soc., Dalton Trans.* **1977**, 941.

55 Weber, R.; Dehnicke, K.; Müller, U.; Fenske, D. *Z. Anorg. Allg. Chem.* **1984**, *516*, 214.

56 Griffith, W.P.; Koh, T.Y.; White, A.J.P.; Williams, D.J. *Polyhedron* **1995**, *14*, 2019.

57 Griffith, W.P.; Skapski, A.C.; Woode, K.A.; Wright, M.J. *Inorg. Chim. Acta* **1978**, *31*, L413.

58 Svendsen, J.S.; Markó, I.; Jacobsen, E.N.; Rao, Ch.P.; Bott, S.; Sharpless, K.B. *J. Org. Chem.* **1989**, *54*, 2264.

59 Corey, E.J.; Sepehar, S.; Azimioara, M.D.; Newbold, R.C.; Noe, M.C. *J. Am. Chem. Soc.* **1996**, *118*, 7851.

60 Nelson, D.W.; Gypser, A.; Ho, P.T.; Kolb, H.C.; Kondo, T.; Kwong, H.-L.; McGrath, D.V.; Rubin, A.E.; Norrby, P.-O.; Gable, K.P.; Sharpless, K.B. *J. Am. Chem. Soc.* **1997**, *119*, 1840.

61 Bailey, A.J.; Bhowon, M.G.; Griffith, W.P.; Shoir, A.G.F; White, A.J.P.; Williams, D.J. *J. Chem. Soc., Dalton Trans.* **1997**, 3245.

62 Nikol'skii, A.B.; D'yachenko, Yu.I. *Russ. J. Inorg. Chem.* **1974**, *19*, 1031; *Zh. Neorg. Khim.* **1974**, *19*, 1889.

63 Krauss, F.; Wilken, D. *Z. Anorg. Allg. Chem.* **1925**, *145*, 151.

64 Griffith, W.P. *J. Chem. Soc.* **1964**, 245.

65 Griffith, W.P. *J. Chem. Soc. A* **1969**, 211.

66 Nevskii, N.N.; Ivanov-Emin, B.N.; Nevskaya, N.A. *Dokl. Akad. Nauk. SSSR* **1982**, *266*, 628; *Chem. Abstr.* **1983**, *98*, 25832j.

67 Nevskii, N.N.; Ivanov-Emin, B.N.; Nevskaya, N.A.; Belov, N.V. *Dokl. Akad. Nauk. SSSR* **1982**, *266*, 1138; *Chem. Abstr.* **1983**, *98*, 63603t.

68 Nevskii, N.N.; Porai-Koshits, M.A. *Dokl. Akad. Nauk. SSSR* **1983**, *270*, 1392;

Chem. Abstr. **1983**, *99*, 185330t.

69 Nevskii, N.N.; Porai-Koshits, M.A. *Dokl. Akad. Nauk. SSSR* **1983**, *272*, 1123; *Chem. Abstr.* **1984**, *100*, 43385e.

70 Ivanov-Emin, B.N.; Nevskaya, N.A.; Zaitsev, B.E.; Nevskii, N.N.; Izmailovich, A.S. *Russ. J. Inorg. Chem.* **1984**, *29*, 710; *Zh. Neorg. Khim.* **1984**, *29*, 1241.

71 Jewiss, H.C.; Levason, W.; Tajik, M.; Webster, M.; Walker, N.P.C. *J. Chem. Soc., Dalton Trans.* **1985**, 199.

72 Jones, P.J.; Levason, W.; Tajik, M. *J. Fluorine Chem.* **1984**, *25*, 195.

73 Ivanov-Emin, B.N.; Nevskaya, N.A.; Medvedev, Yu.N.; Zaitsev, B.E.; Lin'ko, I.V. *Russ. J. Inorg. Chem.* **1986**, *31*, 1088; *Zh. Neorg. Khim.* **1986**, *31*, 1889.

74 Brewer, S.A.; Brisdon, A.K.; Holloway, J.H.; Hope, E.G.; Levason, W.; Ogden, J.S.; Saad, A.K. *J. Fluorine Chem.* **1993**, *60*, 13.

75 Clifford, A.F.; Kobajashi, C.S. *Inorg. Synth.* **1960**, *6*, 204.

76 Nugent, W.A.; Harlow, R.L.; McKinney, R.J. *J. Am. Chem. Soc.* **1979**, *101*, 7265.

77 Wigley, D.E. *Prog. Inorg. Chem.* **1994**, *42*, 239.

78 Griffith, W.P.; McManus, N.T.; Skapski, A.C.; White, A.D. *Inorg. Chim. Acta* **1985**, *105*, L11.

79 Leung, W.-H.; Chim. J.L.C.; Wong, W.-T. *J. Chem. Soc., Dalton Trans.* **1996**, 3153.

80 Leung, W.-H.; Chim. J.L.C.; Wong, W.-T. *J. Chem. Soc., Dalton Trans.* **1997**, 3277.

81 Chong, A.O.; Oshima, K.; Sharpless, K.B. *J. Am. Chem. Soc.* **1977**, *99*, 3420.

82 Danopoulos, A.A.; Wilkinson, G. *Polyhedron* **1990**, *9*, 1009.

83 Rankin, D.W.H.; Robertson, H.E.; Danopoulos, A.A.; Lyne, P.D.; Mingos, D.M.P.; Wilkinson, G. *J. Chem. Soc., Dalton Trans.* **1944**, 1563.

84 Sunder, W.A.; Stevie, F.A. *J. Fluorine Chem.* **1975**, *6*, 449.

85 Hepworth, M.A.; Robinson, P.L. *Inorg. Nucl. Chem.* **1957**, *4*, 24.

86 Beattie, I.R.; Blayden, H.E.; Crocombe, R.A.; Jones, P.J.; Ogden, J.S. *J. Raman Spectrosc.* **1976**, *4*, 313.

87 Nguyen-Nghi, M.M.; Bartlett, N. *C.R. Seances Acad. Sci.* **1969**, *269*, 756.

88 Jeżowska-Trzebiatowska, B.; Hanuza, J.; Bałuka, M. *Acta Phys. Pol.* **1970**, *A38*, 563.

89 Bougon, R. *J. Fluorine Chem.* **1991**, *53*, 419.

90 Christe, K.O.; Bougon, R. *J. Chem. Soc., Chem. Commun.* **1992**, 1056.

91 Casteel, W.J., Jr.; Dixon, D.A.; Mercier, H.P.; Schrobilgen, G.J. *Inorg. Chem.* **1996**, *35*, 4310.

92 Casteel, W.J., Jr.; Dixon, D.A.; LeBlond, N.; Mercier, H.P.A.; Schrobilgen, G.J. *Inorg. Chem.* **1998**, *37*, 340.

93 LeBlond, N.; Dixon, D.A.; Schrobilgen, G.J. *Inorg. Chem.* **2000**, *39*, in press.

94 Casteel, W.J., Jr.; Dixon, D.A.; LeBlond, N.; Lock, P.E.; Mercier, H.P.A.; Schrobilgen, G.J. *Inorg. Chem.* **1999**, *38*, 2340.

95 Engelbrecht, A.; Peterfy, P. *Angew. Chem.* **1969**, *81*, 753; *Angew. Chem., Int. Ed. Engl.* **1969**, *8*, 768.

96 Smart, L.E. *J. Chem. Soc., Chem. Commun.* **1977**, 519.

97 (a) Bartell, L.S.; Clippard, F.B.; Jean Jacob, E. *Inorg. Chem.* **1976**, *15*, 3009; (b) Christe, K.O.; Curtis, E.C.; Dixon, D.A. *J. Am. Chem. Soc.* **1993**, *115*, 9655.

98 (a) Schmeisser, M.; Lang, K. *Angew. Chem.* **1955**, *67*, 156; (b) Kraznai, J.J. Ph.D. Thesis, McMaster University, Hamilton, Canada, **1975**.

99 Christe, K.O.; Schack, C.J. *Adv. Inorg. Chem. Radiochem.* **1976**, *18*, 319.

100 (a) Appelman, E.H.; Studier, M.H. *J. Am. Chem. Soc.* **1969**, *91*, 4561; (b) Gillespie, R.J.; Spekkens, P.H. *Isr. J. Chem.* **1978**, *17*, 11.

101 (a) Gillespie, R.J.; Krasznai, J.P. *Inorg. Chem.* **1976**, *15*, 1251; (b) Syvret, T.R.G. Ph.D. Thesis, McMaster University, Hamilton, Canada, **1987**.

102 Engelbrecht, A.; Peterfy, P.; Schandara, E. *Z. Anorg. Allg. Chem.* **1971**, *384*, 202.

103 Christe, K.O.; Wilson, R.D.; Schack, C.J. *Inorg. Chem.* **1981**, *20*, 2104.

104 Adams, W.J.; Bradford Thompson, H.; Bartell, L.S. *J. Chem. Phys.* **1970**, *53*, 4040.

105 Vogt, T.; Fitch, A.N.; Cockcroft, J.K. *J. Solid State Chem.* **1993**, *103*, 275.

106 Christe, K.O.; Curtis, E.C.; Dixon, D.A. *J. Am. Chem. Soc.* **1993**, *115*, 1520.

107 Marx, R.; Mahjoub, A.R.; Seppelt, K.; Ibberson, R.M. *J. Chem. Phys.* **1994**, *101*, 585.

108 Christe, K.O.; Sanders, J.C.P.; Schrobilgen, G.J.; Wilson, W. *J. Chem. Soc., Chem. Commun.* **1991**, *13*, 837.

109 Mahjoub, A.-R.; Seppelt, K. *J. Chem. Soc., Chem. Commun.* **1991**, *13*, 840.

110 Christe, K.O.; Dixon, D.A.; Mahjoub, A.R.; Mercier, H.P.A.; Sanders, J.C.P.; Seppelt, K.; Schrobilgen, G.J.; Wilson, W.W. *J. Am. Chem. Soc.* **1993**, *115*, 2696.

111 Mahjoub, A.-R.; Drews, T.; Seppelt, K. *Angew. Chem.* **1992**, *104*, 1047; *Angew. Chem., Int. Ed. Engl.* **1992**, *31*, 1036.

112 Zhang, X.; Seppelt, K. *Z. Anorg. Allg. Chem.* **1997**, *623*, 491.

113 Christe, K.O.; Dixon, D.A.; Sanders, J.C.P.; Schrobilgen, G.J.; Wilson, W. *Inorg. Chem.* **1993**, *32*, 4089.

114 (a) Shustorovich, E.M.; Porai-Koshits, M.A.; Buslaev, Yu.A. *Coord. Chem. Rev.* **1975**, *17*, 1; (b) Shustorovich, E.M.; Buslaev, Yu.A. *Inorg. Chem.* **1976**, *15*, 1142.

115 Leimkühler, M.; Mattes, R. *J. Solid State Chem.* **1986**, *65*, 260.

116 Lis, T. *Acta Crystallogr.* **1983**, *C39*, 961.

117 Abrahams, S.C.; Marsh, P.; Ravez, J. *J. Chem. Phys.* **1987**, *87*, 6012.

118 (a) Tötsch, W.; Sladky, F. *J. Chem. Soc., Chem. Commun.* **1980**, 927; (b) Tötsch, W.; Sladky, F. *Chem. Ber.* **1982**, *115*, 1019.

119 Gillespie, R.J.; Bytheway, I.; Tang, T.-H.; Bader, R.F.W. *Inorg. Chem.* **1996**, *35*, 3954.

120 Gillespie, R.J.; Hargittai, I. *The VSEPR Model of Molecular Geometry*; Allyn and Bacon: Boston, MA, 1991.

121 Averdunk, F.; Hoppe, R. *J. Fluorine Chem.* **1989**, *42*, 413.

122 Stomberg, R. *Acta Chem. Scand.* **1983**, *A37*, 453.

123 Crosnier-Lopez, M.P.; Fourquet, J.L. *J. Solid State Chem.* **1993**, *103*, 131.

124 Crosnier-Lopez, M.P.; Fourquet, J.L. *J. Solid State Chem.* **1993**, *105*, 92.

125 Crosnier-Lopez, M.P.; Duroy, H.; Fourquet, J.L. *J. Solid State Chem.* **1993**, *107*,

211.

126 Hurst, H.J.; Taylor, J.C. *Acta Crystallogr.* **1970**, *B26*, 417.

127 Granzin, J.; Saalfeld, H. *Z. Kristallogr.* **1988**, *183*, 71.

128 Hampson, G.C.; Pauling, L. *J. Am. Chem. Soc.* **1938**, *60*, 2702.

129 Hoard, J.L. *J. Am. Chem. Soc.* **1939**, *61*, 1252.

130 Brown, G.M.; Walker, L.A. *Acta Crystallogr.* **1966**, *20*, 220.

131 Torardi, C.C.; Brixner, L.H.; Blasse, G. *J. Solid State Chem.* **1987**, *67*, 21.

132 Agulyanskii, A.I.; Zavodnik, V.E.; Kuznetsov, V. Ya.; Sidorov, N.V.; Stefanovich, S.Yu.; Tsikaeva, D.V.; Kalinnikov, V.T. *Inorg. Mater.* **1991**, *27*, 880; *Izv. Akad. Nauk. SSSR, Neorg. Mat.* **1991**, *27*, 1055.

133 Giese, S.; Seppelt, K. *Angew. Chem.* **1994**, *106*, 473; *Angew. Chem., Int. Ed. Engl.* **1994**, *33*, 461.

134 Vogt, T.; Fitch, A.N.; Cockcroft, J.K. *Science* **1994**, *263*, 1265.

135 Drake, G.W.; Dixon, D.A.; Sheehy, J.A.; Boatz, J.A.; Christe, K.O. *J. Am. Chem. Soc.* **1998**, *120*, 8392.

136 Zachariasen, W.H. *Acta Crystallogr.* **1954**, *7*, 783.

137 Brusset, P.H.; Gillier-Pandraud, H.; Nguyen-Quy-Dao *Acta Crystallogr.* **1969**, *B25*, 67.

138 Crosnier-Lopez, M.P.; Laligand, Y.; Fourquet, J.L. *Eur. J. Solid State Inorg. Chem.* **1993**, *30*, 155.

139 (a) Gavin, R.M., Jr.; Bartell, L.S. *J. Chem. Phys.* **1968**, *48*, 2460; (b) Bartell, L.S.; Gavin, R.M., Jr. *J. Chem. Phys.* **1968**, *48*, 2466.

140 Christe, K.O.; Wilson, W.W.; Drake, G.W.; Dixon, D.A.; Boatz, J.A.; Gnann, R.Z. *J. Am. Chem. Soc.* **1998**, *120*, 4711.

141 Christe, K.O.; Curtis, E.C.; Dixon, D.A.; Mercier, H.P.A.; Sanders, J.C.P.; Schrobilgen, G.J. *J. Am. Chem. Soc.* **1991**, *113*, 3351.

142 Holloway, J.H.; Kaučič, V.; Martin-Rouvet, D.; Russell, D.R.; Schrobilgen, G.J.; Selig, H. *Inorg. Chem.* **1985**, *24*, 678.

143 Christe, K.O.; Dixon, D.A.; Sanders, J.C.P.; Schrobilgen, G.J.; Tsai, S.S.; Wilson,

W.W. *Inorg. Chem.* **1995**, *34*, 1868.

144 (a) Kepert, D.L. *Inorganic Stereochemistry*; Springer-Verlag: Berlin, 1982; (b) Kepert, D.L. In *Comprehensive Coordination Chemistry*; Wilkinson, G., Ed.; Pergamon: Oxford, 1987; Vol.1, Chapter 2, pp. 31.

145 Christe, K.O.; Dixon, D.A.; Sanders, J.C.P.; Schrobilgen, G.J.; Wilson, W.W. *J. Am. Chem. Soc.* **1993**, *115*, 9461.

146 Lin, Z.; Bytheway, I. *Inorg. Chem.* **1996**, *35*, 594.

147 Gillespie, R.J.; Schrobligen, G.J. *J. Chem. Soc., Chem. Commun.* **1977**, 595.

148 Gerken, M.; Schrobilgen, G.J. *Coord. Chem. Rev.* **2000**, *197*, 335.

149 Jacob, E.; Opferkuch, R. *Angew. Chem.* **1976**, *88*, 190; *Angew. Chem., Int. Ed. Engl.* **1976**, *15*, 158.

150 Ogden, J.S.; Turner, J.J. *J. Chem. Soc., Chem. Commun.* **1966**, 693.

151 Mercier, H.P.A.; Sanders, J.C.P.; Schrobilgen, G.J.; Tsai, S.S. *Inorg. Chem.* **1993**, *32*, 386.

152 Gillespie, R.J.; Landa, B.; Schrobilgen, G.J. *J. Chem. Soc., Chem. Commun.* **1972**, 607.

153 Gillespie, R.J.; Schrobilgen, G.J. *Inorg. Chem.* **1974**, *13*, 2370.

154 McKee, D.E.; Adams, C.J.; Zalkin, A.; Bartlett, N. *J. Chem. Soc., Chem. Commun.* **1973**, 26.

155 Gillespie, R.J.; Landa, B.; Schrobilgen, G.J. *Inorg. Chem.* **1976**, *15*, 1256.

156 Pointner, B.E. personal communication

157 Schumacher, G.A.; Schrobilgen, G.J. *Inorg. Chem.* **1984**, *23*, 2923.

158 Tsao, P.; Cobb, C.C.; Claassen, H.H. *J. Chem. Phys.* **1971**, *54*, 5247.

159 Claassen, H.H.; Chernick, C.L.; Malm, J.G. In *Noble Gas Compounds*; Hyman, H.H., Ed.; The University of Chicago Press: Chicago, 1963; pp 287.

160 Martins, J.F.; Wilson, E.B., Jr. *J. Mol. Spectrosc.* **1968**, *26*, 410.

161 Christe, K.O.; Wilson, W.W. *Inorg. Chem.* **1988**, *27*, 2714.

162 Peterson, S.W.; Willett, R.D.; Huston, J.L. *J. Chem. Phys.* **1973**, *59*, 453.

163 Claassen, H.H.; Gasner, E.L.; Kim, H.; Huston, J.L. *J. Chem. Phys.* **1968**, *49*, 253.

164 Christe, K.O.; Wilson, W.W. *Inorg. Chem.* **1988**, *27*, 3763.

165 Hodgson, D.J.; Ibers, J.A. *Inorg. Chem.* **1969**, *8*, 326.

166 LaBonville, P.; Ferraro, J.R.; Spittler, T.M. *J. Chem. Phys.* **1971**, *55*, 631.

167 Emara, A.A.A.; Schrobilgen, G.J. *Inorg. Chem.* **1992**, *31*, 1323.

168 Schrobilgen, G.J Ph.D. Thesis, McMaster University, Hamilton, Canada, **1973**.

169 Winfield, J.M. *J. Fluorine Chem.* **1984**, *25*, 91.

170 Bez'melnitsyn, V.N.; Legasov, V.A; Chainvanov, B.B. *Proc. Acad. Sci. USSR (Engl. Trans.)* **1977**, *235*, 365; *Dokl. Adad. Nauk. SSSR* **1977**, *235*, 96.

171 Kinhead, S.A.; Fitzpatrick, J.R.; Foropoulos, J., Jr.; Kissane, R.J.; Purson, J.D. In *Inorganic Fluorine Chemistry, Towards the 21st Century, ACS Symposium Series 555*; Thrasher, J.S., Strauss, S.H., Eds.; ACS: Washington, D.C., 1994; pp.40.

172 Christe, K.O.; Wilson, W.W.; Wilson, R.D.; Bau, R.; Feng, J.-a. *J. Am. Chem. Soc.* **1990**, *112*, 7619.

173 Christe, K.O.; Wilson, W.W. *J. Fluorine Chem.* **1990**, *47*, 117.

174 Gillespie, R.J.; Landa, B. *Inorg. Chem.* **1973**, *12*, 1383.

175 Christe, K.O.; Schack, C.J.; Wilson, R.D. *Inorg. Chem.* **1975**, *14*, 2224.

176 Jaselskis, B; Spittler, T.M.; Huston, J.L *J. Am. Chem. Soc.* **1966**, *88*, 2149.

177 SMART and SAINT, release 4.05; Siemens Energy and Automation Inc.; Madison, WI, 1996.

178 Sheldrick, G.M. SADABS (Siemens Area Detector Absorption Corrections), personal communication, 1996.

179 Sheldrick, G.M. SHELXTL-Plus, Release 5.03, Siemens Analytical X-ray Instruments, Inc.; Madison, WI, 1994.

180 Gunn, S.R. In *Noble Gas Compounds*; Hyman, H.H., Ed.; The University of Chicago Press: Chicago, 1963; pp. 149.

181 (a) Templeton, D.H.; Zalkin, A.; Forrester, J.D.; Williamson, S.M. *J. Am. Chem. Soc.* **1963**, *85*, 817; (b) Templeton, D.H.; Zalkin, A.; Forrester, J.D.; Williamson, S.M. In *Noble Gas Compounds*; Hyman, H.H., Ed.; The University of Chicago Press: Chicago, 1963; pp. 229.

182 Spittler, T.M.; Jaselskis, B. *J. Am. Chem. Soc.* **1965**, *87*, 3357.

183 Jaselskis, B.; Spittler, T.M.; Huston, J.L. *J. Am. Chem. Soc.* **1966**, *88*, 2149.

184 Ratcliffe, C.I. *Annu. Rep. NMR Spec.* **1998**, *36*, 123.

185 (a) Raftery, D.; Chmelka, B.F. *NMR Basic Principles and Progress* **1994**, *30*, 111; (b) Dybowski, C.; Banal, N.; Duncan, T.M. *Annu. Rev. Phys. Chem.* **1991**, *42*, 433.

186 Luhmer, M.; Reisse, J. *Prog. NMR Spectrosc.* **1998**, *33*, 57.

187 Seppelt, K.; Rupp, H.H. *Z. Anorg. Allg. Chem.* **1974**, *409*, 331.

188 Jameson, C.J.; Gutowsky, H.S. *J. Chem. Phys.* **1964**, *40*, 1714.

189 Dove, M.F.A.; Sanders, J.C.P.; Appelman, E.H. *Magn. Res. Chem.* **1995**, *33*, 44.

190 Reuben, J.; Samuel, D.; Selig, H.; Shamir, J. *Proc. Chem. Soc.* **1963**, 270.

191 Figgis, B.N.; Kidd, R.G.; Nyholm, R.S. *Proc. Roy. Soc., London* **1962**, *269A*, 269.

192 Mason, J. *Multinuclear NMR*; Plenum Press: New York, 1987; pp. 625.

193 Akitt, J.W.; Greenwood, N.N.; Storr, A. *J. Chem. Soc.* **1965**, 4410.

194 Morgan, K.; Sayer, B.G.; Schrobilgen, G.J. *J. Magn. Res.* **1983**, *52*, 139.

195 Pyykkö, P.; Li, J. Report HUKI 1-92, ISSN 0784-0365, 1992.

196 Wehrli, F. *J. Magn. Res.* **1978**, *30*, 193.

197 Seppelt, K.; Rupp, H.H. *Z. Anorg. Allg. Chem.* **1974**, *409*, 338.

198 Ingman, L.P.; Jokisaari, J.; Oikarinen, K.; Seydoux, R. *J. Magn. Res., Ser. A* **1994**, *111*, 155.

199 (a) Schrobilgen, G.J. In *The Encyclopadia of Nuclear Magnetic Resonance*; Grant, D.M., Harris, R.K., Eds.; Wiley: New York, 1996; pp. 3251; (b) Jameson, C.J. In *Multinuclear NMR*; Mason, J., Ed.; Plenum Press: New York, 1987; pp. 463; (c) Schrobilgen, G.J. In *NMR and the Periodic Table*; Harris, R.K., Mann, B.E., Eds.; Academic Press: London, 1979; pp. 439.

200 (a) Günthard, H.H.; Kováts, E. *Helv. Chim. Acta* **1952**, *35*, 1190; (b) Yamadera, R.; Kremm, S. *Spectrochim. Acta* **1968**, *24A*, 1677.

201 Berg, R.W. *Spectrochim. Acta* **1978**, *34A*, 655.

202 Kabisch, G. *J. Raman Spectrosc.* **1980**, *9*, 279.

203. Huston, J.L. *J. Phys. Chem.* **1967**, *71*, 3339.

204. Jameson, C.J.; Mason, J. In *Multinuclear NMR*; Mason, J., Ed.; Plenum Press: New York, 1987; pp. 51.

205. Gillespie, R.J.; Schrobilgen, G.J. *Inorg. Chem.* **1974**, *766*, 765.

206. Akitt, J.W.; McDonald, W.S. *J. Magn. Res.* **1984**, *58*, 401.

207. Frame, H.D. *Chem. Phys. Lett.* **1969**, *3*, 182.

208. Gillespie, R.J.; Netzer, A.; Schrobilgen, G.J. *Inorg. Chem.* **1974**, *13*, 1455.

209. Appelman, E.H.; Anbar, M. *Inorg. Chem.* **1965**, *4*, 1066.

210. (a) Stephenson, C.V.; Jones, E.A. *J. Chem. Phys.* **1952**, *20*, 135; (b) Magnuson, D.W. *J. Chem. Phys.* **1951**, *19*, 1071.

211. Smith, D.F.; Magnuson, D.W. *Phys. Rev.* **1952**, *87*, 226.

212. Pauling, L. *The Nature of the Chemical Bond*, 3rd. ed.; Cornell University Press: Ithaca, NY, 1960; p. 260.

213. Bondi, A. *J. Phys. Chem.* **1964**, *68*, 441.

214. Krebs, B.; Hasse, K.-D. *Acta Crystallogr.* **1976**, *B32*, 1334.

215. Gerken, M.; Dixon, D.A.; Schrobilgen, G.J. *Inorg. Chem.* **2000**, *39*, in press.

216. Kuhlmann, W.; Sawodny, W. *J. Fluorine Chem.* **1977**, *9*, 341.

217. Dehnicke, K.; Pausewang, G.; Rüdorff, W *Z. Anorg. Allg. Chem.* **1969**, *366*, 64.

218. Kaskel, S.; Strähle, J. *Z. Anorg. Allg. Chem.* **1997**, *623*, 456.

219. Fourquet, J.L.; Duroy, H.; Crosnier-Lopez, M.P. *Z. Anorg. Allg. Chem.* **1997**, *623*, 439.

220. Aynsley, E.E.; Hair, M.L. *J. Chem. Phys.* **1958**, 3747.

221. Selig, H.; El-Gad, U. *J. Inorg. Nucl. Chem.* **1973**, *35*, 3517.

222. Beattie, I.R.; Crocombe, R.A.; Ogden, J.S. *J. Chem. Soc., Dalton Trans.* **1977**, 1481.

223. Brisdon, A.K.; Holloway, J.H.; Hope, E.G.; Townson, P.J.; Levason, W.; Ogden, J.S. *J. Chem. Soc., Dalton Trans.* **1991**, 3127.

224. Lotspeich, J.F.; Javan, A.; Engelbrecht, A. *J. Chem. Phys.* **1959**, *31*, 633.

225. (a) Dean, P.A.W.; Gillespie, R.J. *J. Am. Chem. Soc.* **1969**, *91*, 7260; (b) Bacon,

J.; Dean, P.A.W.; Gillespie, R.J. *Can. J. Chem.* **1970**, *48*, 3413.

226 Mazej, Z.; Bormann, H.; Lutar, K.; Žemva, B. *Inorg. Chem.* **1998**, *37*, 5912.

227 Roesky, H.W.; Sotoodeh, M.; Xu, Y.M.; Schrumpf, F.; Noltemeyer, M. *Z. Anorg. Allg. Chem.* **1990**, *580*, 131.

228 Wilson, W.W.; Christe, K.O.; Feng, J.-a.; Bau, R. *Can. J. Chem.* **1989**, *67*, 1898.

229 Braun, T.; Foxon, S.P.; Perutz, R.N.; Walton, P.H. *Angew. Chem.* **1999**, *38*, 3326; *Angew. Chem., Int. Ed. Engl.* **1999**, *111*, 3543.

230 Whittlesey, M.K.; Perutz, R.N.; Greener, B.; Moore, M.H. *J. Chem. Soc., Chem. Commun.* **1997**, 187.

231 Murphy, V.J.; Hascall, T.; Chen, J.Y.; Parkin, G. *J. Am. Chem. Soc.* **1996**, *118*, 7428.

232 Murphy, V.J.; Rabinovich, D.; Hascall, T.; Klooster, W.T.; Koetzle, T.F.; Parkin, G. *J. Am. Chem. Soc.* **1998**, *120*, 4372.

233 Faggiani, R.; Kennepohl, D.K.; Lock, C.J.L.; Schrobilgen, G.J. *Inorg. Chem.* **1986**, *25*, 563.

234 Drews, T.; Seppelt, K. *Angew. Chem.* **1997**, *109*, 264; *Angew. Chem., Int. Ed. Engl.* **1997**, *36*, 273.

235 Edwards, A.J.; Jones, G.R.; Sills, R.J. *J. Chem. Soc., Chem. Commun.* **1968**, 1527.

236 Chen, G.S.H.; Passmore, J. *J. Chem. Soc., Dalton Trans.* **1979**, 1251.

237 Schrobilgen, G.J.; Holloway, J.H.; Russell, D.R. *J. Chem. Soc., Dalton Trans.* **1984**, 1411.

238 Gillespie, R.J.; Schrobilgen, G.J. *Inorg. Chem.* **1976**, *15*, 22.

239 Holloway, J.H.; Hope, E.G.; Raynor, J.B.; Townson, P.T. *J. Chem. Soc., Dalton Trans.* **1992**, 1131.

240 Brusset, H.; Dao, N.Q.; Knidiri, M. *Spectrochim. Acta* **1975**, *21A*, 1819.

241 Abrahams, S.C.; Bernstein, J.L. *J. Chem. Phys.* **1976**, *64*, 3254.

242 Turowsky, L.; Seppelt, K. *Z. Anorg. Allg. Chem.* **1992**, *609*, 153.

243 Gillespie, R.J.; Robinson, E.A. *Angew. Chem.* **1996**, *108*, 539; *Angew. Chem., Int. Ed. Engl.* **1996**, *35*, 495.

244. (a) Carter, H.A.; Aubke, F. *Inorg. Chem.* **1971**, *10*, 2301; (b) Finch, A.; Gates, P.N.; Jenkinson, M.A. *J. Fluorine Chem.* **1972**, *2*, 111.

245. Minkwitz, R.; Nowicki, G. *Angew. Chem.* **1990**, *102*, 692; *Angew. Chem., Int. Ed. Engl.* **1990**, *29*, 688.

246. The ^{17}O NMR spectrum of enriched $[H_3O][AsF_6]$ (21.9% ^{17}O and 42.7% ^{18}O) in the presence of XeF_4 in HF solvent at -10 °C shoed a quartet at -0.76 ppm, $^{1}J(^{19}F\text{-}^{1}H)$ = 103 Hz. The previously reported ^{17}O chemical shift for H_3O^+ of 10.2 ppm was recorded in SO_2 solvent at -20 °C (Olah, G.A.; Berrier, A.L.; Surya Prakash, G.K. *J. Am. Chem. Soc.* **1982**, *104*, 2373.)

247. Sladky, F. *Monatsh. Chem.* **1970**, *101*, 1559.

248. Bartlett, N.; Wechsberg, M.; Sladky, F.O.; Bulliner, P.A.; Jones, G.R.; Burbank, R.D. *J. Chem. Soc., Chem. Commun.* **1969**, 703.

249. Wechsberg, M.; Bulliner, P.A.; Sladky, F.O.; Mews, R.; Bartlett, N. *Inorg. Chem.* **1972**, *11*, 3063.

250. LeBlond, R.D.; DesMarteau, D.D. *J. Chem. Soc., Chem. Commun.* **1974**, 555.

251. Emara, A.A.A.; Schrobilgen, G.J. *J. Chem. Soc., Chem. Commun.* **1988**, 257.

252. Schrobilgen, G.J.; Whalen, M. *Inorg. Chem.* **1994**, *33*, 5207.

253. Argon, P.A.; Begun, G.M.; Levy, H.A.; Mason, A.A.; Jones, C.G.; Smith, D.F. *Science* **1963**, *139*, 842.

254. Schrobilgen, G.J. *J. Chem. Soc., Chem. Commun.* **1988**, 1506.

255. Keller, N.; Schrobilgen, G.J. *Inorg. Chem.* **1981**, *20*, 2118.

256. Minkwitz, R.; Molsbeck, W. *Z. Anorg. Allg. Chem.* **1992**, *612*, 35.

257. Sladky, F. *Monatsh. Chem.* **1970**, *101*, 1571.

258. Syvret, R.G.; Schrobilgen, G.J. *Inorg. Chem.* **1989**, *28*, 1564.

259. Holloway, J.H.; Schrobilgen, G.J. *Inorg. Chem.* **1981**, *20*, 3363.

260. Fir, B.A.; Gerken, M.; Pointner, B.E.; Mercier, H.P.A.; Dixon, D.A.; Schrobilgen, G.J. *J. Fluorine Chem.* **2000**, *105*, 159.

261. Cohen, S.; Selig, H.; Gut, R. *J. Fluorine Chem.* **1982**, *20*, 349.

262. Mootz, D.; Wiebcke, M. *Inorg. Chem.* **1986**, *25*, 3095.

263 Jones, G.R.; Burbank, R.D.; Bartlett, N. *Inorg. Chem.* **1970**, *9*, 1970.

264 Burns, J.H.; Ellison, R.D.; Levy, H.A. *Acta Crystallogr.* **1965**, *18*, 11.

265 Bartlett, N.; Wechsberg, M. *Z. Anorg. Allg. Chem.* **1971**, *385*, 5.

266 Turowsky, L.; Seppelt, K. *Inorg. Chem.* **1990**, *29*, 3226.

APPENDIX

Table A. Atomic Coordinates (x 10^4) and Equivalent Isotropic Displacement Parameters (pm^2 x 10^{-1}) in $[N(CH_3)_4][OsO_4F]$, $[N(CH_3)_4][OsO_3F_3]$, $[OsO_3F][AsF_6]$, $[OsO_3F][HF]_2[AsF_6]$, $[OsO_3F][HF][SbF_6]$, $[OsO_3F][Sb_3F_{16}]$, $[N(CH_3)_4]_2[HF_2][IO_2F_2]$, $[H_2OXeF]_2[F][AsF_6]$, trigonal $[Xe_2F_3][AsF_6]$, and $[Xe_3OF_3][AsF_6]$

	x	y	z	U(eq)[a]
		$[N(CH_3)_4][OsO_4F]$		
Os(1)	9456(1)	2500	1887(1)	17(1)
F(1)	6548(13)	2500	2231(9)	46(2)
O(1)	11840(13)	2500	2232(7)	26(2)
O(2)	9509(16)	2500	356(11)	46(3)
O(3)	8827(15)	1233(8)	2624(9)	51(2)
N(1)	5000	0	4221(9)	20(2)
C(1)	4060(16)	-891(8)	5006(9)	28(2)
C(2)	3589(18)	601(10)	3444(9)	35(2)
H(1C)	3124(16)	-511(8)	5525(9)	42
H(1D)	5010(16)	-1275(8)	5513(9)	42
H(1E)	3434(16)	-1469(8)	4494(9)	42
H(2B)	2662(18)	995(10)	3958(9)	52
H(2C)	2946(18)	30(10)	2932(9)	52

Table A. continued...

	x	y	z	U(eq)[a]
H(2D)	4230(18)	1173(10)	2932(9)	52
		$[N(CH_3)_4][OsO_3F_3]$		
Os(1)	2020(1)	4656(1)	2034(1)	23(1)
F(1)	2086(9)	3199(8)	2116(14)	44(3)
O(2)	764(12)	4545(11)	23(16)	50(4)
N(2)	5000	2853(13)	7500	16(4)
O(3)	2295(12)	5913(8)	2159(16)	37(3)
N(1)	0	2187(16)	-2500	25(5)
O(1)	1585(13)	4595(11)	3020(19)	51(4)
F(2)	3544(9)	4475(8)	4099(13)	40(3)
C(3)	5650(15)	2213(13)	8989(19)	30(4)
C(1)	-522(16)	1539(15)	-3950(22)	36(5)
C(2)	-891(15)	2807(16)	-2827(24)	36(5)
C(4)	5796(15)	3502(14)	7633(23)	32(5)
F(3)	2784(10)	4418(8)	1312(14)	40(3)
H(3B)	5117(15)	1788(13)	8888(19)	44
H(3C)	6066(15)	2635(13)	9955(19)	44
H(3D)	6192(15)	1798(13)	9096(19)	44

Table A. continued...

	x	y	z	U(eq)[a]
H(1C)	73(16)	1133(15)	-3721(22)	54
H(1D)	-883(16)	1957(15)	-4904(22)	54
H(1E)	-1097(16)	1105(15)	-4167(22)	54
H(2C)	-1465(15)	2376(16)	-3038(24)	54
H(2D)	-1254(15)	3226(16)	-3781(24)	54
H(2E)	-542(15)	3226(16)	-1879(24)	54
H(4A)	6332(15)	3091(14)	7723(23)	48
H(4B)	6218(15)	3922(14)	8603(23)	48
H(4C)	5362(15)	3922(14)	6662(23)	48
		$[OsO_3F][AsF_6]$		
Os(1)	2278(1)	8360(1)	3743(1)	22(1)
As(1)	-2337(2)	9976(1)	1982(1)	19(1)
F(2)	-446(10)	8905(7)	2057(8)	31(2)
F(1)	2603(9)	9904(7)	3239(8)	28(2)
O(2)	4153(13)	8010(8)	4889(10)	31(2)
F(7)	-4143(9)	10992(7)	2012(9)	32(2)
F(3)	-751(10)	11089(8)	1741(11)	45(2)
O(1)	315(12)	7925(8)	4699(9)	26(2)

Table A. continued...

	x	y	z	U(eq)[a]
O(3)	2479(12)	7445(9)	2246(10)	28(2)
F(4)	-1991(11)	10128(7)	3935(8)	38(2)
F(5)	-3870(12)	8827(8)	2304(11)	48(2)
F(6)	-2624(10)	9744(8)	108(8)	40(2)
		$[OsO_3F][HF]_2[AsF_6]$		
Os(1)	9036(1)	893(1)	1474(1)	17(1)
As(1)	11825(2)	-3422(1)	1400(1)	16(1)
F(8)	13009(11)	-5260(6)	1682(3)	30(1)
F(4)	14363(10)	-3127(6)	888(2)	28(1)
F(7)	13570(10)	-2347(6)	2031(2)	27(1)
F(3)	10590(10)	-1445(5)	1075(2)	23(1)
F(1)	6636(10)	206(6)	809(3)	31(1)
O(3)	12343(12)	1155(6)	1648(3)	21(1)
F(5)	10033(11)	-4282(5)	721(3)	27(1)
F(6)	9237(10)	-3523(6)	1874(3)	28(1)
F(2)	10216(11)	1895(6)	461(2)	31(1)
O(2)	8186(12)	-185(7)	2141(3)	27(1)
O(1)	7864(12)	2795(7)	1621(3)	29(1)

Table A. continued...

	x	y	z	U(eq)[a]
F(9)	14284(11)	3284(6)	305(3)	31(1)
H(1)	12249	2588	379	282(144)
H(2)	14962	3203	0	38(33)
		$[OsO_3F][HF][SbF_6]$		
Sb(1)	7110(3)	9314(2)	3574(1)	13(1)
Os(1)	13359(1)	4340(1)	3452(1)	15(1)
Os(2)	3179(2)	9018(1)	1213(1)	16(1)
Sb(2)	9054(3)	4369(2)	1046(1)	14(1)
F(1)	11152(31)	4878(13)	2152(10)	19(3)
O(1)	15793(36)	5307(20)	3142(13)	22(4)
O(2)	14663(33)	3624(17)	4390(12)	18(4)
O(3)	11353(32)	5540(16)	3776(11)	15(4)
F(2)	9841(26)	3082(14)	3579(9)	19(3)
F(4)	13474(25)	2806(13)	2733(9)	15(3)
F(21)	9035(29)	8843(16)	4622(10)	26(3)
F(22)	5540(31)	10807(14)	4076(11)	21(4)
F(23)	8571(28)	7990(14)	2915(10)	20(3)
F(24)	4343(30)	8157(16)	3695(10)	28(4)

Table A. continued...

	x	y	z	U(eq)[a]
F(25)	5236(28)	9960(14)	2444(9)	17(3)
F(26)	9680(30)	10647(13)	3331(11)	16(3)
F(10)	6538(30)	5577(14)	1359(11)	20(3)
F(11)	10511(31)	5832(14)	491(11)	21(4)
F(12)	11864(27)	3227(14)	803(9)	22(3)
F(13)	7821(31)	2924(16)	1672(11)	27(4)
F(14)	7072(28)	3866(15)	11(10)	20(3)
O(10)	1584(36)	8593(19)	224(12)	24(4)
O(11)	6383(36)	8773(19)	1023(12)	28(4)
F(31)	954(30)	10280(16)	1582(10)	25(3)
F(30)	4116(31)	11073(16)	607(10)	27(4)
O(14)	2650(35)	7625(18)	1845(12)	24(4)
		$[OsO_3F][Sb_3F_{16}]$		
Os(1)	0	0	0	34(1)
OFA	874(24)	977(24)	-1370(37)	47(7)
FOA	874(24)	977(24)	-1370(37)	47(7)
Sb(1)	-5000	0	-1158(7)	39(1)
F(1)	-3990(44)	703(44)	-3002(39)	37(12)

Table A. continued...

	x	y	z	U(eq)[a]
F(2)	-6032(40)	1486(42)	-1443(57)	60(6)
F(3)	-4217(43)	1190(43)	446(52)	60(6)
Sb(2)	-2678(3)	2322(3)	-3835(6)	42(1)
F(10A)	-1615(64)	1354(54)	-2498(78)	60(6)
F(10B)	-1721(64)	1708(57)	-1891(74)	60(6)
F(11A)	-1803(47)	929(48)	-5082(80)	60(6)
F(11B)	-2370(51)	1298(51)	-5733(62)	60(6)
F(12)	-1466(25)	3534(25)	-4421(48)	59(10)
		$[N(CH_3)_4]_2[HF_2][IO_2F_2]$		
I(1)	2101(1)	5000	7392(1)	22(1)
O(1)	2841(1)	3398(2)	8218(1)	41(1)
F(2)	1195(2)	5000	8110(2)	45(1)
F(1)	2930(2)	5000	6590(2)	45(1)
N(1)	1683(2)	5000	3518(2)	26(1)
C(2)	1260(3)	5000	2295(3)	37(1)
C(3)	1303(2)	3582(3)	3831(2)	34(1)
F(3)	709(1)	7194(2)	5874(1)	44(1)
C(5)	7168(3)	5000	9148(3)	41(1)

Table A. continued...

	x	y	z	U(eq)[a]
C(6)	5651(2)	6415(3)	8975(2)	39(1)
C(4)	5505(3)	5000	7381(3)	37(1)
N(2)	5999(2)	5000	8619(2)	27(1)
C(1)	2865(3)	5000	4124(4)	41(1)
H(62)	5854(20)	7273(32)	8702(22)	32(7)
H(22)	581(34)	5000	1980(32)	36(10)
H(21)	1490(20)	4159(28)	2120(20)	30(7)
H(33)	1593(20)	3616(29)	4595(23)	30(6)
H(52)	7336(24)	5841(35)	8878(26)	50(9)
H(42)	5711(22)	5897(31)	7177(23)	42(7)
H(32)	556(22)	3649(30)	3433(21)	34(7)
H(12)	3059(25)	4128(35)	3893(27)	56(9)
H(11)	3084(31)	5000	4928(36)	43(11)
H(51)	7488(33)	5000	9955(37)	43(11)
H(41)	4754(31)	5000	7045(31)	29(9)
H(31)	1572(19)	2619(33)	3604(21)	32(6)
H(62)	6003(20)	6419(28)	9764(22)	29(6)
H(61)	4896(26)	6431(34)	8619(26)	48(8)
H(1)	0	7175(66)	5000	93(18)

Table A. continued...

	x	y	z	U(eq)[a]
		$[H_2OXeF]_2[F][AsF_6]$		
Xe(1)	2500	2500	2500	23(1)
As(1)	5000	-5000	5000	25(1)
F(1)	3824(4)	1176(4)	3361(3)	50(2)
O(1)	3824(4)	1176(4)	3361(3)	50(2)
F(4)	4060(8)	-3302(7)	5000	77(2)
F(3)	5000	-5000	6319(4)	40(1)
F(2)	5000	0	5000	60(3)
		trigonal $[Xe_2F_3][AsF_6]$		
Xe(1)	3925(1)	2188(1)	7825(1)	37(1)
As(1)	0	3630(2)	8333	29(1)
F(2)	5471(17)	4185(15)	8854(10)	71(3)
F(1)	2010(24)	-280(25)	7063(14)	50(5)
F(5)	-2271(24)	2476(26)	7913(17)	83(5)
F(4)	0	1631(21)	8333	53(4)
F(3)	0	5689(20)	8333	53(4)
F(6)	757(27)	4062(25)	6828(19)	92(5)
F(7)	-588(47)	1822(48)	7378(32)	65(8)

Table A. continued...

	x	y	z	U(eq)[a]
F(8)	-518(45)	4724(46)	7233(30)	62(8)
F(9)	-2238(35)	2561(35)	8881(25)	38(6)
		$[Xe_3OF_3][AsF_6]$		
As(1)	0	5000	5000	20(1)
Xe(2)	-4664(1)	7179(1)	-1477(1)	20(1)
F(1)	-6235(12)	8451(10)	-3032(10)	35(2)
F(2)	-3031(11)	5892(9)	242(11)	28(2)
O(1)	-3031(11)	5892(9)	242(11)	28(2)
Xe(1)	-360(3)	5158(3)	55(3)	21(1)
F(7)	-2470(19)	4559(20)	4217(22)	35(2)
F(5)	1649(23)	4154(20)	3893(21)	35(2)
F(8)	956(26)	3860(19)	3675(20)	35(2)
F(3)	339(30)	6642(16)	4086(22)	35(2)
F(4)	-2056(22)	4661(20)	3581(20)	35(2)
F(6)	-83(31)	6439(17)	3705(20)	35(2)

[a] U(eq) is defined as one third of the trace of the orthogonalized U_{ij} tensor.